ECCENTRIC COMPACT BINARIES: MODELING THE INSPIRAL AND GRAVITATIONAL WAVE EMISSION

by

Nicholas Peter Loutrel

A dissertation submitted in partial fulfillment
of the requirements for the degree

of

Doctor of Philosophy

in

Physics

MONTANA STATE UNIVERSITY
Bozeman, Montana

April 2018

DEDICATION

I dedicate this to my parents, Brian Charles Loutrel & Annette Marie Manzo Loutrel; without their endless love and support, this dissertation would not be possible.

ACKNOWLEDGEMENTS

I would like to thank my Ph.D. advisor, Nicolás Yunes (NY), for providing invaluable advice and helping me become a professional researcher. Further, I would like to thank K. G. Arun, Alejandro Cardenas-Avendaño, Katerina Chatziioannou, Neil Cornish, Samuel Liebersbach, Sean McWilliam, and Frans Pretorius (FP) for supporting this work through discussions and collaborations.

This research was supported by National Science Foundation grants PHY-1065710 (FP), PHY-1305682 (FP), PHY-1114374 (NY), PHY-1250636 (NY), EAPSI Award No. 1614203, NASA grant NNX11AI49G, under sub-award 00001944 (FP and NY), the Simons Foundation (FP).

TABLE OF CONTENTS

TABLE OF CONTENTS – CONTINUED

LIST OF TABLES

LIST OF FIGURES

LIST OF FIGURES – CONTINUED

LIST OF FIGURES – CONTINUED

ABSTRACT

The modeling of the inpsiral and subsequent gravitational wave emission from black hole binary systems has been a long outstanding problem in astrophysics and relativity. Astrophysical models predict that most binaries will have low orbital eccentricity by the time the gravitational wave emission enters the detection band of ground based detectors, and significant success has been made by restricting attention to the this limit, where the binary's orbit is approximately circular. However, exotic formation channels in globular clusters and galactic nuclei predict a small, but non-negligible, fraction of systems will enter the detection band of ground-based detectors with significant orbital eccentricity. In this thesis, we present new methods of modeling eccentric binaries under the influence of gravitational wave emission, focusing on two regimes: (i) the early inspiral of highly eccentric binaries, and (ii) the late inspiral of generic eccentric binaries.

INTRODUCTION

There has never been a more exciting era for gravitational wave (GW) astrophysics. The advanced Laser Interferometer Gravitational Wave Observatory (aLIGO) [85] has made the first detection of GWs [19], and along with the advanced VIRGO detector [21], presented us with a new window through which to observe the universe. These detectors will be joined in the coming years by the KAGRA detector in Japan in 2018 [157], and the LIGO India detector in 2019 [158]. These instruments have already discovered the existence of black holes (BHs) with masses not previously observed [10, 16, 17, 19], restricted the event rates of binary BH mergers [12, 12, 15], placed constraints on modifications to General Relativity [13,18,181], and confirmed the hypothesis connecting kilonovae with binary neutron star (NS) mergers [9, 72, 122, 149]. In future observing runs, the aLIGO and aVIRGO detectors are expected to become more sensitive, increasing their ability to detect fainter signals and amplifying the scientific impact of these missions.

Thus far, the sources detected by ground-based interferometers have been the late inpsiral and coalescence of binary systems comprised of compact objects, specifically NSs and BHs. Over the past several decades, the following primary picture of such binaries has emerged: by the time the orbit has shrunk enough that the GWs emitted are in the sensitivity band of detectors, the binary will necessarily have extremely small orbital eccentricity ($e \ll 0.1$). This is expected because the quadrupolar nature of GWs makes them extremely efficient at circularizing binaries that form with large orbital separations, such as the Hulse-Taylor pulsar [91]. Further, the aLIGO detectors currently cannot measure eccentricities below $e \sim$

0.1 [54,90,145].

In more recent years, however, this view has been challenged. Studies of dense stellar environments, such as globular clusters and galactic nuclei, have shown that more exotic formation channels could lead to a population of binaries with non-negligible eccentricity ($e > 0.1$) that emit GWs in the sensitivity band of ground-based detectors [23–25, 96, 99, 120, 126, 141, 161]. Close encounters between two compact objects on unbound orbits could lead to dynamical captures, either through GW emission or tidal friction, which could have eccentricities close to unity [99, 126]. Similarly, close encounters between multiple objects could form hierarchical triple systems which, through Kozai-Lidov oscillations and other three-body resonances [23–25,96,120,120,141,161], can drive the inner binary to high eccentricity.

Currently, ground-based detectors are registering $\sim 3-5$ events per year, while plausible estimates of the event rates of the inspiral of compact object binaries predict $\sim 10-12$ events per year in the very near future [5, 12, 14]. Based on our current knowledge of the formation channels of eccentric compact binaries [23,24,26,96,100,121,126,141,162], we might expect that one or two of these events will enter the LIGO band with non-negligible orbital eccentricity. Although expected to be rare [5], eccentric binaries could prove to be powerful probes of astrophysical dynamics. Event rates of eccentric inspirals due to dynamical captures have wide error bars, typically around two orders of magnitude [126]. Such large error is primarily due to the unconstrained populations of compact objects within dense environments [5]. Likewise, the tightening of binaries due to three-body interactions in galactic nuclei are similarly uncertain [113]. Hence, the detection of GWs from eccentric inspirals would provide information about the mass function of black holes (BHs) and neutron stars (NSs) in these environments, allowing us to probe astrophysics that has proven difficult to extract from electromagnetic observations [125, 136, 144, 182].

Another promising area of interest for eccentric binaries is testing Einstein's theory of General Relativity (GR). For highly eccentric binaries, the distance of closest approach can be small relative to the semi-major axis of the orbit, leading to systems with pericenter velocities greater than 10% the speed of light. At such high velocities, the GW luminosity *in the inspiral phase* will typically be $\sim (10^{-4} - 10^{-3}) L_{\rm Pl}$, where $L_{\rm Pl}$ is the Planck luminosity. For comparison, a BH-BH, quasi-circular binary emits radiation at $\lesssim 10^{-5} L_{\rm Pl}$ during the early phase of inspiral, increasing rapidly close to merger and eventually reaching $\sim 10^{-2} L_{\rm Pl}$ only at merger. As such, the GWs from eccentric binaries could capture effects from the extreme gravity regime (i.e. where gravity is dynamical, strong and non-linear) during many pericenter passages [108].

What is the best way to detect such events? The most efficient method, assuming stationary and Gaussian noise, is matched filtering [4, 6, 7, 22, 53, 74, 159], provided one knows accurately the shape of the expected signal. In this search strategy, a set of theoretical models or *templates* are used to fit the data and extract the parameters of the model. To construct such templates, precise knowledge of the dynamics of the system generating the GWs is required. Inaccuracies in the templates can potentially throw off detection or systematically bias the recovered parameters [77, 138, 172, 176]. Currently, most matched-filtering searches use non-eccentric template families, which could miss non-eccentric signals altogether if the orbital eccentricity exceeds 0.05 [88, 89].

One potential solution is to construct eccentric template families. Numerical templates, calculated for example through the numerical solution to the post-Newtonian equations of motion, are computationally expensive and can be affected by numerical error in long evolutions. Analytic templates are, in principle, more computationally efficient and provide deeper insight into the physical processes that control GW emission, but their construction is mathematically difficult. Post-circular templates, valid in the small eccentricity limit, were developed in [173] and improved in [88, 118, 148, 150, 151], but by construction they are only valid for small eccentricity binaries.

For highly eccentric binaries, the GW emission resembles a set of discrete bursts somewhat localized in time and frequency. These bursts are centered around pericenter passage, where the orbital velocity is highest and where the binary spends the least amount of time, and thus very little GW power is contained within each individual burst. This issue alone makes matched filtering a rather impractical search strategy for such GWs, but it is further compounded by the fact that there are few, fully-analytic and accurate templates for highly eccentric binaries with which to perform matched filtering computationally efficiently [87, 88].

A promising, though sub-optimal, method of detecting GWs from highly elliptic binaries that relies less on accurate templates is power stacking [146]. If a set of N bursts is found within a detector's data stream, the power can be added within each burst, with the amplification[1] of the signal-to-noise ratio (SNR) scaling as $N^{1/4}$ (assuming all bursts have the same SNR.) Adding up the bursts in a sequence is crucial because any one burst will likely be very weak (SNRs of 1–2), unless the elliptical binary is absurdly close to Earth. Power stacking, however, only works if one has *prior knowledge* of where the bursts will occur in time-frequency space.

Such a burst model was developed in [108] for tracking the bursts in time-frequency space. In general, a burst model is one that treats the bursts as N-dimensional objects in the detector's data stream and tracks the geometric centroid and volume of the bursts from one to the next as the binary inspirals. To do this, [108]

---

[1] The scaling with N is a result of the stacking of power rather than amplitude as done in matched filtering.

considered Keplerian orbits perturbed by quadrupolar gravitational radiation. We will refer to this model as *Newtonian* in the sense that it is obtained from a fully relativistic model expanded to lowest, non-vanishing order about small orbital velocities and weak gravitational fields. The benefit of working in such a simplified scenario was that it allowed for the exploration of whether such burst signals could be used to test well-motivated deviations from GR with eccentric signals as a proof-of-concept.

The ultimate goal, of course, is to create a model that is as accurate as possible relative to the signals present in nature. The modeling of the coalescence of compact objects in full GR is an exceedingly difficult problem, which has only been solved numerically (predominantly for quasicircular binaries) in the past several years. For eccentric binaries, numerical simulations in full GR are more computationally expensive, and thus, to obtain only a few orbits at the desired numerical accuracy requires much more computational time than that needed in the evolution of quasicircular binaries. At least for the moment, the pure numerical modeling of eccentric binaries over the last thousand orbits in full GR is currently an intractable problem. On the other hand, we could work to extend the Newtonian burst model by considering relativistic corrections to Newtonian dynamics.

The post-Newtonian (PN) formalism [42, 59–61, 104, 131] allows for a systematic treatment of v/c corrections to Newtonian dynamics, where v is the orbital velocity and c is the speed of light. For bound binaries, the orbital velocity is connected to the gravitational field strength through a Virial relation: a term of $\mathcal{O}(v^2/c^2)$ is comparable to a term of $\mathcal{O}[GM/(Rc^2)]$, where M and R are the characteristic mass and orbital separation of the system, and G is Newton's gravitational constant. Hence, the PN formalism for binaries is simultaneously a post-Minkowskian expansion, i.e. it is both an expansion in $v/c \ll 1$ and an expansion in $GM/(Rc^2) \ll 1$. A term proportional to $(v/c)^{2N}$ relative to its controlling factor will be said to be of N PN order.

The PN formalism has had a wide range of success in the modeling of binaries and their GW emission. At present, the GW emission from quasicircular binaries has been calculated to 3.5 PN order [42] and to 4PN order in the effective one-body Hamiltonian [70]. To leading order in the mass ratio, the radiation fluxes at spatial infinity are currently known to 22 PN order [80], due to the formulaic nature of the calculation. The PN corrections to Newtonian dynamics for eccentric binaries have proven more difficult to calculate. Damour and Deruelle [67, 68] found a Keplerian parameterization of the solution to the 1PN order equations of motion in terms of the eccentric anomaly u. This quasi-Keplerian (QK) representation was extended to 2PN order in [163] and to 3PN order in [112].

The QK parametrization must be enhanced to include dissipation if one wishes to obtain accurate waveform models. This parameterization is a purely conservative representation of the orbital motion of eccentric binaries, because the orbital energy and angular momentum are assumed to be conserved. For eccentric binaries, the GW energy and angular momentum fluxes have been computed to full 3PN order [28, 31]. With these fluxes at hand and assuming small eccentricities ($e \lesssim 0.1$), Refs. [118, 150, 151, 174] constructed time-domain and frequency domain waveforms to 2PN order. Waveform templates also exist for higher eccentricity systems ($e \lesssim 0.4$), for example through the hybrid time-domain x-model of [87] and the hybrid frequency-domain model of [88]. These models, however are really not applicable to highly eccentric binaries.

Although power stacking is far more robust to systematic mismodeling error than matched filtering, it is still not immune [146], in particular when considering the accuracy of GW fluxes. The latter provide a radiation-reaction force in the PN formalism that forces the binary to inspiral, through the balance of the binary energy lost by the system to the energy carried away by GWs from the system. In template based searches, inaccurate GW fluxes introduce errors in the Fourier transform of the waveform through the stationary phase approximation used in the post-circular extensions [173] of the so-called TaylorF2 waveform family [88]. In power stacking searches, similar inaccuracies introduce an error in the evolution of the orbital elements as the orbit osculates due to the emission of bursts, affecting the time-frequency tracks of the burst model [108]. An accurate and complete treatment of the GW fluxes is clearly essential to extend any PN template family, the post-circular waveform family and the burst model to higher PN order.

In Ch. 2, we review the mathematical structures necessary to describe eccentric binaries in GR, starting with the mathematical formulation of radiation reaction. We discuss the generation of GWs through the time varying multipole moments of the binary system and the separation of the fluxes of radiation into instantaneous and hereditary contributions. In order to evaluate these, we present the QK parametrization of eccentric binaries at 1PN order. For hereditary effects, one must consider a Fourier decomposition of the multipole moments of the binary, which completes this chapter.

With the description of radiation reaction in hand, Ch. 3 presents the problem of evaluating hereditary effects for eccentric binaries and our solution for how to do this, which is published in Classical & Quantum Gravity in [107]. We begin the chapter with a discussion of the physical interpretations of the hereditary effects, and their mathematical description in terms of hereditary integrals and enhancement factors. The problem with evaluating hereditary effects for eccentric binaries relies on the need to work with a Fourier decomposition of the binary's multipole moments. In this formalism, enhancement factors become infinite summations of Bessel functions of the first kind, which do not lend themselves to resummation easily. In this chapter, we present the solution to the problem through asymptotic analysis and provide closed form expressions for the hereditary enhancement factors.

Once we have analytic expressions for the tail enhancement factors, the description of both the conservative and dissipative dynamics of eccentric binaries in GR is complete to 3PN order. We thus have all of the ingredients necessary to develop a model of the early inspiral of the highly eccentric binaries described above. In Ch. 4, we present the details of the so-called burst model, used to track the time-frequency centroids and volumes of the bursts as the binary evolves due to GW emission. We begin with the simple case of eccentric GW bursts at leading PN, or so-called Newtonian, order, before presenting the more complicated calculation up to 3PN order. This chapter is based on the work published in Classical & Quantum Gravity and Physical Review D [106, 108].

The construction of models for the GW emission of compact binary systems is not solely to detect such events, but to extract invaluable information about the astrophysical and gravitational dynamics of these systems. One of these important applications is to test GR, and as described above, eccentric binaries may provide improved constraints on modified theories of gravity. In Ch. 5, we present the details of a burst model in the parameterized post-Einsteinian formalism, which is published in Physical Review D in [108]. We show how one can parametrize generic deformation of the PN burst sequence due to generic non-GR effects, such as dipole radiation, and discuss how well one could constrain these deviations using such a model.

Finally, as eccentric binaries inspiral, the system loses orbital eccentricity due to the emission of GWs and is said to circularize. By the time the binary reaches the last stable orbit and enters the merger phase, the eccentricity is expected to be negligibly small. In Ch. 6, we present a detailed calculation of the behavior of the eccentricity in the late inspiral, before the binary reaches the last stable orbit. We include the effect of the radiation reaction force, which allows us to work beyond the usual orbit averaged approximation, and show that the eccentricity exhibits a strong secular growth several orbital cycles before the last stable orbit. We discuss how this behavior arises in a multiple scale analysis, and its possible impact on current and future GW observations. This chapter is based on work that has been submitted for publication in Physical Review Letters and may be found on the arXiv [105].

ECCENTRIC BINARIES IN GENERAL RELATIVITY

The problem of modeling compact binary systems within GR has a rich history, and eccentric binaries have proven particularly troublesome. Damour & Deruelle [67, 68] were the first to find an exact solution to the conservative dynamics of eccentric binaries within the PN formalism. Their work, known as the quasi-Keplerian formalism, was later adopted as the standard formalism for performing any calculations of eccentric binaries in PN theory due to the physical peculiarities that plagued other methods [103, 131]. The dissipative dynamics, due to the emission of GWs, were studied as early as 1964 by Peters to leading PN order [129]. The need for high PN order calculations was not realized until much later. Currently, both the conservative and dissipative dynamics, not including memory contributions, are known completely up to 3PN [28, 29, 31, 107, 112], with limited results available at 4PN order [34, 35, 110, 111]. This chapter provides a brief review of the dynamics of eccentric binaries within the PN formalism.

Radiation Reaction in General Relativity

We begin by providing a review of the mathematical structure of the GW fluxes and the machinery that is necessary to evaluate them, including a description of the quasi-Keplerian (QK) parameterization and orbit-averaging.

Basics

Consider a binary of compact objects inspiralling due to the emission of gravitational radiation. As the GWs propagate to spatial infinity, they extract orbital energy, E, and angular momentum, L_i, from the binary. The loss of orbital energy and angular momentum are given by the balance laws [41],

$$\frac{dE}{dt} = -\mathcal{P}\,, \quad \frac{dL_i}{dt} = -\mathcal{G}^i = -\frac{1}{2}\epsilon_{ijk}\mathcal{G}^{jk} = -\mathcal{G}\ \hat{L}^i\,, \tag{2.1}$$

where ϵ_{ijk} is the three-dimensional Levi-Civita symbol, while $\mathcal{P}$ and $\mathcal{G}^{jk}$ are the energy and angular momentum flux due to the emission of gravitational radiation. Typically, these quantities have two components. The first are the fluxes of energy and angular momentum that reach spatial infinity, specifically $\mathcal{P}_\infty$ and $\mathcal{G}^{jk}_\infty$. The second occurs in binary systems where at least one component is a BH, specifically the energy and angular momentum fluxes through the BH's horizon, $\mathcal{P}_H$ and $\mathcal{G}^{jk}_H$ [114]. However, the fluxes through the horizon are typically small compared to the fluxes to spatial infinity, and we thus neglect them here.

The energy and angular momentum fluxes to spatial infinity can be calculated using the short-wave approximation [92, 93, 131],

$$\mathcal{P}_\infty = \frac{1}{32\pi}\oint_{R\to\infty} R^2 \left(\partial_{t_R} h^{jk}_{\rm TT} \partial_{t_R} h^{\rm TT}_{jk}\right) d\Omega\,, \tag{2.2}$$

$$\mathcal{G}^{jk}_\infty = \frac{1}{16\pi}\oint_{R\to\infty} R^2 \left[2 h^{p[j}_{\rm TT}\partial_{t_R} h^{k]{\rm TT}}_{p} - \partial_{t_R} h^{pq}_{\rm TT} x^{[j}\partial^{k]} h^{\rm TT}_{pq}\right] d\Omega\,, \tag{2.3}$$

where h_{jk} is a metric perturbation (away from Minkowski spacetime) that describes GWs, $t_R = t - R$ is the retarded time of the binary, ∂_{t_R} denotes a partial derivative with respect to t_R, and [ ] corresponds to the anti-symmetrization of the appropriate indices. The TT symbol indicates that h_{jk} has been projected into the transverse traceless subspace, using

$$P_{ijkl} = P_{i(k}P_{l)j} - \frac{1}{2}P_{ij}P_{kl}\,, \tag{2.4}$$

$$P_{ij} = \delta_{ij} - N_i N_j \tag{2.5}$$

where $N_i = [\sin\theta\ \cos\phi, \sin\theta\ \sin\phi, \cos\theta]$ denotes the location of the source in the sky, and ( ) is the symmetrization of the corresponding indices.

In order to calculate what these fluxes are for the binaries under consideration, we first need to compute h_{jk}. Using the post-Minkowskian (PM) formulation [41, 43, 131, 154] to solve the relaxed Einstein field equations, h_{jk} is given to all orders by

$$h_{jk} = \frac{4}{R} \sum_{l=2}^{\infty} \frac{1}{l!} \left[N_{L-2} U_{jk}^{L-2}(t_R) - \frac{2l}{l+1} N^a_{L-2} \epsilon_{ab(j} V_{k)}^{bL-2}(t_R) \right] \tag{2.6}$$

where U_L and V_L are the mass and current-type radiative multipole moments [43, 131, 154]. The subscript L is shorthand notation for the multi-index $L = i_1 i_2 ... i_l$. Formally, the summation on l goes to infinity, but in practice it is truncated at some PM order. Since the PM and PN formalisms are interconnected, the PM order of truncation is typically taken to be the same as the PN order.

The radiative multipole moments U_L and V_L, which are functions of retarded time, are related to the source multipole moments by matching the wave zone and the near zone metric perturbations in an overlap or buffer region. For our purposes, the most important multipoles are the mass quadrupole and octopole, and the current quadrupole. As an example, the radiative mass quadrupole to 3PN order can be broken down as follows [46–49, 78]

$$U_{jk} = U_{jk}^{\text{inst}} + U_{jk}^{\text{tails}} + U_{jk}^{\text{mem}}\,, \tag{2.7}$$

where the instantaneous radiative mass quadrupole is related to the source multipoles by

$$\begin{aligned} U^{\rm inst}_{jk}(t_R) = {} & \ddot{I}_{jk} + \frac{1}{7}\overset{(5)}{I}_{a<j}I^a_{k>} - \frac{5}{7}\overset{(4)}{I}_{a<j}\dot{I}^a_{k>} - \frac{2}{7}\overset{(3)}{I}_{a<j}\ddot{I}^a_{k>} + \frac{1}{3}\epsilon_{ab<j}\overset{(4)}{I}{}^a_{k>}J^b \\ & + 4\frac{d^2}{dt^2}\left[\ddot{W}I_{jk} - \dot{W}\dot{I}_{jk}\right] . \end{aligned} \tag{2.8}$$

In this equation,

$$I_{jk} = \mu x_{<j}x_{k>} + \mathcal{O}(1\text{PN}) \tag{2.9}$$

is the source mass quadrupole, J_b is the source current dipole, W is the gauge monopole moment defined in [49] and the $<>$ brackets stand for the symmetric trace-free (STF) projection. Similarly, the radiative mass octopole and current quadrupole can be written in terms of the source mass octopole and the source current quadrupole

$$I_{jkl} = \mu\sqrt{1-4\eta}\; x_{<j}x_k x_{l>} + \mathcal{O}(1\text{PN})\,, \tag{2.10}$$

$$J_{jk} = \mu\sqrt{1-4\eta}\; \epsilon_{ab<j}x_{k>}x^a v^b + \mathcal{O}(1\text{PN})\,, \tag{2.11}$$

respectively. In Eq. (2.7), the tail and memory radiative mass quadrupoles are related to the source multipoles through

$$\begin{aligned} U^{\rm tails}_{jk}(t_R) = {} & 2M\int_0^\infty d\tau\,\overset{(4)}{I}_{jk}(t_R-\tau)\left[\ln\left(\frac{\tau}{2r_0}\right) + \frac{11}{12}\right] \\ & + 2M^2\int_0^\infty d\tau\,\overset{(5)}{I}_{jk}(t_R-\tau)\left[\ln^2\left(\frac{\tau}{2r_0}\right) + \frac{57}{70}\ln\left(\frac{\tau}{2r_0}\right) + \frac{124627}{44100}\right]\,, \end{aligned} \tag{2.12}$$

$$U^{\rm mem}_{jk}(t_R) = -\frac{2}{7}\int_0^\infty d\tau\,\overset{(3)}{I}_{a<j}(t_R-\tau)\overset{(3)}{I}{}^a{}_{k>}(t_R-\tau)\,. \tag{2.13}$$

where M is the Arnowitt-Deser-Misner (ADM) mass [132] corresponding to the total energy of the spacetime of the binary, and r_0 is a regularization factor that drops out after performing the integration and computing an observable. The contribution proportional to M in Eq. (2.12) is the 1.5PN[1] order tail term, while the term proportional to M^2 is the 3PN order tail-of-tail term. Notice that although the instantaneous contribution depends on the source multipoles evaluated only at retarded time t_R, the tail and memory contributions depend on the integrals of the source mass quadrupole over the lifetime of the source, and thus, they are referred to as *hereditary* terms.

Summarizing, the energy and angular momentum fluxes at spatial infinity can be computed by simply performing the TT projection of h_{jk} in Eq. (2.6), with the radiative multipole moments expressed in terms of the source multipole moment, and inserting the result into Eqs. (2.2) and (2.3) [28, 29, 31, 46–49]. Since the radiative multipoles can be split into instantaneous, tail, and memory contributions, we similarly split the fluxes as

$$\mathcal{P}_\infty = \mathcal{P}_\infty^{\text{inst}} + \mathcal{P}_\infty^{\text{tails}} + \mathcal{P}_\infty^{\text{mem}} \,, \tag{2.14}$$

$$\mathcal{G}_\infty = \mathcal{G}_\infty^{\text{inst}} + \mathcal{G}_\infty^{\text{tails}} + \mathcal{G}_\infty^{\text{mem}} \,, \tag{2.15}$$

and consider each of them separately. The instantaneous fluxes have been computed previously for arbitrary eccentricity and to 3PN order in [28,31]. In Ch. 3, we compute the tail and memory contributions to the fluxes to 3PN order.

Quasi-Keplerian Parametrization

The picture from the previous section is clear: the GWs emitted by a binary system depend on the time varying source multipole moments, and thus, if we desire to compute $\mathcal{P}_\infty$ and $\mathcal{G}_\infty$, we need to first calculate the orbital trajectories of the binary components. We recall that to obtain the fluxes to 3PN order, we only need

---

[1] Recall that this corresponds to a term thats $\mathcal{O}(v^3/c^3)$ relative to the leading order term.

the source moments to leading PN or *Newtonian* order, with the exception of the source mass quadrupole, which must be calculated to 1PN order. For this reason, we detail below the calculation of the orbital trajectories of the binary components also to 1PN order, although this can easily be extended to higher PN order if needed.

We begin by describing our binary system in more detail. Let the two objects in the binary have masses m_1 and m_2. For simplicity, we work in an effective one body frame where a body of mass $m = m_1 + m_2$ sits stationary at the center-of-mass of the binary, corresponding to the focus of an ellipse, and a smaller mass $\mu = m_1 m_2 / m$ moves around the ellipse. We take the system to be orbiting in the xy-plane, so that the orbital angular momentum is aligned with the z-axis. We take the longitude of pericenter to be zero, so that pericenter is aligned with the positive x-axis. The radius of the orbit r is the length of the line connecting μ and m, with the true anomaly V being the angle between the positive x-axis and r. Figure 2.1 details this, as well as the definition of the eccentric anomaly u, which is similar to the true anomaly only defined in an elliptical coordinate system.

The QK parametrization [67,68,71,112,140,163] provides a solution to the PN equations of motion that govern the orbital dynamics of the binary system by treating the orbits as Keplerian ellipses in a suitably chosen precessing reference frame. There are three equations that govern the solution to the equations of motion in the QK parametrization. The first is the radial equation:

$$r = a\left[1 - e_r \cos(u)\right] , \tag{2.16}$$

where r is the radius of the orbit, a is the semi-major axis of the Keplerian ellipse, e_r is the radial eccentricity, and u is the eccentric anomaly (see Fig. 2.1). The second is the

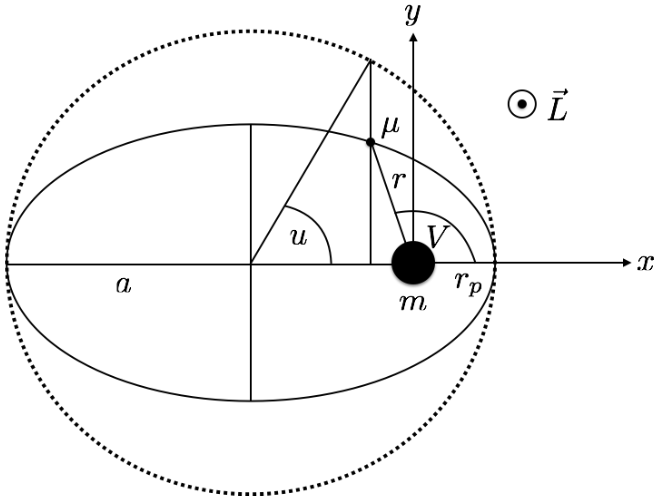

Figure 2.1: Diagram of Keplerian elliptical orbits in an effective one body frame. A point mass μ orbits around a central mass m located at the focus of the ellipse. The semi-major axis a, pericenter distance r_p, and orbital angular momentum $\vec{L}$ are constants of the orbit when radiation reaction is neglected. The orbital radius r is the line connecting m and μ, while the true anomaly V is the angle from pericenter, which is located along the x-axis, to r. The eccentric anomaly u is the angle measured from the x-axis to a line whose end points are the center of the ellipse and a point on a circle that is concentric to the ellipse and of radius a, where the end point on the circle is determined by a line parallel to the y-axis that passes through μ.

famous Kepler equation, which governs the time evolution of the eccentric anomaly,

$$\ell = u - e_t \sin(u) + \mathcal{O}(2\text{PN})\,, \tag{2.17}$$

where e_t is the temporal eccentricity, $\ell = n(t - t_p)$ is the mean anomaly, $n = 2\pi/P$ is the mean motion where P is the orbital period, and t_p is the time of pericenter passage. Finally, the azimuthal equation governs the evolution of the orbital phase ϕ,

$$\phi - \phi_p = KV(u) + \mathcal{O}(2\text{PN})\,, \tag{2.18}$$

where ϕ_p is the longitude of pericenter, K is the periastron advance due to relativistic precession, and $V(u)$ is the true anomaly given by [29, 69]

$$V(u) = u + 2 \arctan \left[\frac{\beta_\phi \sin(\mathrm{u})}{1 - \beta_\phi \cos(\mathrm{u})} \right] , \tag{2.19}$$

with

$$\beta_\phi = \frac{1 - \sqrt{1 - e_\phi^2}}{e_\phi} , \tag{2.20}$$

and e_ϕ the azimuthal eccentricity. At Newtonian order, all three of the eccentricities in the QK parametrization reduce to the Newtonian orbital eccentricity and $K = 1$. Although the radial equation [Eq. (2.16)] is valid to all PN orders, Eqs. (2.17) and (2.18) are only valid up to 1PN order. At higher PN orders, additional orbital elements appear in these equations that have no Newtonian analog and couple to higher harmonics of u and V.

The mass and current-type multipole moments depend on the orbital trajectory x_j and velocity v_j. Within the QK parametrization, these are simply

$$x_j = [r \cos(\phi), r \sin(\phi), 0] , \tag{2.21}$$

$$v_j = \frac{dx_j}{dt} . \tag{2.22}$$

The trajectory x_j can easily be expressed in terms of the eccentric anomaly through Eq. (2.16), and (2.18)-(2.20). The orbital velocity v_j requires us to calculate $\dot{r}$ and $\dot{\phi}$, which we now detail.

The presence of the various eccentricities can often complicate the analysis of quantities in the QK parametrization, so we choose one to work with and express all of the results in terms of it. The one most commonly used in the literature is e_t

(see [28, 29, 31, 69] for example), which is related to e_r and e_ϕ via

$$e_r = e_t \left[1 + \frac{x}{2}(8 - 3\eta)\right] , \tag{2.23}$$

$$e_\phi = e_t \left[1 + x(4 - \eta)\right] , \tag{2.24}$$

with $\eta = \mu/m$ is the symmetric mass ratio. The expansion parameter in PN theory for eccentric binaries is defined via $x := (m\omega)^{2/3}$, with $\omega = Kn$; at 1PN order, the PN expansion parameter becomes

$$x = \varepsilon - \frac{\varepsilon^2}{1 - e_t^2}\left[-\frac{3}{4} - \frac{\eta}{12} + e_t^2\left(-\frac{5}{4} + \frac{\eta}{12}\right)\right] , \tag{2.25}$$

where $\varepsilon = -2E/\mu > 0$ is the reduced orbital energy. We work in the regime $x \ll 1$ and expand all expressions accordingly, truncating at 1PN order. The reduced energy ε is also related to the semi-major axis a of the orbit through

$$a = \frac{m}{\varepsilon}\left[1 + \frac{\varepsilon}{4}\left(-7 + \eta\right)\right] . \tag{2.26}$$

Similarly, the mean motion n is

$$n = \frac{\varepsilon^{3/2}}{m}\left[1 + \frac{\varepsilon}{8}\left(-15 + \eta\right)\right] . \tag{2.27}$$

By combining Eq. (2.25) with Eqs. (2.26) and (2.27), we can write a and n in terms of x, specifically

$$a = \frac{m}{x}\left[1 - x\frac{3 - \eta + e_t^2\left(-9 + \eta\right)}{1 - e_t^2}\right] , \tag{2.28}$$

$$n = \frac{x^{3/2}}{m}\left(1 - \frac{3x}{1 - e_t^2}\right) . \tag{2.29}$$

The last variable we need to relate to x is k, which is simply

$$k = \frac{3x}{1-e_t^2}\,. \tag{2.30}$$

With all of the orbital variables expressed in terms of e_t and x, we can write the QK equations in terms of those variables and u, specifically $r[e_t, x; u], \dot{r}[e_t, x; u]$, etc. Starting with the radial equation from Eq. (2.16), we obtain

$$\begin{aligned} r = {} & \frac{m}{x}\left[1 - e_t\cos(u)\right] - \frac{m}{6(1-e_t^2)}\left\{6 - 2\eta + e_t^2(-9+\eta)\right. \\ & \left. +[18 - 7\eta + e_t^2(-6+7\eta)]e_t\cos(u)\right\}\,. \end{aligned} \tag{2.31}$$

The temporal equation in Eq. (2.17) is already expressed in terms of e_t and u, so it does not require any re-writing. To obtain $\dot{r}$, we begin by taking a time derivative of Eq. (2.17), and solving for $\dot{u}$ to obtain

$$\dot{u} = \frac{n}{1 - e_t\cos(u)}\,. \tag{2.32}$$

We then apply the chain rule to Eq. (2.16) to obtain $\dot{r}$,

$$\dot{r} = \sqrt{x}\frac{e_t\sin(u)}{1-e_t\cos(u)}\left[1 + \frac{x}{6}\frac{-7\eta + e_t^2(-6+7\eta)}{1-e_t^2}\right]\,. \tag{2.33}$$

The same procedure can be applied to Eq. (2.18) to obtain

$$\dot{\phi} = \frac{x^{3/2}}{m}\frac{\sqrt{1-e_t^2}}{[1-e_t\cos(u)]^2}\left\{1 + x\frac{(-4+\eta)e_t\left[e_t - \cos(u)\right]}{(1-e_t^2)[1-e_t\cos(u)]}\right\} \tag{2.34}$$

With $\dot{r}$ and $\dot{\phi}$ specified, it is straight forward to express v_j and v^2 as functions of u. This completes the calculation of all quantities necessary to evaluate the source multipole moments to 1PN order. We provide a detailed description of the QK parametrization to 3PN order in Appendix D.

Averaging and Enhancement Factors

While we now have all of the expressions necessary in order to calculate the GW fluxes, there is still one bit of mathematical machinery that we need to discuss. The effect of radiation reaction is to induce changes in the orbital elements of the binary. These changes can be broken down into *secular* effects, which describe monotonic changes in the orbital elements, and *oscillatory* effects. The oscillatory effects are typically small over one orbit, and thus one averages the fluxes over the orbital period in order to extract the more important secular changes of the orbital elements [92,93]:

$$\langle \mathcal{P}_\infty \rangle = \frac{1}{P}\int_0^P \mathcal{P}_\infty(t)dt\,, \tag{2.35}$$

$$\langle \mathcal{G}_\infty \rangle = \frac{1}{P}\int_0^P \mathcal{G}_\infty(t)dt\,. \tag{2.36}$$

Further, the orbit-averaged fluxes are invariant with respect to radiation reaction gauge transformations [131]. These averaged fluxes will, in general, still depend on the coordinate system used to determine the conservative orbital dynamics. Of course, this can be averted by writing the fluxes in terms of gauge invariants of the conservative dynamics, such as the orbital energy and angular momentum, to make the averaged fluxes completely gauge invariant. As a result, it is very straightforward to obtain observables from the averaged fluxes, such as the amount of orbital energy and angular momentum that is lost per orbit.

Before we move on, however, there is one important contention that we should note about the above argument. As the eccentricity increases from the circular limit, most of the GW power gets emitted during pericenter passage. Once we move toward the parabolic limit, nearly all of the power is emitted in a short burst around pericenter and as a result, the timescale over which the orbit changes becomes much smaller than the orbital period. This is significantly different from the case described above, where the effect of radiation reaction occurs over a timescale much longer than the orbital period. As a result, orbit averaging is not really suitable when the eccentricity is sufficiently close to unity and the orbit averaged fluxes in Eqs. (2.35) and (2.36) break down [102]. The eccentricity at which this occurs, however, is sufficiently close to the parabolic limit that the averaged fluxes are still a very accurate approximation of radiation reaction for a wide range of eccentricities. Indeed, we know this to be true up to at least $e_t = 0.7$, as can be seen from Figs. (12.3) and (12.4) in [131].

The end result of the averaging procedure for an nPN order term in the fluxes generally has the form

$$\langle \mathcal{P}_{\infty}^{(\mathrm{nPN})} \rangle = \frac{32}{5} \eta^2 x^{5+n} p_n f_n(e_t, \eta) \,, \tag{2.37}$$

$$\langle \mathcal{G}_{\infty}^{(\mathrm{nPN})} \rangle = \frac{32}{5} m \eta^2 x^{7/2+n} l_n g_n(e_t, \eta) \,, \tag{2.38}$$

where p_n and l_n are rational numbers. When $n = 0$, we obtain the Newtonian order fluxes, which were computed in [129, 130]. The functions $f_n(e_t, \eta)$ and $g_n(e_t, \eta)$ are referred to as enhancement factors. In the circular limit ($e_t = 0$), they are typically defined to be equal to one, with the exception of the 3PN order enhancement factors from the tail-squared and tail-of-tail terms, which are defined to be zero. As we go toward the parabolic limit ($e_t = 1$), the enhancement factors diverge, thus “enhancing” the fluxes.

We would like to note that the above mentioned behavior is actually unphysical, and that the term ”enhancement factors” is actually a misnomer. Naturally, there isn’t an infinite amount of energy and angular momentum emitted in the parabolic limit as suggested by the nature of the enhancement factors. This behavior can be understood by realizing that when taking the parabolic limit in the above discussion, we held x fixed, corresponding to holding the semi-major axis fixed since $x = m/a + \mathcal{O}(1\text{PN})$. Now, recall that at Newtonian order $a = r_p/(1 - e_t)$. As we increase e_t, the only way that the semi-major axis can remain fixed is if r_p decreases. However, there is a lower bound on what r_p can be in PN theory, specifically corresponding to the last stable orbit. Thus, keeping x (or a) fixed as we increase e_t, actually corresponds to pushing the binary closer to the last stable orbit and the merger phase of the coalescence. The divergence observed in the enhancement factors is simply due to the coordinate separation of the binary components becoming zero at pericenter when taking the parabolic limit in this way. In fact, this limiting behavior is also responsible for the concept that, in general, eccentric inspiralling binaries spend less time in the detection band of ground based detectors than their quasi-circular counterparts[2].

A more reasonable way of taking the parabolic limit in these orbit averaged expressions is to hold the minimum length scale of the orbit constant, or more specifically, holding r_p fixed as $e_t \to 1$. To understand this limit, it is useful to consider an example case. Consider the leading PN order energy flux, specifically

$$\langle \mathcal{P}_\infty^{\text{N}} \rangle = \frac{32}{5} \eta^2 \left(\frac{m}{a} \right)^5 f_0(e) \,, \tag{2.39}$$

$$f_0(e) = \frac{1 + \frac{73}{24} e^2 + \frac{37}{96} e^4}{(1 - e^2)^{7/2}} \,, \tag{2.40}$$

where we have truncated all PN quantities at Newtonian order. We now transform

---

[2] This concept is not wrong per se, only that it require the qualifier of the orbital frequency (and thus semi-major axis) being the same between the two scenarios.

from the semi-major axis to the pericenter distance using $a = r_p/(1-e)$, obtaining

$$\langle \mathcal{P}_\infty^{\rm N} \rangle = \frac{32}{5}\eta^2 \left(\frac{m}{r_p}\right)^5 \bar{f}_0(e)\,, \tag{2.41}$$

$$\bar{f}_0(e) = \frac{(1-e)^{3/2}\left(1+\frac{73}{24}e^2+\frac{37}{96}e^4\right)}{(1+e)^{7/2}}\,. \tag{2.42}$$

The new enhancement factor $\bar{f}_0(e)$ now vanishes in the parabolic limit. This behavior is still unphysical, since GWs are still emitted in a parabolic binary. However, this behavior is more realistic when we consider that the definition of the orbit averaged energy flux is $\langle \mathcal{P} \rangle = \Delta E/P$, where ΔE is the amount of orbital energy lost in one orbital period. For a generic orbit, regardless of whether it is bound or not, ΔE is finite, while for a parabolic orbit, P becomes infinite. Thus, from this simple argument, $\langle \mathcal{P} \rangle$ vanishes in the parabolic limit, which is precisely the scaling we obtain when we express the orbit averaged energy flux in terms of r_p. From a physical standpoint, this corresponds to fixing the peak frequency of the GW power spectrum, and as a result, eccentric binaries spend more time in the detection band of ground based detectors. Ultimately, the choice of enhancement factor, or of PN parametrization (i.e. x or r_p), does not matter when computing observable quantities, since the unphysical behavior of the enhancement factors does not affect these quantities. We here work with the enhancement factors as defined via Eqs. (2.37)-(2.38), since these are the enhancement factors that typically appear in PN literature.

The enhancement factors for the instantaneous fluxes can actually be evaluated within the time domain by performing a change of variables in the averaging integral from t to u. The tail enhancement factors, on the other hand, cannot usually be evaluated for eccentric binaries by using the source multipole moments in the time domain due to the complicated structure of the hereditary integrals. The integrals can be done in the time domain for small eccentricities ($e_t \ll 1$), but for arbitrary eccentricities, one typically has to evaluate the source multipoles in a Fourier series [29, 50]. Finally, the memory enhancement factors, which only enter into the averaged angular momentum flux, involves an integral over the time varying orbital elements due to the presence of radiation reaction. In order to evaluate this, we would have to solve the equations for $\langle \dot{e}_t \rangle$ and $\langle \dot{x} \rangle$, which can be directly obtained from Eqs. (2.35) and (2.36). However, due to the stated issue regarding the inapplicability of the orbit averaged procedure to sufficiently eccentric systems, such an approach would eventually break down.

Fourier Decomposition of Multipole Moments

We here derive the Fourier decomposition of source multipole moments, which is necessary in order to evaluate the tail terms in the fluxes. We begin by reviewing how to perform the Fourier decomposition of the mass quadrupole to Newtonian order. We then proceed to derive the Fourier decomposition of the mass quadrupole at 1PN order.

Multipole Moments at Newtonian Order

Before we derive the 1PN Fourier decomposition of the mass quadrupole, it is useful to review the Fourier decomposition at Newtonian order. At this order, the mass quadrupole is simply given by Eq. (2.9), where x_j is the trajectory of μ for the system in Fig. 2.1. The trajectory can easily be written in terms of the eccentric anomaly using the results from our discussion of the QK parametrization.

The Fourier decomposition of the mass quadrupole at Newtonian order with respect to the mean anomaly ℓ[3] takes the form

$$I_{jk} = \sum_{p=-\infty}^{\infty} \underset{(p)}{\mathcal{I}_{jk}} e^{ip\ell}\,, \tag{2.43}$$

where we have truncated all expressions to leading order in x, used the fact that at Newtonian order $x = m/a$ and $e_t = e$, and where the Fourier coefficients are given by

$$\underset{(p)}{\mathcal{I}_{jk}} = \int_0^{2\pi} \frac{d\ell}{2\pi} I_{jk}(t) e^{-ip\ell}\,, \tag{2.44}$$

with i the imaginary unit. The integrals in the Fourier coefficients can be easily computed using Eq. (2.17) to change the integration variable from ℓ to u, with $e_t = e$, and the integral representation of the Bessel function

$$\int_0^{2\pi} \frac{du}{2\pi} e^{i[pu - x\sin(u)]} = J_p(x)\,. \tag{2.45}$$

The necessary integrals that need to be evaluated are of the form

$$\int_0^{2\pi} \frac{du}{2\pi} \cos(qu) e^{-ip[u - e\sin(u)]} = \frac{1}{2}\left[J_{p-q}(pe) + J_{p+q}(pe)\right]\,, \tag{2.46}$$

$$\int_0^{2\pi} \frac{du}{2\pi} \sin(qu) e^{-ip[u - e\sin(u)]} = \frac{1}{2i}\left[J_{p-q}(pe) - J_{p+q}(pe)\right]\,, \tag{2.47}$$

where q is a positive integer and i is the imaginary number.

There is one final step of simplification that will be crucial later on in Ch. 3: to order-reduce the Bessel functions $J_{p-q}(pe)$ and $J_{p+q}(pe)$ by using the recursion

---

[3] Recall that the mean anomaly is related to the time variable t via $\ell = n(t - t_p)$, where n is the mean motion and t_p is the pericenter passage time.

relation [127]

$$J_{\nu-1}(x) + J_{\nu+1}(x) = \frac{2\nu}{x} J_\nu(x) \tag{2.48}$$

until we obtain the Fourier coefficients in terms of just $J_p(pe)$ and $J_{p\pm1}(pe)$. We then replace the $J_{p\pm1}(pe)$ terms with the derivative of $J_p(pe)$ with respect to its argument through [127]

$$J'_\nu(x) = J_{\nu-1}(x) - \frac{\nu}{x} J_\nu(x)\,, \tag{2.49}$$

$$J'_\nu(x) = -J_{\nu+1}(x) + \frac{\nu}{x} J_\nu(x)\,. \tag{2.50}$$

The end result for the Newtonian Fourier coefficients of the mass quadrupole are

$$\underset{(p)}{\hat{\mathcal{I}}_{xx}} = -\frac{2}{3}\frac{3-e^2}{e^2}\frac{J_p(pe)}{p^2} + 2\frac{1-e^2}{e}\frac{J'_p(pe)}{p}\,, \tag{2.51}$$

$$\underset{(p)}{\hat{\mathcal{I}}_{xy}} = 2i\sqrt{1-e^2}\left[-\frac{1-e^2}{e^2}\frac{J_p(pe)}{p} + \frac{1}{e}\frac{J'_p(pe)}{p^2}\right]\,, \tag{2.52}$$

$$\underset{(p)}{\hat{\mathcal{I}}_{yy}} = \frac{2}{3}\frac{3-2e^2}{e^2}\frac{J_p(pe)}{p^2} - 2\frac{1-e^2}{e}\frac{J'_p(pe)}{p}\,, \tag{2.53}$$

$$\underset{(p)}{\hat{\mathcal{I}}_{zz}} = \frac{2}{3}\frac{J_p(pe)}{p^2}\,, \tag{2.54}$$

where we have introduced the reduced mass quadrupole

$$\hat{I}_{jk} \equiv \frac{x^2}{\mu m^2} I_{jk}\,. \tag{2.55}$$

which reduces to $\hat{I}_{jk} = (\mu a^2)^{-1} I_{jk}$ in the Newtonian limit.

When calculating the tail fluxes complete to 3PN order, one must also consider the 2.5PN order mass octopole and current quadrupole tails. The procedure for the Fourier decomposition of these multipoles, given by Eqs. (2.10) and (2.11), is exactly the same at that presented above to Newtonian order. For completeness, we present the Fourier coefficients for these two multipoles in Appendix A.

Mass Quadruple at 1PN Order

In order to complete the calculation of the fluxes to 3PN order, we need the Fourier decomposition of the mass quadrupole at 1PN order. The calculation at 1PN order is not as straightforward, due to the fact that relativistic precession modifies the structure of the Fourier decomposition. We begin by computing the mass quadrupole at 1PN order in terms of the eccentric anomaly u. To this order, the mass quadrupole is

$$I_{jk} = \mu A(v,r) x_{<j}x_{k>} + \mu r^2 B v_{<j}v_{k>} + 2\mu r\dot{r} C x_{<j}v_{k>} \,, \tag{2.56}$$

where

$$A(v,r) = 1 + \left[v^2 \left(\frac{29}{42} - \frac{29}{14}\eta \right) + \frac{m}{r} \left(-\frac{5}{7} + \frac{8}{7}\eta \right) \right] \,, \tag{2.57}$$

$$B = \frac{11}{21} - \frac{11}{7}\eta \,, \qquad C = -\frac{2}{7} + \frac{6}{7}\eta \,. \tag{2.58}$$

The first step is to write the mass quadrupole in terms of $r, v, \dot{r}, \dot{\phi}$, and ϕ which can be done through Eqs. (2.21) and (2.22). Although the variables $r, v, \dot{r}$, and $\dot{\phi}$ can all be directly related to u using the results of Section 2, we instead split the orbital phase ϕ into two terms: one with period 2π and one with period $2\pi K$, namely

$$\phi = K\ell + W(\ell) \tag{2.59}$$

where at 1PN order $W = K(V - \ell)$. This allows us to separate the different harmonics of the precession terms using the "magnetic-type" index m [29], i.e.

$$I_{jk} = \sum_{m=-2}^{2} \underset{(m)}{I_{jk}}\, e^{imk\ell} \tag{2.60}$$

where $k = K - 1$. The coefficients in this expansion, in turn, can be written in terms of STF tensors as

$$\underset{(m)}{I_{jk}} = \underset{(m)}{I}\, \underset{(m)}{\mathrm{M}_{jk}} \tag{2.61}$$

where

$$\begin{aligned} \underset{(\pm 2)}{I} &= \frac{1}{4}\mu r^2 e^{\pm 2i(\ell + W)} \left[1 - \frac{5m}{7r} + \frac{9\dot{r}^2}{14} \pm \frac{10ir\dot{r}\dot{\phi}}{21} + \frac{r^2\dot{\phi}^2}{6} \right. \\ &\quad \left. +\eta\left(\frac{8m}{7r} - \frac{27\dot{r}^2}{14} \mp \frac{10ir\dot{r}\dot{\phi}}{7} - \frac{r^2\dot{\phi}^2}{2}\right)\right] \end{aligned} \tag{2.62}$$

$$\begin{aligned} \underset{(0)}{I} &= \frac{1}{6}\mu r^2 \left\{1 - \frac{5m}{7r} + \frac{1}{14}\left[9\dot{r}^2 + 17r^2\dot{\phi}^2\right] \right. \\ &\quad \left. +\eta\left[\frac{8m}{7r} - \frac{1}{14}\left(27\dot{r}^2 - 51r^2\dot{\phi}^2\right)\right]\right\}, \end{aligned} \tag{2.63}$$

and

$$\underset{(\pm 2)}{\mathrm{M}_{jk}} = \begin{bmatrix} 1 & \mp i & 0 \\ - & -1 & 0 \\ - & - & 0 \end{bmatrix}, \qquad \underset{(0)}{\mathrm{M}_{jk}} = \begin{bmatrix} 1 & 0 & 0 \\ - & 1 & 0 \\ - & - & -2 \end{bmatrix}, \tag{2.64}$$

and all other coefficients vanish. We are now left with writing $\underset{(\pm 2)}{I}$ and $\underset{(0)}{I}$ in terms of the eccentric anomaly u, which can be done straightforwardly in the QK parametrization.

Before proceeding, let us discuss how to deal with the exponential terms in

Eq. (2.62). The combination $\ell + W$ can be written as

$$\begin{aligned} \ell + W &= \ell + (1+k)(V-\ell) \\ &= V(e_\phi; u) + k[V(e_\phi; u) - u + e_t \sin(u)]\,, \end{aligned} \tag{2.65}$$

where recall that V is a function of e_ϕ and not e_t. In order to properly handle the exponentials at 1PN order, we PN expand about $k \ll 1$ (which we are free to do since k is directly related to x) to obtain

$$e^{\pm 2i(\ell+W)} = e^{\pm 2iV(e_\phi;u)} \pm 2ike^{\pm 2iV(e_\phi;u)}\left[V(e_\phi;u) - u + e_t \sin(u)\right]\,. \tag{2.66}$$

The quantity k can be replaced with its expression in terms of x without loss of accuracy. The exponential prefactor now only depends on V, and it can thus be immediately rewritten in terms of trigonometric functions. To 1PN order, these expressions are still given by their Newtonian counterpart, except with the replacement $e \to e_\phi$. After inserting these expressions into Eq. (2.66), we simply write e_ϕ in term of e_t using Eq. (2.24) and PN expand. For the 1PN terms in Eq. (2.66) (i.e. the terms proportional to k) that depend on V, we can immediately replace $V(e_\phi; u)$ with $V(e_t; u)$, since any correction to this generates 2PN terms.

With this at hand, we can now calculate the magnetic type quadrupole moments entirely in terms of u. Working with the reduced quadrupole moment of Eq. (2.55) to 1PN order, we have [29]

$$\underset{(m)}{\hat{I}}(x,\eta;u) = \underset{(m)}{\hat{I}^{00}}(u) + x\left[\underset{(m)}{\hat{I}^{01}}(u) + \eta\,\underset{(m)}{\hat{I}^{11}}(u)\right]\,. \tag{2.67}$$

By writing the moments in this way, we separate out the dependence on the system parameters x and η, and are left with functions solely of u. We proceed by Fourier decomposing the magnetic coefficients via

$$\underset{(m)}{\hat{I}}{}^{ab}(u) = \sum_{p=-\infty}^{\infty} \underset{(p,m)}{\hat{\mathcal{I}}}{}^{ab}\, e^{ip\ell}\,, \tag{2.68}$$

where $(a,b) \in [0,1]$ and the Fourier coefficients are given by

$$\underset{(p,m)}{\hat{\mathcal{I}}}{}^{ab} = \int_0^{2\pi} \frac{d\ell}{2\pi}\; \underset{(m)}{\hat{I}}{}^{ab}(u)\; e^{-ip\ell}\,. \tag{2.69}$$

Most of these integrals can be easily computed using Eqs. (2.46) and (2.47). The only terms that cannot be evaluated are those proportional to $V(e_t;u) - u$, where $V(e_t;u)$ is given by Eq. (2.19) with the replacement $e_\phi \to e_t$. As far as we are aware, there is no closed-form expression for these integrals. We simply leave them as undetermined integrals for the time being, and detail how to evaluate them when they appear in the enhancement factors in Ch. 3.

After evaluating the Fourier integrals, we can once again perform the reduction of order on the resulting Bessel functions using the recurrence relations in Eqs. (2.48)-(2.50). The end result gives the desired Fourier coefficients, specifically

$$\begin{aligned}
\underset{(p,\pm2)}{\hat{\mathcal{I}}}{}^{00} &= \frac{J_p(pe_t)}{2e_t^2p^2}\left[-2 \pm 2p\sqrt{1-e_t^2} + e_t^2\left(1 \mp 2p\sqrt{1-e_t^2}\right)\right] \\
&\mp \frac{J_p'(pe_t)}{e_tp^2}\left[\sqrt{1-e_t^2} \mp p(1-e_t^2)\right] \\
\underset{(p,\pm2)}{\hat{\mathcal{I}}}{}^{01} &= -\frac{J_p(pe_t)}{84e_t^2(1-e_t^2)p^3}\Big[\mp1512 - 222p + 2268p\sqrt{1-e_t^2} \mp 756p^2 \pm 226p^2\sqrt{1-e_t^2} \\
&-4p^3 + 4e_t^6p^3 + e_t^4\left(57p \mp 756p^2 \pm 44p^2\sqrt{1-e_t^2} - 12p^3\right) \\
&+e_t^2\left(\pm756 + 333p - 1260p\sqrt{1-e_t^2} \pm 1512p^2 \mp 270p^2\sqrt{1-e_t^2} + 12p^3\right)\Big] \\
&+ \frac{J_p'(pe_t)}{42e_t(1-e_t^2)^{3/2}p^3}\Big[756 \pm 111p \mp 1134p\sqrt{1-e_t^2} + 378p^2 - 113p^2\sqrt{1-e_t^2} \\
&\pm2p^3 \mp 2e_t^6p^3 + e_t^4\left(\pm111p + 378p^2 - 23p^2\sqrt{1-e_t^2} \pm 6p^3\right)
\end{aligned}$$

$$
\begin{aligned}
&+e_t^2\left(-756 \mp 222p \pm 819p\sqrt{1-e_t^2} - 756p^2 + 136p^2\sqrt{1-e_t^2} \mp 6p^3\right)\Big]\\
&+\frac{3}{4(1-e_t^2)}\int_0^{2\pi}\frac{d\ell}{2\pi}e^{-ip\ell}\left[V(e_t;u)-u\right]\Big[\pm 3ie_t^2 \mp 4ie_t\cos(u) \mp i\left(-2+e_t^2\right)\cos(2u)\\
&+4e_t\sqrt{1-e_t^2}\,\sin(u) - 2\sqrt{1-e_t^2}\,\sin(2u)\Big]\,, \qquad (2.70)
\end{aligned}
$$

$$
\begin{aligned}
\underset{(p,\pm2)}{\hat{\mathcal{I}}^{11}} &= \frac{J_p(pe_t)}{84e_t^2p^2}\Big[-134 \pm 146p\sqrt{1-e_t^2} - 12p^2 - 12e_t^4p^2\\
&+e_t^2\left(-17 \pm 22p\sqrt{1-e_t^2} + 24p^2\right)\Big] + \frac{J_p'(pe_t)}{42e_t\sqrt{1-e_t^2}p^2}\Big[\mp 67 + 73p\sqrt{1-e_t^2} \mp 6p^2\\
&\mp 6e_t^4p^2 + e_t^2\left(\pm 25 + 8p\sqrt{1-e_t^2} \pm 12p^2\right)\Big]\,, \qquad (2.71)
\end{aligned}
$$

$$
\begin{aligned}
\underset{(p,0)}{\hat{\mathcal{I}}^{00}} &= -\frac{1}{3}\frac{J_p(pe_t)}{p^2}\,, \qquad \underset{(p,0)}{\hat{\mathcal{I}}^{01}} = -\frac{75-19e_t^2}{42(1-e_t^2)p^2}J_p(pe_t) + \frac{26e_t}{21p}J_p'(pe_t)\,,\\
\underset{(p,0)}{\hat{\mathcal{I}}^{11}} &= \frac{17}{126p^2}J_p(pe_t) - \frac{e_t}{21p}J_p'(pe_t)\,, \qquad (2.72)
\end{aligned}
$$

which completes the calculation of the 1PN mass quadrupole. How to obtain the Newtonian result in Eq. (2.51) from the above expressions may not seem obvious. However, one simply has to go back to the separation of magnetic type precession terms in Eq. (2.61), consider the (00) terms of the moments $\underset{(\pm2)}{I}$ and $\underset{(0)}{I}$, and take the limits $k \to 0$ and $e_t \to e$.

Let us conclude by summarizing the construction of the 1PN mass quadrupole moment. The latter is given by Eq. (2.61) in terms of STF tensors and the magnetic type quadrupole moment. The former are given in Eq. (2.64), while the latter is PN decomposed in Eq. (2.67). The coefficients of this expansion are Fourier decomposed in Eq. (2.68), with the Fourier coefficients given in Eqs. (2.70)-(2.72). In the next chapter, we will use these 1PN mass quadrupole in the 3PN part of the fluxes.

HEREDITARY EFFECTS IN ECCENTRIC COMPACT BINARY INSPIRALS

Within the PN framework, the GW fluxes can be broken down into two distinct sets – the *instantaneous* terms and the *hereditary* terms [42] – that represent physically distinct processes. Consider a compact binary that inspirals due to GW emission and an observer at spatial infinity. As the binary inspirals, the GWs propagate along the curved spacetime generated by the binary and they are observed at spatial infinity some retarded time later. To leading PN order, the GWs are, however, treated as though they are propagating on flat spacetime. The instantaneous flux describes the direct linear emission of GWs from the source at the instant corresponding to the current retarded time. These terms depend on the time variation of the binary's multipole moments and enter the fluxes at integer PN orders.

Hereditary terms, on the other hand, are a result of the nonlinear nature of GR, and they are labeled "hereditary" because they depend on integrals over the entire past lifetime of the source. Hereditary terms can be further broken down into two distinct subsets: the *tail* terms and the *memory* terms. The tail terms [29, 37, 38, 43–45, 50, 135] describe how the time varying radiative multipole moments interact with the curved spacetime of the binary, which to leading PN order is characterized by the ADM mass of the system. This nonlinear interaction causes the waves to scatter as they propagate, and since they are odd under time reversal, they enter the fluxes at half-integer PN orders. Tail terms enter first at 1.5PN order relative to the leading PN order instantaneous flux through a quadratic monopole-quadrupole interaction. Similar tail terms also result from higher-order multipoles; at 3PN order, the so-called "tail squared", $(\text{tail})^2$, and tail-of-tails, tail(tails), terms enter the fluxes [39, 40] through cubic monopole-quadrupole interactions that describe double scattering (i.e. the GWs scatter twice off of binary's curved spacetime as they propagate to spatial infinity).

The second type of hereditary fluxes are the memory terms [30, 40, 45, 62, 75, 76, 155, 168]. The GWs emitted by the binary are not simply waves that propagate along a background spacetime, but they are themselves a source of spacetime curvature. As a result, the GWs generate their own GWs as they propagate to spatial infinity. The memory is also responsible for permanently changing length scales, for example, of a ring of test particles or the arms of an interferometer (see e.g. [81, 98] for a recent discussion of the detectability of this effect in aLIGO.) The memory enters the fluxes beginning at 2.5PN order relative to the leading PN order instantaneous flux through the integral of derivatives of the quadrupole moment squared.

If we desire to create a model that is as accurate a representation of Nature as possible, we must include the nonlinear tail and memory terms in the GW fluxes. As it currently stands, the tail terms are only known numerically for arbitrary eccentricity through infinite sums of Bessel functions [29]. Closed-form, analytic results are available for small eccentricities as Taylor series. Other closed-form, analytic results approximately valid at all eccentricities are available through Padé approximants [148] or through the "factoring" of high-eccentricity terms [79]. The latter two methods fundamentally rely on re-summing a Taylor series about small eccentricity, and thus their accuracy can be problematic unless a sufficiently high number of terms in the small-eccentricity expansion are kept.

The goal of this chapter is to find closed-form, analytic expressions for the tail flux terms that are valid for arbitrarily eccentric compact binaries and to 3PN order relative to the leading PN order instantaneous flux. As we shall see, this will require the construction of superasymptotic and hyperasymptotic [51] series for the tail fluxes. Within the orbit averaged approximation, the memory contributions are small compared to those of the tail terms [107]. As a result, the oscillatory corrections to the memory, which vanish upon averaging, become the dominate contributions. In order to properly account for the memory terms, one needs to abandon the orbit averaged approximation and work within a multiple scale analysis along the lines of [105, 131]. However, these contributions are suppressed by 2.5PN order, and thus would enter the fluxes at absolute 5PN order. Since we are only concerned with the contributions to 3PN order, we do not consider the memory terms here.

The calculation of the tail terms begins with a Fourier decomposition in multipole moments, as detailed in [29]. To compute the energy and angular momentum fluxes to 3PN order, one requires the Fourier decomposition of the 1PN mass quadrupole moment, which was first discussed in [29], but was presented in detail for the first time in [107], and reviewed in Ch. 2. With the Fourier decomposition at hand, one can then define the enhancement factors for each of the PN terms in the fluxes. These enhancement factors depend on sums of the Fourier coefficients of the multipole moments, which can be expressed in terms of the Bessel function $J_p(pe_t)$ and its derivative with respect to the argument, with p the Fourier index and e_t the "temporal" eccentricity.

We re-sum the Bessel series expressions for all of the tail enhancement factors to 3PN order by employing the uniform asymptotic expansion of the Bessel function:

$$J_p(pe_t) \sim K_{1/3}\left(\frac{2}{3}\zeta^{3/2}p\right) + \mathcal{O}\left(\frac{1}{p}\right) \tag{3.1}$$

$$J_p'(pe_t) \sim K_{2/3}\left(\frac{2}{3}\zeta^{3/2}p\right) + \mathcal{O}\left(\frac{1}{p}\right) \tag{3.2}$$

where K is the modified Bessel function of the second kind and ζ is a known function of e_t. This asymptotic expansion is valid when $p \to \infty$, and in this limit, we can replace the sums in the enhancement factors with integrals over the Fourier index. These steps are fundamentally valid in the high eccentricity limit ($e_t \sim 1$), so we expand the result of the integral about $\epsilon = 1 - e_t^2 \ll 1$. Through comparison with numerical PN results for the enhancement factors, we show that the resulting series in ϵ are asymptotic and that they can be truncated at very low order to achieve an optimally-truncated, *superasymptotic series* [51], i.e. one that achieves the minimum possible error relative to an "exact" numerical answer. We also show that these optimally-truncated superasymptotic series can have their accuracy further improved by matching them to small eccentricity expansion of the enhancement factors, generating a *hyperasymptotic series* [51] with typical relative errors of $\lesssim 10^{-8}$ compared to numerical PN results at *all* eccentricities; the only exceptions are two 2.5PN order enhancement factors that are accurate to $\lesssim 10^{-4}$.

The remainder of this chapter presents the details of the results discussed above. The main results of this chapter are closed-form, analytic expressions for the tail terms [Eqs. (3.3)-(3.4), (3.16)-(3.23), (3.72)-(3.77), (3.84)-(3.85), (3.101)-(3.104), (3.108)-(3.109), (3.114)-(3.119)] to 3PN order.

Energy & Angular Momentum Fluxes: Tail Effects

We begin by considering the tail energy and angular momentum fluxes. These quantities involve integrals over the entire past history of the source, i.e. over the source's past light cone. This section presents the formal definition of these fluxes and the orbit-averaged expressions in terms of enhancement factors that depend on the Fourier decomposition of the multipole moments.

Integral Definitions and Orbit-Averages

Let us begin by decomposing the tails terms in the energy and angular momentum fluxes [see Eq. (2.14)-(2.15)] in terms of multipolar interactions:

$$\mathcal{P}_{\infty}^{\rm tails} = \mathcal{P}_{\infty}^{\rm MQtail} + \left(\mathcal{P}_{\infty}^{\rm MOtail} + \mathcal{P}_{\infty}^{\rm CQtail}\right) + \left(\mathcal{P}_{\infty}^{\rm MQ(tail)^2} + \mathcal{P}_{\infty}^{\rm MQtail(tails)}\right)\,, \tag{3.3}$$

$$\mathcal{G}_{\infty}^{\rm tails} = \mathcal{G}_{\infty}^{\rm MQtail} + \left(\mathcal{G}_{\infty}^{\rm MOtail} + \mathcal{G}_{\infty}^{\rm CQtail}\right) + \left(\mathcal{G}_{\infty}^{\rm (tail)^2} + \mathcal{G}_{\infty}^{\rm tail(tails)}\right)\,. \tag{3.4}$$

The first terms in both equations, the so-called mass quadrupole tails, first enters at 1.5PN order relative to the leading-order instantaneous fluxes. The second terms, the so-called mass octopole and current quadrupole tails, enter at 2.5PN order, while the last term, the so-called tails-squared and tails-of-tails terms, enter at 3PN order.

The mass quadrupole tail, defined via[1]

$$\mathcal{P}_{\infty}^{\rm MQtail} = \frac{4M}{5}\dddot{I}^{jk}(t)\int_0^{\infty} d\tau\, \overset{(5)}{I}_{jk}(t-\tau)\left[\ln\left(\frac{\tau}{2r_0}\right)+\frac{11}{12}\right]\,, \tag{3.5}$$

$$\begin{aligned}\mathcal{G}_{\infty}^{\rm MQtail} &= \frac{4M}{5}\epsilon^{iab}\hat{L}_i\left\{\ddot{I}_{aj}(t)\int_0^{\infty} d\tau \overset{(5)}{I^{j}}{}_{b}(t-\tau)\left[\ln\left(\frac{\tau}{2r_0}\right)+\frac{11}{12}\right]\right.\\ &\left.\quad+\dddot{I}_{bj}(t)\int_0^{\infty} d\tau \overset{(4)}{I^{j}}{}_{a}(t-\tau)\left[\ln\left(\frac{\tau}{2r_0}\right)+\frac{11}{12}\right]\right\}\,,\end{aligned} \tag{3.6}$$

is a quadratic non-linear interaction between the source quadrupole moment and the conserved mass monopole of the system, i.e. the ADM mass

$$M = m\left[1-\frac{1}{2}\eta x+\mathcal{O}(2\mathrm{PN})\right]\,. \tag{3.7}$$

---

[1] The quantity r_0 in the logarithm is a regularization factor that accounts for the zero point of retarded time being different between wave-zone and harmonic coordinates [29, 50]; this regularization factor is unphysical and it drops out of any calculation that deals with observables.

The mass octopole and current quadrupole tails are

$$\mathcal{P}_\infty^{\rm MOtail} = \frac{4M}{189}\overset{(4)}{I}_{jkl}(t)\int_0^\infty d\tau \overset{(6)}{I}{}^{jkl}(t-\tau)\left[\ln\left(\frac{\tau}{2r_0}\right)+\frac{97}{60}\right], \tag{3.8}$$

$$\mathcal{P}_\infty^{\rm CQtail} = \frac{64M}{45}\overset{(3)}{J}_{jk}(t)\int_0^\infty d\tau \overset{(5)}{J}{}^{jk}(t-\tau)\left[\ln\left(\frac{\tau}{2r_0}\right)+\frac{7}{6}\right], \tag{3.9}$$

$$\begin{aligned}\mathcal{G}_\infty^{\rm MOtail} &= \frac{2M}{63}\epsilon^{iab}\hat{L}_i\left\{\dddot{I}_{ajk}\int_0^\infty d\tau \overset{(6)}{I}{}^{jk}{}_b(t-\tau)\left[\ln\left(\frac{\tau}{2r_0}\right)+\frac{97}{60}\right]\right.\\ &\left.+\overset{(4)}{I}_{bjk}(t)\int_0^\infty d\tau \overset{(5)}{I}{}^{jk}{}_a(t-\tau)\left[\ln\left(\frac{\tau}{2r_0}\right)+\frac{97}{60}\right]\right\},\end{aligned} \tag{3.10}$$

$$\begin{aligned}\mathcal{G}_\infty^{\rm CQtail} &= \frac{64M}{45}\epsilon^{iab}\hat{L}_i\left\{\ddot{J}_{aj}(t)\int_0^\infty d\tau \overset{(5)}{J}{}^{j}{}_b(t-\tau)\left[\ln\left(\frac{\tau}{2r_0}\right)+\frac{7}{6}\right]\right.\\ &\left.+\dddot{J}_{bj}(t)\int_0^\infty d\tau \overset{(4)}{J}{}^{j}{}_a(t-\tau)\left[\ln\left(\frac{\tau}{2r_0}\right)+\frac{7}{6}\right]\right\},\end{aligned} \tag{3.11}$$

while the tail-squared and tail-of-tails terms are

$$\mathcal{P}_\infty^{\rm MQ(tail)^2} = \frac{4M^2}{5}\left\{\int_0^\infty d\tau \overset{(5)}{I}{}_{jk}(t-\tau)\left[\ln\left(\frac{\tau}{2r_0}\right)+\frac{11}{12}\right]\right\}^2, \tag{3.12}$$

$$\mathcal{P}_\infty^{\rm MQtail(tails)} = \frac{4M^2}{5}\overset{(3)}{I}{}_{jk}(t)\int_0^\infty d\tau \overset{(6)}{I}{}^{jk}(t-\tau)\left[\ln^2\left(\frac{\tau}{2r_0}\right)+\frac{57}{50}\ln\left(\frac{\tau}{2r_0}\right)+\frac{124627}{44100}\right], \tag{3.13}$$

$$\begin{aligned}\mathcal{G}_\infty^{\rm MQ(tail)^2} &= \frac{8M^2}{5}\epsilon^{iab}\hat{L}_i\left\{\int_0^\infty d\tau \overset{(4)}{I}{}_{aj}(t-\tau)\left[\ln\left(\frac{\tau}{2r_0}\right)+\frac{11}{12}\right]\right\}\\ &\times\left\{\int_0^\infty d\tau \overset{(5)}{I}{}^{j}{}_b(t-\tau)\left[\ln\left(\frac{\tau}{2r_0}\right)+\frac{11}{12}\right]\right\},\end{aligned} \tag{3.14}$$

$$\begin{aligned}\mathcal{G}_\infty^{\rm MQtail(tail)} &= \frac{4M^2}{5}\epsilon^{iab}\hat{L}_i\left\{\ddot{I}_{aj}(t)\int_0^\infty d\tau \overset{(6)}{I}{}^{j}{}_b(t-\tau)\left[\ln^2\left(\frac{\tau}{2r_0}\right)+\frac{57}{70}\ln\left(\frac{\tau}{2r_0}\right)+\frac{124627}{44100}\right]\right.\\ &\left.+\dddot{I}{}_{bj}(t)\int_0^\infty d\tau \overset{(5)}{I}{}^{j}{}_a(t-\tau)\left[\ln^2\left(\frac{\tau}{2r_0}\right)+\frac{57}{70}\ln\left(\frac{\tau}{2r_0}\right)+\frac{124627}{44100}\right]\right\}.\end{aligned} \tag{3.15}$$

The calculation of the energy and angular momentum fluxes to 3PN order requires the mass quadrupole tail term to 1PN order, but all other tail terms to leading PN order. The former, in turn, requires the mass quadrupole moment to 1PN order, but all other multipole moments can be computed to leading PN order. In particular, we can replace any eccentricity parameter appearing in these multipoles by e_t, since PN corrections to these would enter at higher PN order. Similarly, 2PN order modifications to the orbital dynamics introduce corrections at 3.5 PN order and higher, so they can also be neglected. Radiation-reaction in the hereditary integrals can also be neglected because these effects enter at 2.5PN order in the orbital dynamics, and thus they introduce modifications in the tail fluxes at 4PN order [50].

After orbit-averaging, the tail terms in the energy and angular momentum flux take the form of Eqs. (2.37)-(2.38) in terms of enhancement factors [29]. In particular, the mass quadrupole tail terms are

$$\langle \mathcal{P}_\infty^{\rm MQtail} \rangle = \frac{32}{5}\eta^2 x^5 \left\{ 4\pi x^{3/2}\varphi(e_t) + \pi x^{5/2}\left[-\frac{428}{21}\alpha(e_t) + \frac{178}{21}\eta\theta(e_t) \right] \right\} , \tag{3.16}$$

$$\langle \mathcal{G}_\infty^{\rm MQtail} \rangle = \frac{32}{5}m\eta^2 x^{7/2} \left\{ 4\pi x^{3/2}\tilde{\varphi}(e_t) + \pi x^{5/2}\left[-\frac{428}{21}\tilde{\alpha}(e_t) + \frac{178}{21}\eta\tilde{\theta}(e_t) \right] \right\} , \tag{3.17}$$

which depend on six enhancement factors: the first two $[\varphi(e_t), \tilde{\varphi}(e_t)]$ come from the Newtonian contribution to the mass quadrupole and enter at 1.5PN order; the other four $[\alpha(e_t), \tilde{\alpha}(e_t)]$ and $[\theta(e_t), \tilde{\theta}(e_t)]$ come from the 1PN contribution to the mass quadrupole and enter at 2.5PN order. The mass octopole and current quadrupole tail terms are

$$\langle \mathcal{P}_\infty^{\rm MOtail} \rangle = \frac{32}{5}\eta^2 x^5 \left[\frac{16403}{2016}\pi(1-4\eta)x^{5/2}\beta(e_t) \right] , \tag{3.18}$$

$$\langle \mathcal{P}_\infty^{\rm CQtail} \rangle = \frac{32}{5}\eta^2 x^5 \left[\frac{\pi}{18}(1-4\eta)x^{5/2}\gamma(e_t) \right] , \tag{3.19}$$

$$\langle \mathcal{G}_\infty^{\rm MOtail} \rangle = \frac{32}{5}m\eta^2 x^{7/2} \left[\frac{16403}{2016}\pi(1-4\eta)x^{5/2}\tilde{\beta}(e_t) \right] , \tag{3.20}$$

$$\langle \mathcal{G}_{\infty}^{\text{CQtail}} \rangle = \frac{32}{5} m\eta^2 x^{7/2} \left[\frac{\pi}{18}(1-4\eta) x^{5/2} \tilde{\gamma}(e_t) \right] , \tag{3.21}$$

which enter at 2.5PN order and depend on four enhancement factors: the first two $[\beta(e_t), \tilde{\beta}(e_t)]$ come from the mass octopole and the second two $[\gamma(e_t), \tilde{\gamma}(e_t)]$ come from the current quadrupole. Finally, the tail-squared and tail-of-tails terms enter at 3PN order and are given by

$$\begin{aligned} \langle \mathcal{P}_{\infty}^{(\text{tail})^2+\text{tail(tails)}} \rangle &= \frac{32}{5}\eta^2 x^8 \left\{ -\frac{1712}{105}\chi(e_t) \right. \\ &\left. + \left[-\frac{116761}{3675} + \frac{16}{3}\pi^2 - \frac{1712}{105}\left(\ln(4\omega r_0) + \gamma_E\right) \right] F(e_t) \right\} \end{aligned} \tag{3.22}$$

$$\begin{aligned} \langle \mathcal{G}_{\infty}^{(\text{tail})^2+\text{tail(tails)}} \rangle &= \frac{32}{5} m\eta^2 x^{13/2} \left\{ -\frac{1712}{105}\tilde{\chi}(e_t) \right. \\ &\left. + \left[-\frac{116761}{3675} + \frac{16}{3}\pi^2 - \frac{1712}{105}\left(\ln(4\omega r_0) + \gamma_E\right) \right] \tilde{F}(e_t) \right\} , \end{aligned} \tag{3.23}$$

which depends on two enhancement factors $[\chi(e_t), \tilde{\chi}(e_t)]$.

Tail Enhancement Factors

The tail terms of the orbit-averaged energy and angular momentum fluxes depend on enhancement factors that must be evaluated to calculate how compact binaries inspiral. These enhancement factors can be expressed as sums over the Fourier components of the multipole moments. The enhancement factors that enter the mass quadrupole tail terms are

$$\varphi(e_t) = \frac{1}{32}\sum_{p=1}^{\infty} p^7 |\underset{(p)}{\mathcal{I}_{jk}^{00}}|^2 , \qquad \tilde{\varphi}(e_t) = -\frac{i}{16}\epsilon^{ijk}\hat{L}_i \sum_{p=1}^{\infty} p^5 \, \underset{(p)}{\mathcal{I}_{ja}^{00}} \; \underset{(p)}{\mathcal{I}_{ka}^{00*}} , \tag{3.24}$$

$$\begin{aligned} \alpha(e_t) &= \frac{441}{3424(1-e_t^2)} \sum_{p=1}^{\infty} p^7 |\underset{(p)}{\mathcal{I}_{jk}^{00}}|^2 - \frac{63}{3424(1-e_t^2)} \sum_{m,s=-2}^{2} \sum_{p=1}^{\infty} p^6 (4s+3m) \, \underset{(p,m)}{\mathcal{I}_{jk}^{00*}} \, \underset{(p,s)}{\mathcal{I}_{00}^{jk}} \\ &- \frac{21}{3424}\sum_{p=1}^{\infty} p^7 \left[\underset{(p)}{\mathcal{I}_{jk}^{01*}} \underset{(p)}{\mathcal{I}_{00}^{jk}} + \underset{(p)}{\mathcal{I}_{jk}^{00*}} \underset{(p)}{\mathcal{I}_{01}^{jk}} \right] , \end{aligned} \tag{3.25}$$

$$\begin{aligned}\tilde{\alpha}(e_t) = &-\frac{189i}{856(1-e_t^2)}\epsilon^{ijk}\hat{L}_i\sum_{p=1}^{\infty}p^6\,\underset{(p)}{\mathcal{I}^{00}_{ja}}\,\underset{(p)}{\mathcal{I}^{a00*}_{k}}\\ &+\frac{189i}{1712(1-e_t^2)}\epsilon^{ijk}\hat{L}_i\sum_{m,s=-2}^{2}\sum_{p=1}^{\infty}p^5(m+s)\,\underset{(p,s)}{\mathcal{I}^{00}_{ja}}\,\underset{(p,m)}{\mathcal{I}^{a00*}_{k}}\\ &+\frac{21i}{1712}\epsilon^{ijk}\hat{L}_i\sum_{p=1}^{\infty}p^6\left[\underset{(p)}{\mathcal{I}^{00}_{ja}}\,\underset{(p)}{\mathcal{I}^{a01*}_{k}}+\underset{(p)}{\mathcal{I}^{01}_{ja}}\,\underset{(p)}{\mathcal{I}^{a00*}_{k}}\right]\end{aligned}\tag{3.26}$$

$$\theta(e_t) = -\frac{21}{2848}\sum_{p=1}^{\infty}p^7|\underset{(p)}{\mathcal{I}^{00}_{jk}}|^2+\frac{21}{1424}\sum_{p=1}^{\infty}p^7\left[\underset{(p)}{\mathcal{I}^{11*}_{jk}}\underset{(p)}{\mathcal{I}^{jk}_{00}}+\underset{(p)}{\mathcal{I}^{00*}_{jk}}\underset{(p)}{\mathcal{I}^{jk}_{11}}\right].\tag{3.27}$$

$$\tilde{\theta}(e_t) = \frac{21i}{1424}\epsilon^{ijk}\hat{L}_i\sum_{p=1}^{\infty}p^6\underset{(p)}{\mathcal{I}^{00}_{ja}}\,\underset{(p)}{\mathcal{I}^{a00*}_{k}}-\frac{21i}{712}\epsilon^{ijk}\hat{L}_i\sum_{p=1}^{\infty}p^6\left[\underset{(p)}{\mathcal{I}^{00}_{ja}}\,\underset{(p)}{\mathcal{I}^{a11*}_{k}}+\underset{(p)}{\mathcal{I}^{11}_{ja}}\,\underset{(p)}{\mathcal{I}^{a00*}_{k}}\right]\tag{3.28}$$

Those that enter the mass octopole and current quadrupole terms are

$$\beta(e_t) = \frac{20}{49209}\sum_{p=1}^{\infty}p^9|\underset{(p)}{\hat{\mathcal{I}}_{jkl}}|^2\,,\tag{3.29}$$

$$\tilde{\beta}(e_t) = -\frac{20i}{16403}\epsilon^{ijk}\hat{L}_i\sum_{p=1}^{\infty}p^8\,\underset{(p)}{\mathcal{I}_{jab}}\,\underset{(p)}{\mathcal{I}^{ab*}_{k}}\,,\tag{3.30}$$

$$\gamma(e_t) = 4\sum_{p=1}^{\infty}p^7|\underset{(p)}{\hat{\mathcal{J}}_{jk}}|^2\,,\tag{3.31}$$

$$\tilde{\gamma}(e_t) = -8i\epsilon^{ijk}\hat{L}_i\sum_{p=1}^{\infty}p^6\underset{(p)}{\mathcal{J}_{ja}}\underset{(p)}{\mathcal{J}_{ka}}{}^*\,,\tag{3.32}$$

and those that enter the tail-squared and tail-of-tails terms are

$$\chi(e_t) = \frac{1}{64}\sum_{p=1}^{\infty}p^8\ln\left(\frac{p}{2}\right)|\underset{(p)}{\hat{\mathcal{I}}_{jk}}|^2\,,\tag{3.33}$$

$$\tilde{\chi}(e_t) = -\frac{i}{32}\epsilon^{ijk}\hat{L}_i\sum_{p=1}^{\infty}p^7\ln\left(\frac{p}{2}\right)\underset{(p)}{\mathcal{I}_{ja}}\underset{(p)}{\mathcal{I}_{ka}}{}^*\,.\tag{3.34}$$

In these expressions, a superscript asterisk stands for complex conjugation, i is the imaginary number, $\hat{L}^i$ is the unit orbital angular momentum, and ϵ^{ijk} is the three-dimensional Levi-Civita symbol.

Let us now explain how these expressions are derived. Much of this was initially done in [29], so we will not repeat the analysis here in detail, but rather sketch how the calculation is done for the 1PN mass quadrupole tail term in the energy flux (the mass quadrupole tail term in the angular momentum flux follows the exact same procedure.) Following the notation of [29], the Fourier decomposition of the 1PN mass quadrupole is

$$I_{jk}(t) = \sum_{m=-2}^{2} \sum_{p=-\infty}^{\infty} \underset{(p,m)}{\mathcal{I}^{jk}} \, e^{i(p+mk)\ell} \,, \tag{3.35}$$

where the Fourier coefficients are

$$\underset{(p,m)}{\mathcal{I}^{jk}} = \underset{(p,m)}{\mathcal{I}} \; \underset{(m)}{\mathrm{M}^{jk}} \,. \tag{3.36}$$

After taking time derivatives on $I_{jk}(t)$ and inserting these into Eq. (3.5), one finds

$$\begin{aligned} \langle \mathcal{P}_{\infty}^{\mathrm{MQtail}} \rangle = \frac{4Mn^8}{5} \sum_{p,q=-\infty}^{\infty} \sum_{m,s=-2}^{2} (p+mk)^3 (q+sk)^5 \underset{(p,m)}{\mathcal{I}^{jk}} \; \underset{(q,s)}{\mathcal{I}_{jk}} \langle e^{i[p+q+(m+s)k]\ell} \rangle \\ \times \int_0^{\infty} d\tau e^{-i(q+sk)n\tau} \left[\ln\left(\frac{\tau}{2r_0}\right) + \frac{11}{12} \right] \end{aligned} \tag{3.37}$$

We have two integrals that we have to evaluate in this expression, the orbital average and the hereditary integral. The orbital average is defined via

$$\langle e^{i[p+q+(m+s)k]\ell} \rangle = \int_0^{2\pi} \frac{d\ell}{2\pi} e^{i[p+q+(m+s)k]\ell} \tag{3.38}$$

where (p, q, m, s) are integers. Normally, this would evaluate to the discrete Kronecker delta, but the presence of k in the exponential complicates things. In general, k is not an integer and the end result will not take the simple form of a the Kronecker delta. To evaluate the integral, we simply expand about $k \ll 1$, to obtain

$$\langle e^{i[p+q+(m+s)k]\ell}\rangle = \begin{cases} \frac{m+s}{p+q}k & p \neq -q \\ 1 + i\pi(m+s)k & p = -q \end{cases}, \tag{3.39}$$

The hereditary integral on the other hand is a little more involved. To evaluate this integral, we rotate the mean motion into the complex plane using $n = -i\nu$. By doing this, we replace the complex exponential in the hereditary integral with a decaying real exponential, which regularizes the behavior of the integrand when $\tau \to \infty$. The integral can then be performed using an integral table or `Mathematica`. To obtain the final answer, we rotate back using $\nu = in$ and PN expand about k to obtain

$$\int_0^\infty d\tau e^{-i(q+sk)n\tau} \ln\left(\frac{\tau}{2r_0}\right) = \frac{isk}{q^2 n} - \frac{1}{qn}\left(1 - \frac{sk}{q}\right)\left[\frac{\pi}{2}\text{sign}(q) - i\left(\ln\left(2n|q|r_0\right) + \gamma_E\right)\right], \tag{3.40}$$

where $\gamma_E = 0.5772...$ is the Euler constant.

The structure of the average of the exponential in Eq. (3.39) indicates that we need to be cautious when evaluating the summation over p. For convenience, we write the summation as

$$\sum_{p=-\infty}^{\infty} \langle e^{i[p+q+(m+s)k]\ell}\rangle = \sum_{p=-\infty}^{-q-1} \frac{m+s}{p+q}k + \lim_{p\to -q}\left[1 + i\pi(m+s)k\right] + \sum_{p=-q+1}^{\infty} \frac{m+s}{p+q}k\,. \tag{3.41}$$

The terms that depend on summations over p lead to terms in $\langle \mathcal{P}_\infty^{\rm MQtail} \rangle$ of the form

$$S_1 = -\frac{k}{n} \sum_{m,s=-2}^{2} \sum_{q=-\infty}^{\infty} \sum_{p=-\infty}^{-q-1} \frac{m+s}{p+q}\, p^3 q^4 \underset{(p,m)}{\mathcal{I}^{jk}_{00}} \underset{(q,s)}{\mathcal{I}^{00}_{jk}} \left\{ \frac{\pi}{2} \text{sign}(q) - i \left[\ln(2n|q|r_0) + \gamma_E \right] \right\} , \tag{3.42}$$

$$S_2 = -\frac{k}{n} \sum_{m,s=-2}^{2} \sum_{q=-\infty}^{\infty} \sum_{p=-q+1}^{\infty} \frac{m+s}{p+q}\, p^3 q^5 \underset{(p,m)}{\mathcal{I}^{jk}_{00}} \underset{(q,s)}{\mathcal{I}^{00}_{jk}} \left\{ \frac{\pi}{2} \text{sign}(q) - i \left[\ln(2n|q|r_0) + \gamma_E \right] \right\} , \tag{3.43}$$

but these vanish by noting that

$$\sum_{m,s=-2}^{2} (m+s) \underset{(p,m)}{\mathcal{I}^{jk}_{00}} \underset{(q,s)}{\mathcal{I}^{00}_{jk}} = 0 \,. \tag{3.44}$$

The terms that depend on the limit lead to six different terms in $\langle \mathcal{P}_\infty^{\rm MQtail} \rangle$ after PN expanding in x. The first of these terms is

$$L_1 = \frac{1}{n} \sum_{m,s=-2}^{2} \sum_{q=-\infty}^{\infty} q^7 \underset{(-q,m)}{\mathcal{I}^{00}_{jk}} \underset{(q,s)}{\mathcal{I}^{jk}_{00}} \left\{ \frac{\pi}{2} \text{sign}(q) - i \left[\ln(2n|q|r_0) + \gamma_E \right] \right\} . \tag{3.45}$$

Splitting the summation over q into separate sums (over positive and negative values) allows us to evaluate the sign function of q individually in each sum. Next, we make the transformation $q \to -q$ in the sum over negative values, $m \to -m$ in the sum over positive values, and $s \to -s$ in the sum over negative values. After regrouping terms, we have

$$\begin{aligned} L_1 = \frac{\pi}{2n} \sum_{m,s=-2}^{2} \sum_{q=1}^{\infty} q^7 &\left[\underset{(-q,-m)}{\mathcal{I}^{00}_{jk}} \underset{(q,s)}{\mathcal{I}^{jk}_{00}} + \underset{(q,m)}{\mathcal{I}^{00}_{jk}} \underset{(-q,-s)}{\mathcal{I}^{jk}_{00}} \right] \\ + i \sum_{m,s=-2}^{2} \sum_{q=1}^{\infty} q^7 &\left[\underset{(-q,-m)}{\mathcal{I}^{00}_{jk}} \underset{(q,s)}{\mathcal{I}^{jk}_{00}} - \underset{(q,m)}{\mathcal{I}^{00}_{jk}} \underset{(-q,-s)}{\mathcal{I}^{jk}_{00}} \right] \left[\ln(2nqr_0) + \gamma_E \right] . \end{aligned} \tag{3.46}$$

Taking $m \leftrightarrow s$ in the second term in both of the square brackets, which we are free to do since m and s run over the same values, makes the term proportional to $\ln(2nqr_0)$ vanish, as it must since it depends on the unphysical regularization scale r_0. Reconstructing the Fourier components via

$$\underset{(q)}{\mathcal{I}^{00}_{jk}} = \sum_{m=-2}^{2} \underset{(q,m)}{\mathcal{I}^{00}_{jk}} \,. \tag{3.47}$$

one finds

$$L_1 = \frac{\pi}{n} \sum_{p=1}^{\infty} p^7 |\underset{(p)}{\mathcal{I}^{00}_{jk}}|^2 \,, \tag{3.48}$$

where we have replaced q with p and used the fact that the mass quadrupole is a real valued function, so the Fourier coefficients satisfy

$$\underset{(p,m)}{\mathcal{I}^{00\,*}_{jk}} = \underset{(-p,-m)}{\mathcal{I}^{00}_{jk}} \,. \tag{3.49}$$

The analysis of the remaining terms follows the exact same procedure. The non-vanishing terms are

$$L_2 = \frac{3\pi x}{(1-e_t^2)n} \sum_{m,s=-2}^{2} \sum_{p=1}^{\infty} p^6 (4s+3m)\, \underset{(p,m)}{\mathcal{I}^{00}_{jk}}{}^{*} \underset{(p,s)}{\mathcal{I}^{jk}_{00}} \,, \tag{3.50}$$

$$L_3 = \frac{\pi x}{n} \sum_{p=1}^{\infty} p^7 \left[\underset{(p)}{\mathcal{I}^{01*}_{jk}} \underset{(p)}{\mathcal{I}^{jk}_{00}} + \underset{(p)}{\mathcal{I}^{00*}_{jk}} \underset{(p)}{\mathcal{I}^{jk}_{01}} \right] \,, \tag{3.51}$$

$$L_4 = \frac{\pi x \eta}{n} \sum_{p=1}^{\infty} p^7 \left[\underset{(p)}{\mathcal{I}^{11*}_{jk}} \underset{(p)}{\mathcal{I}^{jk}_{00}} + \underset{(p)}{\mathcal{I}^{00*}_{jk}} \underset{(p)}{\mathcal{I}^{jk}_{11}} \right] \,. \tag{3.52}$$

The remaining two terms vanish either directly from the simplification procedure or due to the summations over m and s, just like S_1 and S_2 did. To obtain the result in Eq. (3.16), one simply has to regroup terms to obtain the desired enhancement factors.

Tail Fluxes: Resummation of Asymptotic Enhancement Factors

The enhancement factors are given in terms of infinite sums over the Fourier components of the multipole moments, which is not a practical representation for evaluation of a compact binary inspiral. In particular, if the binary is highly elliptical, a very large number of terms would have to be kept to obtain an accurate representation of the fluxes. This section details how to resum these infinite sums through uniform asymptotic expansions. The truncation of these will lead to superasymptotic series (i.e. an optically truncated asymptotic expansion), and by correcting the behavior of these series at small eccentricity, we will arrive at hyperasymptotic series. We conclude this section by comparing our resummed results to numerically-evaluated tail terms in the fluxes.

Asymptotic Resummation Method for the Enhancement factors

The structure of the Fourier coefficients in Chapter 2 shows that they depend on the Bessel functions $J_p(pe_t)$ and $J'_p(pe_t)$. Sums that involve these particular Bessel functions are referred to as Kapteyn series [160]. There are a host of techniques, both exact and approximate, for re-summing Kapteyn series, many of which are detailed in [123]. We focus on one particular method which relies on the asymptotic properties of $J_p(pe_t)$. The re-summation procedure is the following:

I. Replace the Bessel functions $J_p(pe_t)$ and $J'_p(pe_t)$ in the tail enhancement factors with their uniform asymptotic expansions.

II. Replace the summation over p with an integral.

III. Series expand the result of the integrals about $\epsilon = 1 - e_t^2 \ll 1$.

The first step requires the uniform asymptotic expansion of the Bessel functions as $p \to \infty$ [127], namely

$$J_p(pe_t) = \left(\frac{4\zeta}{1-e_t^2}\right)^{1/4}\left[\frac{\mathrm{Ai}\left(p^{2/3}\zeta\right)}{p^{1/3}}\sum_{k=0}^{\infty}\frac{a_k\left(\zeta\right)}{p^{2k}} + \frac{\mathrm{Ai}'\left(p^{2/3}\zeta\right)}{p^{5/3}}\sum_{k=0}^{\infty}\frac{b_k(\zeta)}{p^{2k}}\right] , \tag{3.53}$$

$$J_p'(pe_t) = -\frac{2}{e_t}\left(\frac{1-e_t^2}{4\zeta}\right)^{1/4}\left[\frac{\mathrm{Ai}\left(p^{2/3}\zeta\right)}{p^{4/3}}\sum_{k=0}^{\infty}\frac{c_k\left(\zeta\right)}{p^{2k}} + \frac{\mathrm{Ai}'\left(p^{2/3}\zeta\right)}{p^{2/3}}\sum_{k=0}^{\infty}\frac{d_k(\zeta)}{p^{2k}}\right] , \tag{3.54}$$

which is valid uniformly for $e_t \in (0,1)$, where Ai and Ai$'$ are the Airy function and its derivative, and

$$\zeta = \left[\frac{3}{2}\ln\left(\frac{1-\sqrt{1-e_t^2}}{e_t}\right) - \frac{3}{2}\sqrt{1-e_t^2}\right]^{2/3} . \tag{3.55}$$

We can replace the Airy functions with their representations as modified Bessel functions of the second kind, specifically [127]

$$\mathrm{Ai}(x) = \frac{1}{\pi}\sqrt{\frac{x}{3}}K_{1/3}\left(\frac{2}{3}x^{3/2}\right) , \tag{3.56}$$

$$\mathrm{Ai}'(x) = -\frac{1}{\pi}\frac{x}{\sqrt{3}}K_{2/3}\left(\frac{2}{3}x^{3/2}\right) . \tag{3.57}$$

The functions (a_k, b_k, c_k, d_k) are given by

$$a_k = \sum_{s=0}^{2k}\mu_s\zeta^{-3s/2}u_{2k-s}\left[(1-e_t^2)^{-1/2}\right] \tag{3.58}$$

$$b_k = -\zeta^{-1/2}\sum_{s=0}^{2k+1}\lambda_s\zeta^{-3s/2}u_{2k-s+1}\left[(1-e_t^2)^{-1/2}\right] \tag{3.59}$$

$$c_k = -\zeta^{1/2}\sum_{s=0}^{2k+1}\mu_s\zeta^{-3s/2}v_{2k-s+1}\left[(1-e_t^2)^{-1/2}\right] \tag{3.60}$$

$$d_k = \sum_{s=0}^{2k}\lambda_s\zeta^{-3s/2}v_{2k-s}\left[(1-e_t^2)^{-1/2}\right] \tag{3.61}$$

with the coefficients

$$\mu_s = -\frac{6s+1}{6s-1}\lambda_s\,, \tag{3.62}$$

$$\lambda_s = \frac{1}{(144)^s s!}\prod_{j=0}^{2s-1}(2s+2j+1)\,, \tag{3.63}$$

and the functions u_k and v_k are defined as

$$u_{k+1}(t) = \frac{1}{2}t^2\left(1-t^2\right)\frac{du_k(t)}{dt} + \frac{1}{8}\int_0^t dz\left(1-5z^2\right)u_k(z)\,, \tag{3.64}$$

$$v_{k+1}(t) = u_{k+1}(t) + t\left(t^2-1\right)\left[\frac{1}{2}u_k(t) + t\frac{du_k(t)}{dt}\right]\,. \tag{3.65}$$

Are we justified in replacing Bessel functions by an expansion about $p = \infty$? The accuracy of typical Taylor series is usually very poor when evaluating the series far from its expansion point. However, the series in question is asymptotic, and thus, its properties are very different from standard convergent power series. Asymptotic series generally approximate a function faster than a convergent power series provided one keeps the right number of terms. This is sometimes summarized by Carrier's rule: "divergent series converge faster than convergent series because they do not have to converge" [51]. What is meant by this is that we need only keep a few terms in the asymptotic expansion to obtain a good approximation to the function in question (but if we keep more terms than optimal, then the series will typically diverge).

For our purposes, this can be shown by comparing $J_p(pe_t)$ with its asymptotic expansion at different orders. Figure 3.1 shows the relative error between the Bessel function and its asymptotic expansion, up to seventh order, using an eccentricity of $e_t = 0.9$. Observe that at sixth and seventh order, the accuracy of the asymptotic series rapidly approaches machine precision for $p > 30$, while still being highly accurate for values $p \leq 30$. Observe also that the series achieves a minimum error at sixth order and that going to higher order only results in worse accuracy. This is a typical feature of divergent asymptotic series, which signals the order of an optimal asymptotic expansion or a *superasymptotic expansion* for short. It is worth noting that these properties change depending on the value of e_t. The smaller e_t is, the higher the order in the expansion that is needed to obtain the superasymptotic expansion. Further the value of p where the error becomes comparable to machine precision is also dependent on e_t. For the case considered in Fig. 3.1, the properties do not change provided $e_t \in (0.85, 0.95)$, but one would need more (less) terms if one wished to consider smaller (larger) values of the eccentricity. As we will show below, the order to which we keep the asymptotic expansion of the Bessel function is not crucial, provided it is high enough to allow for a robust calculation of the superasymptotic expansions for the enhancement factors.

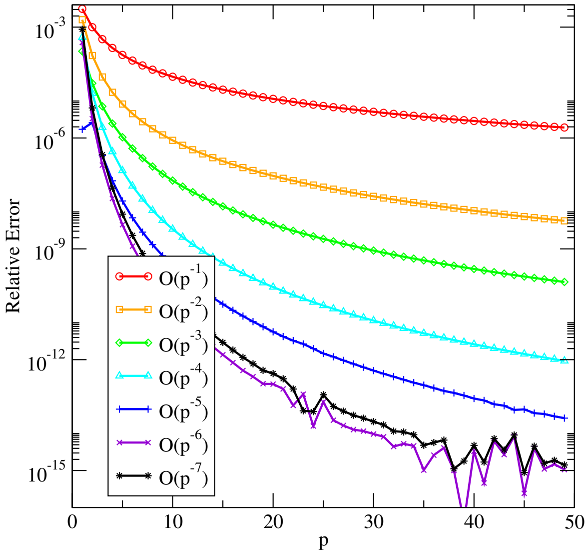

Figure 3.1: Accuracy of the uniform asymptotic expansion of the Bessel function $J_p(pe_t)$ as a function of p and for eccentricity $e_t = 0.9$. Going to higher order in the asymptotic expansion causes the series to become more accurate compared to the Bessel function, but at sixth order in $1/p$, the relative error achieves a minimum.

One may wonder whether one can replace the summations with integrals of the form

$$\sum_{p=1}^{\infty} \to \int_{1}^{\infty} dp\,, \tag{3.66}$$

when the asymptotic expansion is formally only valid as $p \to \infty$. The Fourier decomposition can be thought of as a way to modify circular orbits through the introduction of epicycles of frequency $\omega = np$ in such a way to generate an elliptical orbit. If the eccentricity is small, then only a finite number of terms contribute to the overall Fourier series. However, in the limit as $e_t \to 1$, an infinite number of epicycles contributes. The spacing between consecutive values of the Fourier index $\delta p = 1$ becomes infinitesimal in this limit and the summation collapses to an integral without loss of accuracy. Hence, we are justified in taking the summation to an integral provided we work in the high-eccentricity limit. This is the reason for the third step in the re-summation procedure, i.e. expanding the result of the integral about small eccentricity $\epsilon = 1 - e_t^2 \ll 1$.

A final issue of practice, not principle, is whether the integrals that are obtained after replacing the sums can actually be evaluated in closed form. As it turns out, the integrals take the form

$$\int_{1}^{\infty} dp\, p^n K_a\left(\frac{2}{3}\zeta^{3/2}p\right) K_b\left(\frac{2}{3}\zeta^{3/2}p\right)\,, \tag{3.67}$$

where (a, b) are either $1/3$ or $2/3$. This structure occurs in all of the enhancement factors except for those at 3PN order, which also contain a logarithmic term in the integrands. In all cases, these integrals can be evaluated in closed form in terms of hypergeometric functions with integral tables [83] or `Mathematica`.

The high-eccentricity expansion of the closed-form expression of these integrals depends on the sign of n. At low order in the asymptotic expansion of the Bessel functions [Eqs. (3.53) and (3.54)] one typically generates terms with $n > 0$, but at sufficiently high order, terms with $n < 0$ are also generated. When n is positive, the integrand resembles a Gaussian that peaks at a value $p > 1$, and the larger the eccentricity, the higher in p the integrand peaks at, as expected from the epicycle nature of the Fourier decomposition. In such a case, the lower n is, the higher order in ϵ the integrated result becomes, as shown in Table 3.1; this table also shows that the leading-order in ϵ behavior of the integrated result is independent of a and b.

When n is negative, the integrand peaks at $p = 1$ for all values of eccentricity, and to leading order in $1/p$, the integrand becomes

$$p^{-|n|} K_a \left(\frac{2}{3}\zeta^{3/2} p\right) K_b \left(\frac{2}{3}\zeta^{3/2} p\right) \sim \frac{3^{a+b}\Gamma(a)\Gamma(b)}{4p^{a+b+|n|}\zeta^{(3/2)(a+b)}} \,, \tag{3.68}$$

where observe that the power of ζ does not depend on n. Since ζ is the only quantity that contains any eccentricity dependence in the above expression, all $n < 0$ terms contribute at the same eccentricity order. In fact, when $e_t \sim 1$, $\zeta \sim \epsilon$, and the leading order expansion in ϵ of the integral is

$$\int_1^\infty dp \; p^{-|n|} K_a \left(\frac{2}{3}\zeta^{3/2} p\right) K_b \left(\frac{2}{3}\zeta^{3/2} p\right) \sim \epsilon^{-(3/2)(a+b)} \,. \tag{3.69}$$

Thus, when $n < 0$, all terms with the same values of (a, b) in the asymptotic expansion enter at the same order in ϵ, effectively generating an infinite number of terms starting at orders $\epsilon^{-2}, \epsilon^{-3/2}$ and ϵ^{-1}, depending on the term considered in the asymptotic expansion. We refer to the lowest order in ϵ at which this happens for a given term in the asymptotic expansion as the *breakdown order*.

This might seem like an unsurmountable problem for the re-summation procedure. The previous discussion, however, has left out a few important considerations that ameliorate the problem. The first is that the above analysis neglected the prefactors of the integral in Eq. (3.67), which also depend on eccentricity. For the

$n=8$	$n=7$	$n=6$	$n=5$	$n=4$
$\epsilon^{-27/2}$	ϵ^{-12}	$\epsilon^{-21/2}$	ϵ^{-9}	$\epsilon^{-15/2}$

Table 3.1: Leading order dependence on $\epsilon = 1 - e_t^2$ of the integrals in Eq. (3.67) for various positive powers of n.

enhancement factors being considered, these pre-factors take the breakdown order to higher order in ϵ [usually $\mathcal{O}(\epsilon^0)$, but sometimes higher order in ϵ for example in the 3PN enhancement factor $\tilde{\chi}(e_t)$.] Thus, if we can obtain accurate superasymptotic series expressions for the enhancement factors that terminate at an order lower than the breakdown order, then we will not need to concern ourselves with this problem. As we show in the next section, this is in fact the case for the enhancement factors considered in this work.

A second argument for why this apparent problem is not present in practice is the following. The uniform asymptotic expansion of the Bessel functions is actually divergent, so at the breakdown order, the more terms one keeps, the worse the approximation becomes. One could thus determine the superasymptotic expansion by comparing the asymptotic approximation to a numerical result, thus finding the optimal number of terms at the breakdown order that would need to be kept. As said in the previous paragraph, however, one does not need to worry about this to the order in ϵ we work. For the analysis of the enhancement factors to 3PN order, it is sufficient to cut the expansion of the Bessel functions in Eqs. (3.53) and (3.54) at seventh order in $1/p$ ($k = 3$).

Superasymptotic Enhancement Factors

The resummation method detailed above generates asymptotic series in ϵ for the enhancement factors that must be optimally truncated to obtain the best approximation to the exact enhancement factors. The truncation of the asymptotic series at its optimal order generates a superasymptotic series for the enhancement factors. Let us then construct such superasymptotic series by first carrying out a uniform asymptotic expansion of the Bessel functions to seventh order, then performing the integrals over the Fourier index and series expanding the resulting expressions about $\epsilon \ll 1$, and finally truncating the resulting asymptotic series in ϵ (at a given order in ϵ) to compare them to the numerical enhancement factors and determine the optimal truncation order.

The numerical enhancement factors that we compare the asymptotic expansions to are computed by directly evaluating the Bessel sums numerically, thus breaking from previous methods used in [29]. To do this, we define a numerical tolerance δ and mandate that for any enhancement factor $E(e_t)$,

$$\left| \frac{E_{Q+1}(e_t)}{\sum_{q=1}^{Q} E_q(e_t)} \right| < \delta \,, \tag{3.70}$$

where E_q is the summand in the enhancement factors of Sec. 2 (see e.g. Eq. (3.24)). For example, for $\varphi(e_t)$,

$$\begin{aligned} \varphi_q(e_t) &= \frac{q^3}{12 e_t^4} J_q^2(q e_t) \left[-3 e_t^6 q^2 + 3(1+q^2) - 3 e_t^2 (1 + 3q^2) + e_t^4 (1 + 9q^2) \right] \\ &\quad + \frac{(1-e_t^2) q^3}{4 e_t^2} J_q'^2(q e_t) \left[1 + (1 - e_t^2) q^2 \right] - \frac{q^4}{4 e_t^3} J_q(q e_t) J_q'(q e_t) \left[4 - 7 e_t^2 + 3 e_t^4 \right] . \end{aligned} \tag{3.71}$$

We adopt $\delta = 10^{-15}$ for our computation. We have verified that these expressions are consistent with the data of [31].

Let us begin by comparing the numerical and the asymptotic series for the $\varphi(e_t)$ enhancement factor in Figure 3.2. Observe that the minimum error occurs when truncating the series at $\mathcal{O}(\epsilon^{-2})$ for $e_t \lesssim 0.9$ and $\mathcal{O}(\epsilon^{-1})$ for $e_t \gtrsim 0.9$. This change in the order of the optimally truncated series can sometimes happen with asymptotic series; in our case, however, the turnover occurs at a relatively small overall error $< 10^{-8}$, and thus the difference generated by switching orders is negligible. As a result, we choose the $\varphi(e_t)$ superasymptotic series to include terms up to $\mathcal{O}(\epsilon^{-2})$ for all values of $e_t < 1$:

$$\begin{aligned}\varphi_{\text{super}}(e_t) = \frac{1}{\Gamma\left(\frac{1}{3}\right)\Gamma\left(\frac{2}{3}\right)} &\left[\frac{1328}{27(1-e_t^2)^5} - \frac{992}{15(1-e_t^2)^4} + \frac{33982}{1575(1-e_t^2)^3}\right. \\ &\left. - \frac{1577}{1575(1-e_t^2)^2}\right] . \end{aligned} \tag{3.72}$$

Observe that although the superasymptotic series is most accurate when $e_t \sim 1$ [with an accuracy of $\mathcal{O}(10^{-10})$], it can be as accurate as $10^{-3} - 10^{-4}$ in the limit $e_t \to 0$, a key property of asymptotic series.

This analysis can be repeated for the remaining enhancement factors to obtain superasymptotic series. For the 1.5PN order enhancement factor for the mass quadrupole tail in the angular momentum flux, we find

$$\begin{aligned}\tilde{\varphi}_{\text{super}}(e_t) = \frac{1}{\Gamma\left(\frac{1}{3}\right)\Gamma\left(\frac{2}{3}\right)} &\left[\frac{16}{(1-e_t^2)^{7/2}} - \frac{206}{15(1-e_t^2)^{5/2}} + \frac{47}{35(1-e_t^2)^{3/2}}\right. \\ &\left. + \frac{1}{50(1-e_t^2)^{1/2}}\right] . \end{aligned} \tag{3.73}$$

Notice that the powers of $1 - e_t^2$ are half-integer powers, while the powers in $\varphi(e_t)$ are integer powers. This property occurs for all enhancement factors that enter the angular momentum flux at half integer PN orders. Similarly, for the 2.5PN

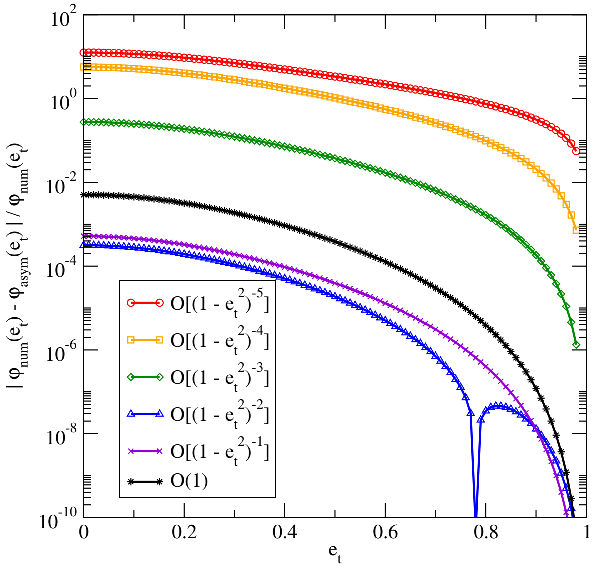

Figure 3.2: Accuracy of the asymptotic series for the enhancement factor $\varphi(e_t)$. The relative error to numerical results increases as we go to higher order in the series, but reaches a minimum at $\mathcal{O}\left[(1-e_t^2)^{-2}\right]$. The series can thus be optimally truncated at this order, generating the superasymptotic series for $\varphi(e_t)$.

enhancement factors coming from the mass octopole and current quadrupole tails, we find

$$\beta_{\rm super}(e_t) = \frac{1}{\Gamma\left(\frac{1}{3}\right)\Gamma\left(\frac{2}{3}\right)}\left[\frac{7244800}{49209(1-e_t^2)^6} - \frac{39162880}{147627(1-e_t^2)^5} + \frac{16731136}{114821(1-e_t^2)^4}\right.$$
$$\left. - \frac{14146304}{574105(1-e_t^2)^3} + \frac{1052528}{1722315(1-e_t^2)^2} - \frac{260144}{2052425375(1-e_t^2)}\right], \qquad (3.74)$$
$$\gamma_{\rm super}(e_t) = \frac{1}{\Gamma\left(\frac{1}{3}\right)\Gamma\left(\frac{2}{3}\right)}\left[\frac{1280}{3(1-e_t^2)^6} - \frac{7808}{9(1-e_t^2)^5} + \frac{97472}{175(1-e_t^2)^4} - \frac{20368}{175(1-e_t^2)^3}\right.$$
$$\left. + \frac{113228}{28875(1-e_t^2)^2} - \frac{122}{625625(1-e_t^2)}\right] \qquad (3.75)$$

for the energy flux and

$$\tilde{\beta}_{\rm super}(e_t) = \frac{1}{\Gamma\left(\frac{1}{3}\right)\Gamma\left(\frac{2}{3}\right)}\left[\frac{6732800}{147627(1-e_t^2)^{9/2}} - \frac{988160}{16403(1-e_t^2)^{7/2}} + \frac{2192128}{114821(1-e_t^2)^{5/2}}\right.$$

$$-\frac{40640}{49209(1-e_t^2)^{3/2}} - \frac{93424}{31575775(1-e_t^2)^{1/2}}\Bigg] \tag{3.76}$$

$$\tilde{\gamma}_{\text{super}}(e_t) = \frac{1}{\Gamma\left(\frac{1}{3}\right)\Gamma\left(\frac{2}{3}\right)}\left[\frac{640}{9(1-e_t^2)^{9/2}} - \frac{512}{5(1-e_t^2)^{7/2}} + \frac{6448}{175(1-e_t^2)^{5/2}}\right.$$
$$\left. -\frac{1024}{525(1-e_t^2)^{3/2}} + \frac{14}{1375(1-e_t^2)^{1/2}} + \frac{568}{56875}(1-e_t^2)^{1/2}\right], \tag{3.77}$$

for the angular momentum flux. Notice that the optimal truncation order can change when considering different enhancement factors, and recall that this optimal order is here determined by comparing each of the asymptotic enhancement factors to numerical factors, as explained in the $\varphi(e_t)$ case.

For the 2.5PN order enhancement factors that come from the mass quadrupole tail, specifically $[\alpha(e_t), \tilde{\alpha}(e_t)]$ and $[\theta(e_t), \tilde{\theta}(e_t)]$, it is easiest to break each of them into the distinct sums shown in Eq. (3.25) and (3.27), and consider the re-summation of each summation individually. Let us consider $[\theta(e_t), \tilde{\theta}(e_t)]$ first, which can be split as follows

$$\theta(e_t) = \theta_1(e_t) + \theta_2(e_t)\,, \tag{3.78}$$

$$\tilde{\theta}(e_t) = \tilde{\theta}_1(e_t) + \tilde{\theta}_2(e_t)\,, \tag{3.79}$$

$$\theta_1(e_t) = -\frac{21}{2848}\sum_{p=1}^{\infty} p^7 |\underset{(p)}{\mathcal{I}^{00}_{jk}}|^2 \tag{3.80}$$

$$\theta_2(e_t) = \frac{21}{1424}\sum_{p=1}^{\infty} p^7 \left[\underset{(p)}{\mathcal{I}^{11*}_{jk}}\underset{(p)}{\mathcal{I}^{jk}_{00}} + \underset{(p)}{\mathcal{I}^{00*}_{jk}}\underset{(p)}{\mathcal{I}^{jk}_{11}}\right], \tag{3.81}$$

$$\tilde{\theta}_1(e_t) = \frac{21i}{1424}\epsilon^{ijk}\hat{L}_i \sum_{p=1}^{\infty} p^6 \underset{(p)}{\mathcal{I}^{00}_{ja}}\,\underset{(p)}{\mathcal{I}^{a00*}_{k}}\,, \tag{3.82}$$

$$\tilde{\theta}_2(e_t) = -\frac{21i}{712}\epsilon^{ijk}\hat{L}_i \sum_{p=1}^{\infty} p^6 \left[\underset{(p)}{\mathcal{I}^{00}_{ja}}\,\underset{(p)}{\mathcal{I}^{a11*}_{k}} + \underset{(p)}{\mathcal{I}^{11}_{ja}}\,\underset{(p)}{\mathcal{I}^{a00*}_{k}}\right]. \tag{3.83}$$

The terms $[\theta_1(e_t), \tilde{\theta}_1(e_t)]$ are simply re-scalings of $[\varphi(e_t), \tilde{\varphi}(e_t)]$ respectively, so the superasymptotic expansions of those sums are simply re-scalings of Eq. (3.72) and (3.73). We apply the re-summation procedure on $[\theta_2(e_t), \tilde{\theta}_2(e_t)]$ to obtain superasymptotic expressions for them. To obtain the superasymptotic series for $[\theta(e_t), \tilde{\theta}(e_t)]$, we simply combine the superasymptotics of the individual terms to obtain

$$\theta_{\text{super}}(e_t) = \frac{1}{\Gamma\left(\frac{1}{3}\right)\Gamma\left(\frac{2}{3}\right)}\left[\frac{34240}{801(1-e_t^2)^6} - \frac{132560}{2403(1-e_t^2)^5} + \frac{794344}{46725(1-e_t^2)^4}\right.$$
$$\left. - \frac{141994}{140175(1-e_t^2)^3} + \frac{465188}{7709625(1-e_t^2)^2} - \frac{500627}{334083750(1-e_t^2)}\right] \tag{3.84}$$
$$\tilde{\theta}_{\text{super}}(e_t) = \frac{1}{\Gamma\left(\frac{1}{3}\right)\Gamma\left(\frac{2}{3}\right)}\left[\frac{4672}{267(1-e_t^2)^{9/2}} - \frac{1452}{89(1-e_t^2)^{7/2}} + \frac{119776}{46725(1-e_t^2)^{5/2}}\right.$$
$$\left. - \frac{266}{2225(1-e_t^2)^{3/2}} - \frac{21}{4450(1-e_t^2)^{1/2}}\right] \tag{3.85}$$

Let us now consider $[\alpha(e_t), \tilde{\alpha}(e_t)]$, which we can break down in a similar manner:

$$\alpha(e_t) = \alpha_1(e_t) + \alpha_2(e_t) + \alpha_3(e_t)\,, \tag{3.86}$$

$$\tilde{\alpha}(e_t) = \tilde{\alpha}_1(e_t) + \tilde{\alpha}_2(e_t) + \tilde{\alpha}_3(e_t)\,, \tag{3.87}$$

$$\alpha_1(e_t) = \frac{441}{3424(1-e_t^2)}\sum_{p=1}^{\infty} p^7 |\underset{(p)}{\mathcal{I}_{jk}^{00}}|^2\,, \tag{3.88}$$

$$\alpha_2(e_t) = \frac{63}{3424(1-e_t^2)}\sum_{m,s=-2}^{2}\sum_{p=1}^{\infty}(4s+3m)p^6\, \underset{(p,m)}{\mathcal{I}_{jk}^{00}}{}^{*}\underset{(p,s)}{\mathcal{I}_{00}^{jk}}\,, \tag{3.89}$$

$$\alpha_3(e_t) = -\frac{21}{3424}\sum_{p=1}^{\infty} p^7\left[\underset{(p)}{\mathcal{I}_{jk}^{01*}}\underset{(p)}{\mathcal{I}_{00}^{jk}} + \underset{(p)}{\mathcal{I}_{jk}^{00*}}\underset{(p)}{\mathcal{I}_{01}^{jk}}\right]\,, \tag{3.90}$$

$$\tilde{\alpha}_1(e_t) = -\frac{189i}{856(1-e_t^2)}\epsilon^{ijk}\hat{L}_i\sum_{p=1}^{\infty} p^6 \underset{(p)}{\mathcal{I}_{ja}^{00}}\ \underset{(p)}{\mathcal{I}_{k}^{a00*}}\,, \tag{3.91}$$

$$\tilde{\alpha}_2(e_t) = \frac{189i}{1712(1-e_t^2)}\epsilon^{ijk}\hat{L}_i\sum_{m,s=-2}^{2}\sum_{p=1}^{\infty} p^5(m+s)\underset{(p,s)}{\mathcal{I}_{ja}^{00}}\ \underset{(p,m)}{\mathcal{I}_{k}^{a00*}}\,, \tag{3.92}$$

$$\tilde{\alpha}_3(e_t) = \frac{21i}{1712}\epsilon^{ijk}\hat{L}_i\sum_{p=1}^{\infty} p^6\left[\underset{(p)}{\mathcal{I}_{ja}^{00}}\ \underset{(p)}{\mathcal{I}_{k}^{a01*}} + \underset{(p)}{\mathcal{I}_{ja}^{01}}\ \underset{(p)}{\mathcal{I}_{k}^{a00*}}\right]\,. \tag{3.93}$$

Like with $[\theta(e_t), \tilde{\theta}(e_t)]$, the first terms $[\alpha_1(e_t), \tilde{\alpha}_1(e_t)]$ are once again re-scalings of $[\varphi(e_t), \tilde{\varphi}(e_t)]$ and we thus do not need to apply the re-summation procedure again on them. The second terms $[\alpha_2(e_t), \tilde{\alpha}_2(e_t)]$, however, do need to be resummed, and we thus apply the same techniques discussed above.

The last two terms $[\alpha_3(e_t), \tilde{\alpha}_3(e_t)]$ require some additional handling, since they contain undetermined integrals involving $V(e_t; u) - u$ [see e.g. Eq. (2.70)]. To evaluate $[\alpha_3(e_t), \tilde{\alpha}_3(e_t)]$, we separate out the terms that do not depend on these integrals, i.e. those with summands that are proportional to $[J_p(pe_t)^2, J_p'(pe_t)^2, J_p(pe_t)J_p'(pe_t)]$, which we call $[\alpha_3^{(1)}(e_t), \tilde{\alpha}_3^{(1)}(e_t)]$, specifically

$$\begin{aligned}
\alpha_3^{(1)}(e_t) = {} & \frac{8J_p(pe_t)^2p^3}{21e_t^4(1-e_t^2)^{3/2}}\left[1890 - 4221e_t^2 + 3024e_t^4 - 693e_t^6\right. \\
& \left. + \sqrt{1-e_t^2}\left(-111 + 222e_t^2 - 36e_t^4 - 19e_t^6\right)\right] + \frac{8J_p(pe_t)^2p^5}{21e_t^4}(1-e_t^2)^{3/2}\left[378\right. \\
& \left. -378e_t^2 + \sqrt{1-e_t^2}\left(-115 + 23e_t^2\right)\right] + \frac{8J_p'(pe_t)^2p^3}{7e_t^2\sqrt{1-e_t^2}}\left[630 - 525e_t^2\right. \\
& \left. + \sqrt{1-e_t^2}\left(-37 + 37e_t^2\right)\right] + \frac{8J_p'(pe_t)^2p^5}{21e_t^2}(1-e_t^2)\left[-115 + 25e_t^2 + 378\sqrt{1-e_t^2}\right] \\
& + \frac{288J_p(pe_t)J_p'(pe_t)p^2}{e_t^3\sqrt{1-e_t^2}}\left(-2 + e_t^2\right) + \frac{32J_p(pe_t)J_p'(pe_t)p^6}{21e_t^3}\left(1-e_t^2\right)^3 \\
& + \frac{8J_p(pe_t)J_p'(pe_t)p^4}{21e_t^3\sqrt{1-e_t^2}}\left[-3024 + 5040e_t^2 - 2016e_t^4\right. \\
& \left. + \sqrt{1-e_t^2}\left(448 - 603e_t^2 + 103e_t^4\right)\right], \qquad (3.94)
\end{aligned}$$

$$\begin{aligned}
\tilde{\alpha}_3^{(1)}(e_t) = {} & -\frac{144J_p(pe_t)^2p}{e_t^4(1-e_t^2)}\left(-2 + e_t^2\right)^2 - \frac{8J_p(pe_t)^2p^3}{3e_t^4}\sqrt{1-e_t^2}\left[-64 + 70e_t^2 + 5e_t^4\right. \\
& \left. + \sqrt{1-e_t^2}\left(432 - 234e_t^2\right)\right] + \frac{32J_p(pe_t)^2p^5}{21e_t^4}\left(1-e_t^2\right)^{7/2} - \frac{576J_p'(pe_t)^2p}{e_t^2} \\
& + \frac{32J_p(pe_t)^2p^5}{21e_t^4}(1-e_t^2)^{5/2} + \frac{16J_p'(pe_t)^2p^3}{21e_t^2\sqrt{1-e_t^2}}\left[224 - 358e_t^2 + 134e_t^4\right. \\
& \left. - \sqrt{1-e_t^2}\left(-1512 + 1197e_t^2\right)\right] + \frac{8J_p(pe_t)J_p'(pe_t)p^2}{7e_t^3(1-e_t^2)^{3/2}}\left[-148 + 370e_t^2 - 240e_t^4\right.
\end{aligned}$$

$$
\begin{aligned}
&+18e_t^6+\sqrt{1-e_t^2}\left(2520-3864e_t^2+1449e_t^4\right)\Big]\\
&+\frac{32J_p(pe_t)J_p'(pe_t)p^4}{21e_t^3}\left(-115+24+378\sqrt{1-e_t^2}\right)\,.
\end{aligned}
\tag{3.95}
$$

Since these expressions are of the form of the other tail enhancement factors, we simply apply our re-summation procedure to them and find their superasymptotic expressions. The remaining terms, which we denote $[\alpha_3^{(2)}(e_t),\tilde{\alpha}_3^{(2)}(e_t)]$, do contain the undetermined integrals. Although these terms are complex, the enhancement factors $[\alpha_3^{(2)}(e_t),\tilde{\alpha}_3^{(2)}(e_t)]$ are real valued. Hence the imaginary part vanishes upon integration, and we are left with solely the real part, specifically

$$
\begin{aligned}
\alpha_3^{(2)}(e_t)=\;&\frac{12p^5J_p(pe_t)}{\pi e_t^2\sqrt{1-e_t^2}}\int_0^{2\pi}du\,[1-e_t\cos(u)]\,\arctan\left[\frac{\beta_t\,\sin(u)}{1-\beta_t\,\cos(u)}\right]\\
&\times\big\{2(-2+e_t^2)[e_t-\cos(u)]\cos\{p[u-e_t\sin(u)]\}\sin(u)\\
&+(-1+e_t^2)p[-3e_t^2+4e_t\cos(u)+(-2+e_t^2)\cos(2u)]\sin\{p[u-e_t\sin(u)]\}\big\}\\
&-\frac{12p^5J_p'(pe_t)}{\pi e_t\sqrt{1-e_t^2}}\int_0^{2\pi}du\,[1-e_t\cos(u)]\arctan\left[\frac{\beta_t\,\sin(u)}{1-\beta_t\,\cos(u)}\right]\\
&\times\big\{4(-1+e_t^2)p[e_t-\cos(u)]\cos\{p[u-e_t\sin(u)]\}\sin(u)\\
&+[3e_t^2-4e_t\cos(u)-(-2+e_t^2)\cos(2u)]\sin\{p[u-e_t\sin(u)]\}\big\}\;,
\end{aligned}
\tag{3.96}
$$

$$
\begin{aligned}
\tilde{\alpha}_3^{(2)}(e_t)=\;&-\frac{12p^4J_p(pe_t)}{\pi e_t^2(1-e_t^2)}\int_0^{2\pi}du\,[1-e_t\cos(u)]\,\arctan\left[\frac{\beta_t\,\sin(u)}{1-\beta_t\,\cos(u)}\right]\\
&\times\big\{8(-1+e_t^2)^2p[-e_t+\cos(u)]\cos\{p[u-e_t\sin(u)]\}\sin(u)\\
&+(-2+e_t^2)[-3e_t^2+4e_t\cos(u)+(-2+e_t^2)\cos(2u)]\sin\{p(u-e_t\sin(u)]\}\big\}\\
&+\frac{24p^4J_p'(pe_t)}{\pi e_t}\int_0^{2\pi}du\,[1-e_t\cos(u)]\arctan\left[\frac{\beta_t\,\sin(u)}{1-\beta_t\,\cos(u)}\right]\\
&\times\{4[-e_t+\cos(u)]\cos\{n[u-e_t\sin(u)]\}\sin(u)\\
&+p[3e_t^2-4e_t\cos(u)-(-2+e_t^2)\cos(2u)]\sin\{p[u-e_t\sin(u)]\}\big\}\;.
\end{aligned}
\tag{3.97}
$$

To obtain analytic expressions for these terms, we follow the procedure of [79] and begin by factoring out the high eccentricity dependence, which can be determined by comparison to other 2.5PN order enhancement factors. For the energy flux, the controlling factor is $(1-e_t^2)^{-6}$, while for the angular momentum flux it is $(1-e_t^2)^{-9/2}$. After factoring out this dependence, we perform an expansion about $e_t \ll 1$ to $\mathcal{O}(e_t^{30})$, which allows us to evaluate the necessary integrals, and obtain approximants of the form

$$\alpha_3^{(2)}(e_t) = \frac{A(e_t)}{(1-e_t^2)^6}\,, \tag{3.98}$$

$$\tilde{\alpha}_3^{(2)}(e_t) = \frac{\tilde{A}(e_t)}{(1-e_t^2)^{9/2}}\,, \tag{3.99}$$

where $[A(e_t), \tilde{A}(e_t)]$ are polynomials to $\mathcal{O}(e_t^{30})$. Finally, we perform a Padé resummation of the resulting polynomial in e_t by writing

$$A^{\rm PD}(e_t) = \frac{\sum_{n=0}^{N} A^{(n)} e_t^n}{1 + \sum_{m=1}^{M} A_{(m)} e_t^m} \tag{3.100}$$

and likewise for $\tilde{A}(e_t)$. We obtain Padé approximants of order $(M, N) = (14, 16)$ for each of these enhancement factors. We chose the order of the Padé approximants such that they are the most accurate compared to numerical results given the order we work to in the small eccentricity expansion. We list the coefficients of these Padé approximants in Appendix B. To obtain the final superasymptotic expressions for $[\alpha(e_t), \tilde{\alpha}(e_t)]$, we simply combine all of the terms back together to find

$$\alpha_{\rm super}(e_t) = \frac{1}{\Gamma\left(\frac{1}{3}\right)\Gamma\left(\frac{2}{3}\right)}\left[\frac{77776}{321(1-e_t^2)^6} - \frac{15904}{107(1-e_t^2)^{11/2}} + \frac{300512}{963(1-e_t^2)^5}\right.$$
$$+\frac{19530}{107(1-e_t^2)^{9/2}} - \frac{4871974}{56175(1-e_t^2)^4} - \frac{26952}{535(1-e_t^2)^{7/2}} + \frac{111533}{56175(1-e_t^2)^3}$$

$$
\begin{aligned}
&+\frac{8313}{5350(1-e_t^2)^{5/2}}-\frac{2280749}{6179250(1-e_t^2)^2}-\frac{4293}{294250(1-e_t^2)^{3/2}}\Bigg] \\
&+\frac{A^{\mathrm{PD}}(e_t)}{(1-e_t^2)^6}
\end{aligned}
\tag{3.101}
$$

$$
\begin{aligned}
\tilde{\alpha}_{\mathrm{super}}(e_t) = {}& \frac{1}{\Gamma\left(\frac{1}{3}\right)\Gamma\left(\frac{2}{3}\right)}\Bigg[\frac{67688}{963(1-e_t^2)^{9/2}}-\frac{4893}{107(1-e_t^2)^4}-\frac{5996}{107(1-e_t^2)^{7/2}} \\
&+\frac{38157}{1070(1-e_t^2)^3}+\frac{89699}{56175(1-e_t^2)^{5/2}}-\frac{5877}{2140(1-e_t^2)^2} \\
&+\frac{944}{1605(1-e_t^2)^{3/2}}\Bigg]+\frac{\tilde{A}^{\mathrm{PD}}(e_t)}{(1-e_t^2)^{9/2}}
\end{aligned}
\tag{3.102}
$$

Finally, we apply the re-summation procedure to the 3PN tail-of-tails and tail-squared enhancement factors $[\chi(e_t), \tilde{\chi}(e_t)]$ to obtain the following superasymptotic expressions,

$$
\begin{aligned}
\chi_{\mathrm{super}}(e_t) = {}& \frac{1}{(1-e_t^2)^{13/2}}\Bigg[\frac{421543}{1536}-\frac{52745\gamma_E}{1024}-\frac{52745\ln(2)}{256}-\frac{52745\ln(3)}{2048} \\
&-\frac{158235\ln(1-e_t^2)}{2048}\Bigg]+\frac{1}{(1-e_t^2)^{11/2}}\Bigg[-\frac{2777339}{5120}+\frac{24717\gamma_E}{256}+\frac{24717\ln(2)}{64} \\
&+\frac{24717\ln(3)}{512}+\frac{74151\ln(1-e_t^2)}{512}\Bigg]+\frac{1}{(1-e_t^2)^{9/2}}\Bigg[\frac{10449133}{30720}-\frac{86065\gamma_E}{1536} \\
&-\frac{86065\ln(2)}{384}-\frac{86065\ln(3)}{3072}-\frac{86065\ln(1-e_t^2)}{1024}\Bigg]+\frac{1}{(1-e_t^2)^{7/2}}\Bigg[-\frac{1090519}{15360} \\
&+\frac{7895\gamma_E}{768}+\frac{7895\ln(2)}{192}+\frac{355271\ln(3)}{69120}+\frac{\ln(243)}{86400}+\frac{7895\ln(1-e_t^2)}{512}\Bigg] \\
&+\frac{1}{(1-e_t^2)^{5/2}}\Bigg[\frac{760247221}{275968000}-\frac{297\gamma_E}{1024}-\frac{297\ln(2)}{256}-\frac{1024063\ln(3)}{7096320} \\
&-\frac{2521\ln(243)}{17740800}-\frac{891\ln(1-e_t^2)}{2048}\Bigg]+\frac{1}{(1-e_t^2)^{3/2}}\Bigg[\frac{568287127}{67267200000}+\frac{71\ln(2)}{682500} \\
&+\frac{1327283\ln(3)}{2882880000}-\frac{19843\ln(243)}{221760000}-\frac{71\ln(768)}{5460000}\Bigg] \\
&+\frac{1}{(1-e_t^2)^{1/2}}\Bigg[-\frac{4896210901}{4708704000000}+\frac{12270499\ln(2)}{24324300000}+\frac{423525727\ln(3)}{5448643200000} \\
&-\frac{410009\ln(243)}{139708800000}-\frac{12270499\ln(768)}{194594400000}\Bigg],
\end{aligned}
\tag{3.103}
$$

$$
\begin{aligned}
\tilde{\chi}_{\text{super}}(e_t) = {} & \frac{1}{(1-e_t^2)^5}\left[\frac{35583}{512} - \frac{3465\gamma_E}{256} - \frac{3465\ln(2)}{64} - \frac{3465\ln(3)}{512}\right. \\
& \left. - \frac{10395\ln(1-e_t^2)}{512}\right] + \frac{1}{(1-e_t^2)^4}\left[-\frac{51359}{512} + \frac{4655\gamma_E}{256} + \frac{4655\ln(2)}{64}\right. \\
& \left. + \frac{4655\ln(3)}{512} + \frac{13965\ln(1-e_t^2)}{512}\right] + \frac{1}{(1-e_t^2)^3}\left[\frac{47481}{1280} - \frac{1515\gamma_E}{256}\right. \\
& \left. - \frac{1515\ln(2)}{64} - \frac{1519\ln(3)}{512} + \frac{\ln(243)}{640} - \frac{4545\ln(1-e_t^2)}{512}\right] \\
& + \frac{1}{(1-e_t^2)^2}\left[-\frac{53091}{22400} + \frac{69\gamma_E}{256} + \frac{69\ln(2)}{64} + \frac{3041\ln(3)}{23040} + \frac{\ln(243)}{1800}\right. \\
& \left. + \frac{207\ln(1-e_t^2)}{512}\right] + \frac{1}{(1-e_t^2)}\left[-\frac{956569}{68992000} + \frac{\ln(2)}{700} - \frac{6269\ln(3)}{4435200}\right. \\
& \left. + \frac{7061\ln(243)}{22176000} - \frac{\ln(768)}{5600}\right] + \frac{15822507}{22422400000} - \frac{553\ln(2)}{6435000} \\
& - \frac{553\ln(3)}{51480000} + \frac{553\ln(768)}{51480000}\,. \qquad (3.104)
\end{aligned}
$$

This completes the calculation of the superasymptotic expansion of the enhancement factors.

Hyperasymptotic Enhancement Factors

The main concern with the superasymptotic series for the enhancement factors is their relatively poor accuracy when the eccentricity is small, especially compared to other methods for evaluating the enhancement factors. Post-circular methods, like those in [79, 148], give better accuracy when $e_t \ll 1$, whereas the superasymptotic series are better for $\epsilon = 1 - e_t^2 \ll 1$. We can resolve this concern by producing a *hyperasymptotic series* through a combination of the superasymptotic expansions we already derived with the post-circular expansion of the enhancement factors in [79, 148]

Consider an enhancement factor $E(e_t)$ with a superasymptotic expression $E_{\text{super}}(e_t)$. The simplest way of improve the accuracy of the superasymptotic series in the small eccentricity limit is to consider the remainder functional

$$E_{\text{remainder}}(e_t) = E(e_t) - E_{\text{super}}(e_t)\,. \tag{3.105}$$

To study the behavior of the remainder when the eccentricity is small, we create a Taylor series of order N for the remainder by

$$\delta E^N(e_t) = \hat{\mathcal{T}}^N_{e_t} E_{\text{remainder}}(e_t)\,, \tag{3.106}$$

where $\hat{\mathcal{T}}^N_{e_t}$ is a differential operator that generates the Taylor series. We could have chosen a different representation for the remainder, such as a Padé resummation of the resulting Taylor expansion, but as we will see below, a simple Taylor expansion is sufficiently accurate and the most appropriate in the $e_t \ll 1$ limit. With an accurate representation of the small eccentricity behavior, we can then generate a hyperasymptotic series for the enhancement factor $E(e_t)$ via

$$E_{\text{hyper}}(e_t) = E_{\text{super}}(e_t) + \delta E^N(e_t)\,. \tag{3.107}$$

These hyperasymptotic expressions have two important properties: (1) they have the right limiting behavior at small eccentricity and (2) we have analytic control over the remainder.

Figure 3.3 compares the numerical $\varphi(e_t)$ and the hyperasymptotic $\varphi_{\text{hyper}}(e_t)$. Observe that the hyperasymptotic series is well-behaved in the small eccentricity limit as expected, with a relative error that collapses to the level of the tolerance δ in the circular limit. Further, the error can be increasingly improved by going to higher order in e_t in the remainder. The remainder functionals at twentieth order for

$[\varphi(e_t), \tilde{\varphi}(e_t)]$ are

$$\begin{aligned}
\delta\varphi^{20}(e_t) &= 1 - \frac{3427}{945\Gamma(\frac{1}{3})\Gamma(\frac{2}{3})} + e_t^2\left[\frac{2335}{192} - \frac{208456}{4725\Gamma(\frac{1}{3})\Gamma(\frac{2}{3})}\right] \\
&\quad + e_t^4\left[\frac{42955}{768} - \frac{319561}{1575\Gamma(\frac{1}{3})\Gamma(\frac{2}{3})}\right] + e_t^6\left[\frac{6204647}{36864} - \frac{2884936}{4725\Gamma(\frac{1}{3})\Gamma(\frac{2}{3})}\right] \\
&\quad + e_t^8\left[\frac{352891481}{884736} - \frac{1367347}{945\Gamma(\frac{1}{3})\Gamma(\frac{2}{3})}\right] + e_t^{10}\left[\frac{286907786543}{353894400} - \frac{61760}{21\Gamma(\frac{1}{3})\Gamma(\frac{2}{3})}\right] \\
&\quad + e_t^{12}\left[\frac{6287456255443}{4246732800} - \frac{1208431}{225\Gamma(\frac{1}{3})\Gamma(\frac{2}{3})}\right] + e_t^{14}\Bigg[\frac{5545903772613817}{2219625676800} \\
&\quad - \frac{4758512}{525\Gamma(\frac{1}{3})\Gamma(\frac{2}{3})}\Bigg] + e_t^{16}\left[\frac{422825073954708079}{106542032486400} - \frac{7558199}{525\Gamma(\frac{1}{3})\Gamma(\frac{2}{3})}\right] \\
&\quad + e_t^{18}\left[\frac{16591601184982867763339}{2761569482047488800} - \frac{20596024}{945\Gamma(\frac{1}{3})\Gamma(\frac{2}{3})}\right] \\
&\quad + e_t^{20}\left[\frac{7247233720423054544448081}{828470844614246400000} - \frac{29987903}{945\Gamma(\frac{1}{3})\Gamma(\frac{2}{3})}\right]
\end{aligned} \tag{3.108}$$

$$\begin{aligned}
\delta\tilde{\varphi}^{20}(e_t) &= 1 - \frac{3811}{1050\Gamma(\frac{1}{3})\Gamma(\frac{2}{3})} + e_t^2\left[\frac{209}{32} - \frac{49751}{2100\Gamma(\frac{1}{3})\Gamma(\frac{2}{3})}\right] \\
&\quad + e_t^4\left[\frac{2415}{128} - \frac{574913}{8400\Gamma(\frac{1}{3})\Gamma(\frac{2}{3})}\right] + e_t^6\left[\frac{730751}{18432} - \frac{23011}{160\Gamma(\frac{1}{3})\Gamma(\frac{2}{3})}\right] \\
&\quad + e_t^8\left[\frac{10355719}{147456} - \frac{326097}{1280\Gamma(\frac{1}{3})\Gamma(\frac{2}{3})}\right] + e_t^{10}\left[\frac{6594861233}{58982400} - \frac{5191733}{12800\Gamma(\frac{1}{3})\Gamma(\frac{2}{3})}\right] \\
&\quad + e_t^{12}\left[\frac{23422887967}{141557760} - \frac{30732361}{51200\Gamma(\frac{1}{3})\Gamma(\frac{2}{3})}\right] + e_t^{14}\Bigg[\frac{51535146547541}{221962567680} \\
&\quad - \frac{603727553}{716800\Gamma(\frac{1}{3})\Gamma(\frac{2}{3})}\Bigg] + e_t^{16}\left[\frac{16666910315347223}{53271016243200} - \frac{2603342599}{2293760\Gamma(\frac{1}{3})\Gamma(\frac{2}{3})}\right] \\
&\quad + e_t^{18}\left[\frac{805584253308027441 7}{19725496300339200} - \frac{20389261321}{13762560\Gamma(\frac{1}{3})\Gamma(\frac{2}{3})}\right] \\
&\quad + e_t^{20}\left[\frac{1024885995293794354963}{1972549630033920000} - \frac{74113622297}{39321600\Gamma(\frac{1}{3})\Gamma(\frac{2}{3})}\right]
\end{aligned} \tag{3.109}$$

Obviously, the more terms one keeps in the expansion of the remainder, the more accurate the approximation will be at small eccentricity; in practice, how many terms to keep will depend on the accuracy desired in this limit.

This procedure can be applied for the remaining enhancement factors through

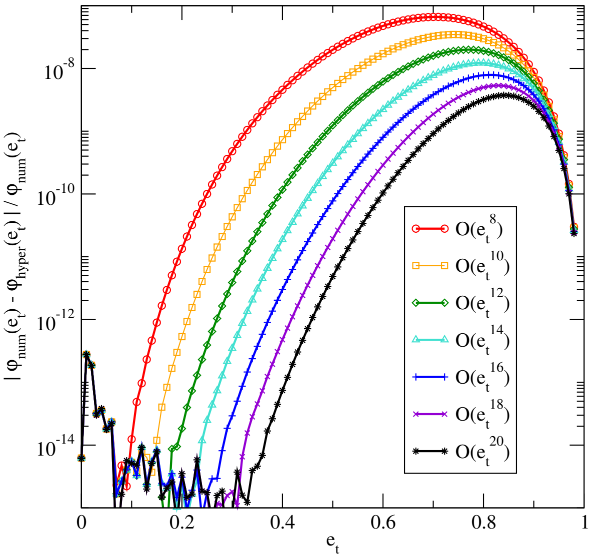

Figure 3.3: Comparison of the numerical results for $\varphi(e_t)$ with its hyperasymptotic series, $\varphi_{\text{hyper}}(e_t)$, at different orders in e_t. The addition of the remainder improves the accuracy at small eccentricity by about nine orders of magnitude.

3PN order. For the 2.5PN order enhancement factors, it is simplest to consider the total 2.5PN order fluxes

$$\langle \mathcal{P}_\infty^{\text{2.5PNtails}} \rangle = \frac{32}{5}\pi\eta^2 x^{15/2}\left[-\frac{8191}{672}\psi(e_t) - \frac{583}{24}\eta\zeta(e_t)\right], \tag{3.110}$$

$$\langle \mathcal{G}_\infty^{\text{2.5PNtails}} \rangle = \frac{32}{5}\pi\eta^2 x^{15/2}\left[-\frac{8191}{672}\tilde{\psi}(e_t) - \frac{583}{24}\eta\tilde{\zeta}(e_t)\right], \tag{3.111}$$

where the new enhancement factors $\psi(e_t)$ and $\zeta(e_t)$ are

$$\psi(e_t) = \frac{13696}{8191}\alpha(e_t) - \frac{16403}{24573}\beta(e_t) - \frac{112}{24573}\gamma(e_t)\,, \tag{3.112}$$

$$\zeta(e_t) = -\frac{1424}{4081}\theta(e_t) + \frac{16403}{12243}\beta(e_t) + \frac{16}{1749}\gamma(e_t)\,, \tag{3.113}$$

The analogs $\tilde{\psi}(e_t)$ and $\tilde{\zeta}(e_t)$ have the same definitions as those above except with $[\tilde{\alpha}(e_t), \tilde{\theta}(e_t), \tilde{\beta}(e_t), \tilde{\gamma}(e_t)]$. The superasymptotic expressions for these new enhancement factors are simply the superasymptotics of the individual enhancement factors from which they are constructed. Applying the scheme to generate hyperasymptotic expression for these new enhancement factors, we find the remainders

$$
\begin{aligned}
\delta\psi^{20}(e_t) = 1 &- \frac{241580064}{66551875\Gamma(\frac{1}{3})\Gamma(\frac{2}{3})} + e_t^2\left[\frac{188440}{8191} - \frac{1283135619824}{15373483125\Gamma(\frac{1}{3})\Gamma(\frac{2}{3})}\right] \\
&+ e_t^4\left[\frac{78746077}{524224} - \frac{8377507600624}{15373483125\Gamma(\frac{1}{3})\Gamma(\frac{2}{3})}\right] + e_t^6\left[\frac{2769593143}{4718016}\right. \\
&\left.- \frac{10912663062368}{5124494375\Gamma(\frac{1}{3})\Gamma(\frac{2}{3})}\right] + e_t^8\left[\frac{1038414910159}{603906048} - \frac{8717702789819}{1397589375\Gamma(\frac{1}{3})\Gamma(\frac{2}{3})}\right] \\
&+ e_t^{10}\left[\frac{10517947248419}{2516275200} - \frac{233112310241024}{15373483125\Gamma(\frac{1}{3})\Gamma(\frac{2}{3})}\right] \\
&+ e_t^{12}\left[\frac{51677468559131363}{5797498060800} - \frac{1325626967291149}{40995955000\Gamma(\frac{1}{3})\Gamma(\frac{2}{3})}\right] \\
&+ e_t^{14}\left[\frac{1469879396225616469 7}{852232214937600} - \frac{366425963194427}{5856565000\Gamma(\frac{1}{3})\Gamma(\frac{2}{3})}\right] \\
&+ e_t^{16}\left[\frac{1350835701827482712840 9}{436342894048051200} - \frac{147327907838689583}{1311870560000\Gamma(\frac{1}{3})\Gamma(\frac{2}{3})}\right] \\
&+ e_t^{18}\left[\frac{462509893308626646120797}{8835943604473036800} - \frac{124551349162839959}{655935280000\Gamma(\frac{1}{3})\Gamma(\frac{2}{3})}\right] \\
&+ e_t^{20}\left[\frac{4766936073001835060207935793}{56550039068627435520000} - \frac{962782005725736765 7}{31484893440000\Gamma(\frac{1}{3})\Gamma(\frac{2}{3})}\right],
\end{aligned}
\tag{3.114}
$$

$$
\begin{aligned}
\delta\tilde{\psi}^{20}(e_t) = 1 &- \frac{55624031984}{15373483125\Gamma(\frac{1}{3})\Gamma(\frac{2}{3})} + e_t^2\left[\frac{102536}{8191} - \frac{698208327368}{15373483125\Gamma(\frac{1}{3})\Gamma(\frac{2}{3})}\right] \\
&+ e_t^4\left[\frac{27975523}{524224} - \frac{2976133354982}{15373483125\Gamma(\frac{1}{3})\Gamma(\frac{2}{3})}\right] + e_t^6\left[\frac{709642057}{4718016}\right. \\
&\left.- \frac{8388221641661}{15373483125\Gamma(\frac{1}{3})\Gamma(\frac{2}{3})}\right] + e_t^8\left[\frac{203853989947}{603906048} - \frac{4302911627633}{3513939000\Gamma(\frac{1}{3})\Gamma(\frac{2}{3})}\right] \\
&+ e_t^{10}\left[\frac{4944184758677}{7548825600} - \frac{83488815643601}{35139390000\Gamma(\frac{1}{3})\Gamma(\frac{2}{3})}\right] \\
&+ e_t^{12}\left[\frac{6658083547039409}{5797498060800} - \frac{17744668624161}{4259320000\Gamma(\frac{1}{3})\Gamma(\frac{2}{3})}\right] \\
&+ e_t^{14}\left[\frac{35397103550602159}{18938493665280} - \frac{404305552234341}{59630480000\Gamma(\frac{1}{3})\Gamma(\frac{2}{3})}\right]
\end{aligned}
$$

$$\begin{aligned}
&+ e_t^{16}\left[\frac{179071486944184743991}{62334699149721600} - \frac{764822533448511}{73391360000\Gamma(\frac{1}{3})\Gamma(\frac{2}{3})}\right] \\
&+ e_t^{18}\left[\frac{7457576214411997508197}{1767188720894607360} - \frac{1348218095132281}{88069632000\Gamma(\frac{1}{3})\Gamma(\frac{2}{3})}\right] \\
&+ e_t^{20}\left[\frac{337929898617545561543145703}{56550039068627435520000} - \frac{38182917211753667}{1761392640000\Gamma(\frac{1}{3})\Gamma(\frac{2}{3})}\right],
\end{aligned} \tag{3.115}$$

$$\begin{aligned}
\delta\zeta^{20}(e_t) = {} & 1 - \frac{250066100248}{68935741875\Gamma(\frac{1}{3})\Gamma(\frac{2}{3})} + e_t^{2}\left[\frac{1011565}{48972} - \frac{5165477150408}{68935741875\Gamma(\frac{1}{3})\Gamma(\frac{2}{3})}\right] \\
&+ e_t^{4}\left[\frac{106573021}{783552} - \frac{1619660334008}{3282654375\Gamma(\frac{1}{3})\Gamma(\frac{2}{3})}\right] + e_t^{6}\left[\frac{456977827}{854784}\right. \\
&\left. - \frac{133691089979528}{68935741875\Gamma(\frac{1}{3})\Gamma(\frac{2}{3})}\right] + e_t^{8}\left[\frac{128491074157}{82059264} - \frac{55938524367784}{9847963125\Gamma(\frac{1}{3})\Gamma(\frac{2}{3})}\right] \\
&+ e_t^{10}\left[\frac{342306246988373}{90265190400} - \frac{105369692129672}{7659526875\Gamma(\frac{1}{3})\Gamma(\frac{2}{3})}\right] \\
&+ e_t^{12}\left[\frac{69677817044303231}{8665458278400} - \frac{8704718214568}{298423125\Gamma(\frac{1}{3})\Gamma(\frac{2}{3})}\right] \\
&+ e_t^{14}\left[\frac{2386244038997979551}{154402711142400} - \frac{429418866068552}{7659526875\Gamma(\frac{1}{3})\Gamma(\frac{2}{3})}\right] \\
&+ e_t^{16}\left[\frac{5987988065386963552943}{217399017288499200} - \frac{765322594645592}{7659526875\Gamma(\frac{1}{3})\Gamma(\frac{2}{3})}\right] \\
&+ e_t^{18}\left[\frac{61448938675545297383797}{1329005313235353600} - \frac{1651784262696184}{9847963125\Gamma(\frac{1}{3})\Gamma(\frac{2}{3})}\right] \\
&+ e_t^{20}\left[\frac{6249104916857243979130332809}{84524737921768488960000}\right. \\
&\left. - \frac{18488329739373848}{68935741875\Gamma(\frac{1}{3})\Gamma(\frac{2}{3})}\right],
\end{aligned} \tag{3.116}$$

$$\begin{aligned}
\delta\tilde{\zeta}^{20}(e_t) = {} & 1 - \frac{83380049048}{22978580625\Gamma(\frac{1}{3})\Gamma(\frac{2}{3})} + e_t^{2}\left[\frac{102371}{8162} - \frac{348496717732}{7659526875\Gamma(\frac{1}{3})\Gamma(\frac{2}{3})}\right] \\
&+ e_t^{4}\left[\frac{14250725}{261184} - \frac{1516042558243}{7659526875\Gamma(\frac{1}{3})\Gamma(\frac{2}{3})}\right] + e_t^{6}\left[\frac{722230667}{4701312}\right. \\
&\left. - \frac{8537054301053}{15319053750\Gamma(\frac{1}{3})\Gamma(\frac{2}{3})}\right] + e_t^{8}\left[\frac{102744533069}{300883968} - \frac{4337433374609}{3501498000\Gamma(\frac{1}{3})\Gamma(\frac{2}{3})}\right] \\
&+ e_t^{10}\left[\frac{9843430194463}{15044198400} - \frac{83109477430673}{35014980000\Gamma(\frac{1}{3})\Gamma(\frac{2}{3})}\right] + e_t^{12}\left[\frac{43605309737981}{38513147904}\right.
\end{aligned}$$

$$
\begin{aligned}
&-\frac{52296280129859}{12732720000\Gamma(\frac{1}{3})\Gamma(\frac{2}{3})}\Bigg] + e_t^{14}\Bigg[\frac{19069924628449467}{10484134707200} \\
&-\frac{392069990496293}{59419360000\Gamma(\frac{1}{3})\Gamma(\frac{2}{3})}\Bigg] + e_t^{16}\Bigg[\frac{600336343160521814159}{217399017288499200} \\
&-\frac{732589863363103}{73131520000\Gamma(\frac{1}{3})\Gamma(\frac{2}{3})}\Bigg] + e_t^{18}\Bigg[\frac{2824443514954333794172 1}{70437281601473740 80} \\
&-\frac{3829628554688939}{263273472000\Gamma(\frac{1}{3})\Gamma(\frac{2}{3})}\Bigg] + e_t^{20}\Bigg[\frac{15826416734383150662021 2273}{28174912640589496320000} \\
&-\frac{35764742675504291}{1755156480000\Gamma(\frac{1}{3})\Gamma(\frac{2}{3})}\Bigg] . \qquad (3.117)
\end{aligned}
$$

Finally, for the 3PN order enhancement factors from the tail-of-tails and tail-squared terms, we have to tenth order in e_t

$$
\begin{aligned}
\delta\chi^{10}(e_t) = {} & -\frac{36718454998853}{9417408000000} + \gamma_E + \frac{\ln(3)}{2} + \ln(16) + e_t^2\Bigg[-\frac{131766997689301}{1448832000000} \\
& +\frac{62\gamma_E}{3} + 57\ln(2) + \frac{27619\ln(3)}{768}\Bigg] + e_t^4\Bigg[-\frac{17257920310633973}{25113088000000} + \frac{9177\gamma_E}{64} \\
& +\frac{182657\ln(2)}{192} - \frac{51243\ln(3)}{1024}\Bigg] + e_t^6\Bigg[-\frac{92129506724738033}{30135705600000} + \frac{76615\gamma_E}{128} \\
& -\frac{296449\ln(2)}{384} + \frac{8680309\ln(3)}{16384} + \frac{244140625\ln(5)}{147456}\Bigg] \\
& + e_t^8\Bigg[-\frac{343678592520953093}{34440806400000} + \frac{1903055\gamma_E}{1024} + \frac{59103559\ln(2)}{3072} \\
& +\frac{1180327577\ln(3)}{131072} - \frac{10498046875\ln(5)}{1179648}\Bigg] + e_t^{10}\Bigg[-\frac{3051437850147557459}{114802688000000} \\
& +\frac{9732723\gamma_E}{2048} - \frac{55480099157\ln(2)}{1382400} - \frac{4787048773551\ln(3)}{104857600} \\
& +\frac{2342041015625\ln(5)}{113246208} + \frac{33232930569601\ln(7)}{943718400}\Bigg] , \qquad (3.118) \\
\delta\tilde{\chi}^{10}(e_t) = {} & -\frac{6244218863}{1601600000} + \gamma_E + \frac{\ln(3)}{2} + \ln(16) + e_t^2\Bigg[-\frac{3744713821}{68992000} + \frac{389\gamma_E}{32} \\
& +\frac{1007\ln(2)}{32} + \frac{2965\ln(3)}{128}\Bigg] + e_t^4\Bigg[-\frac{18889494241}{68992000} + \frac{3577\gamma_E}{64} + \frac{27699\ln(2)}{64} \\
& -\frac{27245\ln(3)}{512}\Bigg] + e_t^6\Bigg[-\frac{60790558061}{68992000} + \frac{43049\gamma_E}{256} - \frac{1804397\ln(2)}{2304}
\end{aligned}
$$

$$
\begin{aligned}
&+\frac{1946309\ln(3)}{8192}+\frac{48828125\ln(5)}{73728}\Bigg]+e_t^8\Bigg[-\frac{151724371031}{68992000}+\frac{102005\gamma_E}{256}\\
&+\frac{15307525\ln(2)}{2304}+\frac{184515253\ln(3)}{65536}-\frac{2099609375\ln(5)}{589824}\Bigg]\\
&+e_t^{10}\Bigg[-\frac{160776312313}{34496000}+\frac{207311\gamma_E}{256}-\frac{107117837\ln(2)}{6400}-\frac{815824256293\ln(3)}{52428800}\\
&+\frac{156103515625\ln(5)}{18874368}+\frac{4747561509943\ln(7)}{471859200}\Bigg]\,. \qquad (3.119)
\end{aligned}
$$

One can easily extend these expressions to higher order in eccentricity, but then they become quite lengthy.

For comparison, we display the relative error in all hyperasymptotic series relative to the numerical enhancement factors in the two panels of Fig. 3.4. As can be seen from Fig. 3.3 and Fig. 3.4, the error for the enhancement factors that we were able to complete the superasymptotic analysis on are typically less that 10^{-8} for arbitrary eccentricity. The exceptions to this are the 2.5PN order enhancement factors $[\psi(e_t), \tilde{\psi}(e_t)]$, which have relative errors of $\sim [1 \times 10^{-4}, 5 \times 10^{-5}]$ at $e_t = 0.95$. The reason for the poor accuracy in these enhancement factors is that the high eccentricity dependence is very sensitive to $[\alpha_3^{(2)}(e_t), \tilde{\alpha}_3^{(2)}(e_t)]$, whose re-summation does not follow the usual procedure of obtaining superasymptotic expressions (and rather we had to Padé a small eccentricity expansion for these).

Discussion

We have here constructed analytic approximations to all non-linear tail effects in compact binary inspirals to 3PN order. We constructed superasymptotic and hyperasymptotic series that are typically accurate to better than 10^{-8} relative to numerical PN results, except for two 2.5PN factors that are accurate to better than 10^{-4}. We have checked that the numerical calculation of the orbital phase with the hereditary fluxes prescribed through our analytic, closed-form expressions is within double precision of the numerical phase obtained with the fluxes prescribed through infinite Bessel sums. The advantage of these analytic approximations is not only that they are accurate, but that they are controlled (meaning one can in principle go to higher order in perturbation theory to obtain more accurate expressions) and they are fast (meaning they can be directly evaluated without need for additional numerical simulations).

With these analytic results at hand, we can now begin to consider the creation of closed-form, analytic waveform models and burst models for GW data analysis of binaries with generic eccentricity. These calculations would allow us to determine more precisely whether the accuracy of the fluxes calculated here is enough for GW data analysis or whether one needs to go to higher order in perturbation theory. To do so, one would carry out a Bayesian parameter estimation study (whether using waveforms and matched filtering or a burst model with an informative prior) to estimate whether models constructed with analytic fluxes are efficient and faithful at recovering numerical signals. Such an analysis would reveal, for example, whether the posterior probability distribution obtained with models that use analytic fluxes biases the recovery of parameters. One thing is clear, however, the analytic calculations presented here have moved us one step close to the creation of generic models for the GWs emitted in the inspiral of binary systems.

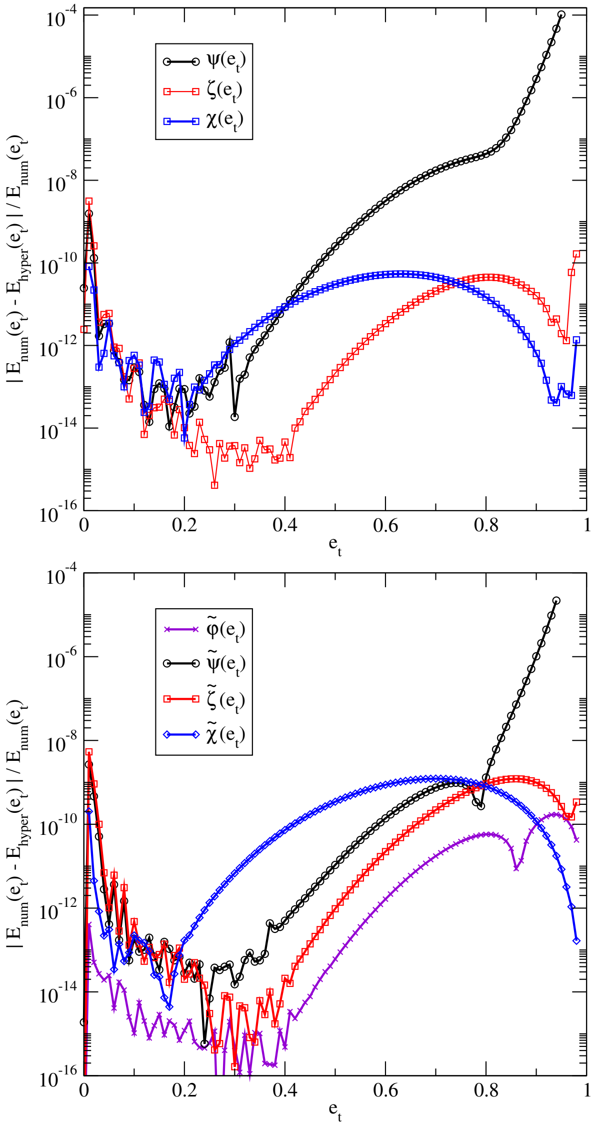

Figure 3.4: Comparison of numerical results for tail enhancement factors with their hyperasymptotic expressions for the energy flux (left) and angular momentum flux (right). With the exception of the 2.5PN order enhancement factors $[\psi(e_t), \tilde{\psi}(e_t)]$, the hyperasymptotic expressions are accurate to relative errors better than 10^{-8} for all eccentricities. For $[\psi(e_t), \tilde{\psi}(e_t)]$, the relative errors at the last data point, which is $e_t = 0.95$ for these enhancement factors, are approximately $[1 \times 10^{-4}, 5 \times 10^{-5}]$, respectively.

ECCENTRIC GRAVITATIONAL WAVE BURSTS IN THE POST-NEWTONIAN FORMALISM

In the previous chapter, we completed the calculation of the GW fluxes necessary to model the inspiral of eccentric binaries. With these in hand, we may now proceed to build a model of the GW emission from highly eccentric binaries. In general, a burst model is one that treats the bursts as N-dimensional objects in the detector's data stream and tracks the geometric centroid and volume of the bursts from one to the next as the binary inspirals. In this chapter, we present the details of how to construct a burst model within the PN formalism [106, 108], which is currently the only purely analytic model for highly eccentric orbits. We here focus on the inspiral of highly eccentric binaries within the PN framework. The motivation for developing a purely analytic model of the inspiral is the potential for the later construction of phenomenological inspiral-merger-ringdown models, a quasi-circular version of which played a pivotal role in the first gravitational wave observations by aLIGO [11]. Here, we treat the bursts as two dimensional regions of excess power in a time-frequency decomposition of a detectors data stream. We treat the bursts as boxes with characteristic time and frequency widths, which allows for a discretization of the time-frequency decomposition into tiles, with the burst being those tiles that contain excess power [11, 146]. We characterize the sequence of bursts using the time and frequency centroids of the bursts, as well as the widths of the burst tiles, or alternatively the volume of the tiles, used to capture a certain amount of power within each bursts. These time-frequency observables are supplemented by a model describing the orbital evolution of the binary as a set of discrete, osculating Keplerian ellipses.

The PN burst sequence will be a parameterized deformation of the Newtonian order sequence. The deformations will scale with an increasing power of a particular PN expansion parameter, which we choose to be the pericenter velocity v_p. The coefficients of a $k/2$-PN order term, which scales as v_p^k, are then a set of functions $[\mathcal{V}_k, \mathcal{D}_k, P_k, R_k]$ which are dependent on the physical parameters of the compact binary system. These functions correspond to the PN corrections to the rates of change of pericenter velocity and time eccentricity, and the expressions for the orbital period and pericenter distance, respectively. In this work, we neglect the spin of the compact objects and work in a point particle limit, such that these functions are only dependent on the time eccentricity e_t and the symmetric mass ratio η. Hence, when working to $k/2$-PN order, one needs $4k$ functions $[\mathcal{V}_k(e_t,\eta), \mathcal{D}_k(e_t,\eta), P_k(e_t,\eta), R_k(e_t,\eta)]$ to parametrize all of the PN defomations.

We parametrize the PN burst sequence in time-frequency space by

$$\frac{(t_i - t_{i-1})_{\rm PN}}{(t_i - t_{i-1})_{\rm N}} = 1 + \vec{P}(e_{t,i}, \eta; v_p) \cdot \vec{X}(v_{p,i}) \tag{4.1}$$

$$\frac{f_i^{\rm PN}}{f_i^{\rm N}} = 1 + \vec{R}^{(-1)}(e_{t,i}, \eta; v_p) \cdot \vec{X}(v_{p,i}) \tag{4.2}$$

$$\frac{\delta t_i^{\rm PN}}{\delta t_i^{k\rm N}} = 1 + \vec{R}(e_{t,i}, \eta; v_p) \cdot \vec{X}(v_{p,i}) \tag{4.3}$$

$$\frac{\delta f_i^{\rm PN}}{\delta f_i^{\rm N}} = 1 + \vec{R}^{(-1)}(e_{t,i}, \eta; v_p) \cdot \vec{X}(v_{p,i}) \tag{4.4}$$

where (t_i, f_i) are the centroid of the bursts and $(\delta t_i, \delta f_i)$ are the width and height of the tiles. We create the *amplitude vector fields* $[\vec{P}, \vec{R}]$, whose components are the functions $[P_k(e_t, \eta; v_p), R_k(e_t, \eta; v_p)]$, which we further specify as implicit functions of the PN expansion parameter v_p since their form changes depending on the choice of expansion parameter. The components of $\vec{R}^{(-1)}$ are defined such that

$$\left[1 + \vec{R}(e_t, \eta; v_p) \cdot \vec{X}(v_p)\right]^{(-1)} \doteq 1 + \vec{R}^{(-1)}(e_t, \eta; v_p) \cdot \vec{X}(v_p)\,, \tag{4.5}$$

where the equality $\doteq$ should be understood as working in the limit of $v_p \ll 1$. The *state vector* $\vec{X}(v_p)$ contains the powers of v_p that characterized each PN order corrections, specifically $\vec{X}(v_p) = (v_p, v_p^2, ..., v_p^k)$. Hence the dot products provide the complete sum of all terms in a PN expansion up to $k/2$-PN order.

These time-frequency burst parameters, specifically $(t_i, f_i, \delta t_i, \delta f_i)$, are functions of the symmetric mass ratio and the total mass of the binary, which are constant in time, as well as the pericenter velocity $v_{p,i}$ and eccentricity $e_{t,i}$ during each burst, which are evolving in time under the influence of radiation reaction. Hence, we must supplement the time-frequency sequence described above with the orbital evolution of the binary. To do this, we apply an osculating approximation that assumes the bursts are emitted instantaneously at pericenter, forcing the binary to move along a discrete set of Keplerian ellipses that osculate onto one another. The parameters of the i-th orbit will be functions of the parameters of the previous orbit, specifically

$$\frac{(v_{p,i} - v_{p,i-1})_{\rm PN}}{(v_{p,i} - v_{p,i-1})_{\rm N}} = 1 + \vec{\mathcal{V}}(e_{t,i-1}, \eta; v_p) \cdot \vec{X}(v_{p,i-1})\,, \tag{4.6}$$

$$\frac{(\delta e_{t,i} - \delta e_{t,i-1})_{\rm PN}}{(\delta e_{t,i} - \delta e_{t,i-1})_{\rm N}} = 1 + \vec{\mathcal{D}}(e_{t,i-1}, \eta; v_p) \cdot \vec{X}(v_{p,i-1})\,. \tag{4.7}$$

where we have introduced the two new amplitude vector fields $[\vec{\mathcal{V}}, \vec{\mathcal{D}}]$. In this work, we provide explicit expressions for the amplitude vector fields $\lambda^a_{\rm PNburst} \equiv (\vec{P}, \vec{R}, \vec{\mathcal{V}}, \vec{\mathcal{D}})$ complete to 3PN order. Equations (4.1)-(4.4) and (4.6)-(4.7) provide the complete PN burst model, which we use to calculate the burst model to 3PN order using the results for $\lambda^a_{\rm PNburst}$. The remainder of this chapter is dedicated to deriving the results presented above.

Constructing Burst Models

This section is dedicated to reviewing how to create a burst model and the elements that go into such a model. We begin by reviewing the Newtonian burst model and how it was constructed. We then describe a new method of constructing burst models in general without any assumptions of the regime or theory of gravity we are working in. This new method greatly simplifies the construction of burst models, and will allow us to develop a completely generic GR PN model in the next section.

The Newtonian Burst Model

How do we construct a burst model? Recall that we defined a burst model as a theoretical model prior to describe how the bursts evolve in time-frequency space. Such a model would tell us how the centroid and the volume of the bursts evolve in time and frequency from one burst to the next. But this evolution depends on the orbital parameters of the system, which themselves are also changing in time due to dissipative effects, such as the emission of GWs. Therefore, a complete burst model must provide a one-to-one mapping between the evolution of the system's physical parameters and how the bursts evolve in time and frequency. This requires the following ingredients:

I. *Orbital Evolution:* A mapping that prescribes the evolution of the orbital parameters from one orbit to the next, including GW radiation-reaction.

II. *Centroid Mapping:* A mapping that provides the time-frequency centroid of the burst (t_i, f_i), given the centroid of the previous burst (t_{i-1}, f_{i-1}), in terms of the orbital parameters of the system.

III. *Volume Mapping:* A mapping that describes how the time-frequency volume of the bursts changes from one to the next, in terms of the orbital parameters of the system.

Orbit Evolution Let us start by reviewing how the ingredients listed above can be computed to leading (i.e. Newtonian) order, focusing first on ingredient I (the orbital evolution). In Newtonian gravity, the orbital motion of two test particles can be described though Keplerian ellipses, which are characterized by two conserved quantities, the orbital energy E and the orbital angular momentum L. Alternatively, one can parameterize any such orbit in terms of its pericenter distance r_p and its orbital eccentricity e, which are related to E and L at Newtonian order in a PN expansion by

$$E = -\frac{M^2\eta\,(1-e)}{2r_p}\,, \tag{4.8}$$

$$L = \eta\sqrt{M^3 r_p\,(1+e)}\,. \tag{4.9}$$

where $\eta = m_1 m_2/M^2$ is the symmetric mass ratio and $M = m_1 + m_2$ is the total mass of the system.

The burst model requires knowledge of how (E, L) or (r_p, e) evolve from one orbit to the next. Due to the nature of the emission of gravitational radiation in highly elliptic systems, we may treat the problem as a set of Keplerian orbits that change effectively instantaneously at pericenter, allowing the orbits to *osculate* onto one another. Hence, we may write

$$E_i = E_{i-1} + \Delta E_{(i,i-1)}\,, \tag{4.10}$$

$$L_i = L_{i-1} + \Delta L_{(i,i-1)}\,, \tag{4.11}$$

where $\Delta E_{(i,i-1)}$ and $\Delta L_{(i,i-1)}$ are the changes in orbital energy and angular momentum due to GW emission from one orbit to the next, and the labels represent which orbit the above quantities are evaluated on. By "osculating orbits," we mean that the elements of the Keplerian orbit are constant throughout the orbit except at pericenter, where they change drastically and the new elements define a new Keplerian orbit. In this approximation, one thus treats the radiation, and all changes generated by it, as arising instantaneously at pericenter.

In general, the total change in energy and angular momentum between times T_{i-1} and T_i due to GW emission is given by

$$\Delta E_{(i,i-1)} = \int_{T_{i-1}}^{T_i} \dot{E}\left(r_p, e, \psi\right) dt\,, \tag{4.12}$$

$$\Delta L_{(i,i-1)} = \int_{T_{i-1}}^{T_i} \dot{L}\left(r_p, e, \psi\right) dt\,, \tag{4.13}$$

where ψ is the true anomaly, T_{i-1} and T_i are the times of consecutive pericenter passages, and the dot refers to derivatives with respect to time. At Newtonian order, the GW energy and angular momentum fluxes, $\dot{E}$ and $\dot{L}$, are given, for example, by Eq. (12.78) in [131]. The fluxes are functions of the orbital elements, which are themselves functions of time through the true anomaly ψ. Thus, the above definitions would have to be supplemented with the time evolution of ψ itself, namely $\dot{\psi}\left(r_p, e, \psi\right)$. In addition, since the fluxes depend on the true anomaly, they contain gauge-dependent terms [131]. However, these terms vanish upon integration, leaving $\Delta E_{(i,i-1)}$ and $\Delta L_{(i,i-1)}$ independent of the radiation reaction gauge.

To evaluate the integrals in Eqs. (4.12) and (4.13), we perform a change of variable from t to the true anomaly, using $dt = d\psi/\dot{\psi}$. The new limits of integration become ψ_{i-1} and $\psi_i = \psi_{i-1} + 2\pi$, or more simply $[0, 2\pi]$. The orbital elements now depend on the true anomaly rather than time, which simplifies the integrands, but this is still not enough to evaluate them analytically. To do so, we use the fact that the orbits are osculating and the GW emission occurs instantaneously at pericenter, which ensures that r_p and e are constant everywhere except at closest approach. With this, the integrals become

$$\Delta E_{(i,i-1)} = \int_0^{2\pi} \frac{\dot{E}\left(r_{p,i-1}, e_{i-1}, \psi\right)}{\dot{\psi}\left(r_{p,i-1}, e_{i-1}, \psi\right)} d\psi\,, \tag{4.14}$$

$$\Delta L_{(i,i-1)} = \int_0^{2\pi} \frac{\dot{L}\left(r_{p,i-1}, e_{i-1}, \psi\right)}{\dot{\psi}\left(r_{p,i-1}, e_{i-1}, \psi\right)} d\psi\,, \tag{4.15}$$

which can be evaluated analytically.

Alternatively, we can exploit the definition of orbital averaged GW fluxes to rewrite these changes in a simpler way. The orbital averaged energy flux, for example, is given by $\langle \dot{E} \rangle \equiv \Delta E_{(i,i-1)}/P$, where P is the orbital period of the binary, and likewise for the angular momentum flux. With this definition, we are free to write

$$E_i = E_{i-1} + P_{i-1} \langle \dot{E} \rangle_{i-1}\,, \tag{4.16}$$

$$L_i = L_{i-1} + P_{i-1} \langle \dot{L} \rangle_{i-1}\,. \tag{4.17}$$

Indeed, we recognize the integral expressions in Eqs. (4.14) as simply the product of the orbital period and $\langle \dot{E} \rangle_{i-1}$ or $\langle \dot{L} \rangle_{i-1}$ by definition. It might seem odd that orbit averaged quantities appear in the above expressions since the GW emission is happening mostly during pericenter passage, and thus smearing the emission over the entire orbit would appear incorrect. However, this is purely a result of the *definition* of the orbital averaged quantities, and has nothing to do with the nature of the GW emission or the validity of the orbital averaged approximation for the systems we are considering [102].

The orbital energy and angular momentum have a clear physical meaning, but r_p and e allow us to straightforwardly visualize the geometry of the system that is generating the bursts (at least at Newtonian order). At this order, it does not matter which set of quantities, (E, L) or (r_p, e), we decide to use for the orbital evolution. For the Newtonian model in [108], we decided to use (r_p, e), so let us continue to do so here. We need to solve the system given by Eqs. (4.8) and (4.9) for the functionals $r_p\left(E, L\right)$ and $e\left(E, L\right)$. To obtain the evolution of the pericenter distance and the orbital eccentricity, we evaluate the functionals at the desired orbit, specifically $r_{p,i} = r_p\left[E_i\left(E_{i-1}, L_{i-1}\right), L_i\left(E_{i-1}, L_{i-1}\right)\right]$ and $e_i = e\left[E_i\left(E_{i-1}, L_{i-1}\right), L_i\left(E_{i-1}, L_{i-1}\right)\right]$. Evaluating the functionals with Eqs. (4.16) and (4.17) gives

$$r_{p,i} = r_{p,i-1}\left[1 - \frac{59\pi\sqrt{2}}{24}\eta\left(\frac{M}{r_{p,i-1}}\right)^{5/2}\left(1 + \frac{121}{236}\delta e_{i-1}\right)\right]\,, \tag{4.18}$$

$$\delta e_i = \delta e_{i-1} + \frac{85\pi\sqrt{2}}{12}\eta\left(\frac{M}{r_{p,i-1}}\right)^{5/2}\left(1 - \frac{1718}{1800}\delta e_{i-1}\right)\,, \tag{4.19}$$

where we have kept only leading-order terms in $\delta e \equiv 1 - e \ll 1$ and in $M/r_p \ll 1$ in all expressions (since we are working to Newtonian order). These equations recursively describe how the orbit shrinks and circularizes as the binary inspirals, thus completely describing the orbital evolution.

Centroid Mapping The second ingredient we need for any burst model is the centroid mapping. The centroids of the bursts are given by the set (t_i, f_i) at which the bursts occur. What we desire is the mapping $t_{i-1} \to t_i$ and $f_{i-1} \to f_i$. Since the orbits are osculating, the time between bursts is trivially given by the orbital period P to Newtonian order, which is given by

$$P = \frac{2\pi r_p^{3/2}}{M^{1/2}(1-e)^{3/2}}\,. \tag{4.20}$$

Thus to obtain the time mapping, we simply have to evaluate the orbital period at the desired orbit,

$$t_i = t_{i-1} + \frac{2\pi}{M^{1/2}} \left[\frac{r_{p,i}\left(r_{p,i-1}, \delta e_{i-1}\right)}{\delta e_i \left(r_{p,i-1}, \delta e_{i-1}\right)} \right]^{3/2} \tag{4.21}$$

where the mappings $r_{p,i}\left(r_{p,i-1}, \delta e_{i-1}\right)$ and $\delta e_i\left(r_{p,i-1}, \delta e_{i-1}\right)$ are given by Eqs. (4.18) and (4.19), respectively.

The fact that the bursts are separated by an orbital period can be seen more generally by writing $\dot{\psi} = \dot{\psi}_{\text{cons}} + \dot{\psi}_{\text{diss}}$, where $\dot{\psi}_{\text{cons}}$ is the conservative part coming from Keplerian orbital dynamics, and $\dot{\psi}_{\text{diss}}$ is the dissipative piece that comes from radiation reaction. The time between successive pericenter passages, i.e. the orbital period, is then

$$t_i - t_{i-1} = \int_0^{2\pi} \frac{d\psi}{\dot{\psi}} \, . \tag{4.22}$$

The dissipative part contains terms that depend on the radiation reaction gauge, which vanish upon integration. Thus we are left with only the conservative piece of $\dot{\psi}$, and by assuming the orbits are osculating and the GW emission is instantaneous, this evaluates upon integration to the orbital period for an unperturbed, purely conservative orbit. This does not mean that the orbital period is not evolving. GW emission carries energy and angular momentum away from the binary that changes the orbital period. The dissipative part of the above integral does vanish, but the dissipative part of P, namely $\dot{P}$, does not. The above result simply implies that the time between pericenter passages is the orbital period of a Keplerian orbit, since radiation reaction is happening rapidly around pericenter.

The GW frequency on the other hand requires knowledge of the Fourier transform of the GWs emitted during each burst, the *Fourier-domain waveform.*

From Fig. 7 in [156], the GW power is highly peaked around

$$f_{\rm GW} = \frac{1}{2\pi\tau_{\rm GW}}\,, \tag{4.23}$$

where $\tau_{\rm GW}$ is the characteristic GW time, defined by

$$\tau_{\rm GW} \equiv \frac{\text{pericenter distance}}{\text{pericenter velocity}}\,. \tag{4.24}$$

At Newtonian order, the pericenter velocity is given by

$$v_p = \sqrt{\frac{M(1+e)}{r_p}} \tag{4.25}$$

and thus $\tau_{\rm GW}$ is

$$\tau_{\rm GW} = \frac{r_p^{3/2}}{\left[M(1+e)\right]^{1/2}}\,, \tag{4.26}$$

which roughly corresponds to the amount of time the system spends at pericenter. This time is a functional of the pericenter distance and eccentricity; hence, to obtain the frequency of the i-th burst f_i, one simply has to evaluate the characteristic GW time associated with the orbit $(r_{p,i}, e_i)$, where the mapping to the parameters of the previous orbit are given by Eqs. (4.18) and (4.19):

$$f_i = \frac{M^{1/2}\left[2 - \delta e_i\left(r_{p,i-1}, \delta e_{i-1}\right)\right]^{1/2}}{2\pi\left[r_{p,i}\left(r_{p,i-1}, \delta e_{i-1}\right)\right]^{3/2}}\,. \tag{4.27}$$

This completes the mapping of the time-frequency centroid of the bursts.

The prescription we provide for the frequency of the bursts is dependent on the frequency domain waveform, or alternatively the GW power, peaking at $\tau_{\rm GW}^{-1}$. This intuition comes from [156], where for parabolic orbits, and at Newtonian order, it is shown that the GW power peaks roughly at $\tau_{\rm GW}^{-1}$. However, for circular binaries, the power peaks at twice the orbital frequency, and it can easily be checked that the prescription given above does not reproduce this result when $e = 0$. This implies that there are uncontrolled remainders that depend on δe that correct the above expression to account for this. However, because we are working in the limit where $\delta e \ll 1$, we expect such corrections to be subdominant.

Volume Mapping The last ingredient we need is the volume mapping. The bursts are not instantaneously emitted at pericenter and are not solely peaked at one frequency. The emission is instead spread out over the full pericenter passage and over multiple frequencies. To complete the burst model, we need to determine how the time-frequency size of the bursts change from one to another. We may describe the bursts as any two dimensional objects in time and frequency. For simplicity, we choose to model the bursts as boxes with widths

$$\delta t = \xi_t \tau_{\rm GW} \tag{4.28}$$

$$\delta f = \xi_f f_{\rm GW} \tag{4.29}$$

where ξ_t and ξ_f are constants of proportionality that are chosen from data analysis considerations. For example, one can choose these constants such that a desired percentage of the GW power (90% for example) is contained in each box. More general two dimensional objects, such as ellipsoids, could be used for this construction, but boxes are the simplest. To obtain how these widths change from one burst to the next, we simply have to evaluate Eqs. (4.28)-(4.29) at the parameters of the orbit

$(r_{p,i}, e_i)$:

$$\delta t_i = \frac{\xi_t \left[r_{p,i}\left(r_{p,i-1}, \delta e_{i-1}\right)\right]^{3/2}}{M^{1/2}\left[2 - \delta e_{i-1}\left(r_{p,i-1}, \delta e_{i-1}\right)\right]^{1/2}} \tag{4.30}$$

$$\delta f_i = \frac{\xi_f M^{1/2}\left[2 - \delta e_i\left(r_{p,i-1}, \delta e_{i-1}\right)\right]^{1/2}}{2\pi\left[r_{p,i}\left(r_{p,i-1}, \delta e_{i-1}\right)\right]^{3/2}}\,. \tag{4.31}$$

Note that in the case of ellipsoids, the results are the same, but these quantities can instead be interpreted as the semi-minor and semi-major axes of the ellipsoids. For a realistic search, ellipsoids would actually be more appropriate choice since they are a more accurate representation of the time-frequency structure of the bursts. However, for the purposes of this work, this choice is irrelevant, as the goal is to characterize the two dimensional objects via the scales in Eqs. (4.30) and (4.31). This completes the burst model at leading PN order.

In practice, the burst sequence given by iteration of Eqs. (4.18)-(4.19), (4.21), (4.27), (4.30)-(4.31) must be terminated at some point. First, regardless of eccentricity, when the pericenter separation approaches an effective inner-most stable orbit, the binary will merge. If the eccentricity is still large at this moment, the plunge/merger/ringdown could be modeled as the final burst, though it would have different characteristics in the time-frequency plane than the fly-by bursts. For orbits with large initial pericenter passage, the orbit can become sufficiently close to circular before merger that the binary begins to emit high luminosity GWs essentially continuously; i.e. in the burst model, the time-frequency tiles will begin to touch, or even overlap if (ξ_t, ξ_f) are large enough. This is not *a-priori* a problem (see for example [64]), though alternatively it may be more efficient at this stage to analyze the rest of the inspiral with a traditional matched filtering algorithm, using small eccentricity waveform templates.

The Inverse Problem and Degeneracies

The parameter vector that describes the burst algorithms is $\lambda^a = (t_{0,\ldots,N},\ f_{0,\ldots,N},\ \delta t_{0,\ldots,N},\ \delta f_{0,\ldots,N})$ for N bursts detected. That is, each burst is fully described by 4 parameters, thus leading to $4N$ pieces of information. However, an inspiraling, eccentric orbit in GR to leading PN order (neglecting spins) is described by a much smaller vector $\lambda^a_{\rm sys} = (M, \eta, e_0, r_{p,0})$. Given λ^a, the questions then are the following: how do we map back to $\lambda^a_{\rm sys}$; and what are the minimum number of bursts needed to specify this inverse map uniquely, if it exists? Answers to practical versions of these questions would require a more thorough analysis where detector noise is considered; here we just give a simple counting argument, and caution about degeneracies if a simple model, such as the one we use here, is employed.

Detection of the first burst provides four pieces of information, $(t_1, f_1, \delta t_1, \delta f_1)$. The parameter t_1 is unrelated to any physical parameters. The parameter f_1 (for example) depends on M, $r_{p,0}$ and e_0, so it can be used to infer one component of $\lambda^a_{\rm sys}$. The parameters δt_1 and δf_1 both depend on $\tau_{\rm GW}$, which in turn depends only on f_1; thus they do not provide independent information. If a second burst is detected, four more pieces of information are obtained: $(t_2, f_2, \delta t_2, \delta f_2)$. As before, measuring one of $(f_2, \delta t_2, \delta f_2)$ uniquely determines the other two, but now t_2 does depend on the system parameters. Hence in principle we have two new independent pieces of information from the second burst. Similarly for a third burst, but we know there are at most four independent numbers in $\lambda^a_{\rm sys}$ here, and hence three consecutive bursts should suffice to determine it.

This counting argument assumes there are no degeneracies amongst the parameters, which is not the case if leading PN order expressions are used to construct the algorithm. In that case, there is a degeneracy between M, η and r_p, and the burst algorithm actually only depends on the physical parameters $\bar{\lambda}^a_{\rm sys} = (\mathcal{M}, \mathcal{R}_0, e_0)$, where $\mathcal{M} = M\eta^{3/5}$ is the chirp mass and $\mathcal{R} = r_p^{3/2}/M^{1/2}$ is the the leading PN order expression for the radius of curvature of the binary. In principle two bursts would allow complete determination of $\bar{\lambda}^a_{\rm sys}$. This reduced parameter dependence can be seen most clearly if we expand the algorithm in both $M/r_p \ll 1 \gg \delta e$ to find

$$t_i = t_{i-1} + \frac{2\pi\mathcal{R}_{i-1}^{3/2}}{\delta e_{i-1}^{3/2}}\left[1 + \mathcal{O}\left(\frac{\mathcal{M}^{5/2}}{\mathcal{R}_{i-1}^{5/2}}, \delta e_{i-1}\right)\right], \tag{4.32}$$

$$f_i = \frac{1}{\sqrt{2}\pi\mathcal{R}_{i-1}}\left[1 + \mathcal{O}\left(\frac{\mathcal{M}^{5/2}}{\mathcal{R}_{i-1}^{5/2}}, \delta e_{i-1}\right)\right], \tag{4.33}$$

$$\delta t_i = \delta t_{i-1}\left[1 + \mathcal{O}\left(\frac{\mathcal{M}^{5/2}}{\mathcal{R}_{i-1}^{5/2}}, \delta e_{i-1}\right)\right], \tag{4.34}$$

$$\delta f_i = \delta f_{i-1}\left[1 + \mathcal{O}\left(\frac{\mathcal{M}^{5/2}}{\mathcal{R}_{i-1}^{5/2}}, \delta e_{i-1}\right)\right], \tag{4.35}$$

The situation is very reminiscent to degeneracies that arise in the stationary-phase approximation to the Fourier transform of the response function for GWs emitted during quasi-circular inspirals: the Fourier phase only depends on $\mathcal{M}$ to leading PN-order, and not on both m_1 and m_2 independently. Of course, these degeneracies are broken when going to higher PN order.

A Simplified Formalism

Ultimately, we are interested in a PN burst model at generic (presumably very high) PN order. Building a generic order PN model by following the construction above might at first seem like an intractable problem. To start, one would have to take the orbital energy $E_{\rm PN}$ and angular momentum $L_{\rm PN}$ at arbitrary order and invert these expressions to obtain $r_p(E_{\rm PN}, L_{\rm PN})$ and $e(E_{\rm PN}, L_{\rm PN})$. Then, one would need to use the energy and angular momentum fluxes to compute the evolution of the orbital energy and angular momentum. From there, the pericenter and orbital eccentricity mapping would have to be computed using the functionals $r_{p,i}\left[E_i(E_{i-1}, L_{i-1}), L_i(E_{i-1}, L_{i-1})\right]$

and $e_i\left[E_i(E_{i-1}, L_{i-1}), L_i(E_{i-1}, L_{i-1})\right]$. While this may actually be possible from a mathematical standpoint, it will be very non-trivial to do so at arbitrary order. Thus, in this subsection, we will instead seek a simplified formalism that is more practical to implement.

The new method we seek must be more direct than the previous method discussed, removing steps that are redundant and reducing the number of physical quantities we need to work with. We begin by noting a number of assumptions that we will use to simplify the analysis:

I. *Osculating Orbits:* Any changes in the orbital parameters will be modeled as occurring instantaneously around pericenter passage, leaving the orbital parameters constant throughout the rest of the orbit.

II. *High Ellipticity:* The orbits we consider are highly elliptical, so we define a small parameter $\delta e_t \equiv 1 - e_t$ and work perturbatively in the regime $\delta e_t \ll 1$.

III. *PN Orbits:* We will work within the PN framework, expanding all expressions in the pericenter velocity $v_p \ll 1$.

The first and second assumptions follow directly from the nature of the systems we are considering. Note that in the second assumption we are now working with the time eccentricity from the QK parametrization. The reason for this is that in PN theory, there is no unique concept for the orbital eccentricity, as there are actually three eccentricities that enter the QK equations of motion, specifically (e_t, e_r, e_ϕ). All three of these eccentricities reduce to the orbital eccentricity in the Newtonian limit, but they are distinct quantities within PN theory. We choose to work with e_t and will express all quantities in terms of it. We discuss this in more detail in Appendix D.

The final assumption is new to this analysis and replaces the previous Newtonian assumption. At Newtonian order, we worked with the pericenter distance r_p as one of our physical parameters. We will now choose to work with the pericenter velocity v_p instead. This change is meant to put the computation more in line with the standard PN formalism for quasi-circular inspirals, as well as to remove some difficulties that result in there being terms that depend on half-integer powers of r_p in the dissipative sector. The mapping between the pericenter distance and velocity is given explicitly to 1PN order in Eqs. (D.17) and (D.19), with the 2PN and 3PN corrections given in Eqs. (D.35) and (D.36). With the above assumptions, any burst model requires the three ingredients laid out in the Newtonian burst model.

Let's start with the orbital evolution, where now we focus on the evolution of the pericenter velocity and the orbital eccentricity. Rather than starting from the orbital energy and angular momentum, we are free to write the velocity and eccentricity mappings as

$$v_{p,i} = v_{p,i-1} + \Delta v_{p,(i,i-1)} \,, \tag{4.36}$$

$$\delta e_{t,i} = \delta e_{t,i-1} - \Delta e_{t,(i,i-1)} \,, \tag{4.37}$$

where $\Delta v_{p,(i,i-1)}$ and $\Delta e_{t,(i,i-1)}$ are the change in pericenter velocity and time eccentricity between two successive orbits, and we have used the fact that $\delta e_t = 1 - e_t$ to write $\Delta \delta e_t = -\Delta e_t$. These mappings are directly analogous to the mappings of energy and angular momentum in our Newtonian model, given by Eqs. (4.12) and (4.13).

Expressions for $\Delta v_{p,(i,i-1)}$ and $\Delta e_{t,(i,i-1)}$ can be found in exactly the same way as in Eqs. (4.14) and (4.15). We may thus jump ahead and directly write

$$\Delta v_{p,(i,i-1)} = \int_0^{2\pi} \frac{\dot{v}_p\left(v_{p,i-1}, e_{t,i-1}, \psi\right)}{\dot{\psi}\left(v_{p,i-1}, e_{t,i-1}, \psi\right)} d\psi \tag{4.38}$$

$$\Delta e_{t,(i,i-1)} = \int_0^{2\pi} \frac{\dot{e}_t\left(v_{p,i-1}, e_{t,i-1}, \psi\right)}{\dot{\psi}\left(v_{p,i-1}, e_{t,i-1}, \psi\right)} d\psi \tag{4.39}$$

where $\dot{v}_p$ and $\dot{e}$ are the rates of change of pericenter velocity and orbital eccentricity. These rates, once again, depend on the true anomaly and thus have gauge-dependent terms arising from the GW sector. Upon integration, these terms vanish, except now the above quantities are not necessarily gauge-invariant as they depend on the specific coordinate system one chooses to do the PN calculation in.

To our knowledge, the expressions $\dot{v}_p\left(v_p, e_t, \psi\right)$ and $\dot{e}_t\left(v_p, e_t, \psi\right)$ have not yet been explicitly computed and would not be easy to compute, which would leave something of a gap in constructing the orbit evolution for our bursts. However, we may once again exploit the definition of orbit averaging and write Eqs. (4.36) and (4.37) as

$$v_{p,i} = v_{p,i-1} + P_{i-1}\langle \dot{v}_p \rangle_{i-1} \,, \tag{4.40}$$

$$\delta e_{t,i} = \delta e_{t,i-1} - P_{i-1}\langle \dot{e}_t \rangle_{i-1} \,. \tag{4.41}$$

The orbit averaged quantities $\langle \dot{v}_p \rangle$ and $\langle \dot{e}_t \rangle$ can be easily computed from the orbital energy and angular momentum and the corresponding fluxes, which are known to full 3PN order. We have thus completely constructed the orbit evolution for our burst model.

We now focus on the centroid and volume mappings. Once again, we will treat the bursts as boxes in time and frequency, and determine the mapping between the centroids and widths of the boxes. The characteristic GW time is still given by Eq. (4.24). In the Newtonian model, we used the expression $v_p\left(r_p, e_t\right)$ given by Eq. (4.25) to write this time in terms of $\left(r_p, e_t\right)$. Since we are now working with v_p instead of r_p, we can invert the relationship between these two parameters to obtain $r_p\left(v_p, e_t\right)$,which is given explicitly in Eqs. (D.17)-(D.19) and (D.35)-(D.36), and write

$\tau_{\rm GW}$ in terms of (v_p, e_t). Once this time is specified, we may define the characteristic GW frequency by Eq. (4.23). The centroid and volume mappings follow the exact same analysis as the Newtonian model, only parameterized by the pericenter velocity rather than the pericenter distance. Hence, we may write

$$t_i = t_{i-1} + P\left[v_{p,i}\left(v_{p,i-1}, e_{t,i-1}\right), e_{t,i}\left(v_{p,i-1}, e_{t,i-1}\right)\right], \tag{4.42}$$

$$f_i = f_{\rm GW}\left[v_{p,i}\left(v_{p,i-1}, e_{t,i-1}\right), e_{t,i}\left(v_{p,i-1}, e_{t,i-1}\right)\right], \tag{4.43}$$

$$\delta t_i = \delta t\left[v_{p,i}\left(v_{p,i-1}, e_{t,i-1}\right), e_{t,i}\left(v_{p,i-1}, e_{t,i-1}\right)\right], \tag{4.44}$$

$$\delta f_i = \delta f\left[v_{p,i}\left(v_{p,i-1}, e_{t,i-1}\right), e_{t,i}\left(v_{p,i-1}, e_{t,i-1}\right)\right], \tag{4.45}$$

thus completing the last two ingredients we need for our simplified formalism.

A Generic PN Formalism

With the application of assumption I, we have constructed a purely generic burst model through Eqs. (4.40), (4.41), and (4.42)-(4.45) that applies in any theory of gravity. We now seek to use this formalism to create a burst model at generic PN order. We will provide explicit expressions for the burst model at 1PN, 2PN, and 3PN orders in Sec. 4.

The above considerations imply that, to construct our burst model, we need PN expansions for four quantities: the orbital period, the pericenter distance, the rate of change of pericenter velocity, and the rate of change of orbital eccentricity. We can write these expansions to arbitrary PN order as

$$P^{\rm PN} = P^{\rm N}\left(v_p, e_t\right)\left[1 + \vec{P}(e_t, \eta; v_p)\cdot\vec{X}(v_p)\right], \tag{4.46}$$

$$r_p^{\rm PN} = r_p^{\rm N}\left(v_p, e_t\right)\left[1 + \vec{R}(e_t, \eta; v_p)\cdot\vec{X}(v_p)\right], \tag{4.47}$$

$$\langle \dot{v}_p^{\rm PN} \rangle = \langle \dot{v}_p^{\rm N} \rangle \left(v_p, e_t\right) \left[1 + \vec{V}(e_t, \eta; v_p) \cdot \vec{X}(v_p)\right] , \tag{4.48}$$

$$\langle \dot{e}_t^{\rm PN} \rangle = \langle \dot{e}_t^{\rm N} \rangle \left(v_p, e_t\right) \left[1 + \vec{E}(e_t, \eta; v_p) \cdot \vec{X}(v_p)\right] , \tag{4.49}$$

with the Newtonian order quantities

$$P^{\rm N} = \frac{2\pi M}{v_p^3} \left(\frac{1+e_t}{1-e_t}\right)^{3/2} , \tag{4.50}$$

$$r_p^{\rm N} = \frac{M(1+e_t)}{v_p^2} , \tag{4.51}$$

$$\langle \dot{v}_p^{\rm N} \rangle = \frac{32}{5} \frac{\eta}{M} v_p^9 \frac{(1-e_t)^{3/2}}{(1+e_t)^{15/2}} V_{\rm N}(e_t) , \tag{4.52}$$

$$\langle \dot{e}_t^{\rm N} \rangle = -\frac{304}{15} e_t \frac{\eta}{M} v_p^8 \frac{(1-e_t)^{3/2}}{(1+e_t)^{13/2}} \left(1 + \frac{121}{304} e_t^2\right) , \tag{4.53}$$

$$V_{\rm N}(e) = 1 - \frac{13}{6} e_t + \frac{7}{8} e_t^2 - \frac{37}{96} e_t^3 . \tag{4.54}$$

We refer to the vector $\vec{X}$ as the PN *state vector*, which depends on the PN expansion parameter. In our case, the PN expansion parameter is v_p and the components of $\vec{X}$ are simply $X_k = v_p^k$. Furthermore, we refer to the vector fields $(\vec{P}, \vec{R}, \vec{V}, \vec{E})$ as PN *amplitude vectors*, which are functions of the orbital eccentricity and the symmetric mass ratio. In Eq. (4.46)-(4.49), we have chosen to include a v_p label in the amplitude vectors to remind us that the functional form of its components depends on the parameter one expands about, i.e. if we had chosen to work with the x PN expansion parameter instead of v_p, then the eccentricity and symmetric mass ratio dependence of the PN amplitude vectors would be different. The dot products between the state vectors and the amplitude vectors take the simple form

$$\vec{A}(e_t, \eta; v_p) \cdot \vec{X}(v_p) = \sum_{k=2}^{\infty} A_k(e_t, \eta; v_p) v_p^k \tag{4.55}$$

where $\vec{A} \in (\vec{P}, \vec{R}, \vec{V}, \vec{E})$. We recognize the above expression as the summation of PN corrections to the associated quantity. The summation index k acts as the PN order of each term and starts at $k = 2$ corresponding to the corrections at 1PN order. The components of $\vec{A}$, specifically $A_k(e_t, \eta)$, we then recognize as the coefficient of the $k/2$-PN order term.

The components of the amplitude vectors $(\vec{P}, \vec{R}, \vec{V}, \vec{E})$ can be easily computed from known PN quantities. As an example, consider the orbital period. This quantity can be written as a function of the reduced energy ε and angular momentum j through the equation $P = 2\pi/n$, where n is the mean motion, given to 3PN order by Eq. (348a) in [42]. In turn, the reduced energy and angular momentum can also be written in terms of the pericenter velocity and eccentricity, $\varepsilon(v_p, e_t)$ and $j(v_p, e_t)$, which can be inserted into the expression $P(\varepsilon, j)$ and expanded about $v_p \ll 1$. The coefficients of each power of v_p are then the components of the vector field P_k. We will provide expressions for these components at specific PN orders when we construct burst models at specific PN orders.

This generic PN order burst model in characterized by four amplitude vectors fields $\lambda^a_{\rm PN} = (\vec{P}, \vec{R}, \vec{V}, \vec{E})$, which characterize the PN corrections to the Newtonian quantities. When working to $k/2$-PN order, we need $4k$ functions to fully specify the model. Each of the PN vector fields is a function of the parameters of the system, which we have written solely as functions of the eccentricity and the symmetric mass ratio. This will be true at 1PN order, but at higher PN order, the functions can depend on other physical parameters, such as the spins of compact objects, or the equation of state of supranuclear matter when at least one of the binary components is a NS.

The goal of this section will be to write the PN modifications to the Newtonian mappings in terms of the set of PN functions $\lambda^a_{{\rm PN},k} = (P_k, V_k, R_k, E_k)$. We begin with the first ingredient, the orbital evolution, specified in our simplified formalism by Eqs. (4.40) and (4.41). In particular, we concentrate first on the evolution of the pericenter velocity. By exploiting the definition of orbit averaging, we are able to write the change in this quantity as $P\ \langle \dot{v}_p \rangle$, which is exactly the second term in Eq. (4.40). Hence, to obtain the velocity mapping, we simply have to multiply Eqs. (4.46) and (4.48) together and expand in v_p. It is not difficult to see that our expansion is a product of two sums that is equivalent to a double sum of the form

$$\begin{aligned}\left(\vec{P}\cdot\vec{X}\right)\left(\vec{V}\cdot\vec{X}\right) &= \left(\sum_{k=2}^{\infty} P_k\ v_p^k\right)\left(\sum_{k=2}^{\infty} V_k\ v_p^k\right) \\ &= \sum_{k=2}^{\infty}\sum_{j=2}^{k-2} P_{k-j}\ V_j\ v_p^k\,, \\ &= \left(\vec{P}\circ\vec{V}\right)\cdot\vec{X}\,, \end{aligned} \tag{4.56}$$

where we have used the definition of the Cauchy product to rewrite the product of the sums as the discrete convolution of two series. When $k-2<2$, the convolution is exactly zero. Using this result, we write the velocity mapping as

$$v_{p,i} = v_{p,i-1}\left\{1+\frac{\pi}{5}\eta v_{p,i-1}^5 \mathcal{V}_{\rm N}\left(\delta e_{t,i-1}\right)\left[1+\vec{\mathcal{V}}\left(\delta e_{t,i-1},\eta;v_p\right)\cdot\vec{X}(v_{p,i-1})\right]\right\} \tag{4.57}$$

where the Newtonian term in this expression is

$$V_{\rm N}(\delta e_t) = -\frac{65}{96}+\frac{151}{96}\delta e_t-\frac{9}{32}\delta e_t^2+\frac{37}{96}\delta e_t^3\,, \tag{4.58}$$

$$\begin{aligned}\mathcal{V}_{\rm N}(\delta e_t) &= \frac{V_{\rm N}(\delta e_t)}{\left(1-\frac{1}{2}\delta e_t\right)^6} \\ &= -\frac{65}{96}-\frac{11}{24}\delta e_t+\mathcal{O}\left(\delta e_t^2\right)\end{aligned} \tag{4.59}$$

and the new amplitude vector $\vec{\mathcal{V}}$ is

$$\vec{\mathcal{V}}(\delta e_t, \eta; v_p) = \vec{V}(\delta e_t, \eta; v_p) + \vec{P}(\delta e_t, \eta; v_p) + \vec{P}(\delta e_t, \eta; v_p) \circ \vec{V}(\delta e_t, \eta; v_p)\,, \tag{4.60}$$

which should be expanded about $\delta e_t \ll 1$ by Assumption II. In the above expression, the pericenter velocity is decreasing from one orbit to the next for highly elliptic orbits at Newtonian order. We refer to this behavior as *pericenter braking*, which will be explored in more detail later in this chapter.

We may follow the same procedure for the eccentricity mapping to find

$$\delta e_{t,i} = \delta e_{t,i-1} + \frac{85\pi}{48}\eta v_{p,i-1}^5 \mathcal{D}_{\rm N}(\delta e_{t,i-1})\left[1 + \vec{\mathcal{D}}(\delta e_{t,i-1}, \eta; v_p)\cdot \vec{X}(v_{p,i-1})\right]\,, \tag{4.61}$$

with the Newtonian function

$$\begin{aligned}\mathcal{D}_{\rm N}(\delta e) &= \frac{(1-\delta e_t)\left(1 - \frac{242}{425}\delta e_t + \frac{121}{425}\delta e_t^2\right)}{\left(1-\frac{1}{2}\delta e_t\right)^5}\,,\\ &= 1 + \frac{791}{850}\delta e_t + \mathcal{O}\left(\delta e_t^2\right)\,,\end{aligned} \tag{4.62}$$

and the amplitude vector

$$\vec{\mathcal{D}}(\delta e_t, \eta; v_p) = \vec{E}(\delta e_t, \eta; v_p) + \vec{P}(\delta e_t, \eta; v_p) + \vec{P}(\delta e_t, \eta; v_p) \circ \vec{E}(\delta e_t, \eta; v_p)\,. \tag{4.63}$$

We thus find that the PN amplitude vectors $(\vec{\mathcal{V}}, \vec{\mathcal{D}})$ can be expressed in terms of the known PN amplitude vectors $(\vec{P}, \vec{V}, \vec{E})$. The above expressions are purely generic within the PN formalism, allowing them to be applied at any PN order.

Now, let us consider the second ingredient of the PN burst model: the centroid mapping. The GW time is given in Eq. (4.24), while the pericenter distance is given in Eq. (4.47). We thus have that the GW time at arbitrary PN order is

$$\tau_{\rm GW} = \frac{M\left(2-\delta e_t\right)}{v_p^3}\left[1+\vec{R}(\delta e_t,\eta;v_p)\cdot\vec{X}(v_p)\right]\,, \tag{4.64}$$

and the frequency mapping between boxes is

$$\begin{aligned} f_i = {} & \frac{\left[v_{p,i}\left(v_{p,i-1},\delta e_{t,i-1}\right)\right]^3}{2\pi M\left[2-\delta e_{t,i}\left(v_{p,i-1},\delta e_{t,i-1}\right)\right]} \\ & \times\left\{1+\vec{R}^{(-1)}\left[\delta e_{t,i}(r_{p,i-1},\delta e_{t,i-1}),\eta;v_p\right]\cdot\vec{X}\left[v_{p,i}\left(v_{p,i-1},\delta e_{t,i-1}\right)\right]\right\}\,, \end{aligned} \tag{4.65}$$

where the functionals $v_{p,i}(v_{p,i-1},\delta e_{t,i-1})$ and $\delta e_{t,i}(v_{p,i-1},\delta e_{t,i-1})$ are given in Eqs. (4.57) and (4.61), respectively. The components of the amplitude vectors $\vec{R}^{(-1)}$ are defined recursively in Appendix C. The time mapping can trivially be constructed from Eq. (4.46) via

$$\begin{aligned} t_i = t_{i-1} + {} & \frac{2\pi M}{\left[v_{p,i}\left(v_{p,i-1},\delta e_{t,i-1}\right)\right]^3}\frac{\left[2-\delta e_{t,i}\left(v_{p,i-1},\delta e_{t,i-1}\right)\right]^{3/2}}{\left[\delta e_{t,i}\left(v_{p,i-1},\delta e_{t,i-1}\right)\right]^{3/2}} \\ & \times\left\{1+\vec{P}\left[\delta e_{t,i}\left(v_{p,i-1},\delta e_{t,i-1}\right),\eta;v_p\right]\cdot\vec{X}\left[v_{p,i}\left(v_{p,i-1},\delta e_{t,i-1}\right)\right]\right\}\,, \end{aligned} \tag{4.66}$$

which completes our calculation of the centroid mapping.

We have here *not* inserted Eqs. (4.57) and (4.61) into Eqs. (4.66) and (4.65), and re-expanded about the pericenter velocity being small to determine the time and frequency of the bursts. The reason for this is that such an expansion results in a significant loss of accuracy compared to numerical evolutions. This results from the behavior of the orbital period in the burst model which behaves as

$$\frac{1}{\delta e_{t,i}^{3/2}} \sim \frac{1}{\left(\delta e_{t,i-1}+A\,v_{p,i-1}^5\right)^{3/2}}\,, \tag{4.67}$$

where A is a constant. Since both $\delta e_{t,i-1}$ and $v_{p,i-1}$ are assumed to be simultaneously but independently small, expanding such a function about only one of them would impose an assumption on their ratio that is not justified.

Finally, we consider the volume mapping of the bursts. Once again, we treat the bursts as boxes in time and frequency with widths defined by Eqs. (4.28) and (4.29). Hence we simply have to evaluate these expressions within our PN formalism at $(v_{p,i}, e_{t,i})$, thus obtaining

$$\begin{aligned}\delta t_i = {} & \frac{\xi_t M \left[2 - \delta e_{t,i}\left(v_{p,i-1}, \delta e_{t,i-1}\right)\right]}{\left[v_{p,i}\left(v_{p,i-1}, \delta e_{t,i-1}\right)\right]^3} \\ & \times \left\{1 + \vec{R}\left[\delta e_{t,i}(v_{p,i-1}, \delta e_{t,i-1}), \eta; v_p\right] \cdot \vec{X}\left[v_{p,i}\left(v_{p,i-1}, \delta e_{t,i-1}\right)\right]\right\} ,\end{aligned} \tag{4.68}$$

$$\begin{aligned}\delta f_i = {} & \frac{\xi_f \left[v_{p,i}\left(v_{p,i-1}, \delta e_{t,i-1}\right)\right]^3}{2\pi M \left[2 - \delta e_{t,i}\left(v_{p,i-1}, \delta e_{t,i-1}\right)\right]} \\ & \times \left\{1 + \vec{R}^{(-1)}\left[\delta e_{t,i}(r_{p,i-1}, \delta e_{t,i-1}), \eta; v_p\right] \cdot \vec{X}\left[v_{p,i}\left(v_{p,i-1}, \delta e_{t,i-1}\right)\right]\right\} .\end{aligned} \tag{4.69}$$

Not surprisingly, we see that one set of corrections, specifically the PN corrections to the pericenter distance, are the PN corrections to the frequency and box size mappings.

Example PN Burst Models

We have applied the fully general formalism of the previous section to PN theory, developing a burst model at generic PN order. This arbitrary order model is characterized by four amplitude vector fields $\lambda^a_{\mathrm{PNburst}} = \left(\vec{P}, \vec{R}, \vec{\mathcal{V}}, \vec{\mathcal{D}}\right)$, which can easily be constructed from the PN corrections to the orbital period, pericenter velocity, and rate of change of pericenter velocity and orbital eccentricity. These amplitude vectors are dependent on the set of GR parameters that characterize the system, namely

$\lambda^a_{\rm GR} = (\delta e_t, \eta, ...)$. We will now apply this formalism to generate a few example burst models at specific PN orders. There are multiple coordinate systems used to calculate PN quantities. Two that are typically used within the literature are the ADM and modified harmonic coordinates. We will choose to work within the ADM coordinates. The expressions in modified harmonic coordinates can easily be obtained through the appropriate coordinate transformations, which are given for example in Eq. (7.11) in [28].

Burst Model at 1PN Order We begin by calculating the burst model to 1PN order. Recall that the model has three ingredients: the orbit evolution, the centroid mapping, and the volume mapping. We begin with the orbit evolution, which in our generic order model is given by Eqs. (4.57) and (4.61). There are no 0.5PN order corrections to any of the quantities considered here, so the state vector has only one component, specifically

$$\vec{X} = (v_p^2)\,. \tag{4.70}$$

To achieve a burst model at 1PN order, we simply have to compute the 1PN functions $(\mathcal{V}_2, \mathcal{D}_2)$. The functions $(\mathcal{V}_k, \mathcal{D}_k)$ are given in general by Eq. (4.60) and (4.63), respectively. Setting $k = 2$, these functions become

$$\mathcal{V}_2(e_t, \eta; v_p) = V_2(e_t, \eta; v_p) + P_2(e_t, \eta; v_p)\,, \tag{4.71}$$

$$\mathcal{D}_2(\delta e_t, \eta; v_p) = E_2(e_t, \eta; v_p) + P_2(e_t, \eta; v_p)\,. \tag{4.72}$$

where (V_2, E_2, P_2) are given in Appendix D. Working to $\mathcal{O}(\delta e_t)$, the orbit evolution becomes

$$\frac{(v_{p,i} - v_{p,i-1})_{\rm 1PN}}{(v_{p,i} - v_{p,i-1})_{\rm N}} = 1 + \mathcal{V}_2(\delta e_{t,i-1}, \eta; v_p) v_{p,i-1}^2 + \mathcal{O}\left(v_{p,i-1}^3\right) \tag{4.73}$$

$$\frac{\left(\delta e_{t,i}-\delta e_{t,i-1}\right)_{\rm 1PN}}{\left(\delta e_{t,i}-\delta e_{t,i-1}\right)_{\rm N}} = 1+\mathcal{D}_2(\delta e_{t,i-1},\eta;v_p)v_{p,i-1}^2+\mathcal{O}\left(v_{p,i-1}^3\right) \tag{4.74}$$

with

$$\left(v_{p,i}-v_{p,i-1}\right)_{\rm N} = -\frac{13\pi}{96}\eta v_{p,i-1}^6\left[1+\frac{44}{65}\delta e_{t,i-1}+\mathcal{O}\left(\delta e_{t,i-1}^2\right)\right] \tag{4.75}$$

$$\left(\delta e_{t,i}-\delta e_{t,i-1}\right)_{\rm N} = \frac{85\pi}{48}\eta v_{p,i-1}^5\left[1+\frac{791}{850}\delta e_{t,i-1}+\mathcal{O}\left(\delta e_{t,i-1}^2\right)\right] \tag{4.76}$$

$$\mathcal{V}_2(\delta e_{t,i-1},\eta;v_p) = -\frac{251}{104}\eta+\frac{8321}{2080}+\delta e_{t,i-1}\left(\frac{14541}{6760}\eta-\frac{98519}{135200}\right)+\mathcal{O}(\delta e_{t,i-1}^2)\,, \tag{4.77}$$

$$\mathcal{D}_2(\delta e_{t,i-1},\eta;v_p) = -\frac{4017}{680}\eta+\frac{4773}{800}+\delta e_{t,i-1}\left(\frac{225393}{144500}\eta-\frac{602109}{340000}\right)+\mathcal{O}(\delta e_{t,i-1}^2)\,. \tag{4.78}$$

Let us now consider the centroid mapping. The evolution of the time centroid of the bursts is trivially given by the orbital period, so to 1PN order

$$\frac{\left(t_i-t_{i-1}\right)_{\rm 1PN}}{\left(t_i-t_{i-1}\right)_{\rm N}} = 1+P_2\left[\delta e_{t,i}(v_{p,i-1},\delta e_{t,i-1}),\eta;v_p\right]\left[v_{p,i}(v_{p,i-1},\delta e_{t,i-1})\right]^2+\mathcal{O}\left(v_{p,i}^4\right)\,, \tag{4.79}$$

with

$$\begin{aligned}\left(t_i-t_{i-1}\right)_{\rm N} &= P^{\rm N}\left(v_{p,i},\delta e_{t,i}\right)\\ &= \frac{2\pi M}{\left[v_{p,i}(v_{p,i-1},\delta e_{t,i-1})\right]^3}\frac{\left[2-\delta e_{t,i}(v_{p,i-1},\delta e_{t,i-1})\right]^{3/2}}{\left[\delta e_{t,i}(v_{p,i-1},\delta e_{t,i-1})\right]^{3/2}}\,,\end{aligned} \tag{4.80}$$

$$P_2(\delta e_{t,i},\eta;v_p) = \frac{3}{2}\eta-\frac{3}{4}+\delta e_{t,i}\left(-\frac{5}{8}\eta+\frac{3}{4}\right)+\mathcal{O}(\delta e_{t,i}^2)\,, \tag{4.81}$$

where $v_{p,i}(v_{p,i-1},\delta e_{t,i-1})$ and $\delta e_{t,i}(v_{p,i-1},\delta e_{t,i-1})$ are given by Eqs. (4.73) and (4.74), respectively.

We now move onto the frequency centroid mapping, which is characterized by the functions $R_k^{(-1)}$. Using the recursion method is Appendix C, $R_2^{(-1)} = -R_2$, and the frequency centroid mapping becomes

$$\frac{f_i^{\rm PN}}{f_i^{\rm N}} = 1 - R_2\left[\delta e_{t,i}(v_{p,i-1}, \delta e_{t,i-1}), \eta; v_p\right]\left[v_{p,i}(v_{p,i-1}, \delta e_{t,i-1})\right]^2 + \mathcal{O}(v_{p,i}^4) \qquad (4.82)$$

with

$$f_i^{\rm N} = \frac{\left[v_{p,i}\left(v_{p,i-1}, \delta e_{t,i-1}\right)\right]^3}{2\pi M\left[2 - \delta e_{t,i}\left(v_{p,i-1}, \delta e_{t,i-1}\right)\right]} \qquad (4.83)$$

$$R_2(\delta e_{t,i}, \eta; v_p) = \frac{7}{4}\eta - \frac{5}{2} - \frac{5}{8}\eta\delta e_{t,i} + \mathcal{O}(\delta e_{t,i}^2)\,. \qquad (4.84)$$

Finally, we focus on the volume mapping, which is trivially given by the same corrections as the frequency centroid mapping:

$$\frac{\delta t_i^{\rm 1PN}}{\delta t_i^{\rm N}} = 1 + R_2\left[\delta e_{t,i}(v_{p,i-1}, \delta e_{t,i-1}), \eta; v_p\right]\left[v_{p,i}(v_{p,i-1}, \delta e_{t,i-1})\right]^2 + \mathcal{O}(v_{p,i}^4)\,, \qquad (4.85)$$

$$\frac{\delta f_i^{\rm 1PN}}{\delta f_i^{\rm N}} = 1 - R_2\left[\delta e_{t,i}(v_{p,i-1}, \delta e_{t,i-1}), \eta; v_p\right]\left[v_{p,i}(v_{p,i-1}, \delta e_{t,i-1})\right]^2 + \mathcal{O}(v_{p,i}^4) \qquad (4.86)$$

where we have defined

$$\delta t_i^{\rm N} = \frac{\xi_t M\left[2 - \delta e_{t,i}\left(v_{p,i-1}, \delta e_{t,i-1}\right)\right]}{\left[v_{p,i}\left(v_{p,i-1}, \delta e_{t,i-1}\right)\right]^3} \qquad (4.87)$$

$$\delta f_i^{\rm N} = \frac{\xi_f\left[v_{p,i}\left(v_{p,i-1}, \delta e_{t,i-1}\right)\right]^3}{2\pi M\left[2 - \delta e_{t,i}\left(v_{p,i-1}, \delta e_{t,i-1}\right)\right]} \qquad (4.88)$$

This completes the burst model at 1PN order.

Burst Model at 2PN Order Let us now calculate the burst model to 2PN order. The state vector has three components corresponding to 1PN, 1.5PN, and 2PN orders, specifically

$$\vec{X} = (v_p^2, v_p^3, v_p^4)\,. \tag{4.89}$$

We begin by computing the orbital evolution in the burst model. To 2PN order, the pericenter velocity and eccentricity mappings become

$$\begin{aligned}
\frac{(v_{p,i}-v_{p,i-1})_{\rm 2PN}}{(v_{p,i}-v_{p,i-1})_{\rm N}} &= \frac{(v_{p,i}-v_{p,i-1})_{\rm 1PN}}{(v_{p,i}-v_{p,i-1})_{\rm N}} + \mathcal{V}_3(\delta e_{t,i-1},\eta;v_p)v_{p,i-1}^3 \\
&\quad + \mathcal{V}_4(\delta e_{t,i-1},\eta;v_p)v_{p,i-1}^4 + \mathcal{O}(v_{p,i-1}^5) \qquad (4.90)\\
\frac{(\delta e_{t,i}-\delta e_{t,i-1})_{\rm 2PN}}{(\delta e_{t,i}-\delta e_{t,i-1})_{\rm N}} &= \frac{(\delta e_{t,i}-\delta e_{t,i-1})_{\rm 1PN}}{(\delta e_{t,i}-\delta e_{t,i-1})_{\rm N}} + \mathcal{D}_3(\delta e_{t,i-1},\eta;v_p)v_{p,i-1}^3 \\
&\quad + \mathcal{D}_4(\delta e_{t,i-1},\eta;v_p)v_{p,i-1}^4 + \mathcal{O}(v_{p,i-1}^5) \qquad (4.91)
\end{aligned}$$

The Newtonian and 1PN order mappings do not change from the 1PN order model, and they are given in Eqs. (4.75)-(4.76) and Eqs. (4.73)-(4.74), respectively. Generally, the 1.5PN order and 2PN order components of the amplitude fields are given by

$$\mathcal{V}_3(e_t,\eta;v_p) = V_3(e_t,\eta;v_p) \tag{4.92}$$

$$\mathcal{D}_3(e_t,\eta;v_p) = E_3(e_t,\eta;v_p) \tag{4.93}$$

$$\mathcal{V}_4(e_t,\eta;v_p) = V_4(e_t,\eta;v_p) + P_4(e_t,\eta;v_p) + V_2(e_t,\eta;v_p)P_2(e_t,\eta;v_p) \tag{4.94}$$

$$\mathcal{D}_4(e_t,\eta;v_p) = E_4(e_t,\eta;v_p) + P_4(e_t,\eta;v_p) + E_2(e_t,\eta;v_p)P_2(e_t,\eta;v_p) \tag{4.95}$$

Using the results of Appendix D, we obtain

$$\mathcal{V}_3(\delta e_{t,i-1},\eta;v_p) = \frac{3712\sqrt{3}}{585} + \frac{100864\sqrt{3}}{12675}\delta e_{t,i-1} + \mathcal{O}(\delta e_{t,i-1}^2)\,, \tag{4.96}$$

$$\mathcal{D}_3(\delta e_{t,i-1},\eta;v_p) = \frac{10624\sqrt{3}}{3825} + \frac{1098176\sqrt{3}}{541875}\delta e_{t,i-1} + \mathcal{O}(\delta e_{t,i-1}^2)\,, \tag{4.97}$$

$$\mathcal{V}_4(\delta e_{t,i-1},\eta;v_p) = \frac{119432023}{6289920} - \frac{1213031}{49920}\eta - \frac{169}{128}\eta^2 + \delta e_{t,i-1}\Bigg(\frac{29330909}{204422400} + \frac{816679}{202800}\eta$$

$$-\frac{68571}{4160}\eta^2\Big) + \mathcal{O}(\delta e_{t,i-1}^{3/2})\,, \tag{4.98}$$

$$\begin{aligned}\mathcal{D}_4(\delta e_{t,i-1},\eta;v_p) &= \frac{130397759}{4569600} - \frac{5863719}{108800}\eta + \frac{284687}{10880}\eta^2 + \delta e_{t,i-1}^{1/2}\left(\frac{45\sqrt{2}}{32} - \frac{9\sqrt{2}}{16}\eta\right) \\ &+ \delta e_{t,i-1}\left(-\frac{26000488883}{2913120000} + \frac{887490277}{46240000}\eta - \frac{16138299}{1156000}\eta^2\right) \\ &+ \mathcal{O}(\delta e_{t,i-1}^{3/2})\,,\end{aligned} \tag{4.99}$$

where we have used the results of [107] to evaluate the tail enhancement factors.

Next, let us consider the time centroid mapping, which at 2PN order is

$$\begin{aligned}\frac{(t_i - t_{i-1})_{\rm 2PN}}{(t_i - t_{i-1})_{\rm N}} &= \frac{(t_i - t_{i-1})_{\rm 1PN}}{(t_i - t_{i-1})_{\rm N}} + P_4[\delta e_{t,i}(v_{p,i-1},\delta e_{t,i-1}),\eta;v_p]v_{p,i}(v_{p,i-1},\delta e_{t,i-1})^4 \\ &+ \mathcal{O}(v_{p,i}^5)\,,\end{aligned} \tag{4.100}$$

where the mappings $v_{p,i}(v_{p,i-1},\delta e_{t,i-1})$ and $\delta e_{t,i}(v_{p,i-1},\delta e_{t,i-1})$ are now given by Eqs. (4.90) and (4.91), respectively. There is no 1.5PN order correction to these expressions, since $P_3 = 0$. This is a result of the fact that the orbital period comes from the conservative orbital dynamics, and is thus symmetric under time reversal. Once again, the Newtonian time centroid mapping and 1PN order correction do not change from the 1PN order burst model. The 2PN order correction is characterized solely by $P_4(e_t,\eta;v_p)$, which is given in Appendix D. Expanding about $\delta e_t \ll 1$, we obtain

$$\begin{aligned}P_4(\delta e_{t,i},\eta;v_p) &= -\frac{225}{64} + \frac{237}{64}\eta - \frac{39}{32}\eta^2 + \delta e_{t,i}^{1/2}\left(\frac{45\sqrt{2}}{32} - \frac{9\sqrt{2}}{16}\eta\right) \\ &+ \delta e_{t,i}\left(-\frac{135}{64} + \frac{115}{64}\eta + \frac{7}{16}\eta^2\right) + \mathcal{O}(\delta e_{t,i}^{3/2})\,.\end{aligned} \tag{4.101}$$

Finally, consider the frequency centroid and box size mappings, which at 2PN order are

$$\frac{f_i^{\rm 2PN}}{f_i^{\rm N}} = \frac{f_i^{\rm 1PN}}{f_i^{\rm N}} + R_4^{(-1)}[\delta e_{t,i}(v_{p,i-1}, \delta e_{t,i-1}), \eta; v_p] v_{p,i}(v_{p,i-1}, \delta e_{t,i-1})^4 + \mathcal{O}(v_{p,i}^5) \,, \tag{4.102}$$

$$\frac{\delta t_i^{\rm 2PN}}{\delta t_i^{\rm N}} = \frac{\delta t_i^{\rm 1PN}}{\delta t_i^{\rm N}} + R_4[\delta e_{t,i}(v_{p,i-1}, \delta e_{t,i-1}), \eta; v_p] v_{p,i}(v_{p,i-1}, \delta e_{t,i-1})^4 + \mathcal{O}(v_{p,i}^5) \,, \tag{4.103}$$

$$\frac{\delta f_i^{\rm 2PN}}{\delta f_i^{\rm N}} = \frac{\delta f_i^{\rm 1PN}}{\delta f_i^{\rm N}} + R_4^{(-1)}[\delta e_{t,i}(v_{p,i-1}, \delta e_{t,i-1}), \eta; v_p] v_{p,i}(v_{p,i-1}, \delta e_{t,i-1})^4 + \mathcal{O}(v_{p,i}^5) \,, \tag{4.104}$$

The Newtonian and 1PN order terms are the same as those in the 1PN order burst model. Using the results of Appendix C, the field $R_4^{(-1)}$ is in general given by

$$R_4^{(-1)}(e_t, \eta; v_p) = -R_4(e_t, \eta; v_p) + R_2(e_t, \eta; v_p)^2 \,. \tag{4.105}$$

Applying the expressions for (R_2, R_4) from D, we obtain

$$R_4(\delta e_{t,i}, \eta; v_p) = -\frac{47}{16} + \frac{49}{16}\eta - \frac{17}{16}\eta^2 + \delta e_{t,i}\left(-\frac{133}{64} + \frac{155}{64}\eta + \frac{13}{32}\eta^2\right) + \mathcal{O}(\delta e_{t,i}^2) \,, \tag{4.106}$$

$$R_4^{(-1)}(\delta e_{t,i}, \eta, v_p) = \frac{147}{16} - \frac{189}{16}\eta + \frac{33}{8}\eta^2 + \delta e_{t,i}\left(\frac{133}{64} + \frac{45}{64}\eta - \frac{83}{32}\eta^2\right) + \mathcal{O}(\delta e_{t,i}^2) \,. \tag{4.107}$$

This completes the burst model at 2PN order.

Burst Model at 3PN Order Let us now extend the burst model to the current limits of our understanding of eccentric binaries within PN theory, i.e. to 3PN order.

The state vector will now extend to v_p^6, specifically

$$\vec{X} = (v_p^2, v_p^3, v_p^4, v_p^5, v_p^6)\,. \tag{4.108}$$

At 3PN order, the orbital evolution equations become

$$\begin{aligned}
\frac{(v_{p,i}-v_{p,i-1})_{\rm 3PN}}{(v_{p,i}-v_{p,i-1})_{\rm N}} &= \frac{(v_{p,i}-v_{p,i-1})_{\rm 2PN}}{(v_{p,i}-v_{p,i-1})_{\rm N}} + \mathcal{V}_5(\delta e_{t,i-1},\eta;v_p)v_{p,i-1}^5 \\
&\quad + \mathcal{V}_6(\delta e_{t,i-1},\eta;v_p)v_{p,i-1}^6 + \mathcal{O}\left(v_{p,i-1}^7\right)\,, && (4.109)\\
\frac{(\delta e_{t,i}-\delta e_{t,i-1})_{\rm 3PN}}{(\delta e_{t,i}-\delta e_{t,i-1})_{\rm N}} &= \frac{(\delta e_{t,i}-\delta e_{t,i-1})_{\rm 2PN}}{(\delta e_{t,i}-\delta e_{t,i-1})_{\rm N}} + \mathcal{D}_5(\delta e_{t,i-1},\eta;v_p)v_{p,i-1}^5 \\
&\quad + \mathcal{D}_6(\delta e_{t,i-1},\eta;v_p)v_{p,i-1}^6 + \mathcal{O}\left(v_{p,i-1}^7\right)\,. && (4.110)
\end{aligned}$$

The new functions $[\mathcal{V}_5, \mathcal{V}_6]$ and $[\mathcal{D}_5, \mathcal{D}_6]$ give the coefficients of the 2.5PN and 3PN order corrections of the orbital evolutions. In terms of the components of the amplitude vector fields $[\vec{V}, \vec{E}, \vec{P}]$, they are given by

$$\begin{aligned}
\mathcal{V}_5(e_t,\eta;v_p) &= V_5(e_t,\eta;v_p) + V_3(e_t,\eta;v_p)P_2(e_t,\eta;v_p)\,, && (4.111)\\
\mathcal{D}_5(e_t,\eta;v_p) &= E_5(e_t,\eta;v_p) + E_3(e_t,\eta;v_p)P_2(e_t,\eta;v_p)\,, && (4.112)\\
\mathcal{V}_6(e_t,\eta;v_p) &= V_6(e_t,\eta;v_p) + P_6(e_t,\eta;v_p) + V_2(e_t,\eta;v_p)P_4(e_t,\eta;v_p) \\
&\quad + V_4(e_t,\eta;v_p)P_2(e_t,\eta;v_p)\,, && (4.113)\\
\mathcal{D}_6(e_t,\eta;v_p) &= E_6(e_t,\eta;v_p) + P_6(e_t,\eta;v_p) + E_2(e_t,\eta;v_p)P_4(e_t,\eta;v_p) \\
&\quad + E_4(e_t,\eta;v_p)P_2(e_t,\eta;v_p)\,, && (4.114)
\end{aligned}$$

where we have used the fact that $P_3(e_t, \eta; v_p) = 0 = P_5(e_t, \eta; v_p)$. Using the results of Appendix D, we find for the 2.5PN order functions

$$\begin{aligned}\mathcal{V}_5(\delta e_{t,i-1}, \eta; v_p) = &-\frac{128272\sqrt{3}}{4095} - \frac{4832\sqrt{3}}{117}\eta + \nu_0\pi + \frac{1748\sqrt{6}}{65}\delta e_{t,i-1}^{1/2} \\ &+ \delta e_{t,i-1}\left(-\frac{30641528\sqrt{3}}{266175} - \frac{1183488\sqrt{3}}{29575}\eta + \nu_1\pi\right) + \mathcal{O}(\delta e_{t,i-1}^{3/2})\,,\end{aligned} \tag{4.115}$$

$$\begin{aligned}\mathcal{D}_5(\delta e_{t,i-1}, \eta; v_p) = &\frac{13072\sqrt{3}}{8925} - \frac{241664\sqrt{3}}{8925}\eta + \rho_0\pi + \frac{4544\sqrt{6}}{425}\delta e_{t,i-1}^{1/2} \\ &+ \delta e_{t,i-1}\left(-\frac{81300056\sqrt{3}}{3793125} - \frac{52270208\sqrt{3}}{3793125}\eta + \rho_1\pi\right) + \mathcal{O}(\delta e_{t,i-1}^{3/2})\,,\end{aligned} \tag{4.116}$$

where we have used the results of Ch. 3 [107] and neglected the 2.5PN memory terms. The constants $[\nu_0, \nu_1, \rho_0, \rho_1]$ depend on the coefficients of the Padé approximants created for the 2.5PN order tail enhancement factors $[\psi(e_t), \tilde{\psi}(e_t)]$ in Ch. 3 [107]. The exact rational form of the coefficients are too lengthy to provide here. We simply give their numeric values, which are

$$\nu_0 = 34.82829720\,, \qquad \nu_1 = -38.97374189\,, \tag{4.117}$$

$$\rho_0 = 11.90237615\,, \qquad \rho_1 = -36.89484102\,, \tag{4.118}$$

For the 3PN order functions, we find

$$\begin{aligned}\mathcal{V}_6(\delta e_{t,i-1}, \eta; v_p) = &\frac{48102359171}{402554880} + \frac{385\pi^2}{128} + \frac{1177\ln(2)}{64} + \frac{1177\ln(3)}{256} \\ &- \left(\frac{508363\pi^2}{266240} + \frac{80844193}{430080}\right)\eta + \frac{3379743}{53248}\eta^2 + \frac{543189}{13312}\eta^3 \\ &- \frac{1177}{256}\ln(v_{p,i-1}^2) + \delta e_{t,i-1}\left[\frac{1690426235921}{26166067200} + \frac{48839\pi^2}{8320}\right.\end{aligned}$$

$$+\frac{746539\ln(2)}{20800}+\frac{746539\ln(3)}{83200}-\left(\frac{112925149}{83865600}+\frac{80684263\pi^2}{17305600}\right)\eta$$
$$-\frac{753359873}{10383360}\eta^2+\frac{61283003}{865280}\eta^3-\frac{746539}{83200}\ln(v_{p,i-1}^2)\Bigg]+\mathcal{O}\left(\delta e_{t,i-1}^{3/2}\right)\,, \tag{4.119}$$

$$\begin{aligned}\mathcal{D}_6(\delta e_{t,i-1},\eta;v_p) &= \frac{7318191053}{51609600}+\frac{10549\pi^2}{10880}+\frac{161249\ln(2)}{27200}+\frac{161249\ln(3)}{108800}\\ &-\left(\frac{8119255961}{21934080}+\frac{155561\pi^2}{1740800}\right)\eta+\frac{11789862391}{36556800}\eta^2-\frac{9152141}{87040}\eta^3\\ &-\frac{161249}{108800}\ln(v_{p,i-1}^2)+\delta e_{t,i-1}^{1/2}\Bigg[\frac{64557\sqrt{2}}{5120}-\Bigg(\frac{4120619\sqrt{2}}{217600}\\ &-\frac{123\pi^2\sqrt{2}}{4096}\Bigg)\eta+\frac{13437\sqrt{2}}{2720}\eta^2\Bigg]+\delta e_{t,i-1}\Bigg[-\frac{11487739123}{552960000}\\ &+\frac{5805723\pi^2}{4624000}+\frac{88744623\ln(2)}{11560000}+\frac{88744623\ln(3)}{46240000}+\Bigg(\frac{639985247281}{6991488000}\\ &+\frac{13567261\pi^2}{92480000}\Bigg)\eta-\frac{689800811001}{5178880000}\eta^2+\frac{1557091039}{18496000}\eta^3\\ &-\frac{88744623}{46240000}\ln(v_{p,i-1}^2)\Bigg]+\mathcal{O}(\delta e_{t,i-1}^{3/2})\,.\end{aligned} \tag{4.120}$$

This completes the orbital evolution to 3PN order.

The time centroid mapping at 3PN order becomes

$$\frac{(t_i-t_{i-1})_{\mathrm{3PN}}}{(t_i-t_{i-1})_{\mathrm{N}}}=\frac{(t_i-t_{i-1})_{\mathrm{2PN}}}{(t_i-t_{i-1})_{\mathrm{N}}}+P_6[\delta e_{t,i}(v_{p,i-1},\delta e_{t,i-1}),\eta;v_p]v_{p,i}^6+\mathcal{O}(v_{p,i}^7)\,, \tag{4.121}$$

where once again there is no 2.5PN order corrections since the orbital period comes from the conservative orbital dynamics. The 3PN order function $P_6(e_t,\eta;v_p)$ is given in Appendix D. Expanding about $\delta e_t \ll 1$, we obtain

$$\begin{aligned}P_6(\delta e_{t,i},\eta;v_p) &= -\frac{2821}{256}+\left(\frac{2123}{128}+\frac{3\pi^2}{16}\right)\eta-\frac{1377}{128}\eta^2+\frac{73}{32}\eta^3+\delta e_{t,i}^{1/2}\Bigg[\frac{405\sqrt{2}}{128}\\ &-\left(\frac{607\sqrt{2}}{128}-\frac{123\pi^2\sqrt{2}}{4096}\right)\eta+\frac{99\sqrt{2}}{128}\eta^2\Bigg]+\delta e_{t,i}\Bigg[-\frac{213}{32}+\Bigg(\frac{591}{128}\end{aligned}$$

$$+\frac{885\pi^2}{2048}\bigg)\eta-\frac{1117}{512}\eta^2-\frac{399}{256}\eta^3\bigg]+\mathcal{O}(\delta e_{t,i}^{3/2})\,. \tag{4.122}$$

Finally, the frequency and box widths mappings at 3PN order are

$$\frac{f_i^{\rm 3PN}}{f_i^{\rm N}}=\frac{f_i^{\rm 2PN}}{f_i^{\rm N}}+R_6^{(-1)}[\delta e_{t,i}(v_{p,i-1},\delta e_{t,i-1}),\eta;v_p]v_{p,i}(v_{p,i-1},\delta e_{t,i-1})^6+\mathcal{O}(v_{p,i}^7)\,, \tag{4.123}$$

$$\frac{\delta t_i^{\rm 3PN}}{\delta t_i^{\rm N}}=\frac{\delta t_i^{\rm 2PN}}{\delta t_i^{\rm N}}+R_6[\delta e_{t,i}(v_{p,i-1},\delta e_{t,i-1}),\eta;v_p]v_{p,i}(v_{p,i-1},\delta e_{t,i-1})^6+\mathcal{O}(v_{p,i}^7)\,, \tag{4.124}$$

$$\frac{\delta f_i^{\rm 3PN}}{\delta f_i^{\rm N}}=\frac{\delta f_i^{\rm 2PN}}{\delta f_i^{\rm N}}+R_6^{(-1)}[\delta e_{t,i}(v_{p,i-1},\delta e_{t,i-1}),\eta;v_p]v_{p,i}(v_{p,i-1},\delta e_{t,i-1})^6+\mathcal{O}(v_{p,i}^7)\,, \tag{4.125}$$

where the functions $R_6^{(-1)}(e_t,\eta;v_p)$ is

$$R_6^{(-1)}(e_t,\eta;v_p)=-R_6(e_t,\eta;v_p)+2R_2(e_t,\eta;v_p)R_4(e_t,\eta;v_p)-R_2(e_t,\eta;v_p)^3\,. \tag{4.126}$$

Using the results in Appendix D, we obtain

$$\begin{aligned}R_6(\delta e_{t,i},\eta;v_p)&=-\frac{305}{32}+\left(\frac{3131}{192}+\frac{11\pi^2}{128}\right)\eta-\frac{19}{2}\eta^2+\frac{67}{32}\eta^3+\delta e_{t,i}\bigg[-\frac{829}{128}\\&+\left(\frac{2245}{256}+\frac{97\pi^2}{512}\right)\eta-\frac{333}{128}\eta^2-\frac{47}{32}\eta^3\bigg]+\mathcal{O}(\delta e_{t,i}^{3/2})\,,\end{aligned} \tag{4.127}$$

$$\begin{aligned}R_6^{(-1)}(\delta e_{t,i},\eta;v_p)&=\frac{1275}{32}-\left(\frac{14345}{192}+\frac{11\pi^2}{128}\right)\eta+\frac{97}{2}\eta^2-\frac{715}{64}\eta^3+\delta e_{t,i}\bigg[\frac{2159}{128}\\&-\left(\frac{3267}{256}+\frac{97\pi^2}{512}\right)\eta-\frac{179}{16}\eta^2+\frac{1275}{128}\eta^3\bigg]+\mathcal{O}(\delta e_{t,i}^{3/2})\,.\end{aligned} \tag{4.128}$$

This completes the burst model at 3PN order.

Properties of the PN Burst Model

With the burst model complete to 3PN order, we complete this chapter with some results that describe properties of the model. We begin by discussing the accuracy of the burst model when compared to numerical evolutions of the PN radiation reaction equations. Finally, we discuss a previously unreported phenomenon associated with the evolution of the pericenter velocity under radiation reaction.

Accuracy of the Burst Model

The burst model is meant to be an accurate representation of GW bursts emitted by highly eccentric binaries in nature. Further, since this model is designed to be used as a prior in data analysis for detecting such systems, it is paramount that we characterize the accuracy of the model. The ideal test of such an analytic model would be to compare the time of arrival and frequency of eccentric bursts from a numerical relativity simulation to the those from the burst model. However, there are currently no accurate numerical relativity waveforms for the highly eccentric systems considered here. Even the second best comparison, the same as above but with accurate PN waveforms, is also currently inapplicable due to the lack of such waveforms. With the two most ideal tests out of reach, we are left with comparing the burst model to the orbital evolution of binary systems (instead of their associated waveforms) under PN radiation reaction. Such a comparison allows us to gauge the accuracy of the approximations used to construct the burst model, as well as estimate the typical error we can expect when comparing to physically accurate waveform models.

We begin by describing the method through which we obtain the numerical evolution. Ideally, the equations we would want to numerically evolve are $\langle \dot{e}_t \rangle (v_p, e_t)$ and $\langle \dot{v}_p \rangle (v_p, e_t)$. However, as we will explain in the next section, there is always a point (v_p, e_t) where $\langle \dot{v}_p \rangle = 0$ during the inspiral, which numerical routines will have difficulty integrating past. An alternative approach is to use a parameterization of the equations that does not present this behavior, e.g. $\langle \dot{e}_t \rangle(x, e_t)$ and $\langle \dot{x} \rangle(x, e_t)$. The expression for $\langle \dot{e}_t \rangle(x, e_t)$ to 3PN order, neglecting memory contributions, is provided in Eqs. (6.18)-(6.19), (6.22), and (6.25) in [31]. To obtain the expression for $\langle \dot{x} \rangle(x, e_t)$ to 3PN order, we follow the method detailed in Appendix D for $\langle \dot{v}_p \rangle$, which we summarize here. We begin by obtaining an expression for $x(\epsilon, j)$ by inverting Eq. (6.5) in [31]. We then take a time derivative and apply the chain rule, using the 3PN order expressions for the energy flux [28] and the angular momentum flux [31]. We expand the resulting expression in x to obtain $\langle \dot{x} \rangle(x, e_t)$.

For our numerical evolutions, we integrate the equations $\langle \dot{x} \rangle(x, e_t)$ and $\langle \dot{e}_t \rangle(x, e_t)$ including all of the instantaneous and tail contributions to 3PN order. For the tail enhancement factors, we use the analytic expressions provided in [107] and Ch. 3. The initial conditions for the evolutions are set to guarantee the initial eccentricity is $e_{t,0} = 0.9$ and the initial GW frequency is $f_{\mathrm{GW},0} = 10\mathrm{Hz}$, i.e. we use these initial conditions to solve for the initial value of v_p using $f_{\mathrm{GW}}(v_p, e_t)$, which is provided in Appendix D. We then use the expression $v_p(x, et)$, which is obtained from the 3PN extension of Eq. (D.13) with Eq. (7.10) in [28], to obtain the initial value of x. For the three systems we study, a $(1.4, 1.4)M_\odot$ NSNS binary, a $(1.4, 10)M_\odot$ NSBH binary, and a $(10, 10)M_\odot$ BHBH binary, the initial conditions are listed in Table 4.1. With the initial conditions set, we numerically integrate the equations using the *NDSolve* routine in `Mathematica` until we reach the time when

$$x_f = \frac{1}{2}\left(\frac{1 - e_t^2}{3 + e_t}\right) , \tag{4.129}$$

which denotes the maximum value of x for which test particle orbits are stable around

System	$m_1[M_\odot]$	$m_2[M_\odot]$	$e_{t,0}$	x_0	$1/x_0$
NSNS	1.4	1.4	0.9	7.35×10^{-4}	1360
NSBH	1.4	10	0.9	1.85×10^{-3}	541
BHBH	10	10	0.9	2.67×10^{-3}	375

Table 4.1: Initial values of the PN expansion parameter x for the set of compact binary systems studied. The values are obtained by requiring the initial GW frequency to be 10Hz. The final column provides an estimate of the semi-major axis of the binary, since $a_r = M/x + \mathcal{O}(1)$ in PN theory.

a Schwarzschild black hole, i.e. we require that $p > 2M(3 + e_t)$, where p is the semi-latus rectum of the orbit and we have used the Newtonian relation $x = (M/p)(1 - e_t^2)$. Beyond this point, we consider the inspiral to be formally over and to use the burst model one would have to extend it to include merger and ringdown.

For the comparison to the burst model, we use $x(t)$ and $e_t(t)$ to construct the pericenter velocity as a function of time $v_p(t)$, which we then use with the results of Appendix D to obtain the orbital period and GW frequency as a function of time, specifically $P(t)$ and $f_{\rm GW}(t)$. To compute the values of these in the burst model to 3PN order, we start the model with the same initial conditions used for the numerical evolution. Once $(v_{p,0}, e_{t,0})$ are specified, all future $(v_{p,i}, e_{t,i})$ are determined from Eqs. (4.109)-(4.110). From here, the orbital period and the GW frequency are determined in the burst model from Eqs. (4.121) and (4.123).

Figure 4.1 shows the orbital period and GW frequency as functions of time in the burst model and the numerical evolution, as well as the relative error between the two. The relative error increases as time increases, but typically the error remains below 1% for the first one hundred bursts. The reason the error increases is twofold.

First, the eccentricity decreases as the binary inspirals due to the loss of energy and angular momentum by GW emission. The burst model uses an expansion about $\delta e_t \ll 1$, and it is thus most accurate in this regime. This error can be improved by going to higher order in δe_t within the burst model if one wishes.

The second reason for the increasing error is that as the binary inspirals, the GW power becomes smeared over more of the orbit. As a result, the binary's evolution resembles less a set of discrete steps. The burst model, which is only valid when $\delta e_t \ll 1$, hinges on the osculating behavior of highly eccentric orbits. This error is more difficult to control, but one way of improving it would be to match the evolution in the burst model to an evolution when the eccentricity is small. However, in this paper, we are only interested in highly elliptic orbits where this matching is unnecessary. Regardless, as the figure shows, the error between the burst model and the numerical evolution is sufficiently small that we can begin to test the burst model in idealized data analysis scenarios.

Pericenter Braking

Let us begin by recalling that within our generic PN burst model, the change of pericenter velocity to Newtonian order is given by

$$\langle \dot{v}_p \rangle = \frac{32}{5}\frac{\eta}{M} v_p^9 \frac{(1-e_t)^{3/2}}{(1+e_t)^{15/2}} V_{\rm N}(e_t) + \mathcal{O}(v_p^{11}) \tag{4.130}$$

where the function $V_{\rm N}(e_t)$ is

$$V_{\rm N}(e_t) = 1 - \frac{13}{6}e_t + \frac{7}{8}e_t^2 - \frac{37}{96}e_t^3 \,. \tag{4.131}$$

Notice from Eq. (4.58), which provides $V_{\rm N}(\delta e_t)$, that to first order in δe_t, the above expression is negative and v_p is thus decreasing. This seems counterintuitive

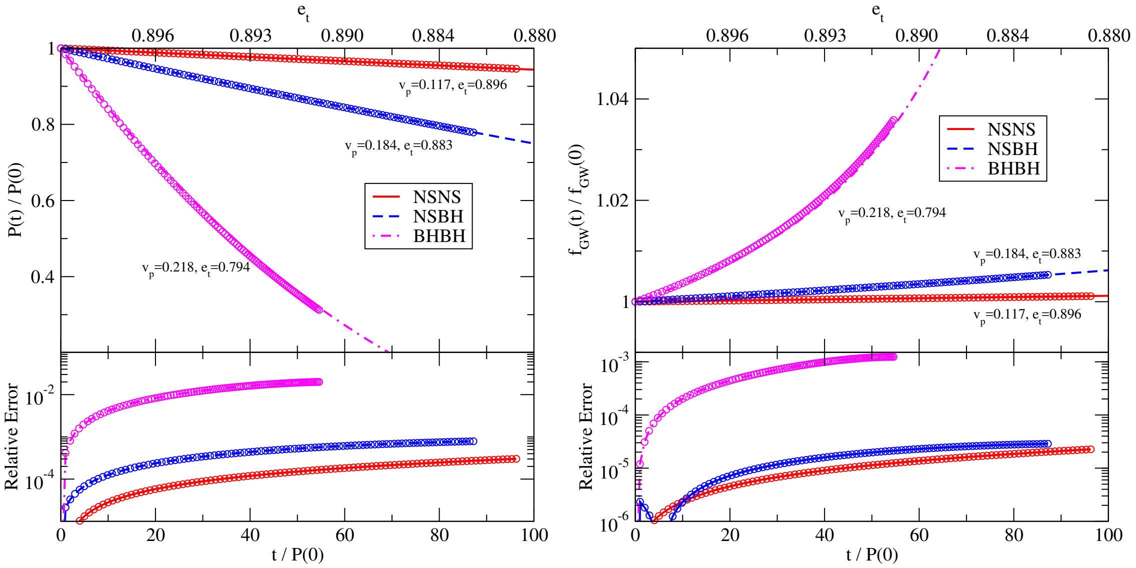

Figure 4.1: Top panel: Comparison of the orbital period P and GW frequency $f_{\rm GW}$ relative to their initial values as functions of time (in units of the initial orbital period) in the burst model (circles) and the numerical evolution (lines). The values of the pericenter velocity and time eccentricity next to each line provide the values during the 100th burst. The labels on the top axis give the value of the time eccentricity for the corresponding time for the NSBH binary. Bottom panel: Relative error between the burst model and the numerical evolutions for the orbital period and GW frequency.

considering what we know about quasi-circular binaries, i.e. as the orbital separation r decreases, the orbital velocity v increases, since v and r are inversely related by Kepler's third law.

This behavior becomes more confusing when we consider the apocenter velocity v_a. Just as we can calculate $\langle \dot{v}_p \rangle$ using the method detailed in Appendix D, we may also compute $\langle \dot{v}_a \rangle$. Following this method, and working to Newtonian order, we have

$$\langle \dot{v}_a \rangle = \frac{32}{5}\frac{\eta}{M} v_p^9 \frac{(1-e_t)^{3/2}}{(1+e_t)^{15/2}} V_{\rm N}(-e_t) + \mathcal{O}\left(v_p^{11}\right) . \tag{4.132}$$

Notice that this expression depends on $V_{\rm N}(-e_t)$, which is always positive. The apocenter velocity is thus always increasing as the binary inspirals, just as we would expect from quasi-circular binaries. As a result, the pericenter and apocenter velocities have very different behavior depending on the eccentricity of the system.

Let us try to understand this counter-intuitive behavior. The function $V_{\rm N}(e_t)$ is a third order polynomial in eccentricity with an oscillating sign and with the coefficient of the $\mathcal{O}(e_t)$ term greater than unity. This means that there will be a critical point $e_{t,{\rm crit}}$ where the function is zero, $\langle \dot{v}_p \rangle (e_{t,{\rm crit}}) = 0$, and due to the aforementioned behavior of the coefficients $e_{t,{\rm crit}} < 1$. Let us solve for this critical point. To Newtonian order we find

$$e_{t,{\rm crit}} = e^{\rm N}_{t,{\rm crit}} \equiv \frac{28}{37} - \frac{2}{111}\sigma + \frac{2672}{37}\sigma^{-1} \,, \tag{4.133}$$

where we have defined

$$\sigma = \left(67770 + 222\sqrt{1399593}\right)^{1/3} \,. \tag{4.134}$$

The Newtonian expression for the critical eccentricity evaluates to $e^{\rm N}_{\rm crit} \approx 0.5557306$. Such a critical point also exists at 1PN order, except that now it is a function of the mass ratio and the pericenter velocity:

$$e_{t,{\rm crit}} = e^{\rm N}_{t,{\rm crit}} + e^{\rm 1PN}_{t,{\rm crit}}(\eta)\; v_p^2 \,, \tag{4.135}$$

where we have defined

$$\begin{aligned}
e^{\rm 1PN}_{t,{\rm crit}}(\eta) = {} & \frac{1}{\sigma \left(2\sigma^2 - 195\sigma - 8016\right)^2 \left(\sigma^4 - 4008\sigma^2 + 16064064\right)} \\
& \times \left[\frac{10112970188463538176}{37}\eta - \frac{277520587592279526604 8}{9583} \right. \\
& + \left(\frac{1494993721722716 16}{37}\eta - \frac{310765153504177889 28}{9583} \right) \sigma \\
& + \left(-\frac{1150598736488448}{37}\eta - \frac{11994925296964608}{9583} \right) \sigma^2
\end{aligned}$$

$$+\left(\frac{62455763578752}{37}\eta-\frac{30800598698771712}{9583}\right)\sigma^{3} \\ +\left(-\frac{383487115344}{37}\eta+\frac{351826743539100}{9583}\right)\sigma^{4} \\ +\left(-\frac{46179281106}{37}\eta+\frac{35571374119917}{19166}\right)\sigma^{5}+\left(\frac{95680418}{37}\eta \right. \\ \left. -\frac{175562247275}{19166}\right)\sigma^{6}+\left(\frac{3887918}{37}\eta-\frac{1917360308}{9583}\right)\sigma^{7}+\left(\frac{53612}{111}\eta \right. \\ \left. +\frac{558902}{28749}\right)\sigma^{8}+\left(\frac{1738}{111}\eta-\frac{361279}{28749}\right)\sigma^{9}+\left(-\frac{88}{333}\eta+\frac{24149}{86247}\right)\sigma^{10}\Bigg] \quad (4.136)$$

This function evaluates to $e_{t,\text{crit}}^{\text{1PN}} \approx 0.5557306 - (0.06536872\eta + 0.3457145)v_p^2$. The overall effect of the 1PN term is to decrease the value of the Newtonian critical point, but there is no value of $v_p < 1$ or $\eta \in (0, 1/4)$ for which $e_{t,\text{crit}} = 0$ at 1PN order.

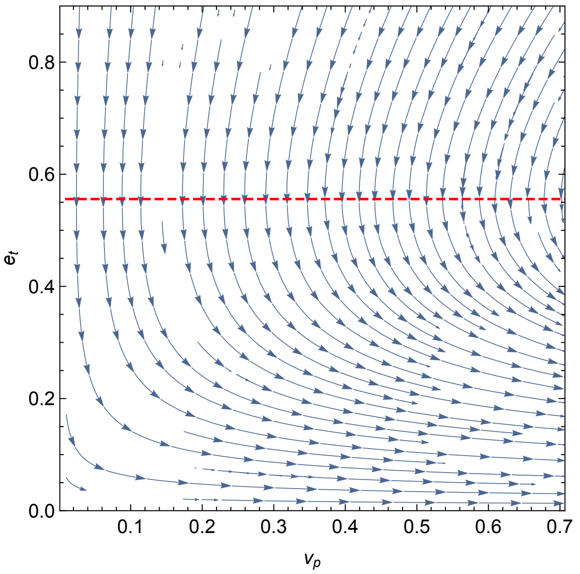

Figure 4.2: Plot of the streamlines of $(10^4\langle \dot{v}_p\rangle, 10^3\langle \dot{e}_t\rangle)$ at Newtonian order. The arrows on the streamlines only indicate the direction of the flow, not the magnitude. The red dashed line displays the value of the critical eccentricity where $\langle \dot{v}_p\rangle = 0$ at Newtonian order. Above the critical eccentricity, the streamlines point to the left as shown in the burst model, while below, they point to the right, as is expected for quasi circular binaries.

Why does this behavior occur physically? The answer to this question lies in

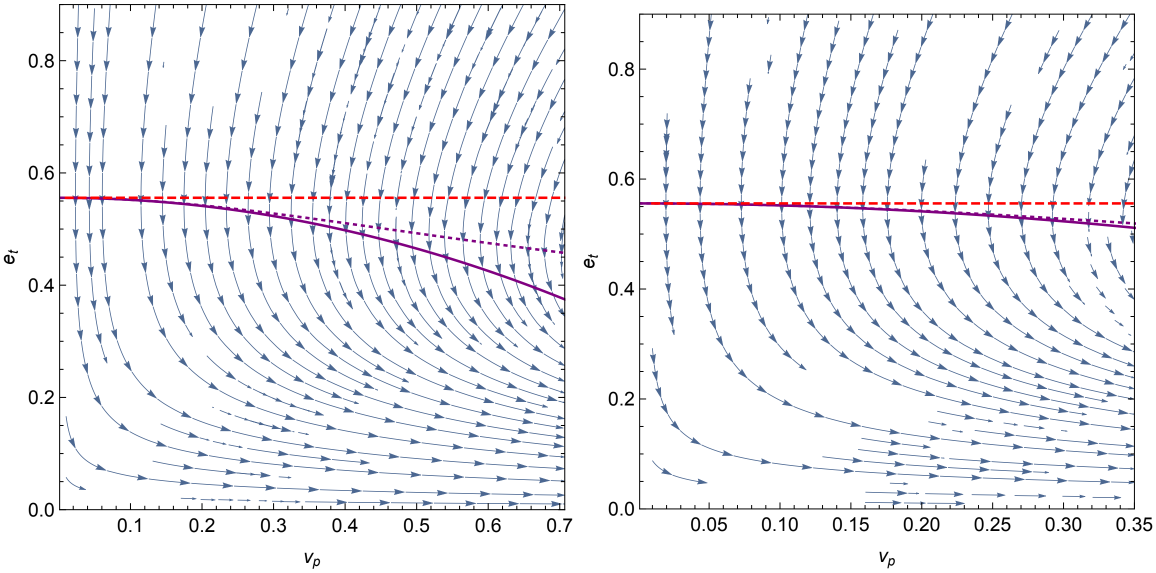

Figure 4.3: Left: Plot of the streamlines of $(10^4\langle\dot{v}_p\rangle, 10^3\langle\dot{e}_t\rangle)$ at 1PN order. The dotted line displays the value of the critical eccentricity where $\langle\dot{v}_p\rangle = 0$ at 1PN order, as determined numerically, while the dashed line is the same result at Newtonian order. The solid line displays the analytic result of the critical eccentricity given in Eqs. (4.135)-(4.136). Right: A zoom in of the plot on the left for the region $v_p = (0, 0.35)$.

circularization. As the binary inspirals, energy and angular momentum are radiated away in such a way that the orbital eccentricity decreases, making the binary more and more circular. For quasicircular binaries, $v_a = v_p + \mathcal{O}(e_t)$, but for highly-elliptic binaries, $v_p \gg v_a$. As a highly-elliptical binary inspirals, v_p and v_a will approach the same value since the eccentricity approaches zero. However, if the eccentricity is above the critical value, the two velocities will not approach the same value if they are both increasing initially. Instead, circularization causes pericenter to *brake* when the eccentricity is above $e_{t,\rm crit}$, so that v_p can approach v_a. In fact, one can easily show from Eqs. (4.130) and (4.132), that v_a and v_p obey the following conservation law at Newtonian order:

$$V_{\rm N}(-e_t)\langle\dot{v}_p\rangle - V_{\rm N}(e_t)\langle\dot{v}_a\rangle = 0\,. \qquad (4.137)$$

To further display this behavior, we plot the streamlines of $(\langle\dot{v}_p\rangle, \langle\dot{e}_t\rangle)$[1] at Newtonian order in Fig 4.2 and at 1PN order in Fig. 4.3. Notice that in both plots, systems with values of (v_p, e_t) above the critical value of the eccentricity, which is represented by the dashed line in Fig. 4.2 and the dotted line in Fig. 4.3, display the pericenter braking behavior that appears in the burst model. On the other hand, the pericenter velocity for systems below the critical eccentricity is always increasing.

This pericenter braking behavior is not a property of the burst model *per se*, but rather it is inherited from the PN radiation-reaction equations. One may worry that this pericenter braking behavior may disappear if treating the problem exactly (for example, through a numerical treatment). The right panel of Fig. 4.3, however, shows a zoom of the streamlines at small velocities, where we see that the braking behavior persists. We thus conclude that it is unlikely that pericenter braking is an artifact of the PN expansion.

Figure (4.3) also allows us to compare the critical eccentricity computed at Newtonian order, at 1PN order and numerically. The latter is obtained by solving the 1PN expression for $\langle\dot{v}_p(e_t)\rangle = 0$ to find $e_{t,\text{crit}}$. As expected, the numerical inversion disagrees with the 1PN expansion at high velocities. We notice, however, that the 1PN expression is closer to the numerical inversion than the Newtonian expression is. If the numerical inversion is correct, then this implies the 1PN expansion of $e_{t,\text{crit}}$ given in Eqs. (4.135)-(4.136) has a larger regime of validity than its Newtonian counterpart.

Finally, it is important to note that while the pericenter velocity has this unique behavior, the GW frequency and the PN parameter x are both monotonically increasing, and the time eccentricity is monotonically decreasing, throughout the inspiral of the binary. In the circular case, there is a one-to-one mapping between the

---

[1] We have rescaled the values of $\langle\dot{v}_p\rangle$ and $\langle\dot{e}_t\rangle$ in these plots to exemplify the behavior of the streamlines. This does not changes the results of this section.

orbital velocity and the GW frequency, and since the orbital velocity is a monotonic function, so is the frequency. For generic eccentric inspirals, the frequency depends on both the pericenter velocity (or alternatively x) and the time eccentricity in such a way that it is also monotonic.

Discussion

We have constructed a generic PN order burst model. This model is characterized by four amplitude vector fields $(\vec{P}, \vec{R}, \vec{\mathcal{V}}, \vec{\mathcal{D}})$, which depend on the orbital period, pericenter distance, and rates of change of pericenter velocity and orbital eccentricity, respectively. While these quantities are not typically reported within the literature, they can be easily calculated from the quantities that are. Thus, the formalism presented here provides a formulaic means of generating burst models to any PN order. We have then applied this formalism to calculate the burst model out to the current limit to which we can compute PN quantities for eccentric binaries, i.e. 3PN order.

One direction of future research is to relax some of the assumptions used to develop this formalism. For example, we have approximated the compact objects as non-spinning point particles, which is appropriate if we are considering non-spinning BHs. However, BHs in the universe are generally considered to be spinning, while on the other hand, NSs are not well approximated by point particles. NSs will typically have small spins, however the inclusion of finite size effects and tidal perturbations would be necessary to effectively model highly eccentric NS binaries. Further, if one of the binary components is a BH, then not all of the GW power travels to spatial infinity. Instead, some of the GWs travel through the horizon of the BH, increasing its mass and spin throughout the evolution of the binary. With these considerations, we can postulate that the generic PN formalism can be extended to include such effects by writing

$$\vec{A} = \vec{A}_{\rm PP} + \vec{A}_{\rm Spin} + \vec{A}_{\rm FS} + \vec{A}_{\rm H} + \vec{A}_{\rm ppE}\,, \tag{4.138}$$

where $\vec{A} \in (\vec{P}, \vec{R}, \vec{\mathcal{V}}, \vec{\mathcal{D}})$. In the above, $\vec{A}_{\rm PP}$ represents the point particle terms, computed here to 3PN order, $\vec{A}_{\rm Spin}$ are the corrections generated by the spins of the compact objects, $\vec{A}_{\rm FS}$ are generated by finite size effects of NSs, and $\vec{A}_{\rm H}$ incorporates the corrections from the GWs fluxes through BH horizons. The final term, $\vec{A}_{\rm ppE}$ represents corrections due to modified theories of gravity [108], which we consider in the next chapter.

One important question to address in the future concerns the most appropriate equations one should use to obtain the numerical evolution of highly elliptic systems under radiation reaction. In this work, we have used the orbit averaged equations for $\langle \dot{e}_t \rangle$ and $\langle \dot{x} \rangle$. These equations are applicable when the GW emission is smeared over the entire orbit and changes to the orbital elements are small on the timescale of one orbit, as is the case in quasi-circular inspirals. However, for the highly eccentric binaries considered here, the GW emission is concentrated at pericenter passage, and changes to the orbital elements happen on timescales significantly shorter than the orbital period. The evolution of such binaries will resemble a set of discrete steps from one orbit to the next. Furthermore, it can be shown that when expressed in terms of variables that are finite in the parabolic limit, the orbit averaged fluxes of energy and angular momentum vanish for parabolic orbits. There is, of course, nothing special about the parabolic limit, and binaries on parabolic orbits will still emit GWs, which suggests a break down of the orbit-averaged formalism in this limit. Since the orbit averaged equations are currently used prolifically in the literature, it is important to determine how big of a deviation in observables is generated by considering evolutions with and without orbit-averaging in the radiation-reaction force, and what set of systems in (f_{GW}, e_t) space are affected by this deviation. Such a study is currently underway [102].

Another avenue for future research is to consider how the 3PN order burst model aids in detecting highly elliptic binaries. In such a study, one would inject a waveform generated by numerically evolving the binary under radiation reaction into a simulated LIGO data stream. One could then perform an analysis to study whether the prior, specifically the burst model, is sufficient to achieve detection of such a signal given a particular noise model. One could also investigate the nature of posterior probability densities of recovered parameters and determine if such a search is accurate enough to perform parameter estimation on actual signals. With such a study completed, a follow up study could be conducted to investigate the search strategy's ability to estimate deviations from the current model, such as those from modified theories of gravity and to constrain the coupling constants of such theories. Such studies will be crucial for understanding our ability to detect and perform important astrophysics with eccentric GW signals.

PARAMETERIZED POST-EINSTEINIAN FRAMEWORK FOR GRAVITATIONAL WAVE BURSTS

The recent detections of GWs by aLIGO and aVIRGO have opened the door to testing the dynamical and non-linear, strong-field regime of General Relativity (GR) [165, 178, 181]. One characterization of this regime is a scenario where a source of large spacetime curvature experiences sufficiently rapid acceleration (as measured by a distant inertial observer) to produce gravitational wave (GW) emission approaching the Planck luminosity $L_p = c^5/G$.

Vacuum GR has no intrinsic scale, so one could argue that there is nothing particularly relevant about L_p compared to any other unit-luminosity in some other system of units. However, if one considers a particular GW emission process with an energy scale $E = Mc^2$ (here M is the total rest mass of the binary) occurring within a region of size R (here, the binary diameter), arguments based on the Hoop Conjecture [153] suggest this can only exceed L_p if cosmic censorship is violated. Thus, in GR L_p is a natural scale to expect the most radical phenomena of the theory to occur. The most luminous GW sources currently observed, the final stages of the merger of two black holes, reach luminosities of $\sim 10^{-2} L_p$.

High-eccentricity mergers may be ideal for testing GR in the dynamical strong field regime, as, other parameters in the system being equal the peak GW luminosity achieved in these systems is typically higher than in a quasi-circular inspiral. Furthermore, although the integrated power radiated is comparable, more of it comes from the high-luminosity regime in eccentric mergers—see for example Fig. 5.1. The goal of this chapter is to lay a theoretical foundation to quantitatively address how well highly eccentric binaries can constrain strong-field gravity.

Using GW observations of compact binary mergers, eccentric or not, to test GR

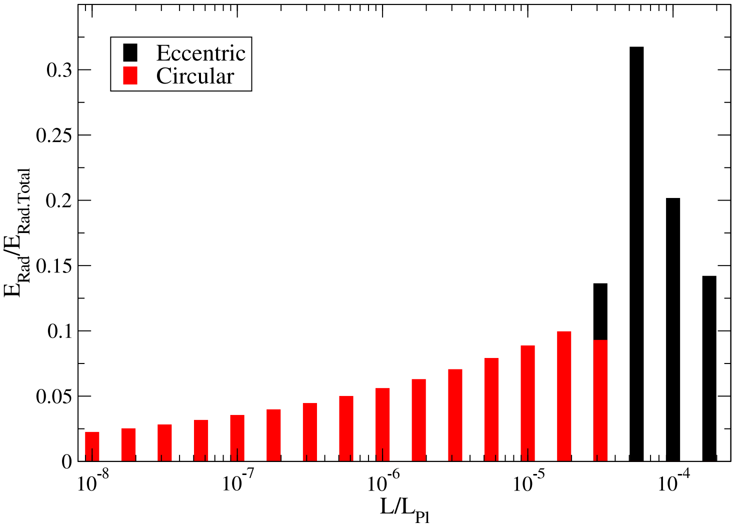

Figure 5.1: Histogram illustrating the fraction of GW energy radiated as a function of the GW luminosity in Planck units for an eccentric (black) and a quasicircular (red) inspiral, computed using the Newtonian orbit plus quadrupole emission model discussed in the text. The eccentric inspiral starts at an initial pericenter of $8M$ and eccentricity of 0.99. The quasicircular inspiral starts at a separation of $800M$, corresponding to the same initial semi-major axis as the eccentric inspiral. Both orbits are terminated at the innermost stable orbit at pericenter distance $r_p = (3 + e_f)/(1 + e_f)2M$, with e_f the "final" eccentricity before plunge. We have thus left out the GW energy emitted during plunge, merger and ringdown, which in both cases would contribute to the energy at luminosities of order 10^{-3} to $10^{-2} L_p$. Observe that while the quasi-circular inspiral emits radiation at all luminosities below this, the eccentric inspiral does not emit energy below $10^{-5} L_p$ for the system considered, concentrating all its power at higher luminosities.

or search for deviations from its predictions is not a straightforward endeavor. One of the problems lies with the reliance on theoretical templates of expected events to go beyond mere detection and infer properties of the source. Any aspect of a detected source not reflected in the template bank, whether due to modeling deficiencies within GR, or problems with the theory itself, will lead to a misidentification of the source as the best-fit member of the template bank, and by inference the theory used to construct it.

This problem of *fundamental theoretical bias* in the GW detection endeavor was the motivation for the development of the parameterized post-Einsteinian (ppE) framework [177]. The basic idea is to begin with a class of sources (quasi-circular, compact binary inspirals in the case of [177]) for which there is decent evidence that GR predictions are sufficiently accurate for some fraction of events to still be detected with GR templates. Then, one considers a set of "well-motivated" plausible alterations to the theory—additional energy emission channels, GW polarizations, new conservative terms that appear at high v/c in an effective Hamiltonian description, examples from specific alternative theories, etc.—and how these alterations imprint on the eventual observable (the response function in the case of [177]). Following this exercise, one proposes a parameterized set of deformations of the baseline GR observable, that capture the particular case studies considered for specific values of the parameters, and reduce to the GR result in the appropriate limit. After a putative detection of a source with GR templates, a follow-up study with ppE templates could then be performed to either *quantify* the consistency of the event with GR as the underlying theory, or give evidence for a correction to GR. Several studies have since illustrated the efficacy of this approach (see e.g. [63, 137, 138, 181]).

We here adapt the ppE framework to highly-eccentric binaries, assuming a power-stacking detection strategy. We follow the same procedure as that outlined above for the original, quasi-circular ppE framework, with the key difference that the observable is now the set of parameters characterizing the burst sequence. As we detailed in Ch. 4, each burst can be described by four numbers that specify the center, width and height of a tile in the time-frequency plane, capturing a desired fraction of the energy of the burst. In GR, the sequence of bursts is uniquely characterized by the small set of parameters describing the "initial conditions" of the binary; to leading, *Newtonian* order in a weak field expansion, these are the symmetric mass ratio η, the total mass M, the pericenter of the first encounter $r_{p,0}$, and the initial orbital eccentricity e_0.

A ppE burst-sequence for a given event is a parameterized deformation of the GR burst sequence. Naïvely, this would require a ppE parameter for each of the $4N$ parameters of an N-burst sequence. However, as with the original ppE, we restrict the class of deviations to those that are well-motivated in the sense described previously. Using a simplified model of the GR sequence to allow for an analytic study, we show that only 8 ppE parameters suffice to capture a wide class of deformations. Physically, these parameters correspond to deformations in the binary's binding energy and angular momentum (i.e. the conservative sector) and their rate of change (i.e. the dissipative sector). We then postulate that this ppE deformation can be applied to an arbitrarily accurate baseline GR burst sequence model.

To be more concrete, we propose the following *burst algorithm*, the first key ingredient of which describes the properties of the GW emission coming from the i^{th} burst in the sequence:

$$t_i^{\rm ppE} = t_{i-1} + \Delta t_{i,i-1}^{\rm GR}(r_{p,i}, e_i) \left[1 + \alpha_{\rm ppE} \left(\frac{M}{r_{p,i}}\right)^{\bar{a}_{\rm ppE}}\right] , \tag{5.1}$$

$$f_i^{\rm ppE} = f_i^{\rm GR}(r_{p,i}, e_i) \left[1 + \beta_{\rm ppE} \left(\frac{M}{r_{p,i}}\right)^{\bar{b}_{\rm ppE}}\right] , \tag{5.2}$$

$$\delta t_i^{\rm ppE} = \delta t_i^{\rm GR}(r_{p,i}, e_i) \left[1 - \beta_{\rm ppE} \left(\frac{M}{r_{p,i}}\right)^{\bar{b}_{\rm ppE}}\right] , \tag{5.3}$$

$$\delta f_i^{\rm ppE} = \delta f_i^{\rm GR}(r_{p,i}, e_i) \left[1 + \beta_{\rm ppE} \left(\frac{M}{r_{p,i}}\right)^{\bar{b}_{\rm ppE}}\right] . \tag{5.4}$$

Here $(\alpha_{\rm ppE}, \beta_{\rm ppE})$ are ppE amplitude parameters, and $(\bar{a}_{\rm ppE}, \bar{b}_{\rm ppE})$ are ppE exponent parameters. Equations (5.1)-(5.4) describe the centroid (t_i, f_i) and width $(\delta t_i, \delta f_i)$ of the i^{th} tile in time and frequency. The quantities with the GR superscripts denote the pure GR values in the limit $(\alpha_{\rm ppE}, \beta_{\rm ppE}) = (0, 0)$, and $\Delta t_{i,i-1}^{\rm GR}(r_{p,i}, e_i)$ is the function giving the period of the orbit preceding the i^{th} burst in GR (see e.g. Eqs. (4.21), (4.27), and (4.30)-(4.31)).

The GR functions and ppE corrections in Eqs. (5.1)-(5.4) depend on the pericenter distance $r_{p,i}$ and eccentricity e_i of the corresponding orbit, however the orbit changes from one burst to the next. Thus the second key ingredient to the burst algorithm describes the mapping from the $(i-1)^{th}$ to the i^{th} orbit:

$$\frac{r_{p,i}^{\rm ppE}(r_{p,i-1}, e_{i-1})}{r_{p,i}^{\rm GR}(r_{p,i-1}, e_{i-1})} = 1 + \gamma_{\rm ppE} \left(\frac{M}{r_{p,i-1}}\right)^{\bar{c}_{\rm ppE}} , \tag{5.5}$$

$$\frac{\Delta\delta e_{i,i-1}^{\rm ppE}(r_{p,i-1}, e_{i-1})}{\Delta\delta e_{i,i-1}^{\rm GR}(r_{p,i-1}, e_{i-1})} = 1 + \delta_{\rm ppE} \left(\frac{M}{r_{p,i-1}}\right)^{\bar{d}_{\rm ppE}} . \tag{5.6}$$

Here $(\gamma_{\rm ppE}, \delta_{\rm ppE})$ are ppE amplitude parameters, and $(\bar{c}_{\rm ppE}, \bar{d}_{\rm ppE})$ are ppE exponent parameters, and we have defined $\Delta\delta e_{i,i-1} = e_{i-1} - e_i$. As before, the quantities with a GR superscript represent the mappings in GR.

We only need 4 ppE amplitude parameters and 4 ppE exponent parameters to characterize deformations to eccentric bursts. The number of parameters makes sense, since such dynamical encounters are really controlled by only 4 quantities to leading-order in a weak-field expansion: the binding energy, the orbital angular momentum, the energy flux and the angular momentum flux. Deforming each of these relations through polynomials of the form $\epsilon_i\ (M/r_p)^{e_i}$, for amplitude coefficients ϵ_i and exponent coefficient e_i, then leads to deformations to the GR burst sequence that can only depend on 4+4 parameters. We also here calculate how the ppE parameters of the burst sequence map to deformations to the binding energy, angular momentum and fluxes, i.e. how $(\alpha_{\rm ppE}, \beta_{\rm ppE}, \gamma_{\rm ppE}, \delta_{\rm ppE})$ and $(\bar{a}_{\rm ppE}, \bar{b}_{\rm ppE}, \bar{c}_{\rm ppE}, \bar{d}_{\rm ppE})$ map to $(\epsilon_1, \epsilon_2, \epsilon_3, \epsilon_4)$ and (e_1, e_2, e_3, e_4).

Finally, we investigate two specific modified theories of gravity, develop burst algorithms for them and determine whether they can be mapped to the above ppE framework. In particular, we consider massless, Brans-Dicke (BD) theory [52, 164] and Einstein-Dilaton-Gauss-Bonnet (EDGB) theory [170, 179]. Both of these modify the Einstein-Hilbert action through a dynamical scalar field, sourced by the matter stress-energy tensor and by a certain combination of quadratic curvature invariants respectively. Both of them lead to dipolar GW emission, which we calculate here for the first time for non-spinning, eccentric inspirals. Such emission leads to a modified burst algorithm, which we prove explicitly maps to the ppE deformations proposed above.

Kepler Problem in the ppE Formalism

To begin, it is useful to consider the two body problem in modified theories of gravity. Since we are interested in a ppE formalism for GW bursts, we will consider parametrized deformations away from Newtonian gravity for simplicity, and assume the orbits are Keplerian. For equatorial orbits, the corrections to the Newtonian kinetic energy and gravitational potential within a modified theory of gravity may be written as

$$\delta T = \frac{1}{2}\mu \left[r^2 \dot{\phi}^2 \tilde{\beta} \left(\frac{M}{r} \right)^{\tilde{b}} + \dot{r}^2 \tilde{\gamma} \left(\frac{M}{r} \right)^{\tilde{c}} \right] , \tag{5.7}$$

$$\delta U = -\frac{\mu M}{r} \left[\tilde{\alpha} \left(\frac{M}{r} \right)^{\tilde{a}} \right] , \tag{5.8}$$

where μ is the reduced mass of the binary, $(\tilde{\alpha}, \tilde{\beta}, \tilde{\gamma})$ are amplitude parameters that depend on the coupling constants of the theory, and $(\tilde{a}, \tilde{b}, \tilde{c}) \in \mathbb{R}$ that control the post-Newtonian (PN) order of the modifications. With this potential, we now compute the corrections to orbital quantities necessary to construct the ppE burst model, namely the orbital energy, angular momentum, period, and pericenter velocity.

The modifications introduced above are reasonable when one is searching for strong-field modifications to GR in the following sense. They must be proportional to a variable that is small in the weak-field to be consistent with existing observations, yet large in the strong-field to offer a chance to be detectable with GW observations. A natural choice is the characteristic velocity of the system during emission, which for an eccentric inspiral occurs at pericenter and is inversely proportional to the pericenter radius. In fact, as we show in later, the above deformations capture the leading order effects from certain modified gravity theories.

Let us begin by considering the Lagrangian for the binary within an effective one-body formalism. At leading (Newtonian) PN order, the Lagrangian for equatorial orbits may be written as $\mathcal{L} = T - U$, with $T = (1/2)\mu(\dot{r}^2 + r^2\dot{\phi}^2) + \delta T$ and $U = -\mu M/r + \delta U$. This Lagrangian admits two conserved quantities associated with stationarity and axisymmetry, specifically

$$E = \frac{1}{2}\mu \dot{r}^2 \left[1 + \tilde{\gamma} \left(\frac{M}{r} \right)^{\tilde{c}} \right] + \frac{L^2}{2\mu r^2} \left[1 - \tilde{\beta} \left(\frac{M}{r} \right)^{\tilde{b}} \right]$$

$$- \frac{\mu M}{r}\left[1+\tilde{\alpha}\left(\frac{M}{r}\right)^{\tilde{a}}\right], \tag{5.9}$$

$$L = \mu r^2 \dot{\phi}\left[1+\tilde{\beta}\left(\frac{M}{r}\right)^{\tilde{b}}\right], \tag{5.10}$$

which we identify as the orbital energy and angular momentum. By studying the turning points ($\dot{r}=0$) of Eq. (5.9), and writing $E = E_{\rm N} + \delta E$ and $L = L_{\rm N} + \delta L$, we find

$$\frac{\delta E}{E_{\rm N}} = -\frac{1}{2}\tilde{\alpha}\left(\frac{M}{r_p}\right)^{\tilde{a}} \mathcal{G}(e;\tilde{a},0,1) - \frac{1}{4}\tilde{\beta}\left(\frac{M}{r_p}\right)^{\tilde{b}} \mathcal{G}(e;\tilde{b},1,1), \tag{5.11}$$

$$\frac{\delta L}{L_{\rm N}} = \frac{1}{4}\tilde{\alpha}\left(\frac{M}{r_p}\right)^{\tilde{a}} \mathcal{G}(e;\tilde{a},1,0) + \frac{1}{8}\tilde{\beta}\left(\frac{M}{r_p}\right)^{\tilde{b}} \mathcal{G}(e;\tilde{b},2,0), \tag{5.12}$$

with the Newtonian energy and angular momentum $(E_{\rm N}, L_{\rm N})$ given in Eqs. (5.2) and (5.3) in [129], and

$$\mathcal{G}(e;q,m,n) = \frac{(1+e)^m(1-e)^n}{e}\left[1-\left(\frac{1-e}{1+e}\right)^{q+m-n}\right]. \tag{5.13}$$

Now, let us consider the orbital period within our ppE formalism. In order to do this, it is useful to parametrize the radius of the orbit as

$$r = \frac{p}{1+e\,\cos\psi}, \tag{5.14}$$

where $p = r_p(1+e)$ is the semi-latus rectum of the orbit and ψ increases monotonically by 2π from one pericenter passage to the next. The reason for this parametrization is that, in general, any deformation to the Newtonian potential will cause the orbits to precess [97], and as a result, the orbit will return to pericenter when $\phi = 2\pi + \mathcal{O}(M/r_p)$. Using ψ to parameterize the orbit allows us to avoid complications from precession when computing integrals of the orbital dynamics.

To obtain the evolution equation for ψ, we insert the radial function of Eq. (5.14) into Eq. (5.9) and solve for $\dot{\psi}$. The orbital period can then be computed by integrating $\dot{\psi}^{-1}$ between pericenter passages. Following this procedure, we obtain $T_{\rm orb} = T_{\rm orb}^{\rm N} + \delta T_{\rm orb}$, where $T_{\rm orb}^{\rm N}$ is given by Eq. (16) in [108] and

$$\begin{aligned}\frac{\delta T_{\rm orb}}{T_{\rm orb}^{\rm N}} &= \frac{1}{8\pi}\tilde{\alpha}\left(\frac{M}{r_p}\right)^{\tilde{a}}\mathcal{P}_1(e;\tilde{a},1) + \frac{1}{16\pi}\tilde{\beta}\left(\frac{M}{r_p}\right)^{\tilde{b}}\mathcal{P}_1(e;\tilde{b},2)\\ &+ \frac{1}{4\pi}\tilde{\gamma}\left(\frac{M}{r_p}\right)^{\tilde{c}}\mathcal{P}_2(e)\,, \qquad (5.15)\end{aligned}$$

with

$$\begin{aligned}\mathcal{P}_1(e;p,n) &= \frac{(1-e^2)^{3/2}}{e^2(1+e)^p}\int_0^{2\pi}\frac{d\psi}{s^2\left(1+e\ c\right)^2}\\ &\times\left[(1-e)^{p+n}(1-c)(2+e+e\ c)\right.\\ &+(1+e)^{p+n}(1+c)(2-e+e\ c)\\ &\left.-4\left(1+e\ c\right)^{p+n}\right]\,, \qquad (5.16)\\ \mathcal{P}_2(e) &= \frac{(1-e^2)^{3/2}}{(1+e)^{\tilde{c}}}\int_0^{2\pi} d\psi(1+e\ c)^{\tilde{c}-2}\,, \qquad (5.17)\end{aligned}$$

and $(c,s) = (\cos\psi, \sin\psi)$.

Finally, consider the pericenter velocity. Pericenter corresponds to one of two points with $\dot{r} = 0$, so the velocity at this point is given by $v_p = r\dot{\phi}$ evaluated at $\psi = 2n\pi$, where $n \in \mathbb{Z}$. Evaluating this, we find $v_p = v_p^{\rm N} + \delta v_p$, where $v_p^{\rm N} = [M(1+e)/r_p]^{1/2}$, and

$$\frac{\delta v_p}{v_p^{\rm N}} = \frac{1}{4}\tilde{\alpha}\left(\frac{M}{r_p}\right)^{\tilde{a}}\mathcal{V}_\alpha(e) - \frac{1}{8}\tilde{\beta}\left(\frac{M}{r_p}\right)^{\tilde{b}}\mathcal{V}_\beta(e)\,, \qquad (5.18)$$

with

$$\mathcal{V}_\alpha(e) = 1 + \left(\frac{1-e}{1+e}\right)^{\tilde{a}} + \frac{1}{e}\left[1 - \left(\frac{1-e}{1+e}\right)^{\tilde{a}}\right], \tag{5.19}$$

$$\mathcal{V}_\beta(e) = 4 + \left[2 - \left(\frac{1+e^2}{e}\right)\right]\left[1 - \left(\frac{1-e}{1+e}\right)^{\tilde{b}}\right]. \tag{5.20}$$

This completes the calculation of the necessary orbital quantities for a burst model in the ppE formalism.

Modeling Beyond GR

In this section, we use the Newtonian order GR burst algorithm developed in Ch. 4 to construct a ppE generalization. We consider model-independent deformations of GR that lead to modifications to the conservative dynamics of the form

$$E = E_{\rm GR}\left[1 + \alpha\left(\frac{M}{r_p}\right)^{\bar{a}}\right], \tag{5.21}$$

$$L = L_{\rm GR}\left[1 + \beta\left(\frac{M}{r_p}\right)^{\bar{b}}\right], \tag{5.22}$$

and modifications to the dissipative dynamics of the form

$$\dot{E} = \dot{E}_{\rm GR}\left[1 + \gamma\left(\frac{M}{r_p}\right)^{\bar{c}}\right], \tag{5.23}$$

$$\dot{L} = \dot{L}_{\rm GR}\left[1 + \delta\left(\frac{M}{r_p}\right)^{\bar{d}}\right], \tag{5.24}$$

where $(E_{\rm GR}, L_{\rm GR})$ are the GR orbital energy and angular momentum, while $(\dot{E}_{\rm GR}, \dot{L}_{\rm GR})$ are the GR orbital energy and angular momentum flux. We may map from the new parameters $(\alpha, \beta, \bar{a}, \bar{b})$ to the old parameters $(\tilde{\alpha}, \tilde{\beta}, \tilde{a}, \tilde{b})$ via

$$\alpha \left(\frac{M}{r_p}\right)^{\bar{a}} \to \text{LO}\left[\frac{\delta E}{E_{\text{N}}}\right] , \qquad \beta \left(\frac{M}{r_p}\right)^{\bar{b}} \to \text{LO}\left[\frac{\delta L}{L_{\text{N}}}\right] ,$$
$$-\frac{\mu M}{2a} \to E_{\text{GR}} , \qquad \mu\sqrt{Ma(1-e^2)} \to L_{\text{GR}} , \tag{5.25}$$

where $\delta E/E_{\text{N}}$ and $\delta L/L_{\text{N}}$ are given in Eqs. (5.11) and (5.12), respectively.

The post-Einsteinian corrections are parameterized by the amplitude coefficients $\delta\lambda^a \equiv (\alpha, \beta, \gamma, \delta) \in \Re$ and the exponent coefficients $\delta\ell^a \equiv (\bar{a}, \bar{b}, \bar{c}, \bar{d}) \in \mathbb{Q}$. In principle, the vector $\delta\lambda^a$ need not be constant, and in fact, it may be a function of other orbital parameters, such as the eccentricity or spin. Nonetheless, if we focus only on small GR deformations, and on orbits that are highly-eccentric, then $\delta\lambda^a$ will be a constant dependent only on the coupling parameters of the theory; we will work here to first-order in $\delta\lambda^a$. On the other hand, $\delta\ell^a$ can have any magnitude, except that $(\bar{a}, \bar{b}) > 0$ if the GR corrections are to lead to well-behaved observables in the weak-field. If this were not the case, then the spacetime that generates such corrections would not be asymptotically flat. The subset $(\bar{c}, \bar{d})$ can be less than zero, as is the case in theories of gravity with dipolar radiation.

One could parameterize GR deviations with a different functional basis, such as natural logarithms, but a power-law basis is perhaps more natural, unless screening is present. In the next subsection, we will investigate how these parameterized post-Einsteinian corrections modify our burst algorithm; most of this analysis will closely follow the work presented in Ch. 4.

Size of Tiles

The first ingredient of the algorithm is the size of the tiles, which is given by the characteristic GW time, $\tau_{\text{GW}}^{\text{ppE}}$, defined in Eq. (4.24). In a modified gravity theory, however, the periastron velocity is not the same function of (r_p, e) as in GR, because of the modification to the binding energy in Eq. (5.21). The corrected expression for the pericenter velocity is given in Eq. (5.18), which then leads to

$$\tau_{\rm GW}^{\rm ppE} = \frac{r_p^{3/2}}{\sqrt{M(1+e)}}\left[1 - \frac{\delta v_p}{v_{p,{\rm N}}}\right] . \tag{5.26}$$

The characteristic GW frequency, $f_{\rm GW}^{\rm ppE}$, then follows straightforwardly from Eq. (4.23).

The next step is to find the dimensions of the tiles. Using the same notation as in Ch. 4, we easily find

$$\delta t^{\rm ppE} = \delta t^{\rm GR}\left[1 - \frac{\delta v_p}{v_{p,{\rm N}}}\right] , \tag{5.27}$$

$$\delta f^{\rm ppE} = \delta f^{\rm GR}\left[1 + \frac{\delta v_p}{v_{p,{\rm N}}}\right] , \tag{5.28}$$

where $\delta t^{\rm GR}$ and $\delta f^{\rm GR}$ are given by Eqs. (4.30) and (4.31) respectively.

Mapping Between Tiles

We now seek to determine how the mapping between tiles is modified in our ppE model. Just as in GR, we need to determine how the orbital quantities map from one burst to the next: $(r_{p,i}, e_i) \to (r_{p,i+1}, e_{i+1})$. Let us begin by mapping the ppE deformations of the energy and angular momentum to the pericenter distance and eccentricity. Using the leading, Newtonian order expressions for $E_{\rm GR}$ and $L_{\rm GR}$ in a weak-field expansion, we find

$$\begin{aligned} r_p^{\rm ppE} = {} & \frac{M}{2\mathcal{E}}\left(1 - \sqrt{1-2\mathcal{E}\mathcal{L}^2}\right) \\ & \times \left[1 - \frac{1 - \mathcal{E}\mathcal{L}^2 - \sqrt{1-2\mathcal{E}\mathcal{L}^2}}{(1-\sqrt{1-2\mathcal{E}\mathcal{L}^2})\sqrt{1-2\mathcal{E}\mathcal{L}^2}}\alpha\left(\frac{M}{r_p}\right)^{\bar{a}}\right. \\ & \left. - \frac{2\mathcal{E}\mathcal{L}^2}{(1-\sqrt{1-2\mathcal{E}\mathcal{L}^2})\sqrt{1-2\mathcal{E}\mathcal{L}^2}}\beta\left(\frac{M}{r_p}\right)^{\bar{b}}\right. \end{aligned}$$

$$+\mathcal{O}(\delta\lambda^a\delta\lambda_a)\Bigg]\,, \tag{5.29}$$

$$e = \sqrt{1-2\mathcal{E}\mathcal{L}^2}\left\{1 + \frac{\mathcal{E}\mathcal{L}^2}{1-2\mathcal{E}\mathcal{L}^2}\right.$$

$$\left.\times\left[\alpha\left(\frac{M}{r_p}\right)^{\bar{a}} + 2\beta\left(\frac{M}{r_p}\right)^{\bar{b}} + \mathcal{O}(\delta\lambda^a\delta\lambda_a)\right]\right\}\,, \tag{5.30}$$

where $\mathcal{E} = -E/\mu$ and $\mathcal{L} = L/M^2$.

The next step is to find how the energy and angular momentum evolve from one burst to the next. We prescribe this evolution through the perturbative algorithm described above Eq. (4.16). The ppE corrected energy and angular momentum flux are given in Eqs. (5.23) and (5.24) respectively, where we take $\dot{E}_{\rm GR}$ and $\dot{L}_{\rm GR}$ to leading, Newtonian order. We can then insert these expressions in Eqs. (5.29) and (5.30) and linearize in $\delta\lambda^a$ and δe_{i-1} to find

$$r_{p,i}^{\rm ppE}(r_{p,i-1},e_{i-1}) =$$

$$r_{p,i-1}\left\{1 - \frac{59\sqrt{2}\pi}{24}\eta\left(\frac{M}{r_{p,i-1}}\right)^{5/2}\left[1 + \frac{26}{59}\alpha\left(\frac{M}{r_{p,i-1}}\right)^{\bar{a}} - \frac{144}{59}\beta\left(\frac{M}{r_{p,i-1}}\right)^{\bar{b}}\right.\right.$$

$$\left.-\frac{85}{59}\gamma\left(\frac{M}{r_{p,i-1}}\right)^{\bar{c}} + \frac{144}{59}\delta\left(\frac{M}{r_{p,i-1}}\right)^{\bar{d}}\right] - \frac{121\sqrt{2}\pi}{96}\eta\left(\frac{M}{r_{p,i-1}}\right)^{5/2}\delta e_{i-1}$$

$$\times\left[1 + \frac{1142}{605}\alpha\left(\frac{M}{r_{p,i-1}}\right)^{\bar{a}} - \frac{2352}{605}\beta\left(\frac{M}{r_{p,i-1}}\right)^{\bar{b}} - \frac{1747}{605}\gamma\left(\frac{M}{r_{p,i-1}}\right)^{\bar{c}}\right.$$

$$\left.\left.+\frac{2352}{605}\delta\left(\frac{M}{r_{p,i-1}}\right)^{\bar{d}}\right] + \mathcal{O}\left[\left(\frac{M}{r_{p,i-1}}\right)^{\delta\ell^a+7/2}, \delta e_{i-1}^2, \delta\lambda^a\delta\lambda_a\right]\right\}\,, \tag{5.31}$$

$$\Delta\delta e_{i,i-1}^{\rm ppE}(r_{p,i-1},e_{i-1}) = \frac{85\sqrt{2}\pi}{12}\eta\left(\frac{M}{r_{p,i-1}}\right)^{5/2}\left[1 - 2\alpha\left(\frac{M}{r_{p,i-1}}\right)^{\bar{a}} + \gamma\left(\frac{M}{r_{p,i-1}}\right)^{\bar{c}}\right]$$

$$-\frac{181\sqrt{2}\pi}{80}\eta\left(\frac{M}{r_{p,i-1}}\right)^{5/2}\left[1 + \frac{118}{181}\alpha\left(\frac{M}{r_{p,i-1}}\right)^{\bar{a}} - \frac{480}{181}\beta\left(\frac{M}{r_{p,i-1}}\right)^{\bar{b}}\right.$$

$$\left.-\frac{299}{181}\gamma\left(\frac{M}{r_{p,i-1}}\right)^{\bar{c}} + \frac{480}{181}\delta\left(\frac{M}{r_{p,i-1}}\right)^{\bar{d}}\right]\delta e_{i-1}$$

$$+\,\mathcal{O}\left[\left(\frac{M}{r_{p,i-1}}\right)^{\delta\ell^a+7/2}, \delta e_{i-1}^2, \delta\lambda^a\delta\lambda_a\right]\,, \tag{5.32}$$

where we have defined $\Delta\delta e_{i,i-1}^{\rm ppE} = \delta e_i^{\rm ppE} - \delta e_{i-1}$.

As before, we can now construct the mapping between tiles. By combining the above results, we find

$$t_i^{\rm ppE} = t_{i-1} + \Delta t_{i,i-1}^{\rm GR}(r_{p,i}, e_i)\left[1 + \frac{\delta T_{\rm orb}(r_{p,i}, \delta e_i)}{T_{\rm orb}^{\rm N}(r_{p,i}, \delta e_i)} + \mathcal{O}\left(\delta\lambda_a\delta\lambda^a\right)\right]\,, \tag{5.33}$$

$$f_i^{\rm ppE} = f_i^{\rm GR}(r_{p,i}, e_i)\left[1 + \frac{\delta v_p(r_{p,i}, e_i)}{v_p^{\rm N}(r_{p,i}, e_i)} + \mathcal{O}\left(\delta\lambda_a\delta\lambda^a\right)\right]\,, \tag{5.34}$$

$$\delta t_i^{\rm ppE} = \delta t_i^{\rm GR}(r_{p,i}, e_i)\left[1 - \frac{\delta v_p(r_{p,i}, e_i)}{v_p^{\rm N}(r_{p,i}, e_i)} + \mathcal{O}\left(\delta\lambda_a\delta\lambda^a\right)\right]\,, \tag{5.35}$$

$$\delta f_i^{\rm ppE} = \delta f_i^{\rm GR}(r_{p,i}, e_i)\left[1 + \frac{\delta v_p(r_{p,i}, e_i)}{v_p^{\rm N}(r_{p,i}, e_i)} + \mathcal{O}\left(\delta\lambda_a\delta\lambda^a\right)\right]\,, \tag{5.36}$$

where $\Delta t_{i,i-1}^{\rm GR}$, $f_i^{\rm GR}$, $\delta t_i^{\rm GR}$ and $f_i^{\rm GR}$ are the GR mappings of Eqs. (4.21), (4.27), and (4.30)-(4.31), respectively. Recall that these quantities are all implicit functions of $(r_{p,i-1}, e_{i-1})$, with the mapping $(r_{p,i}, e_i) \to (r_{p,i-1}, e_{i-1})$ given in Eqs. (5.31) and (5.32). The time to the next burst is obtained by using the ppE-modified orbital period in Eq. (5.33). The frequency to the next burst is given by the inverse of the ppE-modified GW characteristic time in Eq. (5.26), while the size of the burst windows in time-frequency space is given in Eqs. (5.27) and (5.28).

A Parameterized-Post Einsteinian Burst Framework

The previous subsection inspires the ppE burst algorithm presented in Eqs. (5.1)-(5.6), where we have redefined the ppE amplitude and exponent coefficients. Notice that we only need two sets of parameters in Eqs. (5.1)-(5.4), $(\alpha_{\rm ppE}, \bar{a}_{\rm ppE})$ and $(\beta_{\rm ppE}, \bar{b}_{\rm ppE})$, since the frequency of the next burst, the temporal and the frequency sizes of the burst window are all controlled by a single quantity, the characteristic time $\tau_{\rm GW}$.

The amplitude parameters $(\alpha_{\rm ppE}, \beta_{\rm ppE}, \gamma_{\rm ppE}, \delta_{\rm ppE})$ are, in principle, not only functions of the coupling constants of the theory, but also functions of the eccentricity of the i^{th} orbit. When working in the high-eccentricity limit, one can expand these via

$$\epsilon_{\rm ppE}(e_i) = \bar{\epsilon}_{\rm ppE,0} + \bar{\epsilon}_{\rm ppE,1}\delta e_i + \mathcal{O}\left(\delta e_i^2\right) , \tag{5.37}$$

where $\epsilon_{\rm ppE}(e_i)$ is any of $(\alpha_{\rm ppE}, \beta_{\rm ppE}, \gamma_{\rm ppE}, \delta_{\rm ppE})$, while $(\bar{\epsilon}_{\rm ppE,0}, \bar{\epsilon}_{\rm ppE,1})$ are related constants.

One may wonder how the ppE parameters $(\alpha_{\rm ppE},\ \beta_{\rm ppE},\ \gamma_{\rm ppE},\ \delta_{\rm ppE})$ and $(\bar{a}_{\rm ppE},\ \bar{b}_{\rm ppE},\ \bar{c}_{\rm ppE},\ \bar{d}_{\rm ppE})$ in Eqs. (5.1)-(5.6) map to the deformations to the conservative and dissipative dynamics in Eqs. (5.21)-(5.24). The mapping between the parameters depends on which sector is most dominant in PN theory, i.e. which coefficient $(\bar{a}, \bar{b}, \bar{c}, \bar{d})$ is largest. If one knows what the deformations in Eqs. (5.21)-(5.24) are, one can then construct a one-to-one mapping between these and the ppE coefficients:

$$\alpha_{\rm ppE}\left(\frac{M}{r_p}\right)^{\bar{b}_{\rm ppE}} = {\rm LO}\left[\frac{\delta T_{\rm orb}}{T_{\rm orb}^{\rm N}}\right] , \tag{5.38}$$

$$\beta_{\rm ppE}\left(\frac{M}{r_p}\right)^{\bar{b}_{\rm ppE}} = {\rm LO}\left[\frac{\delta v_p}{v_p^{\rm N}}\right] , \tag{5.39}$$

$$\begin{aligned}\gamma_{\rm ppE}\left(\frac{M}{r_p}\right)^{\bar{c}_{\rm ppE}} &= -\frac{59\sqrt{2}\pi}{24}\eta\ {\rm LO}\left[\frac{26}{59}\alpha\left(\frac{M}{r_p}\right)^{\bar{a}+5/2} - \frac{144}{59}\beta\left(\frac{M}{r_p}\right)^{\bar{b}+5/2}\right. \\ &\left. -\frac{85}{59}\gamma\left(\frac{M}{r_p}\right)^{\bar{c}+5/2} + \frac{144}{59}\delta\left(\frac{M}{r_p}\right)^{\bar{d}+5/2}\right] , \end{aligned} \tag{5.40}$$

$$\delta_{\rm ppE}\left(\frac{M}{r_p}\right)^{\bar{d}_{\rm ppE}} = {\rm LO}\left[-2\alpha\left(\frac{M}{r_p}\right)^{\bar{a}} + \gamma\left(\frac{M}{r_p}\right)^{\bar{c}}\right] , \tag{5.41}$$

where LO stands for the leading-order term in an $M/r_p \ll 1$ expansion, which of course depends on the value of $(\bar{a}, \bar{b}, \bar{c}, \bar{d})$.

With this algorithm at hand, one can formulate the following tests of GR. Given a detection of N bursts, one obtains the observables $(t_{0,\ldots,N}, f_{0,\ldots,N}, t_{0,\ldots,N}, f_{0,\ldots,N})$. The data should be completely described by the system parameters $\bar{\lambda}^a_{\rm sys} = (\mathcal{M}, \mathcal{R}_0, e_0)$, the ppE amplitude parameters $(\alpha_{\rm ppE}, \beta_{\rm ppE}, \gamma_{\rm ppE}, \delta_{\rm ppE})$ and the ppE exponent parameters $(\bar{a}_{\rm ppE}, \bar{b}_{\rm ppE}, \bar{c}_{\rm ppE}, \bar{d}_{\rm ppE})$. Provided we detect enough bursts (i.e. N is large enough), one should be able to study whether the data prefers a GR model, i.e. one with $(\alpha_{\rm ppE}, \beta_{\rm ppE}, \gamma_{\rm ppE}, \delta_{\rm ppE}) = (0, 0, 0, 0)$, or not. As in the quasi-circular case, one expects there to be degeneracies between the ppE parameters [63]. The extent to which such degeneracies affect the tests of GR proposed here will be investigated in detail elsewhere. One could of course also extend the ppE parameterization to include more ppE coefficients, but this may dilute the strength of the GR tests.

Burst Models in Modified Gravity

In this section, we study GW bursts in two specific theories of gravity: EDGB and BD theory. In particular, this will require the calculation of the binding energy, angular moment, energy flux and angular momentum flux for eccentric inspirals, some of which had not been calculated before. Such a study will allow us to determine the efficiency of the ppE modifications to capture specific GR modifications.

Einstein-Dilaton-Gauss-Bonnet Gravity

EDGB is a quadratic modified gravity theory that modifies the Einstein-Hilbert action through the product of a dynamical scalar field ϑ and the Gauss-Bonnet invariant. The field equations for the metric and the scalar field are given for example in [179]. Black hole and neutron star solutions were found in [128, 179], while binary systems were analyzed in [170, 179]. This theory contains one coupling constant ξ, with dimensions of length to the fourth power; the theory reduces to GR in the limit $\xi \to 0$. The strongest constraint on ξ has been derived from observations of low-mass X-ray binaries in [169], namely $\xi^{1/4} \lesssim 5 \times 10^3$ m. One of the most important EDGB modifications to GR occurs when considering binary black holes, which emit gravitational dipole radiation due to the excitation of the scalar field, which induces -1PN order corrections [170]. For neutron star binaries, it is not clear that gravitational dipole radiation is excited, so in the rest of this section, we will consider only bursts emitted by systems where at least one of the binary components is a black hole.

We begin by finding the leading-order contributions to the Newtonian gravitational potential in EDGB. To do this, we consider a point particle moving in a background spacetime of a non-rotating black hole in EDGB, which is given by

$$ds^2 = -f(r)\left[1 + h(r)\right] dt^2 + \frac{1}{f(r)}\left[1 + k(r)\right] dr^2 + r^2 d\Omega^2 \tag{5.42}$$

where $f(r) = 1 - 2M/r$ is the Schwarzschild factor, $h(r) = [\zeta/3f(r)](M/r)^3\tilde{h}(r)$, $k(r) = -[\zeta/f(r)](M/r)^2\tilde{k}(r)$, $\tilde{h}(r)$ and $\tilde{k}(r)$ are given by Eqs. (10) and (11) in [180], and $\zeta = \xi/M^4$ is the dimensionless coupling constant of the theory. The Lagrangian for the test particle is given by $\mathcal{L} = \mu\sqrt{-g_{\rho\sigma}v^\rho v^\sigma}$, where $v^\rho = (1, dx^j/dt)$ and we have taken the mass of the particle to be the reduced mass of the binary. By performing a PN expansion of this Lagrangian, we find the corrections to the potential and kinetic energy to lowest order in ζ and M/r to be

$$\delta U = \frac{\zeta}{6}\mu\left(\frac{M}{r}\right)^3, \qquad \delta T = -\frac{\zeta}{2}\mu\dot{r}^2\left(\frac{M}{r}\right)^2. \tag{5.43}$$

Matching this to Eq. (5.8), we have

$$\tilde{\alpha} = -\frac{\zeta}{6}, \qquad \tilde{a} = 2, \tag{5.44}$$

$$\tilde{\gamma} = -\zeta\,, \qquad \tilde{c} = 2\,. \tag{5.45}$$

We do not consider the corrections to the potential that scale as $\dot{\phi}^2$ for two reasons: these contributions are higher PN order, and they do not admit the simple form presented in Eq. (5.7) due to the nonlinearity of the Lagrangian. Neglecting these terms does not affect the leading-order results presented in this section.

We may now directly apply the results of Eqs. (5.11)-(5.12), (5.15), and (5.18) to EDGB gravity. Below we provide expressions for the orbital energy, period, and pericenter velocity for eccentric binaries in EDGB:

$$\frac{\delta E_{\rm EDGB}}{E_{\rm GR}} = \frac{\zeta}{6}\left(\frac{1-e}{1+e}\right)\left(\frac{M}{r_p}\right)^2\,, \tag{5.46}$$

$$\frac{\delta L_{\rm EDGB}}{L_{\rm GR}} = -\frac{\zeta}{12}\frac{3+e^2}{(1+e)^2}\left(\frac{M}{r_p}\right)^2\,, \tag{5.47}$$

$$\frac{\delta T_{\rm orb}^{\rm EDGB}}{T_{\rm orb}^{\rm GR}} = -\frac{\zeta}{4}\left(\frac{1-e}{1+e}\right)\left(1+2\sqrt{1-e^2}\right)\left(\frac{M}{r_p}\right)^2\,, \tag{5.48}$$

$$\frac{\delta v_p^{\rm EDGB}}{v_p^{\rm GR}} = -\frac{\zeta}{12}\left[\frac{3+e^2}{(1+e)^2}\right]\left(\frac{M}{r_p}\right)^2\,. \tag{5.49}$$

Let us now consider how the orbital energy and angular momentum change due to radiation losses. When considering binaries where at least one of the components is a black hole, the dominant radiation loss is due to scalar-field emission [see e.g. Eqs. (122) in [170] and (B23) in [171]]:

$$\dot{E}^{(\vartheta)} = -\frac{4\pi}{3}\beta\left\langle \ddot{D}_i\ddot{D}^i\right\rangle\,, \qquad \dot{L}_i^{(\vartheta)} = \frac{4\pi}{3}\beta\epsilon_{ijk}\left\langle \ddot{D}_j\dot{D}_k\right\rangle\,, \tag{5.50}$$

where $D^i = q_1 x_1^i + q_2 x_2^i$ is an induced dipole moment, with $q_{1,2} = m_{1,2}[\zeta_{1,2}/(4\pi\beta)]^{1/2}$ the scalar charges of the compact objects, $\zeta_{1,2} = \xi/m_{1,2}^4$, $x_{1,2}^i$ the position vector relative to the center of mass, and $\langle\rangle$ stands for orbit averaging. The above expressions have already been angle averaged (i.e. integrated over solid angle at spatial infinity). Carrying out the orbit average, we find

$$\frac{\dot{E}^{(\vartheta)}}{\dot{E}_{\rm GR}} = \frac{5}{96}\mathcal{S}_{\rm EDGB}^{2}\frac{(1+e)(1+\frac{1}{2}e^{2})}{1+\frac{73}{24}e^{2}+\frac{37}{96}e^{4}}\left(\frac{M}{r_p}\right)^{-1}\,, \tag{5.51}$$

$$\frac{\dot{L}^{(\vartheta)}}{\dot{L}_{\rm GR}} = \frac{5}{96}\mathcal{S}_{\rm EDGB}^{2}\frac{1+e}{1+\frac{7}{8}e^{2}}\left(\frac{M}{r_p}\right)^{-1}\,, \tag{5.52}$$

where $\dot{E}_{\rm GR}$ and $\dot{L}_{\rm GR}$ are the energy and angular momentum flux in GR [58, 129, 130], and where we have defined $\mathcal{S}_{\rm EDGB} = \zeta_1^{1/2} - \zeta_2^{1/2}$. Notice that when $m_1 = m_2$, then $\mathcal{S}_{\rm EDGB} = 0$ and dipole radiation vanishes. We have checked that these results agree exactly with those of [171] in the circular limit $e \to 0$. For mixed neutron star-black hole binaries, we set $\zeta_1 = \zeta_{\rm BH} = \xi/m_{\rm BH}^4$ and $\zeta_2 = \zeta_{\rm NS} = 0$.

We can then easily map between the EDGB deformations described above and the ppE deformations of Eqs. (5.21)-(5.24):

$$\begin{aligned}\delta\lambda^{a}_{\rm EDGB} = \Bigg[&\frac{\zeta}{6}\frac{1-e}{1+e}, -\frac{\zeta}{12}\frac{3+e^{2}}{(1+e)^{2}}, \frac{5}{96}\mathcal{S}_{\rm EDGB}^{2}\frac{(1+e)(1+\frac{1}{2}e^{2})}{1+\frac{73}{24}e^{2}+\frac{37}{96}e^{4}},\\ &\frac{5}{96}\mathcal{S}_{\rm EDGB}^{2}\frac{1+e}{1+\frac{7}{8}e^{2}}\Bigg]\,,\end{aligned} \tag{5.53}$$

and $\delta\ell^{a}_{\rm EDGB} = (3, 2, -1, -1)$. Notice that $\delta\lambda^{a}_{\rm EDGB}$ are all functions not only of the coupling constant of the theory ζ, but also of the eccentricity. Expanding to leading-order in $\delta e \ll 1$, we find

$$\delta\lambda^{a}_{\rm EDGB} = \left[\frac{\zeta}{6}\delta e, -\frac{\zeta}{12}, \frac{3}{85}S_{\rm EDGB}^{2}, \frac{1}{18}S_{\rm EDGB}^{2}\right]\,, \tag{5.54}$$

with remainders of $\mathcal{O}(\delta e)$.

When considering GW bursts emitted by binaries where at least one of the components is a black hole, we then have all the necessary ingredients to construct the burst algorithm within EDGB. Combining our results with Eqs. (5.31) and (5.32) and working to leading, PN order and to first order in δe, we find

$$t_i^{\rm EDGB} = t_{i-1} + \Delta t_{i,i-1}^{\rm GR}(r_{p,i}, \delta e_i)\left[1 - \frac{\zeta}{8}\delta e_i \left(\frac{M}{r_{p,i}}\right)^2 + \mathcal{O}\left(\zeta^2, \delta e_i^2\right)\right]\,, \tag{5.55}$$

$$f_i^{\rm EDGB} = f_i^{\rm GR}(r_{p,i}, \delta e_i)\left[1 - \frac{\zeta}{12}\left(\frac{M}{r_{p,i-1}}\right)^2 + \mathcal{O}\left(\zeta^2, \delta e_i\right)\right]\,, \tag{5.56}$$

$$\delta t_i^{\rm EDGB} = \delta t_i^{\rm GR}(r_{p,i}, \delta e_i)\left[1 + \frac{\zeta}{12}\left(\frac{M}{r_{p,i-1}}\right)^2 + \mathcal{O}\left(\zeta^2, \delta e_i\right)\right]\,, \tag{5.57}$$

$$\delta f_i^{\rm EDGB} = \delta f_i^{\rm GR}(r_{p,i}, \delta e_i)\left[1 - \frac{\zeta}{12}\left(\frac{M}{r_{p,i-1}}\right)^2 + \mathcal{O}\left(\zeta^2, \delta e_i\right)\right]\,. \tag{5.58}$$

Recall that $\Delta t_{i,i-1}^{\rm GR}$, $f_i^{\rm GR}$, $\delta t_i^{\rm GR}$, $\delta f_i^{\rm GR}$ are functions of $r_{p,i}$ and δe_i, which are related to the parameters of the previous burst via

$$\frac{r_{p,i}^{\rm EDGB}\left(r_{p,i-1}, \delta e_{i-1}\right)}{r_{p,i}^{\rm GR}\left(r_{p,i-1}, \delta e_{i-1}\right)} = 1 - \frac{5\sqrt{2}\pi}{24}\eta \mathcal{S}_{\rm EDGB}^2 \left(\frac{M}{r_{p,i-1}}\right)^{3/2} + \mathcal{O}\left(\zeta^2, \delta e_{i-1}\right) \tag{5.59}$$

$$\frac{\Delta \delta e_{i,i-1}^{\rm EDGB}\left(r_{p,i-1}, \delta e_{i-1}\right)}{\Delta \delta e_{i,i-1}^{\rm GR}\left(r_{p,i-1}, \delta e_{i-1}\right)} = 1 + \frac{3}{85}\mathcal{S}_{\rm EDGB}^2 \left(\frac{M}{r_{p,i-1}}\right)^{-1} + \mathcal{O}\left(\zeta^2, \delta e_{i-1}\right) \tag{5.60}$$

where recall that $\Delta \delta e_{i,i-1}^{\rm EDGB} = \delta e_i^{\rm EDGB} - \delta e_{i-1}$.

Notice that the above EDGB modified burst algorithm maps exactly to the ppE burst model of Eqs. (5.1)-(5.6). First, focusing on the temporal and frequency mappings of the burst tiles, we see that

$$\alpha_{\rm ppE} = \frac{\zeta}{8}\delta e\,, \qquad \bar{a}_{\rm ppE} = 2\,, \qquad \beta_{\rm ppE} = -\frac{\zeta}{12}\,, \qquad \bar{b}_{\rm ppE} = 2\,, \tag{5.61}$$

For the eccentricity mapping, we find that

$$\delta_{\rm ppE} = \frac{3}{85}\mathcal{S}^2_{\rm EDGB}\,, \qquad \bar{d}_{\rm ppE} = -1\,, \tag{5.62}$$

since $\bar{c} = -1 < \bar{a}$ in EDGB. With this, it then becomes clear that

$$\gamma_{\rm ppE} = -\frac{5\sqrt{2}\pi}{24}\eta\mathcal{S}^2_{\rm EDGB}\,, \qquad \bar{c}_{\rm ppE} = 3/2\,, \tag{5.63}$$

because $5/2 + \bar{c} = 3/2$ in EDGB. We thus see that the EDGB burst model can be mapped to the ppE model to leading-order in the EDGB deformation parameter.

As mentioned at the beginning of this subsection, one must be careful when applying the above ppE corrections to systems that contain neutron stars, since dipolar emission may be suppressed. Thus, in a mixed black hole-neutron star system, only the black hole would emit dipole radiation. Although the scalar charges for neutron stars have not yet been computed explicitly, it is expected that they will introduce corrections that are higher PN order compared to the dipolar radiation corrections described above when in presence of a black hole. This is why, when considering mixed binary systems above, we set $\zeta_2 = \zeta_{\rm NS} = 0$ and only consider the effect of the black hole.

Brans-Dicke Theory of Gravity

BD theory [52] is a particular scalar-tensor theory of gravity that has been extensively studied in the past (for a review, see e.g. [164]). In this theory, the Ricci scalar in the Einstein-Hilbert action is multiplied by a dynamical scalar field ϕ, which has the effect of promoting Newton's gravitational constant G to a function of spacetime. The field equations for the metric and the scalar field can be found e.g. in [52, 164, 166]. Neutron stars in BD theory have been found in [124, 166]; black holes are not modified from their GR solution [73, 86, 143]. Binary systems in BD theory were studied e.g. in [166, 175]. This theory possesses a dimensionless coupling constant $\omega_{\rm BD}$; the theory reduces to GR in the limit $\omega_{\rm BD} \to \infty$. The strongest constraint on the BD coupling constant comes from tracking of the Cassini spacecraft, which requires $\omega_{\rm BD} > 4 \times 10^4$ [36]. One of the most important BD modifications to GR is that the dynamical BD field induces dipolar emission of energy and angular momentum, just as in EDGB. Unlike EDGB, however, the conservative dynamics are not modified to leading PN order.

Let us then consider the rate of change of the binding energy and angular momentum. Since the relation between the orbital period and the binding energy in BD is unchanged from GR, we can easily calculate the luminosity through $\dot{T}_{\rm orb}/T_{\rm orb} = -\frac{3}{2}\dot{E}/E$. Using the leading PN order expression for $\dot{T}_{\rm orb}$ (the second term in Eq. (2.26) of [166]), we can then find

$$\frac{\dot{E}^{(\phi)}}{\dot{E}_{\rm GR}} = \frac{5}{48}\frac{\mathcal{S}_{\rm BD}^2}{\omega_{\rm BD}}\left(\frac{M}{r_p}\right)^{-1}\frac{(1+e)(1+\frac{1}{2}e^2)}{1+\frac{73}{24}e^2+\frac{37}{96}e^4} \tag{5.64}$$

where we have linearized in $1/\omega_{\rm BD}$, and we have defined $\mathcal{S}_{\rm BD} = s_2 - s_1$, with $s_{1,2}$ the star's sensitivities. Alternatively, one can obtain the above by orbit averaging Eq. (6.16) in [115], as we have checked explicitly. Observe that the modification to GR is proportional to the difference of the sensitivities squared, which vanishes for black hole binaries in which $s_1 = 0.5 = s_2$. Similarly, for neutron star binaries, $s_1 \approx s_2$ and the BD modification will be suppressed. For this reason, the largest BD modifications will be produced by black hole-neutron star binaries.

Let us now focus on the rate of change of orbital angular momentum. To leading PN order and again linearizing in $1/\omega_{\rm BD}$, this quantity is controlled by the BD field via

$$\dot{L}_z^{(\phi)} = \frac{\omega_{\rm BD}}{8\pi} \lim_{R\to\infty} \int_{S^2_R} \left\langle \dot{\phi}\, (\vec{n} \times \vec{\nabla})_z \phi \right\rangle R^3 d\Omega\,, \tag{5.65}$$

where $\vec{n}$ and R are the unit vector and distance from the center of mass to a field point respectively, $\vec{\nabla}$ and $\times$ are the flat-space, spatial gradient and cross-product operators respectively (the latter of which is to be evaluated in the $\hat{z}$-direction, normal to the orbital plane) and the cosmological value of the scalar field is $\phi_0 = 1 + \mathcal{O}(1/\omega_{\rm BD})$. Note that the above expression is both an angle average (the $d\Omega$ integral) and an orbit average (the $\langle\rangle$ operator). The far-zone solution for the scalar field is [166]

$$\phi = -2 \frac{\mathcal{S}_{\rm BD}}{\omega_{\rm BD}} \frac{\eta M}{R} \left(\vec{n} \cdot \vec{v}\right) \,, \tag{5.66}$$

to lowest order in the relative orbital velocity $\vec{v} = \dot{\vec{x}}_2 - \dot{\vec{x}}_1$, where recall that η is the binary's symmetric mass ratio, M is the total mass and $\cdot$ is the flat-space inner product operator. Combining all of this and upon angle averaging, we obtain

$$\dot{L}_z^{(\phi)} = \left\langle -\frac{2}{3} \frac{\mathcal{S}^2_{\rm BD}}{\omega_{\rm BD}} \frac{\eta M^2}{r^3} L \right\rangle \,, \tag{5.67}$$

where L is the orbital angular momentum and $r = |\vec{x}_2 - \vec{x}_1|$ is the orbital separation. We now orbit average to obtain

$$\frac{\dot{L}_z^{(\phi)}}{\dot{L}_{\rm GR}} = \frac{5}{48} \frac{\mathcal{S}^2_{\rm BD}}{\omega_{\rm BD}} \left(\frac{M}{r_p}\right)^{-1} \frac{1+e}{1+\frac{7}{8}e^2} \tag{5.68}$$

to linear order in $1/\omega_{\rm BD}$. One can show that *prior to orbit averaging*, $\dot{E}^{(\phi)}$ and $\dot{L}_z^{(\phi)}$ satisfy

$$\frac{\dot{E}^{(\phi)}}{\dot{L}_z^{(\phi)}} = \frac{a}{r} \frac{\Omega_{\rm orb}}{\sqrt{1-e^2}} \tag{5.69}$$

In the above expression, $\dot{E}^{(\phi)}$ is given by Eq. (6.16) in [115] and $\Omega_{\rm orb}$ is the orbital frequency. As in the case of $\dot{E}^{(\phi)}$, note that $\dot{L}_z^{(\phi)}$ is suppressed when considering black hole or neutron star binaries, with the largest modifications arising from mixed binaries.

We can now map the leading, PN order, BD modifications to the binding energy and angular momentum to the ppE deformations of Eqs. (5.21)-(5.24):

$$\delta\lambda^a_{\rm BD} = \left[0, 0, \frac{5}{48}\frac{\mathcal{S}^2_{\rm BD}}{\omega_{\rm BD}}\frac{(1+e)(1+\frac{1}{2}e^2)}{1+\frac{73}{24}e^2+\frac{37}{96}e^4}, \frac{5}{48}\frac{\mathcal{S}^2_{\rm BD}}{\omega_{\rm BD}}\frac{1+e}{1+\frac{7}{8}e^2}\right]\,, \tag{5.70}$$

and $\delta\ell^a_{\rm BD} = (0,0,-1,-1)$. Once again, the dissipative sector corrections control the dominant ppE modifications. Notice also that $\delta\lambda^a_{\rm BD}$ clearly depends on the eccentricity, in addition to the BD coupling parameter. Expanding the above expressions to leading-order in the high-eccentricity limit, we find

$$\delta\lambda^a_{\rm BD} = \left[0, 0, \frac{6}{85}\frac{\mathcal{S}^2_{\rm BD}}{\omega_{\rm BD}}, \frac{1}{9}\frac{\mathcal{S}^2_{\rm BD}}{\omega_{\rm BD}}\right]\,, \tag{5.71}$$

with remainders of $\mathcal{O}(\delta e)$.

With the amplitude and exponent coefficients specified, we can now build the burst algorithm in BD theory. We find that the functionals of the burst algorithm are actually not modified from the GR result:

$$t_i^{\rm BD} = t_i + \Delta t^{\rm GR}_{i,i-1}(r_{p,i}, \delta e_i) \tag{5.72}$$

$$f_i^{\rm BD} = f_i^{\rm GR}(r_{p,i}, \delta e_i) \tag{5.73}$$

$$\delta t_i^{\rm BD} = \delta t_i^{\rm GR}(r_{p,i}, \delta e_i) \tag{5.74}$$

$$\delta f_i^{\rm BD} = \delta f_i^{\rm GR}(r_{p,i}, \delta e_i) \tag{5.75}$$

but the mapping $(r_{p,i}, \delta e_i) \to (r_{p,i-1}, \delta e_{i-1})$ is modified via

$$\frac{r_{p,i}^{\rm BD}\left(r_{p,i-1}, \delta e_{i-1}\right)}{r_{p,i}^{\rm GR}\left(r_{p,i-1}, \delta e_{i-1}\right)} = 1 - \frac{5\sqrt{2}\pi}{12}\frac{\mathcal{S}_{\rm BD}^2}{\omega_{\rm BD}}\eta\left(\frac{M}{r_{p,i-1}}\right)^{3/2} + \mathcal{O}\left(\omega_{\rm BD}^{-2}, \delta e_{i-1}\right)\,, \tag{5.76}$$

$$\frac{\Delta\delta e_{i,i-1}^{\rm BD}\left(r_{p,i-1}, \delta e_{i-1}\right)}{\Delta\delta e_{i,i-1}^{\rm GR}\left(r_{p,i-1}, \delta e_{i-1}\right)} = 1 + \frac{6}{85}\frac{\mathcal{S}_{\rm BD}^2}{\omega_{\rm BD}}\left(\frac{M}{r_{p,i-1}}\right)^{-1} + \mathcal{O}\left(\omega_{\rm BD}^{-2}, \delta e_{i-1}\right)\,, \tag{5.77}$$

Thus the burst algorithm in BD theory does properly map to the proposed ppE burst model. We find that

$$\alpha_{\rm ppE} = \beta_{\rm ppE} = 0\,, \tag{5.78}$$

since there are no corrections to the orbital energy and angular momentum in BD theory. Furthermore, from the pericenter and eccentricity mapping, we see that

$$\gamma_{\rm ppE} = -\frac{5\sqrt{2}\pi}{12}\eta\frac{\mathcal{S}_{\rm BD}^2}{\omega_{\rm BD}}\,, \qquad \bar{c}_{\rm ppE} = 3/2\,, \tag{5.79}$$

$$\delta_{\rm ppE} = \frac{6}{85}\frac{\mathcal{S}_{\rm BD}^2}{\omega_{\rm BD}}\,, \qquad \bar{d}_{\rm ppE} = -1\,, \tag{5.80}$$

which is very similar to the results found in EDGB. This is due to both theories having dipole radiation.

Projected Constraints

We here present a back-of-the-envelope calculation aimed at providing an order-of-magnitude estimate of how well these eccentric burst algorithms could constrain modified gravity theories. We stress that these are not rigorous projected constraints in any way; true projections would require a full data analysis investigation using Bayesian tools, which we leave to future work. We consider the variations in the time and frequency mappings between boxes due to GR parameters and modified gravity coupling constants.

Let us begin by recalling that the mapping between time-frequency windows in GR depends only on the vector $\lambda^a_{\rm GR} = (\mathcal{R}, \mathcal{M}, e)$. Let us further assume that a sufficiently large number of bursts have been detected, such that in GR one could estimate these parameters from these burst observations. In a modified gravity theory, the mapping between time-frequency windows will not only depend on $\lambda^a_{\rm GR}$ but also on $\lambda^a_{\rm ppE} = (\alpha_{\rm ppE}, \beta_{\rm ppE}, \gamma_{\rm ppE}, \delta_{\rm ppE})$ as well as on $(\eta, \mathcal{M}, \mathcal{R})$ due to the (M/r_p) dependence [see Eq. (5.84)]. Therefore, a GW modification can be measured or constrained provided $\lambda^a_{\rm ppE}$ produced a modification to the time-frequency mapping that is *at least* comparable to that introduced by $\lambda^a_{\rm GR}$, i.e.

$$\frac{\delta(\Delta t_{i,i-1}, \Delta f_{i,i-1})}{\delta \lambda^a_{\rm ppE}} \delta\lambda^a_{\rm ppE} > \left(\frac{\delta(\Delta t_{i,i-1}, \Delta f_{i,i-1})}{\delta \lambda^a_{\rm GR}}\right)_{\rm GR} \delta\lambda^a_{\rm GR} \,. \tag{5.81}$$

Let us focus on the frequency mapping. One could also investigate GR deviation in the time mapping, which will depend on $\alpha_{\rm ppE}$ [Eq. (5.33)], $\gamma_{\rm ppE}$ [Eq. (5.5)] and $\delta_{\rm ppE}$ [Eq. (5.6)]. Either way should lead to an order of magnitude estimate for the projected constraint that is comparable. The frequency mapping can be obtained by combining Eqs. (5.2) and (5.5):

$$\Delta f_{i,i-1} = \Delta f^{\rm GR}_{i,i-1} + \Delta f^{\rm ppE}_{i,i-1} \,, \tag{5.82}$$

$$\Delta f^{\rm GR}_{i,i-1} = \frac{23}{12} \frac{\mathcal{M}^{5/3}}{\mathcal{R}^{8/3}_{i-1}} \left(1 + \frac{121}{230} \delta e_{i-1}\right) \,, \tag{5.83}$$

$$\begin{aligned} \Delta f^{\rm ppE}_{i,i-1} = {\rm LO} \Bigg[& \frac{23}{12} \beta_{\rm ppE} \eta^{-2/5\bar{b}} \frac{\mathcal{M}^{5/3+2/3\bar{b}_{\rm ppE}}}{\mathcal{R}^{8/3+2/3\bar{b}_{\rm ppE}}_{i-1}} - \frac{3\sqrt{2}}{4\pi} \gamma_{\rm ppE} \eta^{-2/5\bar{c}_{\rm ppE}} \frac{\mathcal{M}^{2/3\bar{c}_{\rm ppE}}}{\mathcal{R}^{1+2/3\bar{c}_{\rm ppE}}_{i-1}} \\ & - \frac{85}{48} \delta_{\rm ppE} \eta^{-2/5\bar{d}_{\rm ppE}} \frac{\mathcal{M}^{5/3+2/3d^{-}_{\rm ppE}}}{\mathcal{R}^{8/3+2/3\bar{d}}_{i-1}} \Bigg] \,. \end{aligned} \tag{5.84}$$

Using the values of the ppE parameters in BD and EDGB theory, we find,

$$\Delta f^{\rm BD}_{i,i-1} = \frac{1}{2} \frac{\mathcal{S}^2_{\rm BD}}{\omega_{\rm BD}} \frac{\mathcal{M} \eta^{2/5}}{\mathcal{R}^2} \,, \tag{5.85}$$

$$\Delta f^{\mathrm{EDGB}}_{i,i-1} = \frac{1}{4}\mathcal{S}^2_{\mathrm{EDGB}}\frac{\mathcal{M}\eta^{2/5}}{\mathcal{R}^2} \tag{5.86}$$

The form of these modifications is identical, since to leading PN order, both theories lead to a dipolar-type modification.

With this, we can now evaluate projected constraints from Eq. (5.81). This requires that we calculate the variation of $\Delta f_{i,i-1}$ with respect to the coupling constants of the theory. Recall that in BD the latter is $1/\omega_{\mathrm{BD}}$, while in EDGB it is just ξ. The evaluation of Eq. (5.81) also requires us to multiply this variation by $\delta\lambda^a_{\mathrm{GR}}$ and $\delta\lambda^a_{\mathrm{ppE}}$. The latter is simply $1/\omega_{\mathrm{BD}}$ in BD theory and ξ in EDGB theory, because their values in GR are zero.

We will consider the constraints that can be placed using the NSBH system considered in Ch. 4, as it will have the largest dipole contribution of the three systems studied there. This means that $m_{\mathrm{NS}} = 1.4M_{\odot}$ and $m_{\mathrm{BH}} = 10M_{\odot}$, which then automatically means that $\eta \approx 0.108$ and $\mathcal{M} = 1.23M_{\odot}$. In BD, we choose $s_1 = s_{\mathrm{BH}} = 0.5$ and $s_2 = s_{\mathrm{NS}} = 0.2$; the sensitivity of neutron stars varies depending on their mass and equation of state, but the value 0.2 is representative [166]. In EDGB, we set $\zeta_2 = \zeta_{\mathrm{NS}} = 0$ since the corrections we have derived only apply to black holes. We will also need to choose values for the orbital eccentricity and the radius of curvature, which recall was defined as $\mathcal{R} = r_p^{3/2}/M^{1/2}$. We will here choose the initial value of e and r_p from Table 4.1, to calculate δe and $\mathcal{R}$.

In an optimal scenario, $\delta\lambda^a_{\mathrm{GR}}$ scales roughly as $1/\rho_{\mathrm{GR}}$, where ρ_{GR} is the signal-to-noise ratio in GR, defined as

$$\rho^2_{\mathrm{GR}} = 4\int_0^{\infty}\frac{|\tilde{h}_{\mathrm{GR}}(f)|^2}{S_n(f)}df\,, \tag{5.87}$$

where $\tilde{h}_{\mathrm{GR}}(f)$ is the Fourier transform of the GW signal (i.e. the frequency-domain waveform) and $S_n(f)$ is the spectral noise density of the detector considered. For our purposes, we will consider the Advanced LIGO detector, for which $S_n(f)$ is given e.g. in Eq. (2.1) of [116]. To obtain the $\tilde{h}_{\rm GR}(f)$, we use the method described in Ch. 4 to obtain the evolution of the orbit under radiation reaction. We then compute the time-domain waveform using Eq. (11) of [156] and use FFTW to obtain $\tilde{h}(f)$. For the NSBH system considered, we set the distance to the source to be 600 Mpc, for which we obtain $\rho_{\rm GR} = 13.2$, after approximately $3,650$ bursts.

With this at hand, the right-hand side of Eq. (5.81) can be easily computed using the data from Table 4.1. In EDGB, the best constraint is then

$$\begin{aligned} \xi^{1/4} \lesssim 3 \times 10^3 \text{ m} \left(\frac{m_{\rm BH}}{10 M_\odot}\right) \left(\frac{\mathcal{M}}{1.23 M_\odot}\right)^{1/6} \left(\frac{\eta}{0.108}\right)^{-1/10} \\ \times \left(\frac{\mathcal{R}}{391 M}\right)^{-5/12} \left(\frac{\rho_{\rm GR}}{13.2}\right)^{-1/4}, \end{aligned} \tag{5.88}$$

while in BD theory it is

$$\begin{aligned} \omega_{\rm BD} \gtrsim 10^3 \left(\frac{\mathcal{S}_{\rm BD}}{0.3}\right)^2 \left(\frac{\mathcal{M}}{1.23 M_\odot}\right)^{-1/6} \left(\frac{\eta}{0.108}\right)^{1/10} \\ \times \left(\frac{\mathcal{R}}{391 M}\right)^{5/12} \left(\frac{\rho_{\rm GR}}{13.2}\right)^{1/4}. \end{aligned} \tag{5.89}$$

In both cases, the best constraint comes from using $\delta\lambda^a_{\rm GR} = \mathcal{R}$. We should note that $\rho_{\rm GR}$ is not independent of the other parameters, namely $(\mathcal{R}, \mathcal{M}, \eta)$. Thus, if one changes the SNR significantly from the above scaling, the other parameters must also be updated according to Eq. (5.87). These projected constraints are comparable to current constraints in the EDGB case, but not better than current constraints in the BD case. However, one should keep in mind that these projections are not rigorous but rather upper limits, since they do not account for parameter covariances.

Discussion

We have proposed ppE deformations of the GW burst sequences describing highly eccentric compact object mergers, to allow for quantitative tests of dynamical, strong-field GR if detections of such events are made with an excess power stacking algorithm. The ppE model conveniently factors the mathematical description of the burst sequence into the GR prediction multiplied by polynomial functions of the inverse pericenter separation. These polynomials depend on eight parameters in total—four amplitude and four exponent coefficients—which should capture the leading order dynamics of a *class* of generic deviations from GR for non-spinning, highly eccentric mergers.

With the ppE model in hand, given detection of an event, or a population of events with the GR burst sequences, one can in principle quantitatively answer the following questions: How consistent are the signals with GR as the underlying theory governing the dynamics of the sources? If consistent with GR, what constraints can be placed on the coupling constants of specific alternative theories whose leading order deviations can be described by ppE parameters? If inconsistent with GR, what are the most likely ppE parameters, and what then does this tell us about the underlying theory? To see how effectively these questions could be answered in practice will require (for example) a Bayesian analysis as carried out in [63, 137, 138] using ppE templates for quasi-circular inspiral. Issues that need to be addressed here include how well parameters (first GR, then ppE) can be extracted from a burst sequence with models of detector noise, and how accurately the base GR burst sequence needs to be modeled. It would also be interesting to see how much better, if at all, eccentric mergers are versus quasi-circular inspirals to test GR.

Yet another interesting avenue for future research is to see whether a ppE-like approach could be adopted to extract finite size/matter effects from eccentric mergers where one or both members of the binary are neutron stars. In other words, the baseline "GR" component of the burst sequence would be the GR binary black hole model, while the ppE component would characterize tidal deformations, the effects of magnetic fields, the onset of disruption/merger, etc. One of the key pieces of physics governing neutron star structure, namely the equation of state at nuclear densities, is unknown, and properties such as the magnetic strength are expected to vary from one neutron star to the next, which in either case necessitates the introduction of additional parameters within the GR waveform model. If these effects can, at least to leading order, be captured by ppE deformations of vacuum mergers, they could automatically be searched for in a ppE analysis. Furthermore, this analysis would make transparent what the degeneracies between putative deviations from GR and finite body effects are.

SECULAR GROWTH OF ECCENTRICITY IN THE LATE INSPIRAL

The analyses carried out in the previous chapters have focused on highly eccentric systems during the inspiral phase. However, GWs will cause the eccentricity of the binary to monotonically decay during the early inspiral phase of the coalescence. Indeed, only the most relativistic systems will retain significant orbital eccentricity by the time the binary reaches merger. Population studies have shown that most systems, regardless of formation scenario, will likely have small eccentricity, specifically less than $e \sim 0.1$, by the time the binary reaches the last stable orbit and merges. In this chapter, we investigate the behavior of the orbital eccentricity during the end of the inspiral phase and before binary systems reach the last stable orbit.

Radiation Reaction Force

In the PN approximation one solves the Einstein equations assuming small velocities/weak fields, with *radiation reaction*, i.e. the back reaction of gravitational waves on the orbital dynamics of the binary that leads to a decaying orbit, typically included through an *averaged balance law scheme* [93]. The idea is that the averaged rate of change of the orbital binding energy and angular momentum must be balanced by the averaged rate at which gravitational waves carry energy and angular momentum away from the system. Since radiation reaction causes *secular* changes in the orbital dynamics on timescales much longer than the orbital timescale, one then averages the gravitational wave fluxes over the orbital timescale [93] before solving the balance law.

A more accurate picture of the inspiral and coalescence of binary systems can be obtained through the radiation-reaction force, i.e. the force derived from the emission of gravitational waves that forces the orbit to decay. At leading PN order, the relative acceleration between two bodies is $\vec{a} = \vec{f}_{\rm N} + \vec{f}_{\rm 2.5PN}$, where $\vec{f}_N = -(GM/r^2)\,\vec{n}$ is the Newtonian gravitational force with M the total mass of the binary, and $(r, \vec{n})$ the radial separation between the two bodies and its associated unit vector, respectively. The second term in the relative acceleration is the leading PN order, radiation-reaction force, given explicitly in Eq. (12.208) of [131], specifically

$$\vec{f}_{\rm 2.5PN} = \frac{8}{5}\eta\frac{M^2}{r^3}\left[\mathcal{R}\dot{r}\vec{n} + \mathcal{S}\vec{v}\right] \,, \tag{6.1}$$

$$\mathcal{R} = \left(18 + 15a - \frac{45}{4}b\right)v^2 + \left(\frac{2}{3} - \frac{10}{3}a + \frac{25}{4}b\right)\frac{M}{r} - \left(25 + 25a - \frac{75}{4}b\right)\dot{r}^2 \,, \tag{6.2}$$

$$\mathcal{S} = -\left(6 + \frac{35}{6}a - \frac{5}{2}b\right)v^2 + \left(2 + \frac{35}{6}a - \frac{5}{2}b\right)\frac{M}{r} + \left(15 + \frac{35}{2}a - \frac{15}{2}b\right)\dot{r}^2 \,, \tag{6.3}$$

In the above, $\vec{v}$ is the relative velocity of the binary, with $\dot{r}$ it's radial component, and (a, b) are gauge parameters describing the coordinate freedom one has in expressing the dissipative part of the spacetime metric, and consequently, the radiation reaction force. Some common choices for these parameters are the Damour-Deruelle gauge [66] $(a, b) = (-2/3, 4/9)$, the Schäfer gauge [139] $(a, b) = (-2/5, 0)$, and the Burke-Thorne gauge [55,56,117,152] $(a, b) = (0, 0)$. The problem of describing the inspiral of a binary system due to GWs now reduces to solving the above two body problem.

One way of solving this is to use the method of osculating orbits [69, 131, 133], a perturbative method of solving generic two body problems. In this method, we take the solutions for the relative position and velocity of the binary to be the usual Keplerian expressions, but promote the usual Keplerian constants of motion to be functions of time, specifically

$$\vec{r} = \vec{r}_{\rm N}\left[t, \mu^a(t)\right] \,, \qquad \vec{v} = \vec{v}_{\rm N}\left[t, \mu^a(t)\right] \,, \tag{6.4}$$

where μ^a is the set of Keplerian parameters describing the orbit. For example, one description is $\mu^a = (p, e, f, \omega)$. We then require that $\dot{\vec{r}} = \vec{v}_{\rm N}$ and $\vec{a} = \vec{a}_{\rm N} + \vec{f}$, where $\vec{f}$ is the perturbing force. Taking the necessary time derivatives results in the system of equations

$$\sum_a \frac{\partial \vec{r}_{\rm N}}{\partial \mu^a} \frac{d\mu^a}{dt} = 0 \,, \tag{6.5}$$

$$\sum_a \frac{\partial \vec{v}_{\rm N}}{\partial \mu^a} \frac{d\mu^a}{dt} = \vec{f} \,, \tag{6.6}$$

which can be solved to obtain the equations for $d\mu^a/dt$. For the set $\mu^a = (p, e, f, \omega)$, the osculating equations governing the evolution of these quantities under radiation reaction are given in Eqs.(12.223)-(12.224) of [131]. The two-body problem then reduces to simultaneously solving the relative acceleration equation and the evolution equations for the orbital elements.

Although these two methods to describe radiation reaction are distinct, they agree upon orbit averaging the latter, exhibiting the same secular changes to the orbit. The second method, however, allows us to also study the effects of radiation reaction on an orbital timescale, which lead to *oscillatory* modifications that vanish upon orbit-averaging. To illustrate this, Fig. 6.1 presents the temporal evolution of the orbital eccentricity calculated by numerically integrating the radiation-reaction equations given by the osculating orbits method (black line) and the orbit averaged approximation (red dashed line) for an equal-mass binary and a binary with mass ratio of $m_2/m_1 \approx 0.127$. In all cases, we use the initial conditions $(p_0, e_0, \omega_0, f_0) = (20GM/c^2, 10^{-2}, \pi, -\pi)$, where p is the semi-latus rectum, e is the orbital eccentricity, ω is the longitude of pericenter, and f is the true anomaly, stopping the integrations when the system reaches the last stable orbit for a non-spinning test-particle $p = (2GM/c^2)(3 + e)$.

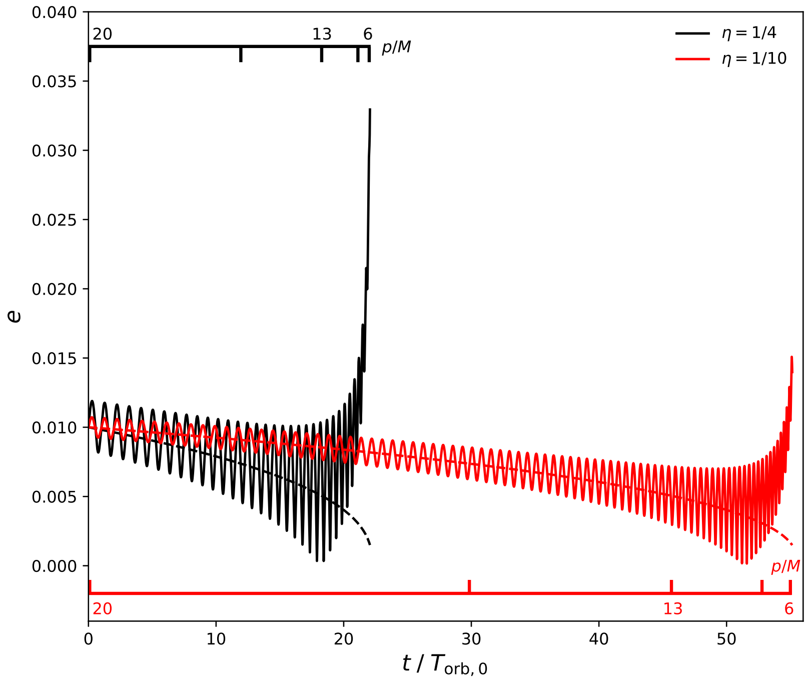

Figure 6.1: Temporal evolution of the orbital eccentricity relative to the orbital timescale $T_{\mathrm{orb},0}$, obtained through the numerical evolution of the orbit averaged (dashed lines) and the osculating orbit (solid lines) equations. The scales display equal increments of the dimensionless semi-latus rectum p/M for each system.

The evolution in the osculating method displays oscillatory behavior on the orbital timescale, while initially its secular change agrees with the orbit-averaged approximation. However, later in the evolution, roughly when the binary's semi-latus rectum is $p \approx 10$–$15M$, corresponding to $p \approx 10^3$ km for a binary with total mass $M = 60M_\odot$, the osculating method produces a *strong secular growth in the eccentricity*, which is opposite to what one obtains in the orbit-averaged approximation for comparable-mass binaries. This behavior seems counterintuitive for comparable-mass binaries, especially considering the wealth of literature on radiation reaction in the PN formalism, in which the eccentricity is always decreasing. However, it is important to remember that PN results are always computed within the orbit-averaged approximation. The radiation-reaction force is capturing effects beyond oscillatory behavior that are not described in the orbit-averaged approximation.

Multiple Scale Analysis

To better understand this behavior, we consider a multiple scale analysis [33,103, 119, 133, 134] of the leading PN order, radiation-reaction equations, following [131]. This analysis is valid provided $T_{\rm orb} \ll T_{RR}$, where $T_{RR} = |p/(dp/dt)|$ is the radiation reaction timescale and $T_{\rm orb}$ is the orbital timescale or simply the period of the orbit. Instead of using the variables (p, e, ω, t) with f the dependent variable, we choose to work with (p, A_x, A_y, t), where $(A_x, A_y) = (e \cos\omega, e \sin\omega)$ are the components of the Runge-Lenz vector, and with the orbital phase $\phi = f + \omega$ as the dependent variable. Working with these variables has the advantage of removing the e^{-1} divergences in $(d\omega/df)$ and (dt/df), as can be see in Eqs. (12.223c) and (12.224) of [131]. With these variables, the Newtonian eccentricity can be easily reconstructed from $e = (A_x^2 + A_y^2)^{1/2}$.

Let us then define a few dimensionless parameters to simplify the evolution system. We let $\epsilon = (8\eta/5)(M/p^\star)^{5/2}$, $\mathsf{p} = p/p^\star$ and $\mathsf{t} = t/(p^{\star 3}/m)^{1/2}$ [131], with $\eta = m_1 m_2/M^2$ the symmetric mass ratio of the binary with component masses m_1 and m_2, and $p^\star$ a representative length scale of the system. The osculating equations then become

$$\frac{d\mathsf{p}}{d\phi} = -\epsilon\, \mathsf{p}^{-3/2} \left\{ k_p^0 + \sum_{n=1}^{3} \left[k_p^{c,n} \cos(n\phi) + k_p^{s,n} \sin(n\phi) \right] \right\} \tag{6.7}$$

$$\frac{dA_{x,y}}{d\phi} = -\epsilon\, \mathsf{p}^{-5/2} \left\{ k_{x,y}^0 + \sum_{n=1}^{5} \left[k_{x,y}^{c,n} \cos(n\phi) + k_{x,y}^{s,n} \sin(n\phi) \right] \right\} \tag{6.8}$$

$$\frac{d\mathsf{t}}{d\phi} = \mathsf{p}^{3/2}\left[1 + A_x \cos(\phi) + A_y \sin(\phi)\right]^{-2} \tag{6.9}$$

where the k-coefficients, which are given in Appendix E, are ϕ-independent but do depend on the components of the Runge-Lenz vector and two gauge parameters (a, b). The evolution equations above do depend on the gauge choice, but this gauge-dependence is unimportant when computing observable quantities. We have explored analytically how these gauge parameters impact the secular growth described here, and we have found that there is not enough gauge freedom to remove this effect.

Let us now carry out a multiple scale analysis by defining a "fast" variable ϕ and a "slow" variable $\tilde{\phi}$, i.e. $\tilde{\phi} = \epsilon\, \phi$ with $\epsilon \ll 1$ the small parameter defined above, seeking solutions of the form $\mu^a = \mu_0^a(\tilde{\phi}, \phi) + \epsilon\, \mu_1^a(\tilde{\phi}, \phi) + \mathcal{O}(\epsilon^2)$, $\mathsf{t} = \epsilon^{-1}\mathsf{t}_{-1}(\tilde{\phi}, \phi) + \mathsf{t}_0(\tilde{\phi}, \phi) + \mathcal{O}(\epsilon)$, where $\mu^a = (\mathsf{p}, A_x, A_y)$. At orders $\mathcal{O}(\epsilon^0)$ and $\mathcal{O}(\epsilon)$, the equations become

$$\frac{\partial \mu_0^a}{\partial \phi} = 0\,, \tag{6.10}$$

$$\frac{\partial \mu_0^a}{\partial \tilde{\phi}} + \frac{\partial \mu_1^a}{\partial \phi} = F^a(\phi, \mu_0^b)\,, \tag{6.11}$$

which we solve order by order by first splitting the solution into a secular and an oscillatory contribution $\mu_\ell^a = \mu_{\ell,\text{sec}}^a(\tilde{\phi}) + \mu_{\ell,\text{osc}}^a(\phi, \tilde{\phi})$. Equation (6.10) then mandates that $\mu_0^a = \mu_{0,\text{sec}}^a(\tilde{\phi})$, i.e. the orbital elements are constants on conservative Keplerian ellipses. We then use that μ_1^a and F^a are periodic in ϕ to orbit average Eq. (6.11), integrating out any oscillatory effects, which then yields a differential equation for $\mu_{0,\text{sec}}^a$, specifically

$$\frac{d\mathsf{p}_0}{d\tilde{\phi}} = -\frac{1}{\mathsf{p}_0^{3/2}}\left[8 + 7\left(A_{x,0}^2 + A_{y,0}^2\right)\right]\,, \tag{6.12}$$

$$\frac{dA_{x,0}}{d\tilde{\phi}} = -\frac{A_{x,0}}{24\mathsf{p}_0^{5/2}}\left[304 + 121\left(A_{x,0}^2 + A_{y,0}^2\right)\right] \,, \tag{6.13}$$

$$\frac{dA_{y,0}}{d\tilde{\phi}} = -\frac{A_{y,0}}{24\mathsf{p}_0^{5/2}}\left[304 + 121\left(A_{x,0}^2 + A_{y,0}^2\right)\right] \,, \tag{6.14}$$

$$\frac{d\mathsf{t}_{-1}}{d\tilde{\phi}} = \left(\frac{\mathsf{p}_0}{1 - A_{x,0}^2 - A_{y,0}^2}\right)^{3/2} \,. \tag{6.15}$$

This system is the same as the orbit-averaged equations obtained from applying the balance laws to the gravitational wave fluxes, and moreover, it is independent of the gauge parameters (a, b). Equations (7)-(8) can be combined with the definition of the eccentricity in terms of the norm of the Runge-Lenz vector to obtain the leading-order secular change of the orbital eccentricity, i.e. to obtain the classic result by Peters [129] and the gravitational wave circularization of binaries. Thus, to leading order in ϵ, the secular evolution of the orbital elements is governed by the orbit-averaged balance law formalism.

At this stage, we have not fully solved Eq. (6.11). Recall, that we split μ_ℓ^a into secular and oscillatory pieces, and apply this to Eq. (6.11) for μ_1^a, we have

$$\frac{d\mu_{1,\text{osc}}(\phi, \tilde{\phi})}{d\phi} = F^a[\phi, \mu_b^a(\tilde{\phi})] - \langle F^a \rangle [\mu^b(\tilde{\phi})] \,, \tag{6.16}$$

where we have used the fact that $d\mu_0^a/d\tilde{\phi}$ is given by the average of Eq. (6.11). We can immediately integrate this to obtain the oscillatory contributions to μ_1^a, specifically

$$\mathsf{p}_{1,\text{osc}}(\phi, \tilde{\phi}) = -\frac{1}{\mathsf{p}_0(\tilde{\phi})^{3/2}} \sum_{n=1}^{3} \frac{1}{n} \left\{ k_p^{c,n}[\mu_0^b(\tilde{\phi})] \sin(n\phi) - k_p^{s,n}[\mu_0^b(\tilde{\phi})] \cos(n\phi) \right\} \,, \tag{6.17}$$

$$A_{x,y}^{1,\text{osc}}(\phi, \tilde{\phi}) = -\frac{1}{\mathsf{p}_0(\tilde{\phi})^{5/2}} \sum_{n=1}^{5} \frac{1}{n} \left\{ k_{x,y}^{c,n}[\mu_0^b(\tilde{\phi})] \sin(n\phi) - k_{x,y}^{s,n}[\mu_0^b(\tilde{\phi})] \cos(n\phi) \right\} \,. \tag{6.18}$$

Notice that these functions are not independent of $\tilde{\phi}$, but depend on it through the purely secularly changing $\mu_0^a(\tilde{\phi})$. The procedure described above can be taken systematically to any order in ϵ by keeping higher-order terms in the expansion and using the lower-order in ϵ solutions.

We are here specifically interested in the evolution of the orbital eccentricity. Expanding its definition in terms of the norm of the Runge-Lenz vector, we find

$$\begin{aligned} e^2 = & \left[A_{x,0}(\tilde{\phi})^2 + A_{y,0}(\tilde{\phi})^2\right] + 2\epsilon\left[A_{x,0}(\tilde{\phi})A_{x,1}(\phi,\tilde{\phi}) + A_{y,0}(\tilde{\phi})A_{y,1}(\phi,\tilde{\phi})\right] \\ & + \epsilon^2\left[A_{x,1}(\phi,\tilde{\phi})^2 + A_{y,1}(\phi,\tilde{\phi})^2 + 2A_{x,0}(\tilde{\phi})A_{x,2}(\phi,\tilde{\phi}) + 2A_{y,0}(\tilde{\phi})A_{y,2}(\phi,\tilde{\phi})\right] \, , \end{aligned} \tag{6.19}$$

keeping terms up to $\mathcal{O}(\epsilon^2)$. In order to better understand the secular growth seen in Fig. 6.1, it is instructive to study how each of these terms behaves as a function of time. To do this, we will seek solutions to the equations obtained by the multiple scale analysis in a low eccentricity limit. We will work to leading order in low eccentricity, which is equivalent to working to leading order in the Runge-Lenz vector. We take $(A_{x,0}, A_{y,0}, e_0) \to \lambda(A_{x,0}, A_{y,0}, e_0)$ with λ an order keeping parameter, and work to leading order in λ.

First consider the leading order equations, given by Eqs. (6.12)-(6.15). It is useful to use one of the functions $(\mathsf{p}_0, A_{x,0}, A_{y,0}, \mathsf{t}_{-1})$ as a proxy for the long variable $\tilde{\phi}$. We choose $A_{x,0}$ for this, and obtain the equations $d\mu_0/dA_{x,0}$ by taking $(d\mu_0/d\tilde{\phi})/(dA_{x,0}/d\tilde{\phi})$, specifically

$$\frac{d\mathsf{p}_0}{dA_{x,0}} = \frac{12\mathsf{p}_0}{19A_{x,0}} \, , \tag{6.20}$$

$$\frac{dA_{y,0}}{dA_{x,0}} = \frac{A_{y,0}}{A_{x,0}} \, , \tag{6.21}$$

$$\frac{d\mathsf{t}_{-1}}{dA_{x,0}} = -\frac{3\mathsf{p}_0}{38A_{x,0}} \, . \tag{6.22}$$

The solution for $A_{y,0}(\tilde{\phi})$ in terms of $A_{x,0}(\tilde{\phi})$ can be obtained immediately, using the initial conditions $[A_{x,0}(0) = e_{\rm in}\cos(\omega_{\rm in}), A_{y,0}(0) = e_{\rm in}\sin(\omega_{\rm in})]$, specifically

$$A_{y,0}(\tilde{\phi}) = A_{x,0}(\tilde{\phi})\tan(\omega_{\rm in})\,, \tag{6.23}$$

where $\omega_{\rm in}$ is the initial longitude of pericenter. This can be inserted into the remaining two equations, which can be solved to obtain

$$\mathsf{p}_0(\tilde{\phi}) = \mathsf{p}_{\rm in}\left[\frac{A_{x,0}(\tilde{\phi})}{e_{\rm in}\cos(\omega_{\rm in})}\right]^{12/19}\,, \tag{6.24}$$

$$\mathsf{t}_{-1}(\tilde{\phi}) = \frac{\mathsf{p}_{\rm in}^4}{32}\left\{1 - \left[\frac{A_{x,0}(\tilde{\phi})}{e_{\rm in}\cos(\omega_{\rm in})}\right]^{48/19}\right\}\,, \tag{6.25}$$

where $\mathsf{p}_{\rm in}$ is the initial value of $\mathsf{p}_0(\tilde{\phi})$. Similarly, we may obtain the relationship between $\tilde{\phi}$ and $A_{x,0}$, by solving $(dA_{x,0}/d\tilde{\phi})^{-1}$, specifically

$$\tilde{\phi} = \frac{\mathsf{p}_{\rm in}^{5/2}}{20}\left\{1 - \left[\frac{A_{x,0}(\tilde{\phi})}{e_{\rm in}\cos(\omega_{\rm in})}\right]^{30/19}\right\}\,. \tag{6.26}$$

This completes the solution of the leading order MSA equations.

At first order in the multiple scale analysis, both secular and oscillatory contributions enter the Runge-Lenz vector, and consequently, the orbital eccentricity. To obtain the oscillatory terms, we have to insert the solutions to the leading order equations into Eqs. (6.17)-(6.18). Expanding these in the low eccentricity limit, we obtain

$$\mathsf{p}_{1,\rm osc} = -\frac{e_{\rm in}}{3\mathsf{p}_{\rm in}^{3/2}}\left[\frac{A_{x,0}(\tilde{\phi})}{e_{\rm in}\cos(\omega_{\rm in})}\right]^{1/19}(84 + 35a - 15b)\,\sin(\phi - \omega_{\rm in})\,, \tag{6.27}$$

$$A_{x,1}^{\rm osc} = -\frac{8}{\mathsf{p}_{\rm in}^{5/2}}\left[\frac{A_{x,0}(\tilde{\phi})}{e_{\rm in}\cos(\omega_{\rm in})}\right]^{-30/19}\sin(\phi)\,, \tag{6.28}$$

$$A_{y,1}^{\rm osc} = \frac{8}{\mathsf{p}_{\rm in}^{5/2}} \left[\frac{A_{x,0}(\tilde{\phi})}{e_{\rm in} \cos(\omega_{\rm in})} \right]^{-30/19} \cos(\phi)\,. \tag{6.29}$$

Obtaining the first order secular terms requires one to go to higher order in the multiple scale analysis. We do not provide the results here, since they are rather lengthy and unilluminating, and can straightforwardly be obtained by following the methods given here. Their behavior in the low eccentricity limit is identical to that of the oscillatory terms.

Several important features are present in this analysis. First, notice that $A_{x,0} = \mathcal{O}(v^0/c^0) = A_{y,0}$, while $A_{x,1} = \mathcal{O}(v^5/c^5) = A_{y,1}$ and $A_{x,2} = \mathcal{O}(v^{10}/c^{10}) = A_{y,2}$. This is because each new order in ϵ is suppressed by the ratio of orbital timescale to the radiation-reaction timescale, which is of $\mathcal{O}(v^5/c^5)$. Second, both $A_{x,0}$ and $A_{y,0}$ are linear in the eccentricity, while all higher-order terms are independent of the eccentricity. This is because to leading-order in ϵ the is eccentricity $e = (A_{x,0}^2 + A_{y,0}^2)^{1/2}$. Third, although terms linear in $A_{x,1}$ and $A_{y,1}$ (in the second line of Eq. (6.19)), or linear in $A_{x,2}$ and $A_{y,2}$ (in the third and fourth lines of Eq. (6.19)) contain oscillatory contributions that average out on the orbital timescale, terms quadratic in $A_{x,1}$ and $A_{y,1}$ at $\mathcal{O}(\epsilon^2)$ do not average out and produce secular growth in the orbital eccentricity. Moreover, even the linear terms contain secular contributions $(A_{x,1}^{\rm sec}, A_{y,1}^{\rm sec})$ at $\mathcal{O}(\epsilon)$ that do not vanish and also contribute to the secular growth; however, this contribution is smaller than that of the third line in Eq. (6.19). Finally, notice that while $\mathsf{p}_{1,\rm osc}$ depends on the gauge parameters (a, b) and can be gauge transformed away, $A_{x,y}^{1,\rm osc}$ are gauge independent and thus cannot be removed via a gauge transformation.

We thus arrive at the physical and mathematical reason for the secular growth in the eccentricity shown in Fig. 6.1. The leading-order contribution to the orbital eccentricity, $(A_{x,0}^2 + A_{y,0}^2)$, does indeed dominate for general initial eccentricities, leading to a monotonic decrease in time, as expected from the work of Peters [129] and subsequent work at higher PN order [31]. Eventually, however, this monotonic decrease forces the eccentricity to be small enough that the leading-order $(A_{x,0}^2 + A_{y,0}^2)$ terms become smaller than terms higher-order in ϵ, forcing the eccentricity to grow monotonically. This occurs when $\mathcal{O}(A_{i,0}^2) = \mathcal{O}(A_{i,0}A_{i,1}) = \mathcal{O}(A_{i,1}^2)$ for any component of the Runge-Lenz vector, which translates to $e \sim v^5/c^5$ because $A_{i,0}^2 \sim e^2$, $A_{i,0}A_{i,1} \sim e\ v^5/c^5$ and $A_{i,1}^2 \sim v^{10}/c^{10}$. Indeed, we see in Fig. 6.1 that the secular growth starts when the eccentricity has decayed to roughly 10^{-3}, so inverting $e \sim v^5/c^5$ this would corresponds to a velocity of $v \sim e^{1/5}c \approx 0.25c$, which corresponds to a semi-latus rectum of roughly $15M$, matching the results shown in the Figure. Therefore, *when the eccentricity becomes small enough, the radiation-reaction force sources a secular growth in the eccentricity that indicates a break down of the orbit-averaged approximation.*

Properties of Secular Growth

The secular growth of the eccentricity is dependent on the mass ratio, as can be seen from Fig. 6.1. In fact, in our analysis, one can make the mass ratio sufficiently small, such that the secular growth does not occur before the system reaches the last stable orbit. Let us then refine our approximation for the critical velocity at which the eccentricity of a binary switches from secular decay to secular growth, $e \sim v^5/c^5$, by including the mass-ratio dependence. Doing so, we find that the critical semi-latus rectum at which this occurs is

$$\mathsf{p}_{\rm crit} = \left(\frac{64\,\eta}{5\,e_{\rm in}}\right)^{12/49} \mathsf{p}_{\rm in}^{19/49} \left(1 - \frac{435}{2888} e_{\rm in}^2\right) \tag{6.30}$$

where $\mathsf{p}_{\rm in} = \mathsf{p}(\tilde{\phi} = 0)$ is the initial semi-latus rectum and we set $p^\star = M$. For the systems we consider in Fig. 6.1, these correspond to $\mathsf{p}_{\rm crit} = 13.12$ for the equal mass case and $\mathsf{p}_{\rm crit} = 10.48$ for the $\eta = 1/10$ case, which agrees with Fig. 6.1. If the critical separation is smaller than the separation at the last stable orbit, then the secular growth will not occur in the inspiral phase. Therefore, there is a separatrix in the initial separation that defines where secular growth occurs in the inspiral, specifically

$$\mathsf{p}_{\rm in,sep} = 6^{49/19} \left(\frac{5\, e_{\rm in}}{64\, \eta} \right)^{12/19} \left(1 + \frac{21315}{54872} e_{\rm in}^2 \right) , \tag{6.31}$$

when we set $p^\star = M$. Figure 6.2 shows this separatrix for different symmetric mass ratios, where the shaded regions correspond to areas where secular growth does not occurs. Observe that if the mass ratio is sufficiently small, or the initial eccentricity is sufficiently large, the growth does not occur before the last stable orbit.

The secular growth discovered here is *not* an artifact of the multiple scale expansion, or of the PN approximation, or of a gauge choice. Our multiple scale analysis is valid when the ratio of the timescale is less than the value of the expansion parameter, i.e. $T_{\rm orb}/T_{\rm RR} \ll \epsilon$. We have verified numerically that this inequality is satisfied in the entire domain for the systems in Fig. 6.1, reaching its worst at the last stable orbit where $T_{\rm orb}/T_{\rm RR} \sim 0.2$ and $\epsilon = 0.4$ for equal-mass binaries. The PN approximation is valid provided the orbital velocities are small, i.e. $v/c = GM/(rc^2) \ll 1$, but the secular growth begins to occur roughly when $v/c \approx 1/4$–$1/3$. We have verified that the PN approximation is not the culprit of the secular growth by including the first PN corrections to both conservative and dissipative dynamics, namely $\vec{f}_{\rm 1PN}$ and $\vec{f}_{\rm 3.5PN}$ [94]. When including these higher PN order terms and numerically solving the osculating equations , we still find the same secular growth in the eccentricity at late times, with the PN corrections only

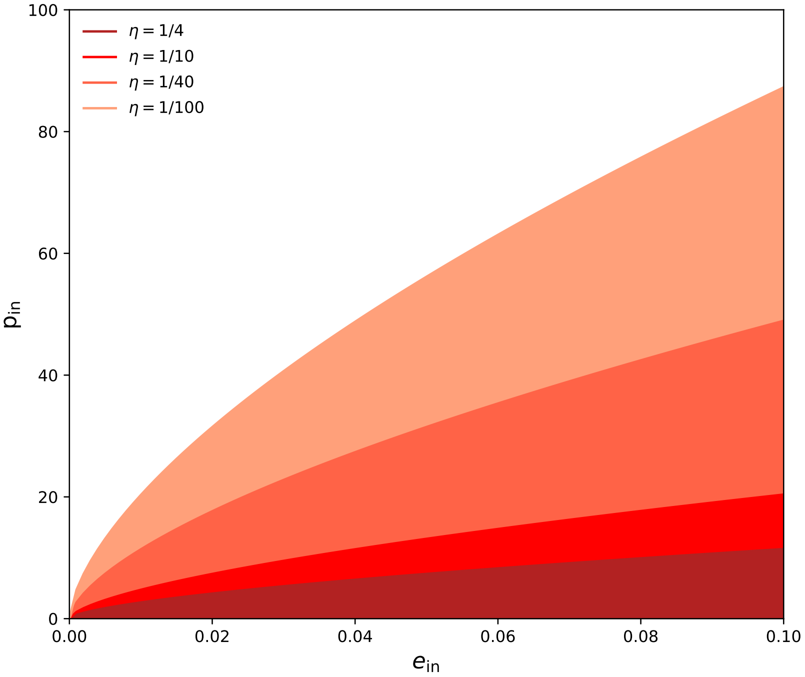

Figure 6.2: Separatrix between secular decay and secular growth for binary systems of different symmetric mass ratio in the initial separation-initial eccentricity ($p_{\rm in}$–$e_{\rm in}$) plane. The shaded regions below each line corresponds to areas where secular growth does not occur.

introducing a small modification. A non-averaged multiple-scale analysis, as that of Eqs. (6.10) and (6.11), is gauge dependent [117, 131], but as can be seen from Eq. (6.18), there is not enough gauge freedom to removed the secular growth found here.

The secular growth of eccentricity has been observed in two other scenarios:

(i) Extreme mass ratio inspirals (EMRIs) and self-force calculations [27, 65, 147], and

(ii) Comparable-mass inspirals in the PN formalism of Lincoln & Will [103].

The secular growth we found here, however, is *not* the same as either of these two other phenomena previously observed. Regarding (i), the EMRI analysis employed orbit-averaged radiation-reaction to evolve the inspiral, and as we explain here, the secular growth we observed vanishes identically with orbit averaging. Furthermore, the growth in eccentricity in the EMRI case scales as $e\ \eta$ and occurs very close to the ISCO, while the growth we see scales as $e^0\eta^2$, and becomes important well before the ISCO is reached for comparable mass systems. Regarding (ii), Lincoln & Will's methodology (osculating Keplerian orbits with conservative 1PN and 2PN forces) does not allow for a clean physical interpretation of secular growth because a circular orbit in this formalism does not have zero Keplerian orbital eccentricity [131]. This is why modern post-Newtonian calculations are performed in the quasi-Keplerian (QK) formalism of Damour and Deruelle [67, 68], in which circular orbits do correspond to zero QK eccentricities. These modern calculations have shown that the QK eccentricities monotonically decrease as the binary inspirals when orbit-averaging radiation reaction [31]. Thus, the results of Lincoln & Will are a consequence of their orbital parameterization and are unrelated to the secular growth found in this paper.

The implications of the secular growth found here are important both from a fundamental physical and mathematical standpoint, as well as from an observational standpoint. Physically and mathematically, our results suggest that the idea of a circular or a quasi-circular orbit is a fiction. If we start with a circular orbit, $e_{\rm in} = 0$, the orbit *will not* remain circular through the late inspiral, and the eccentricity will grow secularly, as can be seen in Fig. 6.3. This figure shows evolutions for the same systems as those presented in Fig. 6.1, only starting with zero initial eccentricity, $e_{\rm in} = 0$ to double-precision. This secular growth is in stark contrast to what one would infer using the orbit-averaged approximation, where the orbit remains circular all throughout the inspiral, and the coalescence is said to be "quasi-circular." Currently, full numerical relativity simulations made by the Simulating Extreme Spacetimes [101] collaboration may have enough resolution to confirm the secular growth, although its existence in those simulations has not yet been verified. All statements about the non-existence of circular orbits made here are absolutely distinct from the astrophysical idea that complicated stellar dynamics in galaxies perturb a binary's evolution away from circularity; our results indicate that, *even in complete isolation*, binary systems cannot remain circular in the late inspiral.

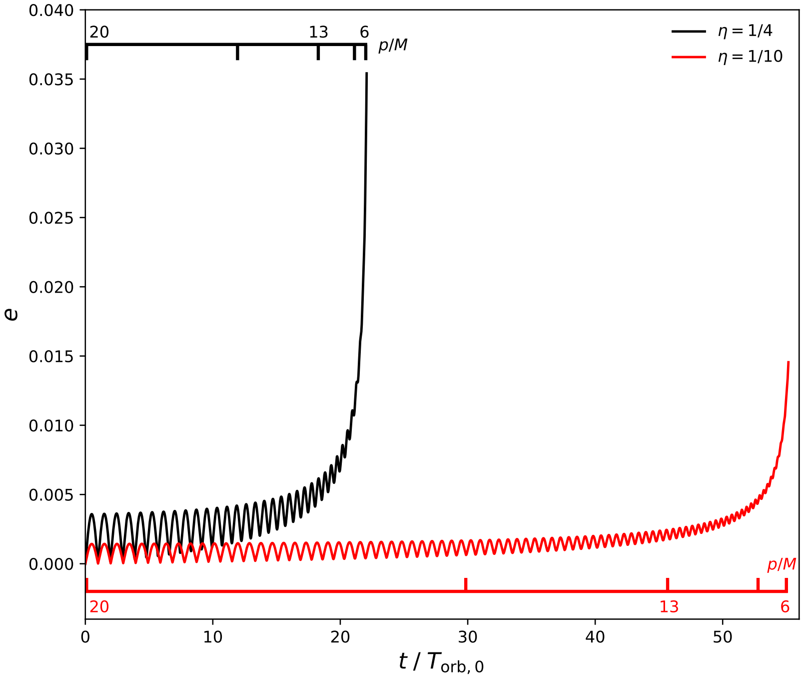

Figure 6.3: Temporal evolution of the eccentricity for initially circular binaries ($e_{\text{in}} = 0$), obtained through the numerical evolution of the the osculating orbits equations.

Eccentricity has an observable effect on the GWs observed by detectors. For a purely circular orbit, and at leading PN order, the waveform only contains one harmonic with frequency twice that of the orbital frequency. For eccentric systems, the waveform contains power in additional harmonics of the orbital frequency beyond just the second harmonic. Further, for sufficiently eccentric systems, the second harmonic does not correspond to the peak harmonic of the GW power spectrum. At leading PN order, it is the osculating Keplerian eccentricity e that governs this extra harmonic structure. As we've discussed, the secular growth found here is also independent of the choice of radiation reaction gauge. Putting all of this together indicates that the secular growth in eccentricity should have an observable effect on the GWs detected from eccentric compact binaries.

From an observational standpoint, our results have an impact on the extraction of the eccentricity from future gravitational wave signals. The gravitational wave observations made by the advanced LIGO and Virgo detectors have not yet been sensitive enough to allow for a measurement of the eccentricity. But as these detectors are improved to achieve design sensitivity and third-generation detectors are built, a measurement of the orbital eccentricity will become a reality. The inclusion of the secular growth of the eccentricity in waveform models for parameter estimation studies may enhance our ability to measure the eccentricity. Such an inclusion is now possible thanks to the analysis carried out in this paper, which then also allows for a detailed data analysis investigation of the accuracy to which eccentricity could be measured by future detectors. These ideas will constitute the basis of future studies.

SUMMARY

In this thesis, we have set out to solve the problem of how to model the inspiral and subsequent GW emission from eccentric binaries, focusing on two regimes: (i) the early inspiral of highly eccentric binaries formed in dynamical captures and (ii) the late inspiral of eccentric systems. The details of this modeling require a complete understanding of radiation reaction in such systems. We began with an overview of the mathematical structure of radiation reaction in eccentric systems. The flux of GWs is governed by the time-varying multipole moments of the binary system, which is well described within the PN formalism. These multipole moments must be supplemented by an orbital parametrization of the binary. Within the PN framework, this is done using the QK parametrization, which is known to 3PN order for eccentric binaries. One complication that arises in the modeling of the conservative dynamics of eccentric binaries is the solutions to Kepler's equation, a transcendental equation giving the relationship between time and the eccentric anomaly of the orbit. To get around this, one works within a Fourier series decomposition of the multipole moments, giving the multipoles as infinite series expressions, and completing the description of radiation reaction of the binary.

The above description of the orbital dynamics creates a problem in the radiation reaction of the binary, namely that the GW fluxes from the so-called tail effects become infinite summations of Bessel functions. These expression do not lend themselves to evaluation easily. Prior to the work presented in this thesis, one either had to evaluate them numerically or work in a low eccentricity expansion. These methods are not well suited if we desire to create analytic waveform models of compact binaries with generic eccentricity. To that end, we provided a method of resumming the GW tail effects in the energy and angular momentum fluxes in

Ch. 3. This method relies on the uniform asymptotic expansion of Bessel functions, and allows us to generate superasymptotic series for the tail enhancement factors. We further showed how these superasymptotic expressions can be matched to analytic results in the low eccentricity limit to obtain hyperasymptotic series. By comparing our hyperasymptotic series to a numerical evaluation of the tail enhancement factors, we found these expression to be accurate to more than one part in 10^8, making these currently the most accurate analytic expressions for the tail enhancement factors known.

With these expressions in hand, we may now apply them to the creation of analytic models of the GW emission of eccentric binaries to high PN order. In this thesis, we focused on binary systems formed via dynamical capture in dense stellar environments. These binaries will necessarily have high orbital eccentricity, and the GW emission from these systems resembles a set of discrete bursts centered around pericenter passage. One detection strategy for these events, although suboptimal, is to use power stacking, whereby the power in each bursts in combined to amplify the SNR of the individual bursts. To do this, we require an analytic model of where the bursts will occur in the time-frequency space of our detectors. In Ch. 4, we developed such a model, which we refer to as the burst model, within the context of GR. We began by considering these GW bursts with the conservative and dissipative dynamics both governed by only the leading PN effects. In this sense, we constructed a Newtonian order burst model by characterizing each burst via a time-frequency centroid and a two-dimensional time-frequency box. The time centroids of the burst are related by the Newtonian orbital period of the binary, while the frequency centroids are related to the peak of the GW power spectrum. The widths of the boxes may be chosen to capture a certain fraction of the total power in each burst, and are proportional to the pericenter passage timescale and the frequency of the burst. We found that these time-frequency parameters must be supplemented by a model of the orbital evolution of the binary. We model the evolution of the binary by assuming that the GW burst, and subsequently any changes to the orbital parameters, are instantaneous at pericenter passage. This allows us to model the evolution of the binary as a discrete set of Keplerian ellipses, and to map parameters of one orbit to those of the next through the inclusion of radiation reaction. In this way, we developed a recursive model for GW bursts from highly eccentric binaries at Newtonian order.

If we desire to use such a model for data analysis, then we would need the burst model to be as accurate as possible compared to Nature. To that end, we extended the Newtonian burst model into the PN formalism in Ch. 4. We showed that the PN burst sequence is simply given by a parametrized deformation of the Newtonian burst sequence, and developed a generic algorithm for computing the burst model at arbitrary PN order. Since conservative and dissipative dynamics of eccentric binaries are only known completely to 3PN order, we used this generic algorithm to develop a burst model complete to this order. We further showed that this model is accurate to better than ten percent when compared to numerical evolutions of the PN radiation reaction equations.

As an application of what the burst model can tell us, we considered the case of modified theories of gravity and our ability to constrain these theories with highly eccentric binaries. To do this, we developed a ppE burst model by considering generic modifications to the conservative and dissipative dynamics of eccentric binaries in Ch. 5. The ppE burst model is then given by a parametrized deformation of the GR burst model, and any modified theories of gravity can be captured by eight parameters. We showed that this parametrization captures the deviation from modified theories by considering two test case, namely EDGB gravity and Brans-Dicke theory, and placed some projected constraints on the coupling constants of these theories.

Finally, as binaries inspiral, it is generally considered that the orbital eccentricity will decrease monotonically in time. In Ch. 6, we computed the evolution of the orbital eccentricity using the radiation reaction force at 2.5PN order and showed that the eccentricity can experience secular growth during the last few orbital cycles, before the binary reaches the last stable orbit and plunges. By working in a multiple scale analysis, we showed that this growth comes from the nonlinear coupling of first order oscillatory terms and higher order secular terms beyond the orbit averaged approximation. Further, we briefly discussed the prospects of being able to extract such an effect with future detections by ground based detectors.

The LIGO and VIRGO detectors have at last ushered in the era of GW astronomy. As these detectors are improved, and are joined by detectors currently under construction, the detection of eccentric binaries will become a reality. The work in this thesis has moved us closer to such a detection, and the possibility of extracting important information about the astrophysical and gravitational dynamics of eccentric binaries.

REFERENCES CITED

[1] Geo600. `www.geo600.uni-hannover.de`.

[2] LIGO. `www.ligo.caltech.edu`.

[3] VIRGO. `www.virgo.infn.it`.

[4] J. Aasi et al. Search for gravitational waves from binary black hole inspiral, merger, and ringdown in LIGO-Virgo data from 2009-2010. *Phys. Rev.*, D87(2):022002, 2013.

[5] J. Abadie et al. Predictions for the Rates of Compact Binary Coalescences Observable by Ground-based Gravitational-wave Detectors. *Class.Quant.Grav.*, 27:173001, 2010.

[6] J. Abadie et al. Search for gravitational waves from binary black hole inspiral, merger and ringdown. *Phys. Rev.*, D83:122005, 2011. [Erratum: Phys. Rev.D86,069903(2012)].

[7] J. Abadie et al. Search for Gravitational Waves from Low Mass Compact Binary Coalescence in LIGO's Sixth Science Run and Virgo's Science Runs 2 and 3. *Phys. Rev.*, D85:082002, 2012.

[8] B. Abbott et al. LIGO: The Laser interferometer gravitational-wave observatory. *Rept.Prog.Phys.*, 72:076901, 2009.

[9] B. Abbott et al. GW170817: Observation of Gravitational Waves from a Binary Neutron Star Inspiral. *Phys. Rev. Lett.*, 119(16):161101, 2017.

[10] B. P. Abbott et al. Binary Black Hole Mergers in the first Advanced LIGO Observing Run. *Phys. Rev.*, X6(4):041015, 2016.

[11] B. P. Abbott et al. Observation of Gravitational Waves from a Binary Black Hole Merger. *Phys. Rev. Lett.*, 116(6):061102, 2016.

[12] B. P. Abbott et al. Supplement: The Rate of Binary Black Hole Mergers Inferred from Advanced LIGO Observations Surrounding GW150914. *Astrophys. J. Suppl.*, 227(2):14, 2016.

[13] B. P. Abbott et al. Tests of general relativity with GW150914. *Phys. Rev. Lett.*, 116(22):221101, 2016.

[14] B. P. Abbott et al. The Rate of Binary Black Hole Mergers Inferred from Advanced LIGO Observations Surrounding GW150914. *Astrophys. J.*, 833(1):L1, 2016.

[15] B. P. Abbott et al. Upper Limits on the Rates of Binary Neutron Star and Neutron Star-black Hole Mergers From Advanced Ligo's First Observing run. *Astrophys. J.*, 832(2):L21, 2016.

[16] B. P. Abbott et al. GW170104: Observation of a 50-Solar-Mass Binary Black Hole Coalescence at Redshift 0.2. *Phys. Rev. Lett.*, 118(22):221101, 2017.

[17] B. P. Abbott et al. GW170814: A Three-Detector Observation of Gravitational Waves from a Binary Black Hole Coalescence. *Phys. Rev. Lett.*, 119(14):141101, 2017.

[18] B. P. Abbott et al. A Search for Tensor, Vector, and Scalar Polarizations in the Stochastic Gravitational-Wave Background. 2018.

[19] Abbott, B. P. et. al. Observation of Gravitational Waves from a Binary Black Hole Merger. *Phys. Rev. Lett.*, 116:061102, Feb 2016.

[20] A. Abramovici, W. E. Althouse, R. W. Drever, Y. Gursel, S. Kawamura, et al. LIGO: The Laser interferometer gravitational wave observatory. *Science*, 256:325–333, 1992.

[21] F. Acernese et al. Advanced Virgo: a second-generation interferometric gravitational wave detector. *Class.Quant.Grav.*, 32(2):024001, 2015.

[22] P. Ajith et al. The NINJA-2 catalog of hybrid post-Newtonian/numerical-relativity waveforms for non-precessing black-hole binaries. *Class. Quant. Grav.*, 29:124001, 2012. [Erratum: Class. Quant. Grav.30,199401(2013)].

[23] J. M. Antognini, B. J. Shappee, T. A. Thompson, and P. Amaro-Seoane. Rapid Eccentricity Oscillations and the Mergers of Compact Objects in Hierarchical Triples. *Mon. Not. Roy. Astron. Soc.*, 439(1):1079–1091, 2014.

[24] F. Antonini, S. Chatterjee, C. L. Rodriguez, M. Morscher, B. Pattabiraman, V. Kalogera, and F. A. Rasio. Black hole mergers and blue stragglers from hierarchical triples formed in globular clusters. *Astrophys. J.*, 816(2):65, 2016.

[25] F. Antonini, N. Murray, and S. Mikkola. Black Hole Triple Dynamics: A Breakdown of the Orbit Average Approximation and Implications for Gravitational Wave Detections. *The Astrophysical Journal*, 781:45, Jan. 2014.

[26] F. Antonini, N. Murray, and S. Mikkola. Black hole triple dynamics: breakdown of the orbit average approximation and implications for gravitational wave detections. *Astrophys. J.*, 781:45, 2014.

[27] T. Apostolatos, D. Kennefick, E. Poisson, and A. Ori. Gravitational radiation from a particle in circular orbit around a black hole. 3: Stability of circular orbits under radiation reaction. *Phys. Rev.*, D47:5376–5388, 1993.

[28] K. Arun, L. Blanchet, B. R. Iyer, and M. S. Qusailah. Inspiralling compact binaries in quasi-elliptical orbits: The Complete 3PN energy flux. *Phys.Rev.*, D77:064035, 2008.

[29] K. Arun, L. Blanchet, B. R. Iyer, and M. S. Qusailah. Tail effects in the 3PN gravitational wave energy flux of compact binaries in quasi-elliptical orbits. *Phys.Rev.*, D77:064034, 2008.

[30] K. G. Arun, L. Blanchet, B. R. Iyer, and M. S. S. Qusailah. The 2.5PN gravitational wave polarisations from inspiralling compact binaries in circular orbits. *Class. Quant. Grav.*, 21:3771–3802, 2004. [Erratum: Class. Quant. Grav.22,3115(2005)].

[31] K. G. Arun, L. Blanchet, B. R. Iyer, and S. Sinha. Third post-Newtonian angular momentum flux and the secular evolution of orbital elements for inspiralling compact binaries in quasi-elliptical orbits. *Phys.Rev.*, D80:124018, 2009.

[32] Y. Aso, Y. Michimura, K. Somiya, M. Ando, O. Miyakawa, et al. Interferometer design of the KAGRA gravitational wave detector. 2013.

[33] C. M. Bender and S. A. Orszag. *Advanced mathematical methods for scientists and engineers 1, Asymptotic methods and perturbation theory.* Springer, New York, 1999.

[34] L. Bernard, L. Blanchet, A. Bohé, G. Faye, and S. Marsat. Conservative Dynamics of Binary Systems of Compact Objects at the Fourth Post-Newtonian Order. 2017.

[35] L. Bernard, L. Blanchet, G. Faye, and T. Marchand. Center-of-Mass Equations of Motion and Conserved Integrals of Compact Binary Systems at the Fourth Post-Newtonian Order. 2017.

[36] B. Bertotti, L. Iess, and P. Tortora. A test of general relativity using radio links with the Cassini spacecraft. *Nature*, 425:374, 2003.

[37] L. Blanchet. Radiative gravitation fields in general relativity ii. asymptotic behaviour at future null infinity. *Proceedings of the Royal Society of London A: Mathematical, Physical and Engineering Sciences*, 409(1837):383–399, 1987.

[38] L. Blanchet. Second postNewtonian generation of gravitational radiation. *Phys. Rev.*, D51:2559–2583, 1995.

[39] L. Blanchet. Gravitational wave tails of tails. *Class. Quant. Grav.*, 15:113–141, 1998. [Erratum: Class. Quant. Grav.22,3381(2005)].

[40] L. Blanchet. Quadrupole-quadrupole gravitational waves. *Class. Quant. Grav.*, 15:89–111, 1998.

[41] L. Blanchet. Gravitational radiation from post-Newtonian sources and inspiralling compact binaries. *Living Rev. Rel.*, 9:4, 2006.

[42] L. Blanchet. Gravitational Radiation from Post-Newtonian Sources and Inspiralling Compact Binaries. *Living Rev.Rel.*, 17:2, 2014.

[43] L. Blanchet and T. Damour. Radiative gravitational fields in general relativity i. general structure of the field outside the source. *Philosophical Transactions of the Royal Society of London A: Mathematical, Physical and Engineering Sciences*, 320(1555):379–430, 1986.

[44] L. Blanchet and T. Damour. Tail-transported temporal correlations in the dynamics of a gravitating system. *Phys. Rev. D*, 37:1410–1435, Mar 1988.

[45] L. Blanchet and T. Damour. Hereditary effects in gravitational radiation. *Phys.Rev.*, D46:4304–4319, 1992.

[46] L. Blanchet, T. Damour, G. Esposito-Farese, and B. R. Iyer. Gravitational radiation from inspiralling compact binaries completed at the third post-Newtonian order. *Phys. Rev. Lett.*, 93:091101, 2004.

[47] L. Blanchet, T. Damour, and B. R. Iyer. Gravitational waves from inspiralling compact binaries: Energy loss and wave form to second postNewtonian order. *Phys.Rev.*, D51:5360, 1995.

[48] L. Blanchet, G. Faye, B. R. Iyer, and B. Joguet. Gravitational wave inspiral of compact binary systems to 7/2 postNewtonian order. *Phys. Rev.*, D65:061501, 2002. [Erratum: Phys. Rev.D71,129902(2005)].

[49] L. Blanchet, B. R. Iyer, and B. Joguet. Gravitational waves from inspiraling compact binaries: Energy flux to third post-Newtonian order. *Phys. Rev. D.*, 65(6):064005–+, Mar. 2002.

[50] L. Blanchet and G. Schaefer. Gravitational wave tails and binary star systems. *Class. Quant. Grav.*, 10:2699–2721, 1993.

[51] J. P. Boyd. The devil's invention: Asymptotic, superasymptotic and hyperasymptotic series. *Acta Applicandae Mathematica*, 56(1):1–98.

[52] C. Brans and R. H. Dicke. Mach's principle and a relativistic theory of gravitation. *Phys. Rev.*, 124:925–935, 1961.

[53] D. A. Brown, P. Kumar, and A. H. Nitz. Template banks to search for low-mass binary black holes in advanced gravitational-wave detectors. *Phys. Rev.*, D87:082004, 2013.

[54] D. A. Brown and P. J. Zimmerman. Effect of eccentricity on searches for gravitational waves from coalescing compact binaries in ground-based detectors. *Phys. Rev. D.*, 81(2):024007, Jan. 2010.

[55] W. L. Burke. *The coupling of gravitational radiation to nonrelativistic sources.* PhD thesis, Caltech, 1969.

[56] W. L. Burke. GRAVITATIONAL RADIATION DAMPING OF SLOWLY MOVING SYSTEMS CALCULATED USING MATCHED ASYMPTOTIC EXPANSIONS. *J. Math. Phys.*, 12:401–418, 1971.

[57] B. Caron, A. Dominjon, C. Drezen, R. Flaminio, X. Grave, et al. The Virgo interferometer. *Class.Quant.Grav.*, 14:1461–1469, 1997.

[58] S. M. Carrol. *An introduction to general relativity, Spacetime and Geometry.* Pearson - Benjamin Cummings, San Francisco, 2003.

[59] S. Chandrasekhar. The Post-Newtonian Equations of Hydrodynamics in General Relativity. *"Astrophys. J."*, 142:1488, Nov. 1965.

[60] S. Chandrasekhar and F. P. Esposito. The 2.5-POST-NEWTONIAN Equations of Hydrodynamics and Radiation Reaction in General Relativity. *"Astrophys. J."*, 160:153, Apr. 1970.

[61] S. Chandrasekhar and Y. Nutku. The Second Post-Newtonian Equations of Hydrodynamics in General Relativity. *"Astrophys. J."*, 158:55, Oct. 1969.

[62] D. Christodoulou. Nonlinear nature of gravitation and gravitational-wave experiments. *Phys. Rev. Lett.*, 67:1486–1489, Sep 1991.

[63] N. Cornish, L. Sampson, N. Yunes, and F. Pretorius. Gravitational Wave Tests of General Relativity with the Parameterized Post-Einsteinian Framework. 2011. Accepted to Phys. Rev. D.

[64] N. J. Cornish and T. B. Littenberg. BayesWave: Bayesian Inference for Gravitational Wave Bursts and Instrument Glitches. *Class. Quant. Grav.*, 32(13):135012, 2015.

[65] C. Cutler, D. Kennefick, and E. Poisson. Gravitational radiation reaction for bound motion around a schwarzschild black hole. *Phys. Rev.*, D50:3816–3835, 1994.

[66] T. Damour and N. Deruelle. Radiation Reaction and Angular Momentum Loss in Small Angle Gravitational Scattering. *Phys. Lett.*, A87:81, 1981.

[67] T. Damour and N. Deruelle. General relativistic celestial mechanics of binary systems. I: The post- Newtonian motion. *Ann. Inst. Henri Poincaré, Phys. Théor.*, 43:107–132, 1985.

[68] T. Damour and N. Deruelle. General relativistic celestial mechanics of binary systems. II. The post- Newtonian timing formula. *Ann. Inst. Henri Poincaré, Phys. Théor.*, 44:263–292, 1986.

[69] T. Damour, A. Gopakumar, and B. R. Iyer. Phasing of gravitational waves from inspiralling eccentric binaries. *Phys. Rev.*, D70:064028, 2004.

[70] T. Damour, P. Jaranowski, and G. Schafer. Nonlocal-in-time action for the fourth post-Newtonian conservative dynamics of two-body systems. *Phys.Rev.*, D89(6):064058, 2014.

[71] T. Damour and G. Schaefer. Higher Order Relativistic Periastron Advances and Binary Pulsars. *Nuovo Cim.*, B101:127, 1988.

[72] P. A. Evans et al. Swift and NuSTAR observations of GW170817: detection of a blue kilonova. *Science*, 358:1565, 2017.

[73] V. Faraoni and T. P. Sotiriou. Absence of scalar hair in scalar-tensor gravity. 2013.

[74] B. Farr, S. Fairhurst, and B. S. Sathyaprakash. Searching for binary coalescences with inspiral templates: Detection and parameter estimation. *Class. Quant. Grav.*, 26:114009, 2009.

[75] M. Favata. Post-Newtonian corrections to the gravitational-wave memory for quasi-circular, inspiralling compact binaries. *Phys. Rev.*, D80:024002, 2009.

[76] M. Favata. The Gravitational-wave memory from eccentric binaries. *Phys. Rev.*, D84:124013, 2011.

[77] M. Favata. Systematic parameter errors in inspiraling neutron star binaries. *Phys. Rev. Lett.*, 112:101101, 2014.

[78] G. Faye, S. Marsat, L. Blanchet, and B. R. Iyer. The third and a half post-Newtonian gravitational wave quadrupole mode for quasi-circular inspiralling compact binaries. *Class. Quant. Grav.*, 29:175004, 2012.

[79] E. Forseth, C. R. Evans, and S. Hopper. Eccentric-orbit extreme-mass-ratio inspiral gravitational wave energy fluxes to 7PN order. *Phys. Rev.*, D93(6):064058, 2016.

[80] R. Fujita. Gravitational Waves from a Particle in Circular Orbits around a Schwarzschild Black Hole to the 22nd Post-Newtonian Order. *Prog.Theor.Phys.*, 128:971–992, 2012.

[81] D. Garfinkle. A simple estimate of gravitational wave memory in binary black hole systems. *Class. Quant. Grav.*, 33(17):177001, 2016.

[82] A. Giazotto. The Virgo Project: A Wide Band Antenna for Gravitational Wave Detection. *Nucl.Instrum.Meth.*, A289:518–525, 1990.

[83] I. S. Gradshteyn and I. M. Ryzhik. *Table of Integrals, Series, and Products.* Academic Press, 2007.

[84] H. Grote. The status of GEO 600. *Class.Quant.Grav.*, 25:114043, 2008.

[85] G. M. Harry. Advanced LIGO: The next generation of gravitational wave detectors. *Class.Quant.Grav.*, 27:084006, 2010.

[86] S. Hawking. Black holes in the Brans-Dicke theory of gravitation. *Commun.Math.Phys.*, 25:167–171, 1972.

[87] I. Hinder, F. Herrmann, P. Laguna, and D. Shoemaker. Comparisons of eccentric binary black hole simulations with post-Newtonian models. *Phys.Rev.*, D82:024033, 2010.

[88] E. Huerta, P. Kumar, S. T. McWilliams, R. O'Shaughnessy, and N. Yunes. Accurate and efficient waveforms for compact binaries on eccentric orbits. *Phys.Rev.*, D90(8):084016, 2014.

[89] E. A. Huerta and D. A. Brown. Effect of eccentricity on binary neutron star searches in Advanced LIGO. *Phys. Rev.*, D87(12):127501, 2013.

[90] E. A. Huerta et al. Eccentric, nonspinning, inspiral, Gaussian-process merger approximant for the detection and characterization of eccentric binary black hole mergers. *Phys. Rev.*, D97(2):024031, 2018.

[91] R. A. Hulse and J. H. Taylor. Discovery of a pulsar in a binary system. *Astrophys. J.*, 195:L51–L53, 1975.

[92] R. A. Isaacson. Gravitational Radiation in the Limit of High Frequency. I. The Linear Approximation and Geometrical Optics. *Phys. Rev.*, 166:1263–1271, Feb. 1968.

[93] R. A. Isaacson. Gravitational Radiation in the Limit of High Frequency. II. Nonlinear Terms and the Effective Stress Tensor. *Phys. Rev.*, 166:1272–1279, Feb. 1968.

[94] C. Konigsdorffer, G. Faye, and G. Schaefer. The Binary black hole dynamics at the third-and-a-half postNewtonian order in the ADM formalism. *Phys. Rev.*, D68:044004, 2003.

[95] M. Kramer, I. H. Stairs, R. Manchester, M. McLaughlin, A. Lyne, et al. Tests of general relativity from timing the double pulsar. *Science*, 314:97–102, 2006.

[96] D. Kushnir, B. Katz, S. Dong, E. Livne, and R. Fernández. Head-on Collisions of White Dwarfs in Triple Systems Could Explain Type Ia Supernovae. *Astrophys.J.*, 778:L37, 2013.

[97] L. D. Landau and E. M. Lifshitz. *Mechanics*, volume 1 of *Course of Theoretical Physics*. Butterworth-Heinemann, Oxford, 1976.

[98] P. D. Lasky, E. Thrane, Y. Levin, J. Blackman, and Y. Chen. Detecting gravitational-wave memory with LIGO: implications of GW150914. *Phys. Rev. Lett.*, 117(6):061102, 2016.

[99] W. H. Lee, E. Ramirez-Ruiz, and G. van de Ven. Short Gamma-ray Bursts from Dynamically Assembled Compact Binaries in Globular Clusters: Pathways, Rates, Hydrodynamics, and Cosmological Setting. *The Astrophysical Journal*, 720:953–975, Sept. 2010.

[100] W. H. Lee, E. Ramirez-Ruiz, and G. van de Ven. Short gamma-ray bursts from dynamically-assembled compact binaries in globular clusters: pathways, rates, hydrodynamics and cosmological setting. *Astrophys. J.*, 720:953–975, 2010.

[101] A. G. M. Lewis, A. Zimmerman, and H. P. Pfeiffer. Fundamental frequencies and resonances from eccentric and precessing binary black hole inspirals. *Class. Quant. Grav.*, 34(12):124001, 2017.

[102] S. Liebersbach, N. Loutrel, N. Yunes, and F. Pretorius. *in preparation*.

[103] C. W. Lincoln and C. M. Will. Coalescing Binary Systems of Compact Objects to (Post)5/2 Newtonian Order: Late Time Evolution and Gravitational Radiation Emission. *Phys. Rev.*, D42:1123–1143, 1990.

[104] H. A. Lorentz and J. Droste. *Collected Papers: Volume V*, chapter The Motion of a System of Bodies under the Influence of their Mutual Attraction, According to Einstein's Theory, pages 330–355. Springer Netherlands, Dordrecht, 1937.

[105] N. Loutrel, S. Liebersbach, N. Yunes, and N. Cornish. Nature Abhors a Circle. 2018.

[106] N. Loutrel and N. Yunes. Eccentric Gravitational Wave Bursts in the Post-Newtonian Formalism. *Class. Quant. Grav.*, 34(13):135011, 2017.

[107] N. Loutrel and N. Yunes. Hereditary Effects in Eccentric Compact Binary Inspirals to Third Post-Newtonian Order. *Class. Quant. Grav.*, 34(4):044003, 2017.

[108] N. Loutrel, N. Yunes, and F. Pretorius. Parametrized post-Einsteinian framework for gravitational wave bursts. *Phys.Rev.*, D90(10):104010, 2014.

[109] H. Luck. The GEO-600 project. *Class.Quant.Grav.*, 14:1471–1476, 1997.

[110] T. Marchand, L. Bernard, L. Blanchet, and G. Faye. Ambiguity-Free Completion of the Equations of Motion of Compact Binary Systems at the Fourth Post-Newtonian Order. 2017.

[111] T. Marchand, L. Blanchet, and G. Faye. Gravitational-wave tail effects to quartic non-linear order. *Class. Quant. Grav.*, 33(24):244003, 2016.

[112] R.-M. Memmesheimer, A. Gopakumar, and G. Schaefer. Third post-Newtonian accurate generalized quasi-Keplerian parametrization for compact binaries in eccentric orbits. *Phys.Rev.*, D70:104011, 2004.

[113] M. C. Miller and V. M. Lauburg. Mergers of Stellar-Mass Black Holes in Nuclear Star Clusters. *Astrophys.J.*, 692:917–923, 2009.

[114] Y. Mino, M. Sasaki, M. Shibata, H. Tagoshi, and T. Tanaka. Black hole perturbation: Chapter 1. *Prog. Theor. Phys. Suppl.*, 128:1–121, 1997.

[115] S. Mirshekari and C. M. Will. Compact binary systems in scalar-tensor gravity: Equations of motion to 2.5 post-Newtonian order. *Phys.Rev.*, D87(8):084070, 2013.

[116] C. K. Mishra, K. G. Arun, B. R. Iyer, and B. S. Sathyaprakash. Parametrized tests of post-Newtonian theory using Advanced LIGO and Einstein Telescope. *Phys. Rev.*, D82:064010, 2010.

[117] C. W. Misner, K. Thorne, and J. A. Wheeler. *Gravitation.* W. H. Freeman & Co., San Francisco, 1973.

[118] B. Moore, M. Favata, K. G. Arun, and C. K. Mishra. Gravitational-wave phasing for low-eccentricity inspiralling compact binaries to 3PN order. *Phys. Rev.*, D93(12):124061, 2016.

[119] T. Mora and C. M. Will. A PostNewtonian diagnostic of quasiequilibrium binary configurations of compact objects. *Phys. Rev.*, D69:104021, 2004. [Erratum: Phys. Rev.D71,129901(2005)].

[120] S. Naoz, B. Kocsis, A. Loeb, and N. Yunes. Resonant Post-Newtonian Eccentricity Excitation in Hierarchical Three-body Systems. *The Astrophysical Journal*, 773:187, Aug. 2013.

[121] S. Naoz, B. Kocsis, A. Loeb, and N. Yunes. Resonant Post-Newtonian Eccentricity Excitation in Hierarchical Three-body Systems. *Astrophys. J.*, 773:187, 2013.

[122] M. Nicholl et al. The Electromagnetic Counterpart of the Binary Neutron Star Merger LIGO/VIRGO GW170817. III. Optical and UV Spectra of a Blue Kilonova From Fast Polar Ejecta. *Astrophys. J.*, 848(2):L18, 2017.

[123] A. I. Nikishov. On summation of Kapteyn series. *ArXiv e-prints*, Feb. 2013.

[124] J. Novak. Spherical neutron star collapse in tensor - scalar theory of gravity. *Phys.Rev.*, D57:4789–4801, 1998.

[125] R. O'Leary, R. W. O'Shaughnessy, and F. Rasio. Dynamical Interactions and the Black Hole Merger Rate of the Universe. *Phys.Rev.*, D76:061504, 2007.

[126] R. M. O'Leary, B. Kocsis, and A. Loeb. Gravitational waves from scattering of stellar-mass black holes in galactic nuclei. *Mon. Not. R. Astron. Soc.*, 395:2127–2146, June 2009.

[127] F. W. J. Olver, D. W. Lozier, R. F. Boisvert, and C. W. Clark, editors. *NIST Handbook of Mathematical Functions.* Cambridge University Press, 2010.

[128] P. Pani, E. Berti, V. Cardoso, and J. Read. Compact stars in alternative theories of gravity. Einstein-Dilaton-Gauss-Bonnet gravity. 2011. * Temporary entry *.

[129] P. Peters. Gravitational Radiation and the Motion of Two Point Masses. *Phys.Rev.*, 136:B1224–B1232, 1964.

[130] P. C. Peters and J. Mathews. Gravitational Radiation from Point Masses in a Keplerian Orbit. *Physical Review*, 131(1):435–440, July 1963.

[131] C. M. Poisson, E. and Will. *Gravity: Newtonian, Post-Newtonian, Relativistic.* Cambridge University Press, Cambridge, 2014.

[132] E. Poisson. *A relativist's toolkit : the mathematics of black-hole mechanics.* Cambridge Univ. Pr., Cambridge, UK, 2004.

[133] A. Pound. Singular perturbation techniques in the gravitational self-force problem. *Phys.Rev.*, D81:124009, 2010.

[134] A. Pound and E. Poisson. Multi-scale analysis of the electromagnetic self-force in a weak gravitational field. *Phys.Rev.*, D77:044012, 2008.

[135] R. Rieth and G. Schaefer. Spin and tail effects in the gravitational-wave emission of compact binaries. *Class. Quant. Grav.*, 14:2357–2380, 1997.

[136] J. F. Rodriguez, J. A. Rueda, and R. Ruffini. What can we really infer from GW 150914? (II). 2016.

[137] L. Sampson, N. Cornish, and N. Yunes. Gravitational Wave Tests of Strong Field General Relativity with Binary Inspirals: Realistic Injections and Optimal Model Selection. *Phys.Rev.*, D87(10):102001, 2013.

[138] L. Sampson, N. Cornish, and N. Yunes. The Trouble With Templates. 2013.

[139] G. Schaefer. ON OFTEN USED GAUGE TRANSFORMATIONS IN GRAVITATIONAL RADIATION REACTION CALCULATIONS. *Lett. Nuovo Cim.*, 36:105–108, 1983.

[140] G. Schaefer and N. Wex. Second post-newtonian motion of compact binaries. *Physics Letters A*, 174(3):196 – 205, 1993.

[141] N. Seto. Highly Eccentric Kozai Mechanism and Gravitational-Wave Observation for Neutron-Star Binaries. *Physical Review Letters*, 111(6):061106, Aug. 2013.

[142] K. Somiya. Detector configuration of KAGRA: The Japanese cryogenic gravitational-wave detector. *Class.Quant.Grav.*, 29:124007, 2012.

[143] T. P. Sotiriou and V. Faraoni. Black holes in scalar-tensor gravity. *Phys.Rev.Lett.*, 108:081103, 2012.

[144] S. Stevenson, C. P. L. Berry, and I. Mandel. Hierarchical analysis of gravitational-wave measurements of binary black hole spin-orbit misalignments. 2017.

[145] B. Sun, Z. Cao, Y. Wang, and H.-C. Yeh. Parameter estimation of eccentric inspiraling compact binaries using an enhanced post circular model for ground-based detectors. *Phys. Rev.*, D92(4):044034, 2015.

[146] K. S. Tai, S. T. McWilliams, and F. Pretorius. Detecting gravitational waves from highly eccentric compact binaries. *Phys. Rev.*, D90(10):103001, 2014.

[147] T. Tanaka, M. Shibata, M. Sasaki, H. Tagoshi, and T. Nakamura. Gravitational wave induced by a particle orbiting around a Schwarzschild black hole. *Prog. Theor. Phys.*, 90:65–84, 1993.

[148] S. Tanay, M. Haney, and A. Gopakumar. Frequency and time domain inspiral templates for comparable mass compact binaries in eccentric orbits. *Phys. Rev.*, D93(6):064031, 2016.

[149] N. R. Tanvir et al. The Emergence of a Lanthanide-Rich Kilonova Following the Merger of Two Neutron Stars. *Astrophys. J.*, 848(2):L27, 2017.

[150] M. Tessmer and G. Schaefer. Full-analytic frequency-domain 1pN-accurate gravitational wave forms from eccentric compact binaries. *Phys. Rev.*, D82:124064, 2010.

[151] M. Tessmer and G. Schaefer. Full-analytic frequency-domain gravitational wave forms from eccentric compact binaries to 2PN accuracy. *Annalen Phys.*, 523:813–864, 2011.

[152] K. S. Thorne. Nonradial Pulsation of General-Relativistic Stellar Models.IV. The Weakfield Limit. *Astrophys. J.*, 158:997, 1969.

[153] K. S. Thorne. In J. Klauder, editor, *Magic Without Magic: John Archibald Wheeler*, page 231, San Francisco, 1972. Freeman.

[154] K. S. Thorne. Multipole expansions of gravitational radiation. *Rev. Mod. Phys.*, 52:299–339, 1980.

[155] K. S. Thorne. Gravitational-wave bursts with memory: The christodoulou effect. *Phys. Rev. D*, 45:520–524, Jan 1992.

[156] M. Turner. Gravitational radiation from point-masses in unbound orbits - Newtonian results. *The Astrophysical Journal*, 216:610–619, Sept. 1977.

[157] T. Uchiyama, K. Kuroda, M. Ohashi, S. Miyoki, H. Ishitsuka, et al. Present status of large-scale cryogenic gravitational wave telescope. *Class.Quant.Grav.*, 21:S1161–S1172, 2004.

[158] C. Unnikrishnan. IndIGO and LIGO-India: Scope and plans for gravitational wave research and precision metrology in India. *Int.J.Mod.Phys.*, D22:1341010, 2013.

[159] C. Van Den Broeck, D. A. Brown, T. Cokelaer, I. Harry, G. Jones, B. S. Sathyaprakash, H. Tagoshi, and H. Takahashi. Template banks to search for compact binaries with spinning components in gravitational wave data. *Phys. Rev.*, D80:024009, 2009.

[160] G. N. Watson. *A Treatise on the Theory of Bessel Functions.* Cambridge University Press, 2nd ed. edition, 1966.

[161] L. Wen. On the Eccentricity Distribution of Coalescing Black Hole Binaries Driven by the Kozai Mechanism in Globular Clusters. *The Astrophysical Journal*, 598:419–430, Nov. 2003.

[162] L. Wen. On the eccentricity distribution of coalescing black hole binaries driven by the Kozai mechanism in globular clusters. *Astrophys. J.*, 598:419–430, 2003.

[163] N. Wex. The second post-newtonian motion of compact binary-star systems with spin. *Classical and Quantum Gravity*, 12(4):983, 1995.

[164] C. M. Will. *Theory and Experiment in Gravitational Physics.* Cambridge University Press, Cambridge, England, 1993.

[165] C. M. Will. The confrontation between general relativity and experiment. *Living Reviews in Relativity*, 9(3), 2006.

[166] C. M. Will and H. W. Zaglauer. Gravitational Radiation, Close Binary Systems, and the Brans-dicke Theory of Gravity. *Astrophys.J.*, 346:366, 1989.

[167] B. Willke, P. Aufmuth, C. Aulbert, S. Babak, R. Balasubramanian, et al. The GEO 600 gravitational wave detector. *Class.Quant.Grav.*, 19:1377–1387, 2002.

[168] A. G. Wiseman and C. M. Will. Christodoulou's nonlinear gravitational-wave memory: Evaluation in the quadrupole approximation. *Phys. Rev. D*, 44:R2945–R2949, Nov 1991.

[169] K. Yagi. A New constraint on scalar Gauss-Bonnet gravity and a possible explanation for the excess of the orbital decay rate in a low-mass X-ray binary. 2012.

[170] K. Yagi, L. C. Stein, N. Yunes, and T. Tanaka. Post-Newtonian, quasicircular binary inspirals in quadratic modified gravity. *Phys. Rev.*, D85(6):064022, Mar. 2012.

[171] K. Yagi, L. C. Stein, N. Yunes, and T. Tanaka. Isolated and Binary Neutron Stars in Dynamical Chern-Simons Gravity. *Phys.Rev.*, D87:084058, 2013.

[172] K. Yagi and N. Yunes. Love can be Tough to Measure. *Phys. Rev.*, D89(2):021303, 2014.

[173] N. Yunes, K. G. Arun, E. Berti, and C. M. Will. Post-circular expansion of eccentric binary inspirals: Fourier-domain waveforms in the stationary phase approximation. *Phys. Rev. D*, 80:084001, Oct 2009.

[174] N. Yunes, K. G. Arun, E. Berti, and C. M. Will. Post-Circular Expansion of Eccentric Binary Inspirals: Fourier-Domain Waveforms in the Stationary Phase Approximation. *Phys. Rev.*, D80(8):084001, 2009. [Erratum: Phys. Rev.D89,no.10,109901(2014)].

[175] N. Yunes, P. Pani, and V. Cardoso. Gravitational Waves from Quasicircular Extreme Mass-Ratio Inspirals as Probes of Scalar-Tensor Theories. *Phys.Rev.*, D85:102003, 2012.

[176] N. Yunes and F. Pretorius. Fundamental Theoretical Bias in Gravitational Wave Astrophysics and the Parameterized Post-Einsteinian Framework. *Phys. Rev.*, D80:122003, 2009.

[177] N. Yunes and F. Pretorius. Fundamental Theoretical Bias in Gravitational Wave Astrophysics and the Parameterized Post-Einsteinian Framework. *Phys.Rev.*, D80:122003, 2009.

[178] N. Yunes and X. Siemens. Gravitational-wave tests of general relativity with ground-based detectors and pulsar-timing arrays. *Living Reviews in Relativity*, 16(9), 2013.

[179] N. Yunes and L. C. Stein. Non-Spinning Black Holes in Alternative Theories of Gravity. *Phys. Rev.*, D83:104002, 2011.

[180] N. Yunes and L. C. Stein. Nonspinning black holes in alternative theories of gravity. *Phys. Rev. D.*, 83(10):104002–+, May 2011.

[181] N. Yunes, K. Yagi, and F. Pretorius. Theoretical Physics Implications of the Binary Black-Hole Mergers GW150914 and GW151226. *Phys. Rev.*, D94(8):084002, 2016.

[182] M. Zevin, C. Pankow, C. L. Rodriguez, L. Sampson, E. Chase, V. Kalogera, and F. A. Rasio. Constraining Models of Binary Black Hole Formation with Gravitational-Wave Observations. 2017.

APPENDICES

APPENDIX A

FOURIER COEFFICIENTS OF THE MASS OCTOPOLE AND CURRENT QUADRUPOLE

We here present the Fourier coefficients of the source mass octopole and current quadrupole necessary to complete the re-summation of the 2.5PN enhancement factors $\beta(e_t)$ and $\gamma(e_t)$. For the mass octopole, we have

$$\underset{(p)}{\hat{\mathcal{I}}_{xxx}} = -\frac{3}{5}\left(-5e^5p^2 + 10e^3p^2 + 6e^3 - 5ep^2 - 10e\right)\frac{J_p'(pe)}{p^3e^3} - \frac{3}{5}\left(5e^4 - 20e^2 + 15\right)\frac{J_p(pe)}{p^2e^3}\,, \tag{A.1}$$

$$\underset{(p)}{\hat{\mathcal{I}}_{xxy}} = -\frac{i}{5}\sqrt{1-e^2}(25e^3 - 45e)\frac{J_p'(pe)}{p^2e^3} - \frac{i}{5}\sqrt{1-e^2}(15e^4p^2 - 30e^2p^2 - 6e^2 + 15p^2 + 30)\frac{J_p(pe)}{p^3e^3}\,, \tag{A.2}$$

$$\underset{(p)}{\hat{\mathcal{I}}_{xyy}} = \frac{1}{5}(-15e^5p^2 + 30e^3p^2 + 24e^3 - 15ep^2 - 30e)\frac{J_p'(pe)}{p^3e^3} + \frac{1}{5}(20e^4 - 65e^2 + 45)\frac{J_p(pe)}{p^2e^3}\,, \tag{A.3}$$

$$\underset{(p)}{\hat{\mathcal{I}}_{yyy}} = \frac{3i}{5}\sqrt{1-e^2}(10e^3 - 15e)\frac{J_p'(pe)}{p^2e^3} + \frac{3i}{5}\sqrt{1-e^2}(5e^4p^2 - 10e^2p^2 - 4e^2 + 5p^2 + 10)\frac{J_p(pe)}{p^3e^3}\,, \tag{A.4}$$

$$\underset{(p)}{\hat{\mathcal{I}}_{zzx}} = -\frac{1}{5}(5e^2 - 5)\frac{J_p(pe)}{ep^2} - \frac{6}{5}\frac{J_p'(pe)}{p^3}\,, \tag{A.5}$$

$$\underset{(p)}{\hat{\mathcal{I}}_{zzy}} = \frac{6i}{5}\sqrt{1-e^2}\frac{J_p(pe)}{ep^3} - i\sqrt{1-e^2}\frac{J_p'(pe)}{p^2}\,, \tag{A.6}$$

and for the current quadrupole

$$\underset{(p)}{\hat{\mathcal{J}}_{zx}} = \frac{1}{2}\sqrt{1-e^2}\frac{J_p'(pe)}{p}\,, \tag{A.7}$$

$$\underset{(p)}{\hat{\mathcal{J}}_{zy}} = \frac{i}{2}(1-e^2)\frac{J_p(pe)}{pe}\,. \tag{A.8}$$

APPENDIX B

PADÉ APPROXIMANT COEFFICIENTS

The analytic expressions for the 2.5PN enhancement factors $[\alpha_3^{(2)}(e_t), \tilde{\alpha}_3^{(2)}(e_t)]$ that we obtain take the form

$$\alpha_3^{(2)}(e_t) = \frac{A^{\rm PD}(e_t)}{(1-e_t^2)^6}\,, \tag{B.1}$$

$$\tilde{\alpha}_3^{(2)}(e_t) = \frac{\tilde{A}^{\rm PD}(e_t)}{(1-e_t^2)^{9/2}}\,, \tag{B.2}$$

where $[A^{\rm PD}(e_t), \tilde{A}^{\rm PD}(e_t)]$ are Padé approximants of the form in Eq. (3.100). We here display the non-zero coefficients of these Padé approximants. The exact fractional form of the coefficients are too lengthy to show here, so we will display their numerical value as given by `Mathematica`. For $A^{\rm PD}(e_t)$, we have

$$\begin{aligned}
A^{(2)} &= 2517\,, \qquad A^{(4)} = -542.748497072893\,,\\
A^{(6)} &= -8106.76855568073\,, \qquad A^{(8)} = 8413.80043346759\,,\\
A^{(10)} &= -1797.84373379634\,, \qquad A^{(12)} = -645.518003878721\,,\\
A^{(14)} &= 196.536287243258\,, \qquad\qquad\qquad\qquad\qquad\qquad\qquad\qquad\qquad\qquad\qquad\qquad (\text{B.3})\\
A_{(2)} &= -2.73321354671152\,, \qquad A_{(4)} = 2.72445722875519\,,\\
A_{(6)} &= -1.18148275600057\,, \qquad A_{(8)} = 0.198189499682584\,,\\
A_{(10)} &= -0.0052713663843431\,, \qquad A_{(12)} = -0.000104564833689961\,,\\
A_{(14)} &= -0.000017353206147761 94\,, \qquad A_{(16)} = -2.68866627647753\times 10^{-6}\,. \qquad (\text{B.4})
\end{aligned}$$

Similarly, for $\tilde{A}^{\rm PD}(e_t)$ we have

$$\begin{aligned}
\tilde{A}^{(2)} &= 1428\,, \qquad \tilde{A}^{(4)} = -3082.0825943902\,,\\
\tilde{A}^{(6)} &= 1251.7504530861\,, \qquad \tilde{A}^{(8)} = 1534.29667420639\,,\\
\tilde{A}^{(10)} &= -1557.48894312597\,, \qquad \tilde{A}^{(12)} = 474.00656591547\,,\\
\tilde{A}^{(14)} &= -44.7331690120333\,, \qquad\qquad\qquad\qquad\qquad\qquad\qquad\qquad\qquad\qquad\qquad\qquad (\text{B.5})\\
\tilde{A}_{(2)} &= -3.15201862352255\,, \qquad \tilde{A}_{(4)} = 3.82292854565682\,,\\
\tilde{A}_{(6)} &= -2.22448315038514\,, \qquad \tilde{A}_{(8)} = 0.6262354256498\,,\\
\tilde{A}_{(10)} &= -0.0738364336330394\,, \qquad \tilde{A}_{(12)} = 0.0021699571134637\,,\\
\tilde{A}_{(14)} &= 0.0000142157331173306\,, \qquad \tilde{A}_{(16)} = -3.8287501968869\times 10^{-6}\,. \qquad (\text{B.6})
\end{aligned}$$

APPENDIX C

POST-NEWTONIAN RECURSION RELATIONS

When computing the burst model to arbitrary PN order, we are often faced will expressions of the form

$$\left(1+\sum_{n=1}^{\infty} A_n x^n\right)^{-m} , \tag{C.1}$$

which need to be perturbatively expanded about $x \ll 1$. In our PN burst model, v_p takes the place of x. The expansion of the above expression can be easily computed term by term, but may not be expressible in terms of an arbitrary sum. We instead define the coefficients as

$$\sum_{n=1}^{\infty} A_n^{(-m)} x^n \equiv \left(1+\sum_{n=1}^{\infty} A_n x^n\right)^{-m} - 1\,, \tag{C.2}$$

where it is understood that we are working perturbatively in x. If one computes the Taylor expansion and calculates the coefficients, one finds

$$\begin{aligned} A_n^{(-m)} &= -mA_n + \frac{m(m+1)}{2!}B_n - \frac{m(m+1)(m+2)}{3!}C_n \\ &+ \frac{m(m+1)(m+2)(m+3)}{4!}D_n - ...\,, \end{aligned} \tag{C.3}$$

where the coefficients (B_n, C_n, D_n) are given by

$$B_n = \sum_{q=1}^{n-1} A_q A_{n-q}\,, \tag{C.4}$$

$$C_n = \sum_{q=1}^{n-1} A_q B_{n-q}\,, \tag{C.5}$$

$$D_n = \sum_{q=1}^{n-1} B_q B_{n-q}\,. \tag{C.6}$$

We have stopped the expansion at fourth order in x, but in principle there will also be fifth order terms with coefficients E_n, sixth order terms with coefficients F_n, etc., where (E_n, F_n, ...) are expressible in terms of the coefficients above. Thus, while the right-hand-side of Eq. (C.3) is not expressible as a closed sum, one can recursively build the coefficients to arbitrary order.

As an example of how this works, consider the case where $m = 1$ and we truncate at third order, i.e. the series only has coefficients (A_1, A_2, A_3). So, the first order term $(n = 1)$ is then

$$A_1^{(-1)} = -A_1 + B_1 - C_1 + ... \tag{C.7}$$

However, from Eq. (C.4)

$$B_1 = \sum_{q=1}^{0} A_q A_{1-q} = 0 \tag{C.8}$$

Likewise, all higher order terms, i.e. $(C_1, D_1, ...)$, will vanish, and thus at first order $A_1^{(-1)} = -A_1$ as one would expect from a first order Taylor expansion. At second order $n = 2$,

$$A_2^{(-1)} = -A_2 + B_2 - C_2 + ... \tag{C.9}$$

However, now the B coefficient doesn't vanish, but the C coefficient (and thus all higher order coefficients) does vanish.

$$B_2 = \sum_{q=1}^{1} A_q A_{2-q} = A_1^2 \tag{C.10}$$

$$C_2 = \sum_{q=1}^{1} A_q B_{2-q} = A_1 B_1 = 0 \tag{C.11}$$

So, the second order coefficient is $A_2^{(-1)} = -A_2 + A_1^2$. Similarly, a calculation of the third order coefficient gives $A_3^{(-1)} = -A_3 + 2A_1A_2 - A_1^3$. Since we are working perturbatively to third order in this example, we now truncate the series and all higher order coefficients will be zero.

The expression in Eq. (C.3) can be written in a more compact form using the notation of Ch. 4. Using the vector convolution $\circ$, we may write

$$A_n^{(-m)} = \sum_{k=1}^{n} \binom{-m}{k-1} \left[(\vec{A}\circ)^{k-1} \vec{A} \right]_n . \tag{C.12}$$

APPENDIX D

THIRD POST-NEWTONIAN QUASI-KEPLERIAN PARAMETRIZATION

PN Vector Fields

We here give explicit expressions for the PN amplitude vector fields (P_k, R_k, V_k, E_k) to 3PN order. We will provide an example calculation at 1PN order to show how to obtain these functions. At higher PN order, we will simply give the results of the calculation.

1PN Amplitude Vector Fields

We begin by calculating the 1PN corrections to the factors (P_2, R_2, V_2, E_2). This naturally amounts to finding the 1PN corrections to the orbital period, pericenter distance, and rates of change of pericenter velocity and orbital eccentricity. Because these are not quantities that are typically computed in the PN literature, we will show explicitly how to calculate them from other known quantities.

Consider first the pericenter velocity and the orbital eccentricity as functions of the orbital energy and angular momentum. Typically, PN quantities are written in terms of the reduced orbital energy $\varepsilon = -2E/\mu$ and the dimensionless orbital angular momentum $j = -2EL^2/\mu^3 M^2$, where μ is the reduced mass of the system. The reason for this is that ε and j do not depend on the coordinate system that one chooses to do calculations in, i.e. they are coordinate invariant quantities. However, we have formulated our burst model in terms of the pericenter velocity and orbital eccentricity, so we need to determine the mappings $(\varepsilon, j) \to (v_p, e)$.

We start from the equations of motion that govern the QK representation, which to 1PN order are [42]

$$r = a_r \left(1 - e_r \cos u\right) \,, \tag{D.1}$$

$$\ell = u - e_t \sin u \,, \tag{D.2}$$

$$\phi - \phi_0 = 2K \ \arctan\left[\left(\frac{1+e_\phi}{1-e_\phi}\right)^{1/2} \tan\left(\frac{u}{2}\right)\right] \,, \tag{D.3}$$

The first of these is the radial equation of the elliptical orbit written in terms of the eccentric anomaly u, where a_r is the semi-major axis of the ellipse and e_r is the radial eccentricity. The second equation is Kepler's equation, which relates the eccentric anomaly to the mean anomaly through the time eccentricity e_t. This equation is itself a direct measure of time since $\ell = n(t - t_p)$ where $n = 2\pi/P$ is the mean motion and t_p is the time of pericenter passage. Finally, the last equation is the azimuthal equation of the orbit, which relates the orbital phase ϕ to the eccentric anomaly through the azimuthal eccentricity e_ϕ and the advance of periastron per orbit K. In Newtonian gravity, $K = 1$ and we recover the Newtonian equations of motion, but at 1PN order $K = 1 + \mathcal{O}(\varepsilon)$. Thus a primary difference in the azimuthal motion at 1PN order is the inclusion of the precession of periastron.

Another difference between Newtonian and 1PN orbits in the QK parametrization is the need for multiple "eccentricities." The latter are not actually separate physical quantities, but instead are a clever notational trick that allows the equations of motion to take the same functional form as their Newtonian analogs[1]. In reality, these eccentricities are related to the Newtonian expression for the orbital eccentricity, which is just $e = \sqrt{1-j}$, through [42]

$$e_r = \sqrt{1-j} + \frac{\varepsilon}{8\sqrt{1-j}}\left[24 - 4\eta + 5j(-3+\eta)\right] , \tag{D.4}$$

$$e_t = \sqrt{1-j} + \frac{\varepsilon}{8\sqrt{1-j}}\left[-8 + 8\eta + j(17-7\eta)\right] , \tag{D.5}$$

$$e_\phi = \sqrt{1-j} + \frac{\varepsilon}{8\sqrt{1-j}}\left[24 + j(-15+\eta)\right] . \tag{D.6}$$

In this paper, and in this Appendix, we choose to parameterize the motion in terms of one of these eccentricities, specifically e_t, and we define $\delta e_t = 1 - e_t$. This choice is arbitrary: one could easily construct the burst model in terms of e_r or e_ϕ or the Newtonian e. With this choice, we now have one of the equations we need to determine $\varepsilon(v_p, e_t)$ and $j(v_p, e_t)$, specifically Eq. (D.5).

Let us now focus on the pericenter velocity. Since pericenter is the minimum turning point of the orbit ($\dot{r} = 0$), we may write $v_p = r_p\dot{\phi}(r = r_p)$. From Eq. (D.1), we see that r is at a minimum when $u = 0$, specifically $r(u = 0) = r_p = a_r(1 - e_r)$. Hence we are left with determining $\dot{\phi}(u)$. Taking the time derivative of Eq. (D.3), we find

$$\dot{\phi} = \frac{K\beta\left[1 + \tan^2\left(\frac{u}{2}\right)\right]}{1 + \beta^2\tan^2\left(\frac{u}{2}\right)}\dot{u} , \tag{D.7}$$

where $\beta = \sqrt{(1+e_\phi)/(1-e_\phi)}$. To find the expression for $\dot{u}$, we take the time derivative of Eq. (D.2) and solve for $\dot{u}$,

$$\dot{u} = \frac{n}{1 - e_t\cos u} . \tag{D.8}$$

We can now put all of this together to find v_p to 1PN order:

$$v_p = a_r n K\beta\frac{1-e_r}{1-e_t} . \tag{D.9}$$

This expression for the pericenter velocity is exact in the sense that we have not performed a PN expansion in ε yet. To obtain $v_p(\varepsilon, j)$, we use Eqs. (D.4)-(D.6) with [42]

$$n = \frac{\varepsilon^{3/2}}{M}\left[1 + \frac{\varepsilon}{8}(-15+\eta)\right] , \tag{D.10}$$

---

[1] Note that while this is true to 1PN order, the same cannot be said at higher PN order. At 2PN order and beyond, Eqs (D.2) and (D.3) pick up higher harmonics of the anomalies.

$$K = 1 + \frac{3\varepsilon}{j}\,, \tag{D.11}$$

$$a_r = \frac{M}{\varepsilon}\left[1 + \frac{\varepsilon}{4}(-7+\eta)\right]\,, \tag{D.12}$$

and expand in ε to find

$$\begin{aligned} v_p = {} & \frac{\varepsilon^{1/2} j^{7/2}}{\left(1-\sqrt{1-j}\right)^4 \left(1+\sqrt{1-j}\right)^3} - \frac{\varepsilon^{3/2} j^{5/2}}{(1-j)\left(1-\sqrt{1-j}\right)^4 \left(1+\sqrt{1-j}\right)^3} \\ & \times \left\{ 8 - 12\eta + j(-11+21\eta) + j^2(3-9\eta) + \sqrt{1-j}\,[8-12\eta+j(-17+11\eta)] \right\}\,. \end{aligned} \tag{D.13}$$

The last step before deriving the functions (P_2, R_2) is to invert Eqs. (D.5) and (D.13) to find $\varepsilon(v_p, e_t)$ and $j(v_p, e_t)$. This can be done very easily order by order in ε (or v_p) to find

$$\varepsilon = v_p^2 \frac{1-e_t}{1+e_t}\left[1 - \frac{v_p^2}{4}\,\frac{-5+3\eta+4\eta e_t + e_t^2(-3+9\eta)}{(1+e_t)^2}\right]\,, \tag{D.14}$$

$$j = \left(1-e_t^2\right)\left[1 + \frac{v_p^2}{4}\,\frac{9+\eta+e_t^2(-17+7\eta)}{(1+e_t)^2}\right]\,. \tag{D.15}$$

We can now construct the functions P_2 and R_2, which recall we define via

$$P = P^{\mathrm{N}}\left(1 + v_p^2\, P_2\right)\,, \tag{D.16}$$

$$r_p = r_p^{\mathrm{N}}\left(1 + v_p^2\, R_2\right)\,. \tag{D.17}$$

The orbital period in the QK representation is given by $P = 2\pi/n(\varepsilon, j)$, with $n(\varepsilon, j)$ given in Eq. (D.10). Inserting our expressions for $\varepsilon(v_p, e_t)$ and $j(v_p, e_t)$ and expanding about $v_p \ll 1$, while keeping terms of relative $\mathcal{O}(v_p^2)$, we find

$$P_2(e_t, \eta) = \frac{2\eta + 3\eta e_t + e_t^2(-6+7\eta)}{2(1+e_t)^2}\,. \tag{D.18}$$

We may follow the same procedure for the pericenter distance, using $r_p = a_r(\varepsilon, j)\,[1 - e_r(\varepsilon, j)]$; we find

$$R_2(e_t, \eta) = \frac{-6 + 2\eta + e_t(-8+5\eta) + e_t^2(-6+7\eta)}{2(1+e_t)^2}\,. \tag{D.19}$$

The functions (V_2, E_2) require a bit more work, since we need to compute the rates of change of pericenter velocity and time eccentricity. We may do this via the chain rule:

$$\langle \dot{v}_p \rangle = \frac{\partial v_p(\varepsilon,h)}{\partial \varepsilon}\left(\frac{-2\langle \dot{E}\rangle}{\mu}\right) + \frac{\partial v_p(\varepsilon,h)}{\partial h}\left(\frac{\langle \dot{L}\rangle}{M}\right) , \tag{D.20}$$

$$\langle \dot{e}_t \rangle = \frac{\partial e_t(\varepsilon,h)}{\partial \varepsilon}\left(\frac{-2\langle \dot{E}\rangle}{\mu}\right) + \frac{\partial e_t(\varepsilon,h)}{\partial h}\left(\frac{\langle \dot{L}\rangle}{M}\right) , \tag{D.21}$$

where $h = L/M$ is the reduced angular momentum, $\dot{E}$ is the energy flux, and $\dot{L}$ is the angular momentum flux. The reason for replacing j with h in the expressions $[v_p(\varepsilon,j), e_t(\varepsilon,j)]$ is that j has a factor of the reduced energy hidden in it, which needlessly obfuscates taking partial derivatives. Furthermore, the expression for $\dot{h}$ can be computed directly and easily from $\dot{L}$. The averaged energy and angular momentum fluxes are given to 1PN order by [28, 31]

$$\langle \dot{E} \rangle = -\frac{32}{5}\eta^2 x^5 \left(\mathcal{I}_{\rm N} + x\,\mathcal{I}_{\rm 1PN}\right) \tag{D.22}$$

$$\langle \dot{L} \rangle = -\frac{4}{5}\eta^2 M x^{7/2} \left(\mathcal{G}_{\rm N} + x\,\mathcal{G}_{\rm 1PN}\right) \tag{D.23}$$

with the enhancement factors

$$\mathcal{I}_{\rm N} = \frac{1 + \frac{73}{24}e_t^2 + \frac{37}{96}e_t^4}{(1-e_t^2)^{7/2}} , \tag{D.24}$$

$$\mathcal{I}_{\rm 1PN} = \frac{1}{(1-e_t^2)^{9/2}}\left[-\frac{1247}{336} - \frac{35}{12}\eta + e_t^2\left(\frac{10475}{672} - \frac{1081}{36}\eta\right) + e_t^4\left(\frac{10043}{384} - \frac{311}{12}\eta\right) + e_t^6\left(\frac{2179}{1792} - \frac{851}{576}\eta\right)\right] , \tag{D.25}$$

and

$$\mathcal{G}_{\rm N} = \frac{8 + 7e_t^2}{(1-e_t^2)^2} , \tag{D.26}$$

$$\mathcal{G}_{\rm 1PN} = \frac{1}{(1-e_t^2)^3}\left[-\frac{1247}{42} - \frac{70}{3}\eta + e_t^2\left(\frac{3019}{42} - \frac{335}{3}\eta\right) + e_t^4\left(\frac{8399}{336} - \frac{275}{12}\eta\right)\right] . \tag{D.27}$$

In the above, the PN expansion parameter $x = (M\Omega)^{2/3}$, with Ω the orbital frequency, which is related to the reduced orbital energy by [42]

$$x = \varepsilon\left[1 + \varepsilon\left(-\frac{5}{4} + \frac{\eta}{12} + \frac{2}{j}\right)\right] . \tag{D.28}$$

The goal at this stage should be clear: we desire to write $\langle \dot{v}_p \rangle$ and $\langle \dot{e}_t \rangle$ in terms of

v_p and e_t instead of x and e_t. The calculation is rather lengthy, but straightforward, so we will simply detail the main steps here. The first step is to replace x with ε in the expressions for $\langle \dot{E} \rangle$ and $\langle \dot{L} \rangle$, working perturbatively in ε. We then use the chain rule combined with our new expressions for the fluxes in Eqs. (D.20) and (D.21). Finally we replace any instances of (ε, h) with (v_p, e_t) and expand in powers of v_p. The end result is

$$\begin{aligned} \langle \dot{v}_p \rangle &= \langle \dot{v}_p^{\mathrm{N}} \rangle (v_p, e_t) \left[1 + v_p^2 \, V_2(e_t, \eta) \right] , && \text{(D.29)} \\ \langle \dot{e}_t \rangle &= \langle \dot{e}^{\mathrm{N}} \rangle (v_p, e_t) \left[1 + v_p^2 \, E_2(e_t, \eta) \right] , && \text{(D.30)} \end{aligned}$$

where $\langle \dot{v}_p^{\mathrm{N}} \rangle$ and $\langle \dot{e}^{\mathrm{N}} \rangle$ are given in Eqs. (4.52) and (4.53) with the replacement $e \to e_t$, and the PN functions are

$$\begin{aligned} V_2(e_t, \eta) = {} & \frac{1}{(1+e_t)^2 \left(1 - \frac{13}{6} e_t + \frac{7}{8} e_t^2 - \frac{37}{96} e_t^3\right)} \left[-\frac{19}{4}\eta + \frac{1273}{336} + \left(\frac{319}{24}\eta - \frac{3887}{224} \right) e_t \right. \\ & + \left(-\frac{421}{16}\eta + \frac{1507}{42} \right) e_t^2 + \left(\frac{1711}{48}\eta - \frac{29605}{672} \right) e_t^3 + \left(-\frac{737}{64}\eta + \frac{35923}{2688} \right) e_t^4 \\ & \left. + \left(\frac{407}{96}\eta - \frac{24149}{5376} \right) e_t^5 \right] , && \text{(D.31)} \\ E_2(e_t, \eta) = {} & \frac{1}{(1+e_t)^2 \left(1 + \frac{121}{304} e_t^2\right)} \left[\frac{543}{76}\eta - \frac{14207}{2128} + 4 e_t \eta + \left(\frac{14073}{608}\eta - \frac{53717}{2128} \right) e_t^2 \right. \\ & \left. + \frac{121}{76} e_t^3 \eta + \left(\frac{421}{76}\eta - \frac{95995}{17024} \right) e_t^4 \right] . && \text{(D.32)} \end{aligned}$$

This completes the construction of the 1PN correction functions (P_2, R_2, V_2, E_2).

Amplitude Vector Fields to 3PN Order

We now provide the components of the amplitude vector fields $(\vec{P}, \vec{R}, \vec{V}, \vec{E})$ to 3PN order. The derivation of the components follows the exact same procedure as the previous section, so we will simply list the components, where recall we work in ADM coordinates. For the orbital period, the non-zero components are

$$\begin{aligned} P_4(e_t, \eta; v_p) = {} & \frac{3(1-e_t)(1+3e_t-e_t^2)(5-2\eta)}{2(1+e_t)^3\sqrt{1-e_t^2}} + \frac{1}{8(1+e_t)^4} \left[19\eta - 6 \right. \\ & + e_t \left(-23\eta^2 + 192\eta - 258 \right) + e_t^2 \left(-75\eta^2 + 242\eta - 186 \right) \\ & \left. + e_t^3 \left(-37\eta^2 + 42\eta \right) + e_t^4 \left(-21\eta^2 - 21\eta \right) \right] , && \text{(D.33)} \\ P_6(e_t, \eta; v_p) = {} & \frac{(1-e_t)}{192(1+e_t)^5\sqrt{1-e_t^2}} \left[123\pi^2\eta + 1152\eta^2 - 13664\eta + 8640 \right. \\ & + e_t \left(369\pi^2\eta + 4032\eta^2 - 42432\eta + 25920 \right) \\ & + e_t^2 \left(-123\pi^2\eta - 2016\eta^2 + 18560\eta - 12960 \right) \end{aligned}$$

$$
\begin{aligned}
&+e_t^3\big(8064\eta^2-25776\eta+21600\big)+e_t^4\big(-1728\eta^2+5040\eta-4320\big)\big]\\
&+\frac{1}{192e_t(1+e_t)^6}\big[-6\eta+e_t\big(1116\pi^2\eta-1536\eta^2-20088\eta+2976\big)\\
&+e_t^2\big(783\pi^2\eta+684\eta^3-16260\eta^2+51264\eta-38304\big)\\
&+e_t^3\big(396\pi^2\eta+3684\eta^3-31572\eta^2+56208\eta-34128\big)\\
&+e_t^4\big(9\pi^2\eta+7320\eta^3-46056\eta^2+77106\eta-45936\big)\\
&+e_t^5\big(10248\eta^3-31488\eta^2+36708\eta-20016\big)\\
&+e_t^6\big(4332\eta^3-5436\eta^2+2844\eta\big)+e_t^7\big(1764\eta^3+156\eta^2-228\eta\big)\big]\ .
\end{aligned}
\tag{D.34}
$$

For the pericenter distance, the non-zero components are

$$
\begin{aligned}
R_4(e_t,\eta;v_p)={}&\frac{3e_t(1-e_t)^2(5-2\eta)}{2(1+e_t)^3\sqrt{1-e_t^2}}+\frac{1}{8(1+e_t)^4}\big[43\eta-30\\
&+e_t\big(-21\eta^2+184\eta-206\big)+e_t^2\big(-63\eta^2+184\eta-140\big)\\
&+e_t^3\big(-31\eta^2+2\eta\big)+e_t^4\big(-21\eta^2-21\eta\big)\big]\ ,
\end{aligned}
\tag{D.35}
$$

$$
\begin{aligned}
R_6(e_t,\eta;v_p)={}&\frac{e_t(1-e_t)^2}{192(1+e_t)^5\sqrt{1-e_t^2}}\big[123\pi^2\eta+864\eta^2-12368\eta+7200\\
&+e_t\big(-2880\eta^2+10656\eta-8640\big)+e_t^2\big(1728\eta^2-5040\eta+4320\big)\big]\\
&+\frac{1}{192e_t(1+e_t)^6}\big[-4\eta+e_t\big(501\pi^2\eta-2112\eta^2-1804\eta-2640\big)\\
&+e_t^2\big(279\pi^2\eta+660\eta^3-14724\eta^2+48952\eta-30288\big)\\
&+e_t^3\big(267\pi^2\eta+3300\eta^3-29508\eta^2+50888\eta-27792\big)\\
&+e_t^4\big(9\pi^2\eta+6648\eta^3-40392\eta^2+68584\eta-39696\big)\\
&+e_t^5\big(9336\eta^3-26520\eta^2+31704\eta-16704\big)\\
&+e_t^6\big(4020\eta^3-3636\eta^2+2292\eta\big)+e_t^7\big(1764\eta^3+156\eta^2-228\eta\big)\big]\ .
\end{aligned}
\tag{D.36}
$$

For $\langle\dot{e}_t\rangle$, we have

$$
E_3(e_t,\eta;v_p)=\frac{985\pi(1-e_t)^3(1-e_t^2)\varphi_e(e_t)}{152(1+\frac{121}{304}e_t^2)}\ ,
\tag{D.37}
$$

$$
\begin{aligned}
E_4(e_t,\eta;v_p)={}&\frac{1}{(1+e_t)^4(1+\frac{121}{304}e_t^2)}\bigg[\frac{1035}{38}\eta^2-\frac{45819}{608}\eta+\frac{1365463}{38304}\\
&+e_t\left(\frac{3399}{76}\eta^2-\frac{207227}{2128}\eta+86\right)\\
&+e_t^2\left(\frac{599243}{2432}\eta^2-\frac{9115835}{17024}\eta+\frac{13816637}{51072}\right)\\
&+e_t^3\left(\frac{82879}{608}\eta^2-\frac{361097}{2128}\eta+\frac{5203}{152}\right)
\end{aligned}
$$

$$
\begin{aligned}
&+e_t^4\left(\frac{97141}{304}\eta^2-\frac{21541341}{34048}\eta+\frac{108773587}{306432}\right)\\
&+e_t^5\left(\frac{10477}{304}\eta^2-\frac{601943}{17024}\eta\right)\\
&+e_t^6\left(\frac{15933}{304}\eta^2-\frac{97941}{1064}\eta+\frac{3284783}{68096}\right)\Bigg]\\
&+\frac{\sqrt{1-e_t^2}}{(1+e_t)^4(1+\frac{121}{304}e_t^2)}\left[-\frac{15}{19}\eta+\frac{75}{38}\right.\\
&+e_t\left(24\eta-60\right)+e_t^2\left(-\frac{8427}{304}\eta+\frac{42135}{608}\right)+e_t^3\left(\frac{363}{38}\eta-\frac{1815}{76}\right)\\
&\left.+e_t^4\left(-\frac{1533}{304}\eta+\frac{7665}{608}\right)\right],
\end{aligned}
\tag{D.38}
$$

$$
\begin{aligned}
E_5(e_t,\eta;v_p)=&\frac{\pi(1-e_t)^3(1-e_t^2)\varphi_e(e_t)}{(1+e_t)^2(1+\frac{121}{304}e_t^2)}\left[-\frac{10835}{456}\eta+\frac{10835}{152}-\frac{10835}{304}e_t\eta\right.\\
&\left.+e_t^2\left(-\frac{75845}{912}\eta+\frac{10835}{152}\right)\right]-\frac{\pi(1-e_t)^5}{(1+\frac{121}{304}e_t^2)}\left[\frac{55691}{4256}\psi_e(e_t)\right.\\
&\left.+\frac{19067\eta}{399}\zeta_e(e_t)\right],
\end{aligned}
\tag{D.39}
$$

$$
\begin{aligned}
E_6(e_t,\eta;v_p)=&\frac{(1-e_t)^5\sqrt{1-e_t^2}\left[-\frac{89789209}{1117200}+\frac{4601}{105}\ln(2)-\frac{234009}{5320}\ln(3)\right]}{(1+e_t)(1+\frac{121}{304}e_t^2)}\kappa_e(e_t)\\
&-\frac{1}{e_t(1-e_t)(1+e_t)^7(1+\frac{121}{304}e_t^2)}\left\{\sum_{k=0}^{11}\mathcal{P}_e^{(k)}(\eta)e_t^k\right.\\
&+\ln\left[\frac{(1-e_t)^{3/2}(1+e_t)^{1/2}v_p}{1+\sqrt{1-e_t^2}}\right]\Bigg(-\frac{61311}{21280}e_t^9-\frac{880931}{12768}e_t^7-\frac{82283}{1064}e_t^5\\
&\left.+\frac{71797}{665}e_t^3+\frac{82283}{1995}e_t\Bigg)\right\}-\frac{\sqrt{1-e_t^2}}{(1-e_t)(1+e_t)^7(1+\sqrt{1-e_t^2})(1+\frac{121}{304}e_t^2)}\\
&\times\left[\frac{91271}{59850}+\sum_{k=2}^{10}\mathcal{S}_e^{(k)}(\eta)e_t^k\right]
\end{aligned}
\tag{D.40}
$$

where $\gamma_E = 0.577...$ is the Euler constant and the tail enhancement factors $[\varphi_e(e_t),\psi_e(e_t),\zeta_e(e_t),\kappa_e(e_t)]$ are defined in [31]. The functions $[\mathcal{P}_e^{(k)}(\eta),\mathcal{S}_e^{(k)}(\eta)]$ are polynomials in η, specifically

$$
\mathcal{P}_e^{(0)}(\eta)=-\frac{\eta}{12}\,,
\tag{D.41}
$$

$$\begin{aligned}\mathcal{P}_e^{(1)}(\eta) = {} & \frac{370599031}{459648}\eta - \frac{24177239}{51072}\eta^2 + \frac{46101}{608}\eta^3 + \frac{82283}{1995}\gamma_E - \frac{72137736667}{126403200} \\ & - \frac{769}{57}\pi^2 + \frac{82283}{665}\ln(2) - \frac{2011}{1216}\pi^2\eta\,,\end{aligned} \tag{D.42}$$

$$\mathcal{P}_e^{(2)}(\eta) = -\frac{9135439}{8512}\eta^2 + \frac{23802845}{25536}\eta - \frac{1655487}{4256} + \frac{77915}{304}\eta^3 + 16\pi^2\eta\,, \tag{D.43}$$

$$\begin{aligned}\mathcal{P}_e^{(3)}(\eta) = {} & -\frac{595512727}{102144}\eta^2 + \frac{6892277}{4864}\eta^3 + \frac{71797}{665}\gamma_E - \frac{6899473429}{1663200} - \frac{671}{19}\pi^2 \\ & + \frac{28354579}{3591}\eta + \frac{215391}{665}\ln(2) - \frac{13525}{9728}\pi^2\eta\,,\end{aligned} \tag{D.44}$$

$$\mathcal{P}_e^{(4)}(\eta) = -\frac{21014717}{4256}\eta^2 - \frac{917485}{532} + \frac{137723689}{25536}\eta + \frac{4144843}{2432}\eta^3 - \frac{278}{19}\pi^2\eta\,, \tag{D.45}$$

$$\begin{aligned}\mathcal{P}_e^{(5)}(\eta) = {} & -\frac{3788393467}{408576}\eta^2 - \frac{82283}{1064}\gamma_E + \frac{16291239}{4864}\eta^3 + \frac{3845}{152}\pi^2 + \frac{30463753231}{3677184}\eta \\ & - \frac{502325236657}{202245120} - \frac{246849}{1064}\ln(2) + \frac{619095}{38912}\pi^2\eta\,,\end{aligned} \tag{D.46}$$

$$\mathcal{P}_e^{(6)}(\eta) = -\frac{16539923}{68096}\eta^2 + \frac{2092715}{51072}\eta - \frac{20806067}{34048} + \frac{745669}{1216}\eta^3 - \frac{1021}{304}\pi^2\eta\,, \tag{D.47}$$

$$\begin{aligned}\mathcal{P}_e^{(7)}(\eta) = {} & \frac{3175811627}{408576}\eta^2 - \frac{35817065233}{3677184}\eta - \frac{85979}{64}\eta^3 - \frac{880931}{12768}\gamma_E + \frac{41165}{1824}\pi^2 \\ & + \frac{80176348783}{14981120} - \frac{880931}{4256}\ln(2) - \frac{745}{64}\pi^2\eta\,,\end{aligned} \tag{D.48}$$

$$\mathcal{P}_e^{(8)}(\eta) = \frac{10498719}{4864} + \frac{88818089}{17024}\eta^2 - \frac{4689915}{896}\eta - \frac{5134385}{2432}\eta^3 + \frac{605}{304}\pi^2\eta\,, \tag{D.49}$$

$$\begin{aligned}\mathcal{P}_e^{(9)}(\eta) = {} & -\frac{467431}{152}\eta^3 - \frac{61311}{21280}\gamma_E - \frac{4101817087}{612864}\eta + \frac{573}{608}\pi^2 + \frac{706474273}{102144}\eta^2 \\ & + \frac{4808376554393}{2696601600} - \frac{183933}{21280}\ln(2) - \frac{47683}{38912}\pi^2\eta\,,\end{aligned} \tag{D.50}$$

$$\mathcal{P}_e^{(10)}(\eta) = \frac{507315}{896} + \frac{10083793}{9728}\eta^2 - \frac{4818031}{4256}\eta - \frac{281279}{608}\eta^3\,, \tag{D.51}$$

$$\mathcal{P}_e^{(11)}(\eta) = -\frac{64379}{152}\eta^3 + \frac{348257375}{5136384} - \frac{18848765}{34048}\eta + \frac{538919}{608}\eta^2\,, \tag{D.52}$$

$$\mathcal{S}_e^{(2)}(\eta) = -\frac{697}{1216}\pi^2\eta - \frac{351}{76}\eta^2 + \frac{7230223}{136800} + \frac{358327}{6384}\eta\,, \tag{D.53}$$

$$\mathcal{S}_e^{(3)}(\eta) = \frac{10245}{38}\eta^2 + \frac{1831605}{2128} - \frac{4225037}{3192}\eta + \frac{41}{8}\pi^2\eta\,, \tag{D.54}$$

$$\mathcal{S}_e^{(4)}(\eta) = -\frac{103033}{19456}\pi^2\eta + \frac{41831239}{25536}\eta - \frac{185949}{608}\eta^2 - \frac{139310891}{106400}\,, \tag{D.55}$$

$$\mathcal{S}_e^{(5)}(\eta) = \frac{129609}{304}\eta^2 - \frac{6189835}{4256}\eta + \frac{1634085}{1064} - \frac{7503}{2432}\pi^2\eta\,, \tag{D.56}$$

$$\mathcal{S}_e^{(6)}(\eta) = \frac{50061}{9728}\pi^2\eta - \frac{261333}{608}\eta^2 + \frac{895061}{896}\eta - \frac{6498062887}{7660800}\,, \tag{D.57}$$

$$\mathcal{S}_e^{(7)}(\eta) = -\frac{31159215}{17024} - \frac{152823}{304}\eta^2 + \frac{53246143}{25536}\eta - \frac{4961}{2432}\pi^2\eta\,, \tag{D.58}$$

$$\mathcal{S}_e^{(8)}(\eta) = \frac{14063}{19456}\pi^2\eta + \frac{3537630247}{1915200} + \frac{387195}{608}\eta^2 - \frac{59812661}{25536}\eta\,, \tag{D.59}$$

$$\mathcal{S}_e^{(9)}(\eta) = -\frac{29373}{152}\eta^2 + \frac{5897721}{8512}\eta - \frac{507315}{896}\,, \tag{D.60}$$

$$\mathcal{S}_e^{(10)}(\eta) = \frac{8717115}{34048} - \frac{5974083}{17024}\eta + \frac{62895}{608}\eta^2\,. \tag{D.61}$$

Finally, for $\langle \dot{v}_p \rangle$, we have

$$V_3(e_t,\eta;v_p) = \frac{4\pi(1-e_t)^4(1+e_t)^2\left[\tilde{\varphi}(e_t) - (1-e_t)\sqrt{1-e_t^2}\varphi(e_t)\right]}{e_t\sqrt{1-e_t^2}\left(1-\frac{13}{6}e_t+\frac{7}{8}e_t^2-\frac{37}{96}e_t^3\right)}\,, \tag{D.62}$$

$$\begin{aligned}
V_4(e_t,\eta;v_p) = {} & \frac{3(1-e_t)\left(1+9e_t-\frac{219}{8}e_t^2+\frac{1039}{48}e_t^3-\frac{251}{32}e_t^4+\frac{37}{24}e_t^5\right)(-5+2\eta)}{2(1+e_t)^3\sqrt{1-e_t^2}\left(1-\frac{13}{6}e_t+\frac{7}{8}e_t^2-\frac{37}{96}e_t^3\right)} \\
& + \frac{1}{(1+e_t)^4\left(1-\frac{13}{6}e_t+\frac{7}{8}e_t^2-\frac{37}{96}e_t^3\right)}\left[\frac{27}{2}\eta^2 - \frac{74243}{2016}\eta + \frac{411671}{18144}\right. \\
& + e_t\left(-\frac{275}{8}\eta^2 + \frac{119705}{1008}\eta - \frac{477359}{36288}\right) \\
& + e_t^2\left(\frac{34627}{192}\eta^2 - \frac{246245}{672}\eta + \frac{1200901}{12096}\right) \\
& + e_t^3\left(-\frac{18457}{64}\eta^2 + \frac{4580099}{5376}\eta - \frac{24721289}{48384}\right) \\
& + e_t^4\left(\frac{272143}{768}\eta^2 - \frac{1484453}{1792}\eta + \frac{26632505}{48384}\right) \\
& + e_t^5\left(-\frac{273941}{768}\eta^2 + \frac{363297}{448}\eta - \frac{16657127}{32256}\right) \\
& + e_t^6\left(\frac{77971}{768}\eta^2 - \frac{2128543}{10752}\eta + \frac{1922899}{16128}\right) \\
& \left. + e_t^7\left(-\frac{3145}{96}\eta^2 + \frac{108099}{1792}\eta - \frac{2162753}{64512}\right)\right]\,,
\end{aligned} \tag{D.63}$$

$$\begin{aligned}
V_5(e_t,\eta;v_p) = {} & \frac{30\pi(1-e_t)^4\left[1-\frac{8}{45}\eta+e_t\left(-\frac{1}{3}\eta-\frac{4}{15}\right)+e_t^2\left(-\frac{79}{45}\eta+\frac{5}{3}\right)\right]}{e_t\sqrt{1-e_t^2}\left(1-\frac{13}{6}e_t+\frac{7}{8}e_t^2-\frac{37}{96}e_t^3\right)}\tilde{\varphi}(e_t) \\
& - \frac{30\pi(1-e_t)^5\left[1-\frac{8}{45}\eta+e_t\left(-\frac{2}{15}\eta-\frac{2}{3}\right)+e_t^2\left(-\frac{64}{45}\eta+\frac{23}{15}\right)\right]}{e_t\left(1-\frac{13}{6}e_t+\frac{7}{8}e_t^2-\frac{37}{96}e_t^3\right)}\varphi(e_t) \\
& - \frac{8191\pi(1-e_t)^4}{672e_t\left(1-\frac{13}{6}e_t+\frac{7}{8}e_t^2-\frac{37}{96}e_t^3\right)}\left[\sqrt{1-e_t^2}\tilde{\psi}(e_t)-(1-e_t)^2(1+e_t)\psi(e_t)\right] \\
& - \frac{583\pi\eta(1-e_t)^4}{24e_t\left(1-\frac{13}{6}e_t+\frac{7}{8}e_t^2-\frac{37}{96}e_t^3\right)}\left[\sqrt{1-e_t^2}\tilde{\zeta}(e_t)-(1-e_t)^2(1+e_t)\zeta(e_t)\right]\,,
\end{aligned} \tag{D.64}$$

$$\begin{aligned}
V_6(e_t,\eta;v_p) = {} & \frac{116761(1-e_t)^5}{3675e_t\sqrt{1-e_t^2}\left(1-\frac{13}{6}e_t+\frac{7}{8}e_t^2-\frac{37}{96}e_t^3\right)}\left[(1-e_t)^2(1+e_t)\kappa(e_t)\right. \\
& \left. -\sqrt{1-e_t^2}\tilde{\kappa}(e_t)\right] + \frac{1}{e_t(1+e_t)^6\sqrt{1-e_t^2}\left(1-\frac{13}{6}e_t+\frac{7}{8}e_t^2-\frac{37}{96}e_t^3\right)} \\
& \times\left[\frac{91271}{18900}+\sum_{k=1}^{10}\mathcal{S}_v^{(k)}e_t^k\right] + \frac{1}{e_t(1+e_t)^6\left(1-\frac{13}{6}e_t+\frac{7}{8}e_t^2-\frac{37}{96}e_t^3\right)} \\
& \times\left\{\sum_{k=0}^{10}\mathcal{P}_v^{(k)}(\eta)e_t^k+\ln\left[\frac{(1-e_t)^{3/2}(1+e_t)^{1/2}v_p}{1+\sqrt{1-e_t^2}}\right]\mathcal{L}_v(e_t)\right\}
\end{aligned} \tag{D.65}$$

where $[\phi(e_t),\psi(e_t),\zeta(e_t),\kappa(e_t)]$ and $[\tilde{\varphi}(e_t),\tilde{\psi}(e_t),\tilde{\zeta}(e_t),\tilde{\kappa}(e_t)]$ are the tail enhancement factors for the energy and angular momentum fluxes, respectively. These functions are defined in [29,31], with analytic representations as functions of e_t given in [107]. The polynomials $[\mathcal{P}_v^{(k)}(\eta),\mathcal{S}_v^{(k)}(\eta),\mathcal{L}_v(e_t)]$ are given as follows,

$$\mathcal{P}_v^{(0)}(\eta) = -\frac{7}{576}\eta-\frac{91271}{18900}\,, \tag{D.66}$$

$$\begin{aligned}
\mathcal{P}_v^{(1)}(\eta) = {} & \frac{928379951}{2851200}-\frac{1712}{35}\ln(2)+\frac{1572589}{8064}\eta^2-\frac{40006439}{72576}\eta+\frac{16}{3}\pi^2+\frac{531}{64}\pi^2\eta \\
& -\frac{957}{32}\eta^3-\frac{1712}{105}\gamma_E\,,
\end{aligned} \tag{D.67}$$

$$\begin{aligned}
\mathcal{P}_v^{(2)}(\eta) = {} & \frac{3263}{96}\eta^3-\frac{2984087}{8064}\eta^2-\frac{2218668437}{2661120}+\frac{160428925}{580608}\eta \\
& +\frac{72011}{630}\gamma_E-\frac{673}{18}\pi^2+\frac{72011}{210}\ln(2)-\frac{275}{128}\pi^2\eta\,,
\end{aligned} \tag{D.68}$$

$$\begin{aligned}
\mathcal{P}_v^{(3)}(\eta) = {} & -\frac{799142495}{580608}\eta+\frac{36167515}{16128}\eta^2-\frac{134803129}{2217600}+\frac{229}{6}\pi^2-\frac{24503}{70}\ln(2) \\
& +\frac{62183}{1536}\pi^2\eta-\frac{99043}{128}\eta^3-\frac{24503}{210}\gamma_E\,,
\end{aligned} \tag{D.69}$$

$$\begin{aligned}
\mathcal{P}_v^{(4)}(\eta) = {} & \frac{340441}{384}\eta^3-\frac{44827219}{8064}\eta^2-\frac{26356578637}{7983360}+\frac{573433099}{96768}\eta+\frac{44833}{126}\gamma_E \\
& -\frac{2095}{18}\pi^2+\frac{44833}{42}\ln(2)+\frac{8155}{512}\pi^2\eta\,,
\end{aligned} \tag{D.70}$$

$$\begin{aligned}
\mathcal{P}_v^{(5)}(\eta) = {} & -\frac{1514002771}{193536}\eta+\frac{203612819}{21504}\eta^2+\frac{20453}{3072}\pi^2\eta+\frac{86977806011}{53222400}+\frac{109}{4}\pi^2 \\
& -\frac{34989}{140}\ln(2)-\frac{5262899}{1536}\eta^3-\frac{11663}{140}\gamma_E\,,
\end{aligned} \tag{D.71}$$

$$\begin{aligned}
\mathcal{P}_v^{(6)}(\eta) = {} & \frac{1795665}{512}\eta^3-\frac{113569023}{7168}\eta^2+\frac{3355299199}{165888}\eta-\frac{1042325420551}{106444800}+\frac{103897}{720}\gamma_E \\
& -\frac{6797}{144}\pi^2+\frac{103897}{240}\ln(2)+\frac{260347}{12288}\pi^2\eta\,,
\end{aligned} \tag{D.72}$$

$$\mathcal{P}_v^{(7)}(\eta) = \frac{66399433}{6144}\eta^2-\frac{58228753}{4608}\eta-\frac{3253}{6144}\pi^2\eta+\frac{103183627181}{17740800}+\frac{23}{16}\pi^2$$

$$- \frac{7383}{560}\ln(2) - \frac{1840299}{512}\eta^3 - \frac{2461}{560}\gamma_E \,, \tag{D.73}$$

$$\begin{aligned} \mathcal{P}_v^{(8)}(\eta) = {} & \frac{4377905}{1536}\eta^3 - \frac{109207321771}{23654400} - \frac{390150899}{43008}\eta^2 + \frac{1361907947}{129024}\eta + \frac{10593}{2240}\gamma_E \\ & - \frac{99}{64}\pi^2 + \frac{31779}{2240}\ln(2) + \frac{4059}{4096}\pi^2\eta \,, \end{aligned} \tag{D.74}$$

$$\mathcal{P}_v^{(9)}(\eta) = \frac{1559222101}{1892352} + \frac{82564327}{43008}\eta^2 - \frac{254674141}{129024}\eta - \frac{390379}{512}\eta^3 \,, \tag{D.75}$$

$$\mathcal{P}_v^{(10)}(\eta) = -\frac{2287742459}{11354112} - \frac{366721}{672}\eta^2 + \frac{11419241}{21504}\eta + \frac{10619}{48}\eta^3 \,, \tag{D.76}$$

$$\mathcal{S}_v^{(1)}(\eta) = -\frac{162703}{1440} - \frac{93}{4}\eta^2 + \frac{42221}{336}\eta - \frac{41}{64}\pi^2\eta \,, \tag{D.77}$$

$$\mathcal{S}_v^{(2)}(\eta) = -\frac{975}{4}\eta^2 - \frac{76684597}{151200} + \frac{138869}{112}\eta - \frac{369}{64}\pi^2\eta \,, \tag{D.78}$$

$$\mathcal{S}_v^{(3)}(\eta) = -\frac{1505201}{336}\eta + \frac{13471}{16}\eta^2 + \frac{997437}{320} + \frac{9307}{512}\pi^2\eta \,, \tag{D.79}$$

$$\mathcal{S}_v^{(4)}(\eta) = -\frac{2727}{2}\eta^2 - \frac{87322003}{16800} + \frac{12042805}{2016}\eta - \frac{24887}{3072}\pi^2\eta \,, \tag{D.80}$$

$$\mathcal{S}_v^{(5)}(\eta) = -\frac{1522313}{336}\eta + \frac{95255}{64}\eta^2 - \frac{25625}{2048}\pi^2\eta + \frac{16734821}{3840} \,, \tag{D.81}$$

$$\mathcal{S}_v^{(6)}(\eta) = \frac{9333}{64}\eta^2 - \frac{7698991}{4032}\eta + \frac{1808126359}{1209600} + \frac{39565}{3072}\pi^2\eta \,, \tag{D.82}$$

$$\mathcal{S}_v^{(7)}(\eta) = -\frac{118445}{64}\eta^2 + \frac{39219179}{5376}\eta - \frac{10291}{2048}\pi^2\eta - \frac{141403667}{23040} \,, \tag{D.83}$$

$$\mathcal{S}_v^{(8)}(\eta) = \frac{4839771539}{1209600} + \frac{88351}{64}\eta^2 - \frac{10136729}{2016}\eta + \frac{1517}{1536}\pi^2\eta \,, \tag{D.84}$$

$$\mathcal{S}_v^{(9)}(\eta) = -\frac{627055}{512} - \frac{14603}{32}\eta^2 + \frac{406929}{256}\eta \,, \tag{D.85}$$

$$\mathcal{S}_v^{(10)}(\eta) = \frac{182905}{896} + \frac{1295}{16}\eta^2 - \frac{123605}{448}\eta \,, \tag{D.86}$$

$$\begin{aligned} \mathcal{L}_v(e_t) = {} & \frac{10593}{2240}e_t^8 - \frac{2461}{560}e_t^7 + \frac{103897}{720}e_t^6 - \frac{11663}{140}e_t^5 + \frac{44833}{126}e_t^4 - \frac{24503}{210}e_t^3 \\ & + \frac{72011}{630}e_t^2 - \frac{1712}{105}e_t \,. \end{aligned} \tag{D.87}$$

This completes the amplitude vector fields to 3PN order.

APPENDIX E

HARMONIC DECOMPOSITION OF THE RADIATION REACTION FORCE

The equations governing the radiation reaction force within the osculating orbits method may be decomposed in a harmonic decomposition, as given by Eqs. (6.7)-(6.8) in the main manuscript. We here provide the coefficients of this harmonic decomposition. First, for $d\mathsf{p}/d\phi$, the coefficients are

$$
\begin{aligned}
k_p^0 &= 8 + 7(A_x^2 + A_y^2)\,, && \text{(E.1)}\\
k_p^{c,1} &= \frac{A_x}{12}\left[336 + 140a - 60b + (54 + 35a)(A_x^2 + A_y^2) - 15b(A_x^2 + A_y^2)\right]\,, && \text{(E.2)}\\
k_p^{c,2} &= \frac{5}{3}(15 + 14a - 6b)(A_x^2 - A_y^2)\,, && \text{(E.3)}\\
k_p^{c,3} &= \frac{5}{4}(6 + 7a - 3b)A_x(A_x^2 - 3A_y^2)\,, && \text{(E.4)}\\
k_p^{s,1} &= \frac{A_y}{12}\left[336 + 140a - 60b + (54 + 35a)(A_x^2 + A_y^2) - 15b(A_x^2 + A_y^2)\right]\,, && \text{(E.5)}\\
k_p^{s,2} &= \frac{10}{3}A_xA_y(15 + 14a - 6b)\,, && \text{(E.6)}\\
k_p^{s,3} &= \frac{5}{4}(6 + 7a - 3b)A_y(3A_x^2 - A_y^2)\,, && \text{(E.7)}
\end{aligned}
$$

Next, for $dA_x/d\phi$ we have

$$
\begin{aligned}
k_x^0 &= \frac{1}{24}A_x\left[304 + 121(A_x^2 + A_y^2)\right]\,, && \text{(E.8)}\\
k_x^{c,1} &= \frac{1}{96}\big\{768 + 3A_y^4(44 + 20a - 15b) + 5A_x^4(60 + 44a - 15b)\\
&\quad -10A_y^2(-80 + 20a + 3b) + 2A_x^2\big[1616 + 660a + 4(54 + 35a)A_y^2\\
&\quad -15(15 + 4A_y^2)b\big]\big\}\,, && \text{(E.9)}\\
k_x^{c,2} &= \frac{5}{12}A_x\left[56 + a(28 + 58A_x^2 - 34A_y^2) + A_x^2(66 - 21b) - 12b\right.\\
&\quad \left.+A_y^2(-16 + 3b)\right]\,, && \text{(E.10)}\\
k_x^{c,3} &= \frac{1}{192}\big\{3A_x^4(468 + 500a - 195b) - A_y^2\big[5056 + 60a(68 + 7A_y^2)\\
&\quad +A_y^2(564 - 315b) - 1980b\big] + A_x^2\big[5056 + 4080a + (-2520 - 3240a)A_y^2\\
&\quad +90(-22 + 9A_y^2)b\big]\big\}\,, && \text{(E.11)}\\
k_x^{c,4} &= \frac{5}{24}A_x(A_x^2 - 3A_y^2)(55 + 52a - 30b)\,, && \text{(E.12)}\\
k_x^{c,5} &= \frac{25}{64}(A_x^4 - 6A_x^2A_y^2 + A_y^4)(4 + 4a - 3b)\,, && \text{(E.13)}\\
k_x^{s,1} &= \frac{1}{48}A_xA_y\left\{1216 + 84(A_x^2 + A_y^2) + 40a\left[19 + 2(A_x^2 + A_y^2)\right]\right.\\
&\quad \left.-15b(14 + A_x^2 + A_y^2)\right\}\,, && \text{(E.14)}\\
k_x^{s,2} &= \frac{5}{12}A_y\left[56 + 4a(7 + 26A_x^2 + 3A_y^2) + A_x^2(107 - 33b)\right.
\end{aligned}
$$

$$+A_y^2(25-9b)-12b\big] \ , \tag{E.15}$$

$$\begin{aligned} k_x^{s,3} &= \frac{1}{24}A_xA_y\left[1264+36A_y^2+30a\left(34+17A_x^2-A_y^2\right)+A_x^2\left(456-180b\right)\right. \\ &\left.-495b-45A_y^2b\right] \ , \end{aligned} \tag{E.16}$$

$$k_x^{s,4} = -\frac{5}{24}A_y\left(-3A_x^2+A_y^2\right)\left(55+52a-30b\right) \ , \tag{E.17}$$

$$k_x^{s,5} = \frac{25}{16}A_xA_y\left(A_x^2-A_y^2\right)\left(4+4a-3b\right), \tag{E.18}$$

Finally, for $dA_y/d\phi$, the coefficients are

$$k_y^0 = \frac{1}{24}A_y\left[304+121(A_x^2+A_y^2)\right] \ , \tag{E.19}$$

$$\begin{aligned} k_y^{c,1} &= \frac{1}{48}A_xA_y\left\{1216+84A_y^2+40a\left[19+2(A_x^2+A_y^2)\right]+A_x^2(84-15b)\right. \\ &\left.-210b-15A_y^2b\right\} \ , \end{aligned} \tag{E.20}$$

$$\begin{aligned} k_y^{c,2} &= \frac{5}{12}A_y\left[-56-66A_y^2+a\left(-28+34A_x^2-58A_y^2\right)+A_x^2(16-3b)\right. \\ &\left.+12b+21A_y^2b\right] \ , \end{aligned} \tag{E.21}$$

$$\begin{aligned} k_y^{c,3} &= \frac{1}{24}A_xA_y\left\{-1264-456A_y^2+30a\left[A_x^2-17(2+A_y^2)\right]+495b\right. \\ &\left.+180A_y^2b+9A_x^2(-4+5b)\right\} \ , \end{aligned} \tag{E.22}$$

$$k_y^{c,4} = \frac{5}{24}A_y(-3A_x^2+A_y^2)(55+52a-30b)\,, \tag{E.23}$$

$$k_y^{c,5} = -\frac{25}{16}A_xA_y(A_x^2-A_y^2)(4+4a-3b)\,, \tag{E.24}$$

$$\begin{aligned} k_y^{s,1} &= \frac{1}{96}\left\{768+2A_y^2(1616+660a-225b)+3A_x^4(44+20a-15b)\right. \\ &+5A_y^4(60+44a-15b)+2A_x^2\big[400+20a(-5+7A_y^2)+A_y^2(216-60b) \\ &\left.-15b\big]\right\} \ , \end{aligned} \tag{E.25}$$

$$\begin{aligned} k_y^{s,2} &= \frac{5}{12}A_x\left[56+107A_y^2+4a(7+3A_x^2+26A_y^2)+A_x^2(25-9b)-12b\right. \\ &\left.-33A_y^2b\right] \ , \end{aligned} \tag{E.26}$$

$$\begin{aligned} k_y^{s,3} &= \frac{1}{192}\left\{A_x^4(564+420a-315b)-A_y^2\big[5056+60a(68+25A_y^2)-1980b\right. \\ &-117A_y^2(-12+5b)\big]+2A_x^2\big[2528+60a(34+27A_y^2)-990b \\ &\left.-45A_y^2(-28+9b)\big]\right\} \ , \end{aligned} \tag{E.27}$$

$$k_y^{s,4} = \frac{5}{24}A_x(A_x^2-3A_y^2)(55+52a-30b)\,, \tag{E.28}$$

$$k_y^{s,5} = \frac{25}{64}\left(A_x^4-6A_x^2A_y^2+A_y^4\right)\left(4+4a-3b\right), \tag{E.29}$$